2012

Controlling magnetic structure in extended solids using targeted chemical compositions

Jakoah Brgoch
Iowa State University

Controlling magnetic structure in extended solids using targeted chemical compositions

by

Jakoah Brgoch

A dissertation submitted to the graduate faculty

in partial fulfillment of the requirements for the degree of

DOCTOR OF PHILOSOPHY

Major: Chemistry

Program of Study Committee:
Gordon J. Miller, Major Professor
John D. Corbett
Patricia A. Thiel
Vitalij K. Pecharsky
Scott P. Beckman

Iowa State University

Ames, Iowa

2012

TABLE OF CONTENTS

ACKNOWLEDGMENTS

I would like to extend my gratitude first and foremost to my advisor, Professor Gordie Miller. I have learned more about chemistry during my time in his group than I could have ever imagined. He has been nothing short of an outstanding mentor in both my professional and personal life. I would also like to thank Professor John Corbett not only for serving on my committee, but also for teaching me to be critical of all research, even my own. Thank you to Professors Patricia A. Thiel, Vitalij K. Pecharsky, and Scott A. Beckman for serving on my Program of Study Committee and being wonderful teachers in and out of the classroom

I would also like to thank Dr. Mike Schmidt, who was an immense help for all things computational. I owe a great deal of gratitude to all of the group members in the Miller and Corbett groups, specifically Dr. Fei Wang, Dr. Srinivasa Thimmaiah, and Dr. Shalabh Gupta who trained me in all of my experimental and computational techniques. Thank you to Debanjan Ghosh and Yassir Mahmoud for their hard work in the lab, I enjoyed teaching them about solid-state chemistry. I would also like to thank our collaborators at the Rheinisch-Westfälische Technische Hochschule (RWTH) in Aachen, Germany. Professor Richard Dronskowski, *Priv. –Doz. Dr. rer. nat.* Boniface P. T Fokwa, and Christian Goerens were gracious hosts during my two visits to Aachen. I am pleased to have formed long lasting connections abroad.

I also express my gratefulness to all of my friends here in Ames: Bernie, Aaron, Kyle, Steve, Selena, Stacey, Justin, Kris, and Robyn made life in Ames a truly enjoyable time with enough stories to last a lifetime. I cannot thank Emily enough for understanding the insanity that is graduate school and sticking with me anyway. Also thank you to my entire family for supporting me during my collegiate tenure.

Finally, none of this research would have been possible with out the generous support of the National Science Foundation, Materials World Network (NSF DMR 08-06507).

J. B.

ABSTRACT

The ability to combine experiment and theory provides the framework for targeting compositions that may exhibit a fascinating magnetic response such as ferromagnetism, antiferromagnetism, or ferrimagnetism. Using solid-state synthesis techniques, structural characterization, and theoretical analysis, two intermetallic borides series were analyzed for their magnetic properties. In $M_2M'(T_{1-x}T'_x)_5B_2$ (M = Sc, Ti, Zr; M′ = 3*d* element; T/T′ = Ru, Rh, Ir), the M′ atom forms chains that when occupied by magnetic atoms, i.e., Mn, Fe, Co, Ni, have interatomic bond distances short enough for one-dimensional, long-range magnetic ordering. The prototypical series, $Sc_2Fe(Ru_{1-x}Rh_x)_5B_2$ ($0 \leq x \leq 1$), was previously identified to change from antiferromagnetic in the Ru-rich structures to ferromagnetic in the Rh-containing compounds. The change in magnetic ordering as a function of composition stems from the occupation of antibonding states at the Fermi level. As a result, theoretical techniques were utilized to identify additional compositions that may form this structure type and show this same unique trend in magnetism. The discovery of a Zr series, by directed synthesis, provided further unique magnetic response by being the first intermetallic boride to order ferrimagnetically.

Additionally, the structures of $Ti_{9-y}M_{2+y}Ru_{18}B_8$, contains M atoms that form dumbbells of Fe atoms in the *ab*-plane that condense along the *c*-direction to form ladders. When Ti atoms are substituted by the M atoms (*y* = ca. 1-2) the resulting structure contains one-dimensional, single-atom chains (as in the $M_2M'T_5B_2$ series) and one-dimensional ladders (as in the $Ti_9M'_2T_{18}B_8$ series) in the same compound. The synthesis of $Ti_8Fe_3Ru_{18}B_8$ was the first compound to show both of these subunits in the same structure. Since the bond distances between the chain and ladder sites is only ca. 3.00 Å, the magnetic atoms form a linear tetramer that we have termed a "magnetic scaffold". Furthermore, $Ti_8Fe_3Ru_{18}B_8$ contains two separate, one-dimensional chain sites allowing independent local magnetic ordering ultimately providing a system to discover new intermetallic ferrimagnets. In fact, experimental investigations indicate $Ti_8Fe_3Ru_{18}B_8$ and the isotypic $Ti_7Fe_4Ru_{18}B_8$ order ferrimagnetically. Computational

results identified complex magnetic exchange in the magnetic scaffold as the origin of the ferrimagnetism in these structures.

The composition-property relationship was extended to investigate non-stoichiometry in tetragonal iron sulfide ($Fe_{1+\delta}S$). A delicate balance between the Madelung energy and the occupation of antibonding orbitals drives the inclusion of interstitial Fe in this structure. The additional Fe atoms change the Fermi surface, as well as create a spin density wave. These predicted changes in properties have implications for identifying potential superconductivity in the new Fe-based compounds.

CHAPTER 1

Introduction

1.1 Magnetic Materials

A long-standing goal of solid-state chemistry has been to identify relationships among the stoichiometry of compounds, structures they adopt, and their physical properties. Recent research incorporating these three principles has manifested in the rapid advance of materials containing cooperative magnetic phenomena, like ferromagnetism, antiferromagnetism, and ferrimagnetism.[1,2] Because materials with these properties form the basis of most new technology, their continued study is of paramount importance.[3] Traditionally, iron ferrite, γ-Fe_2O_3, and chromium oxide, CrO_2, were employed for these applications. The iron-based oxides were used because they were inexpensive and chemically stable. However, synthetic preparation of these compounds yielded a wide dispersion of particle size resulting in lower coercivity.[3] The chromium compounds exhibited the desired magnetic properties, but proper disposal of the chromium-based compounds can be difficult. Newer data storage materials have generally involved shifting previously identified functional materials such as FeCo, $BaFe_{12}O_{19}$, and T_2O_3 (T = Mn, Co, Fe) from the bulk to the nanoscale.[4-7] Their simple stoichiometry and structures make it easier to predict the formation of desired phases and their corresponding physical properties. Although this may be advantageous for applications, the correlation between composition-structure-property of these and related materials are still unclear.

Recent advances in density functional theory (DFT) have provided grounds to use the electronic structure of materials to evaluate these relationships. For instance, DFT has been successfully employed to identify the structure formation of quasicrystals, γ-brasses, and iron nitrides for given compositions. Additionally, GaT (T = Cr, Mn, Fe) compounds were investigated for their composition-property relationships since the long range magnetic ordering changes as a function of T atom.[8-13] Nevertheless, it remains necessary for theoreticians and experimentalists to work closely together to identify new magnetic materials

1.2 Computational Consideration for Directed Synthesis

Predicting the formation of structures using *ab initio* methods is a difficult (if not impossible) task, regardless of the quality of electronic structure calculations. Thermodynamic and kinetic factors will always dominate structure formation. Although recent research by Dronskowski *et al.* has increased our capability to calculate the "thermodynamic" characteristics of solids using computational approaches, there are still many limitations to the methods.[14] One advantage we, as chemists, do have is the ability to draw from our vast knowledge of previously discovered structures. Analyzing the band structures or density of states (DOS) in the vast libraries of known structures will provide the grounds necessary to develop a set of "signs" that may be indicative of which structure type will form for a given composition.

Arguably the most widely recognized feature for (electronic) stability in intermetallic compounds is the presence of a pseudogap at the Fermi level (E_F).[15] Compounds that inherently have a pseudogap present at E_F do not have an energetic driving-force for distortion, and, thus, are more likely to form in the expected structure type. In cases where the DOS at E_F is sufficiently high, a compound is susceptible to structural or electronic distortions. For instance, TiH_2 relieves the high DOS at E_F by undergoing a Jahn-Teller-like structural distortion from the cubic fluorite structure type (space group No. 225) to a tetragonal fluorite structure type (space group No. 139).[16,17] Another distortion pathway due to a high DOS at E_F is a rearrangement of the electronic structure, which can result in the development of long-range magnetic ordering. This reorganization is the basis for the research presented here; hence, it is discussed in detail below. Another common feature in the calculated electronic structure of known extended solids is the optimization of interatomic bonding interactions. As with molecules, populating antibonding orbitals or under-populating bonding orbitals will tend to decrease the orbital overlap populations, which in turn, destabilizes a structure. To identify the overlap populations in solids, tools such as the crystal orbital Hamilton population (COHP) analysis are used.[18-20] Analyzing the point where the COHP curve

crosses from antibonding to bonding states on the energy scale will indicate if the bonding situation is optimized.

Although the simple presence of a pseudogap or optimized bonding interactions does not predict the formation of new structure types, modeling hypothetical compositions in known structure types can identify regions of electronic stability. However, selecting the right combination of elements to optimize bonding or establish a pseudogap can be arduous. The rigid band approximation can expedite this process by assuming the shape of the DOS curve for a known structure will remain constant on a fixed energy scale. Thus, adding or subtracting valence electrons (VEs) will simply move the position of the Fermi level.[21] As a result, varying the composition to target VE counts that place the Fermi level in a pseudogap can be very conducive for the discovery of new compounds. One drawback to the rigid band approximation is that the addition of only a few electrons relative to the base composition can be tolerated before the DOS will tend to change. Regardless, by distinguishing ranges of VE counts, experimental chemists can direct their synthetic strategy and identify new solid-state materials.

These "signs" developed to identify potential new intermetallic compounds have been extended to examine, and even predict, physical properties such as magnetic order. As mentioned above, if the calculated DOS contains a large peak at E_F, the structure will likely distort. In compounds that are prone to developing a magnetic moment, *e.g.*, those containing Mn, Fe, Co, and Ni, a rearrangement of the electronic states may occur rather than a structural distortion due to the large exchange energies. Electronic rearrangements can by investigated by invoking spin-polarization, which occurs by decoupling the "spin-up" and "spin-down" electrons. The DOS of materials that are susceptible to rearrangement will split into a majority and minority component with the former having a larger electron population than the latter. A non-zero difference between these two populations is the formation of a theoretical magnetic moment. This process is illustrated in Figure 1.

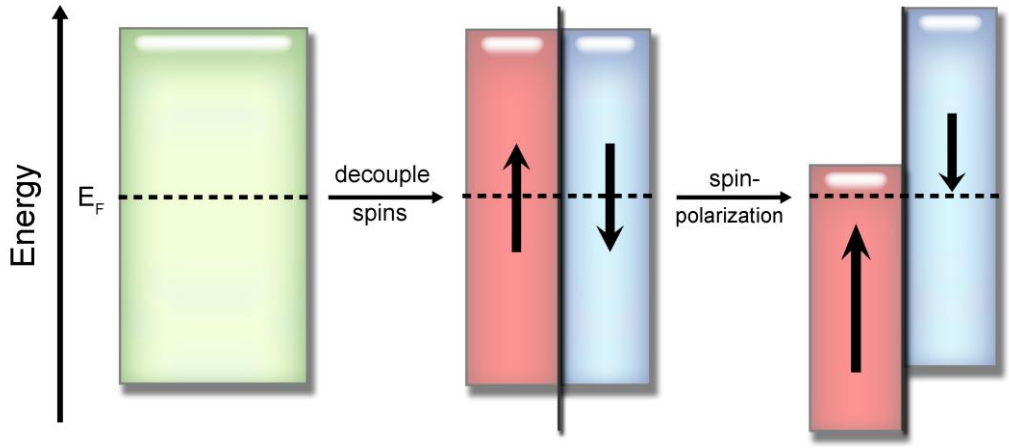

Figure 1. The DOS is represented as a block diagram. The spins are explicitly coupled (left) of the figure, this is the case when using the local density approximation (LDA). When the spins are decoupled, they split into "spin-up" and "spin-down" sublattices (center), this can be completed using the local spin density approximation (LSDA). Spin-polarization splits the degenerate spins into a spin-majority band and minority band (right). The difference between these is the calculated magnetic moment.

The type of long range magnetic ordering that results upon spin-polarization can be identified using the Stoner criterion. By analyzing the number of states (NE_F) at the Fermi level can indicate whether the Stoner criterion [$I(NE_F) > 1$, where I is the intra-atomic exchange energy] is met and if ferromagnetism should result. Unfortunately, this set of rules can only be used to identify ferromagnetism with no such criterion existing to identify antiferromagnetic ordering. Additionally, the Goodenough-Kanamori rules for superexchange interactions[22-24] can be used to predict ferromagnetic or antiferromagnetic ordering. These rules, however, only consider indirect exchange pathways in compounds with highly localized orbitals.

A recent application of chemical bonding analysis has been shown to indicate potential magnetic ordering.[20,25,26] For structures that contain a peak in the LDA-DOS, illustrated in Figure 2a, analyzing the orbital overlap (COHP) curves between two magnetic atoms at E_F can indicate the magnetic rearrangement. If the E_F sits in a nonbonding region or an antibonding region, spin-polarization should result, respectively, in antiferromagnetic or ferromagnetic ordering.[25] The prototypical example of ferromagnetic ordering is bcc-Fe. The Fermi level in the Fe-Fe COHP curve sits in a

region of Fe-Fe antibonding orbitals. When spin-polarization is invoked and the two spin sublattices split, occupation of the Fe-Fe antibonding states are eliminated in the spin-up (↑) channel. Extending this theory to the entire 3*d* series shows that a majority of the 3*d* orbitals lie above E_F for the earlier transition metals, and thus, there is no driving force for magnetic rearrangement.[26] In Cr, however, the Fermi level occurs right at the crossover point between bonding and antibonding states. Since Cr is known to be antiferromagnetic,[27] this is likely indicative of antiferromagnetic ordering. To summarize, the presence of antibonding states at the Fermi level of an M-M COHP curve (where M is a magnetic atom) is characteristic of itinerant ferromagnetism whereas nonbonding states, or a crossover, suggests antiferromagnetism. These M-M COHP curves are illustrated in Figure 2b. However, in both cases sufficient exchange energy is necessary to overcome the potential of structural rather than electronic distortion. Consequently, by combining (LDA) electronic structure calculations of known magnetic compounds and the rigid band approximation, it is possible to find compounds that may show magnetic ordering based on their VE count.

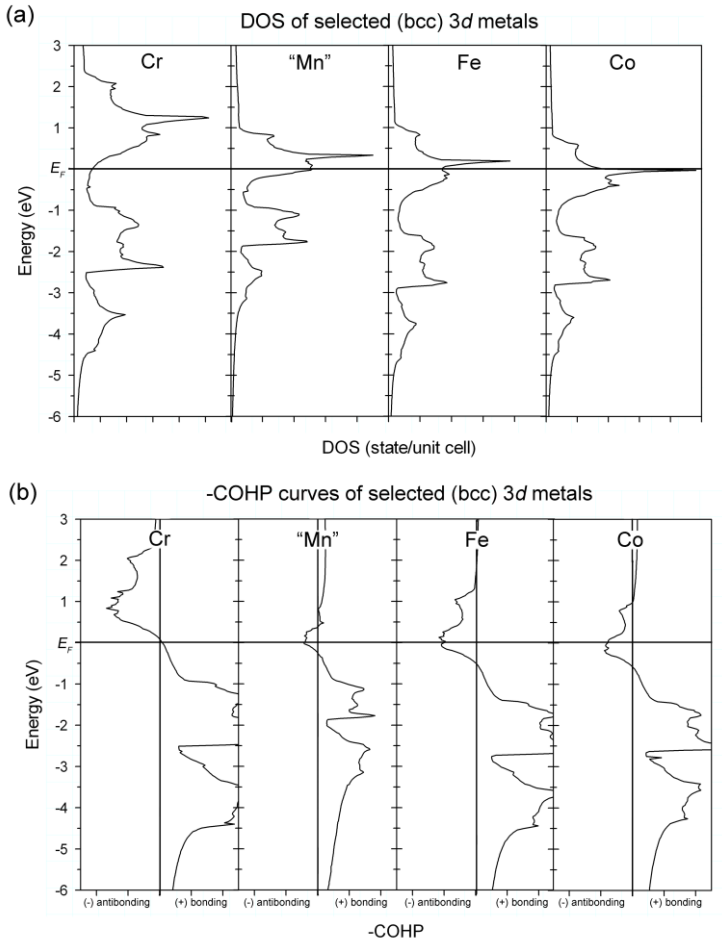

Figure 2. (a) the DOS and (b) –COHP curves of bcc- Cr, "Mn", Fe, and Co. "bcc-Mn" is a hypothetical structure and modeled following previous examples.[20] All electronic structure calculations were completing using TB-LMTO (Stuttgart code).

1.3 Complex Intermetallic Borides

Using the directed synthetic methods described in the previous section, two classes of intermetallic borides have been discovered for a wide range of possible compositions. The first series of compounds follow the general formula $M_2M'T_5B_2$ (M = Mg, Sc, Ti, Zr; M′ = Cr, Mn, Fe, Co, Ni; T = Ru, Rh, Ir) and is illustrated in Figure 3a.[28-35] The compounds crystallize in space group *P*4/*mbm* as a structural variant of the fundamental $Ti_3Co_5B_2$ structure type.[36] Here, planar sheets of the T atoms form triangles, pentagons, and cubes, which create trigonal, pentagonal, and pseudo-cubic prismatic voids when stacked along the [001] direction. The centers of these voids are occupied by

boron in the trigonal prisms, M atoms in the pentagonal prisms, and M′ in the pseudo-cubic prisms. Since these structures contain a relatively short *c*-axis of *ca.* 3.0 Å, magnetically active M′ atoms, such as Mn, Fe, Co, and Ni, will form *magnetic chains* along the [001] direction, Figure 3b. Although each unit cell contains two magnetic chains, the inter-chain distance is *ca.* 6.5 Å, making through-space exchange negligible. However, through-bond exchange is possible in the *ab*-plane, resulting in three-dimensional magnetic systems.

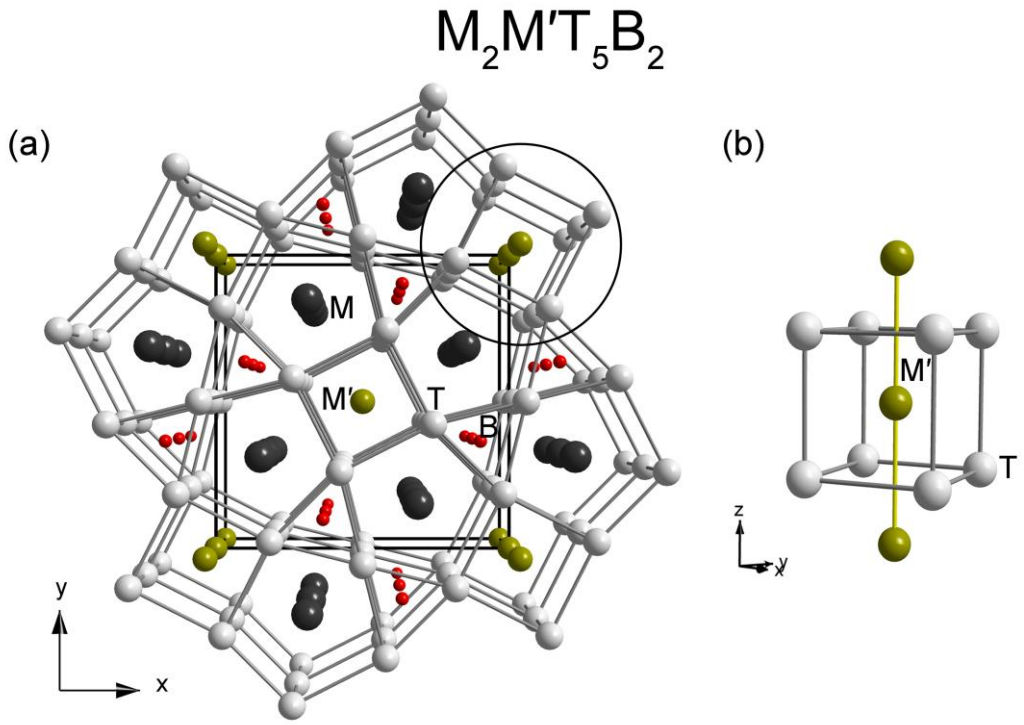

Figure 3. (a) The $M_2M'T_5B_2$ structure shown as a perspective along the [001] direction. The *magnetic chains* are highlighted by the circle. (b) The magnetic chain. The M atoms are dark gray, M′ is yellow, T is light gray, and B is red.

One of the most prolific compounds investigated in this series was the pseudo-quaternary compound $Sc_2Fe(Ru_xRh_{1-x})_5B_2$ ($0 \leq x \leq 1$) with VE counts ranging between 60 $\leq$ VE $\leq$ 65.[30,34] The short Fe-Fe distances and the ability to tune the VE count via directed substitution made this compound ideal to investigate compositionally dependent magnetic ordering. Using SQUID magnetometry, antiferromagnetic ordering was

identified at low electron counts (<62 VE) whereas ferromagnetic ordering was present at VE counts above 63 VE. The observed change in magnetic ordering was understood through the Fe-Fe COHP curve, as discussed above. For the ferromagnetic interactions, the VE count places the Fermi level in Fe-Fe antibonding states. Increasing the number of VE's raises the Fermi level to nonbonding states, and thus, orders antiferromagnetically. Additional work identified the Fe-Fe magnetic exchange (J_{ij}) values further substantiated the observed ferromagnetic and antiferromagnetic orderings. In addition to the calculated Fe-Fe exchange values, the J_{ij} values for Fe-Ru and Fe-Rh contacts yielded some unique results. The exchange energy between Fe-Ru was much smaller (0.07 meV) relative to the Fe-Rh interaction (3.77 meV).[37] Although an explanation for such a large difference has yet to be fully identified, it was postulated to stem from the Rh 4*d* orbitals lying in a lower energy region compared to the Ru 4*d* orbitals. From these calculations, multiple scattering theory was applied to estimate the magnetic ordering temperature (T_C/T_N) in this series and provided good agreement with the experimentally determined temperatures. For instance, $Sc_2FeRu_5B_2$, T_N = 148 K (13 K experimental); $Sc_2FeRh_5B_2$, T_C = 335 K (450 K experimental).[37]

After the discovery of compositionally dependent magnetism in the Sc series, additional analogues including an isostructural Ti, which also exhibited unconventional magnetic behavior, were discovered. In the series of $Ti_2Fe(Ru_xRh_{1-x})_5B_2$ ($0.2 \leq x \leq 1$; $63 \leq VE \leq 67$), ferromagnetic ordering was determined for all VE counts with T_C ranging between 220 K and 390 K.[35] Although the long range magnetic ordering does not change, the coercive behavior was found to have a strong VE dependence. The mechanism behind this behavior is still under investigation. Furthermore, the discovery of a Zr analogue with the general formula $Zr_2Fe_{1-\delta}(Ru_xRh_{1-x})_{5+\delta}B_2$ ($0 \leq x \leq 0.2$; δ = ca. 0.10; $63 \leq VE \leq 64$) was the first known intermetallic boride to order ferrimagnetically as determined by magnetic measurements and computational predictions.[28] Chapter 3 discusses this compound in depth.

The $M_2M'T_5B_2$ structure displays a wide range of potential VE counts by varying the T atoms, however initial attempts to vary the M site resulted in the discovery of a new series and second class of intermetallic borides, $M_9M'_2T_{18}B_8$ (M = Zn, Ti; M′ = Cr, Mn,

Fe, Co, Ni, Cu, Zn; T = Ru, Rh, Os, Ir).[38-40] This class of compounds, illustrated in Figure 4a, is structurally related to $M_2M'T_5B_2$ also crystallizing in space group *P*4/*mbm*, however, it is a structural variant of the $Zn_{11}Rh_{18}B_8$ type structure.[40] Again, the T atoms compose a network forming trigonal prisms filled by boron atoms while M atoms fill the pentagonal prisms and pseudo-cubic prisms. Additionally, the structure contains elongated hexagonal prisms, which are filled by two M′ atoms. The distance between these M′ atoms is short enough (ca. 2.50 Å) to consider this unit a dumbbell, highlighted in Figure 4b. When condensed in the solid state, the dumbbells form a ladder motif along the [001] direction, and is one of the first known examples of a ladder in an intermetallic compound.[39] Analogous to the previous boride series, the incorporation of magnetically active M′ atoms results in the formation of a *magnetic ladder*.

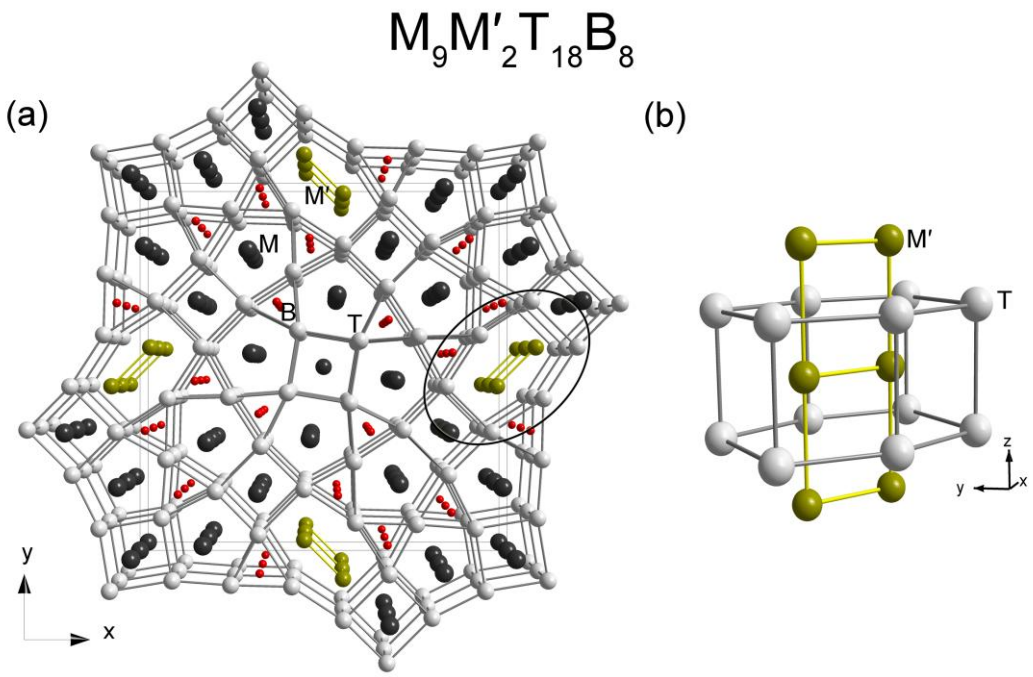

Figure 4. (a) The $M_9M'_2T_{18}B_8$ structure shown as a perspective along the [001] direction. The *magnetic ladders* are highlighted by the circle. (b) The magnetic ladder. The M atoms are dark gray, M′ is yellow, T is light gray, and B is red.

The first structure investigated in this new series was $Ti_9Fe_2Ru_{18}B_8$.[39] As with all of these high-melting point intermetallics, the synthesis was completed using arc-welding and characterized by powder and single crystal X-ray diffraction and Energy Dispersive

X-ray Spectroscopy (EDX). Magnetic measurements indicated ferromagnetic ordering with a Curie temperature of ca. 200 K. Theoretical investigations identified a spin-triplet Fe_2 dimer that is coupled ferromagnetically (identified by COHP curve) to the surrounding Fe_2 dimers forming a ferromagnetic ladder. The VE count of this structure was also varied forming the compositions $Ti_9M'_2Ru_{18}B_8$ (M = Cr, Mn, Co, Ni, Cu, Zn). The compounds most likely to contain long-range magnetic ordering were $Ti_9Co_2Ru_{18}B_8$ and $Ti_9Ni_2Ru_{18}B_8$, yet they were both Pauli paramagnetic.[38] It is not entirely clear why magnetization does not develop for these compositions, and future research is warranted. Further attempts to vary the VE count by substituting the T atoms following the general formula $Ti_9M'_2(Ru_{1-x}T'_x)_{18}B_8$ (T′ = Rh, Ir; $0 \leq x \leq 1$) were explored, though the desired phase was only achieved for substitution values of $x <$ ca. 0.17.[41] These compounds are discussed in chapters 5-7. With the limited substitution of T atoms, the VE count will need to be varied through alternate routes. Potential options include substituting Ti with another early transition metal or substituting B for another main group element, such as carbon. Moreover, the stoichiometry of could be varied to also modify the VE count.

1.4 Research Goals

The unifying theme of this research is to identify trends in crystal chemistry and magnetism as a function of valence electron count. The formation of two independent structure types with a wide range of compositions – $M_2M'T_5B_2$ (M = Mg, Sc, Ti, Zr; M′ = Cr, Mn, Fe, Co, Ni; T = Ru, Rh, Ir) and $M_9M'_2T_{18}B_8$ (M = Zn, Ti; M′ = Cr, Mn, Fe, Co, Ni, Cu, Zn; T = Ru, Rh, Os, Ir) – make these compounds valuable for investigating a structure-composition relationship. We have sought to combine theory and experiment to develop a set of "signs" to identify which structure type will form as a function of the composition. Simultaneously, a composition-physical property relationship was explored in these two classes of borides. These systems were utilized to understand, or even predict, the magnetic ordering in these complex structures. Ultimately, using the collection of rules and insights presented here, future research can benefit from a more directed synthetic approach to chemically controlling itinerant magnetism. Additionally, tetragonal iron sulfide ($Fe_{1+\delta}S$) was explored for its composition-property relationship

based on the interstitial content (δ). We have strived to understand how the electronic properties change due to the addition of Fe in the structure.

1.5 Organization of the Thesis

Chapter 2 of this thesis contains the experimental and computational methods employed to conduct the research.

Chapter 3 expands on the discovery of the Zr based intermetallic boride. Accordingly, the series $Zr_2Fe(Ru_xRh_{1-x})_5B_2$ ($0 \leq x \leq 1$) was explored to investigate its VE dependent magnetic ordering.

[Brgoch, J.; Yeninas, S.; Prozorov, R.; Miller, G. J. "Structure, Bonding, and Magnetic Response in Two Complex Borides: $Zr_2Fe_{1-\delta}Ru_{5+\delta}B2$ and $Zr_2Fe_{1-\delta}(Ru_{1-x}Rh_x)_{5+\delta}B_2$," *J. Solid State Chem.* **2010**, *183*, 2917-2924].

Chapter 4 explains the 'coloring problem' as it pertains to the $M_2M'T_5B_2$ structure. A site preference in the compound is identified as well as the effects on magnetic ordering.

Chapter 5 examines the experimental modification of the stoichiometry in the series $Ti_{9-x}Fe'_{2+x}Ru_{18}B_8$. The synthetic preparation and characterization as well as magnetic measurements are presented.

[Goerens, C.; Brgoch, J.; Miller, G. J.; Fokwa, B. P. T. "Scaffolding, Ladders, Chains, and Rare Ferrimagnetism in Intermetallic Borides: Synthesis, Crystal Chemistry and Magnetism," *Inorg. Chem.* **2011**, *50*, 6289.]

Chapter 6 evaluates the electronic structure of the new series $Ti_{9-x}Fe_{2+x}Ru_{18}B_8$. A site preference for the atomic substitution is identified, bonding in ladder motif investigated, and changes in the magnetic that occur with the addition of Fe are uncovered.

[Brgoch, J.; Goerens, C.; Fokwa, B. P. T.; Miller, G. J. "Scaffolding, Ladders, Chains, and Rare Ferrimagnetism in Intermetallic Borides: Electronic Structure Calculations and Magnetic Ordering," *J. Am. Chem. Soc.* **2011**, *133*, 6832.]

Chapter 7 explores the series $Ti_{9-x}M'_{2+x}Ru_{18}B_8$ (M = Cr-Ni) by theory and experiment. The synthetic preparation, characterization, and magnetic measurements as well as theoretical considerations are presented.

Chapter 8 extends the thesis beyond these intermetallic borides to research the stoichiometry of the mineral Mackinawite (tetragonal $Fe_{1+x}S$).

[Brgoch, J.; Miller, G. J. "Validation of Interstitial Iron and Consequences of Nonstoichiometry in Mackinawite ($Fe_{1+x}S$)," *J. Phys. Chem. A* **2012**, *116*(*9*), 2234.]

Chapter 9 emphasizes the general conclusions of this research presented herein.

1.6 References

(1) Chikazumi, S. *Physics of Ferromagnetism*; Clarendon Press: Oxford, 1997.
(2) Lueken, H. *Magnetochemie*; Teubner: Stuttgart, 1999.
(3) Spaldin, N. A. *Magnetic Materials: Fundamentals and Applications*; Cambridge University Press, 2011.
(4) Hu, Y.; Qian, H.; Mei, T.; Guo, J.; White, T. *Materials Letters*, *64*, 1095.
(5) Li, Y.; Huang, Y.; Yan, L.; Qi, S.; Miao, L.; Wang, Y.; Wang, Q. *Appl. Surf. Sci.* **2011**, *257*, 8974.
(6) Wei, X.-W.; Zhu, G.-X.; Liu, Y.-J.; Ni, Y.-H.; Song, Y.; Xu, Z. *Chem. Mater.* **2008**, *20*, 6248.
(7) Reiss, G.; Hutten, A. *Nat. Mater.* **2005**, *4*, 725.
(8) Lin, Q.; Corbett, J. D. *Inorg. Chem.*, *49*, 10436.
(9) Thimmaiah, S.; Miller, G. J. *Chem. Eur. J.*, *16*, 5461.
(10) Dong, C.; Wang, Q.; Qiang, J. B.; Wang, Y. M.; Jiang, N.; Han, G.; Li, Y. H.; Wu, J.; Xia, J. H. *Journal of Physics D: Applied Physics* **2007**, *40*, R273.
(11) Gourdon, O.; Miller, G. J. *J. Solid State Chem.* **2003**, *173*, 137.
(12) Gourdon, O.; Bud'ko, S. L.; Williams, D.; Miller, G. J. *Inorg. Chem.* **2004**, *43*, 3210.
(13) Ma, X. G.; Jiang, J. J.; Liang, P.; Wang, J.; Ma, Q.; Zhang, Q. K. *Journal of Alloys and Compounds* **2009**, *480*, 475.
(14) Stoffel, R. P.; Wessel, C.; Lumey, M.-W.; Dronskowski, R. *Angew. Chem. Int. Ed.* **2010**, *49*, 5242.
(15) Gourdon, O.; Gout, D.; Miller, G. J. In *Encyclopedia of Condensed Matter Physics*; Franco, B., Gerald, L. L., Peter, W., Eds.; Elsevier: Oxford, 2005, p 409.
(16) Quijano, R.; de Coss, R.; Singh, D. J. *Phys. Rev. B* **2009**, *80*, 184103.
(17) Gupta, M. *Solid State Comm.* **1979**, *29*, 47.
(18) Dronskowski, R.; Blöchl, P. E. *J. Phys. Chem.* **1993**, *97*, 8617.
(19) Hoffmann, R. *Solids and Surfaces: A Chemist's View of Bonding in Extended Structures*; VCH: New York, 1988.
(20) Dronskowski, R.; Hoffmann, R. *Computational Chemistry of Solid State Materials: A Guide for Materials Scientists, Chemists, Physicists and Others*; John Wiley & Sons, 2008.
(21) Massalski, T. B.; Mizutani, U. *Electronic Structure of Hume-Rothery Phases*; Pergamon Press, 1978.
(22) Goodenough, J. B. *Phys. Rev.* **1955**, *100*, 564.

(23) Goodenough, J. B. *J. Phys. Chem. Solids* **1958**, *6*, 287.
(24) Kanamori, J. *J. Phys. Chem. Solids* **1959**, *10*, 87.
(25) Landrum, G. A.; Dronskowski, R. *Angew. Chem. Int. Ed.* **1999**, *38*, 1389.
(26) Landrum, G. A.; Dronskowski, R. *Angew. Chem. Int. Ed.* **2000**, *39*, 1560.
(27) Werner, S. A.; Arrott, A.; Atoji, M. *J. Appl. Phys.* **1968**, *39*, 671.
(28) Brgoch, J.; Yeninas, S.; Prozorov, R.; Miller, G. J. *J. Solid State Chem.* **2010**, *183*, 2917.
(29) Dronskowski, R.; Korczak, K.; Lueken, H.; Walter, J. *Angew. Chem. Int. Ed.* **2002**, *41*, 2528.
(30) Fokwa, B. P. T.; Lueken, H.; Dronskowski, R. *Chem. Eur. J.* **2007**, *13*, 6040.
(31) Hermus, M.; Fokwa, B. P. T. *Z. Anorg. Allg. Chem* **2011**, *637*, 947.
(32) Jung, W.; Schiffer, J. *Z. Anorg. Allg. Chem* **1990**, *581*, 135.
(33) Nagelschmitz, E. A.; Jung, W. *Chem. Mater.* **1998**, *10*, 3189.
(34) Nagelschmitz, E. A.; Jung, W.; Feiten, R.; Müller, P.; Lueken, H. *Z. Anorg. Allg. Chem* **2001**, *627*, 523.
(35) Fokwa, B. P. T.; Lueken, H.; Dronskowski, R. *Eur. J. Inorg. Chem.* **2011**, *2011*, 3926.
(36) Kuz'ma, Y. B.; Yarmolyuk, Y. P. *Zhurnal Strukturnoi Khimii* **1971**, *12*, 458.
(37) Samolyuk, G. D.; Fokwa, B. P. T.; Dronskowski, R.; Miller, G. J. *Phys. Rev. B* **2007**, *76*, 094404.
(38) Fokwa, B. P. T.; Goerens, C.; Gilleßen, M. *Z. Kristallogr.* **2010**, *225*, 180.
(39) Fokwa, B. P. T.; Samolyuk, G. D.; Miller, G. J.; Dronskowski, R. *Inorg. Chem.* **2008**, *47*, 2113.
(40) Eibenstein, U.; Jung, W. *Z. Anorg. Allg. Chem* **1998**, *624*, 802.
(41) Brgoch, J.; Miller, G. J., Unpublished Results.

CHAPTER 2

Experimental and Computational Techniques

This chapter provides a detailed description of the experimental and computational methods utilized to complete the research. Along with each explanation are some of the advantages and disadvantages inherent within the technique. Additional information for each technique is also provided in the corresponding chapters.

2.1 Synthesis

2.1.1 Starting Materials. High purity elements, listed in Table 1, were used as starting materials for all synthetic preparations. All elements were used as received from the manufacturer. The starting materials and prepared samples were stable in air at room temperature as pieces and a finely ground powder for several weeks as determined using powder X-ray diffraction.

Table 1. The starting materials used for all synthetic preparations.

Element	Source	Melting Point (K)	Purity	Form
Ti	Degussa	1933	99%	Chunks
Zr	MPC-Ames Lab	2125	99.99%	Pieces
Cr	ABCR	2130	99.9%	Powder
Mn	ABCR	1518	99.9%	Powder
Fe	Sigma Aldrich	1808	99.98%	Pieces
	ABCR		99.9%	Powder
Co	ABCR	1768	99.9%	Powder
Ni	ABCR	1726	99.9%	Powder
Ru	MPC-Ames Lab	2523	99.99%	Pieces
Rh	MPC-Ames Lab	2239	99.95%	Pieces
B	Alfa Aesar	2573	99.999%	Pieces

2.1.2 Arc-Melting. All materials were synthesized by melting stoichiometric ratios of elemental metals using an electric arc furnace. The weighed elements were placed on a water-cooled copper hearth under an inert argon atmosphere. A thoriated tungsten electrode was used to strike an arc between the electrode and the copper hearth, which

can reach temperatures greater than 2500 K. Arc-melting at such high temperatures minimized the kinetic barriers that traditionally restrict solid-state reactions and was particularly useful for these target compounds, since the melting points of these materials are all greater than 1500 K.

There are many limitations to arc-melting. First, the water-cooled copper crucible creates a large temperature gradient, which can result in compositional variations within the sample. Once molten, the low density and high melting point of boron will cause it to float to the top of the sample, potentially preventing mixing which could limit the formation of the desired phase. This was overcome by turning the sample and repeating the arc-melting procedure (generally six times) until a homogenous sample was achieved. Additionally, the rapid cooling that occurs during melting can result in the formation of metastable phases or other non-equilibrium products. Although direct, e.g., sintering, or mediated synthesis, e.g., flux growth, may be a more desirable route to achieve these phases, all attempts to synthesize these phases using techniques beyond arc-melting have been unsuccessful. These synthetic attempts resulted in the formation of undesired, known phases or no reaction at all

2.1.3 Tube Furnaces. To ensure the samples are homogenous and at equilibrium, tube-furnaces were employed after arc-melting. Each sample was sealed in a tantalum tube then in a fused silica jacked under reduced pressure (ca. 50×10^{-6} torr). Programmable controllers were used to maintain a consistent temperature profile that was monitored by a J-type thermal couple. These furnaces have a temperature limit of ca. 1473 K.

2.2 Characterization

2.2.1 Powder X-ray Diffraction. The initial method of product characterization was powder X-ray diffraction. The prepared samples were sufficiently brittle and not ductile so they could be ground into a fine powder. The samples were measured using the Guinier technique[1] using a *Huber 670* image plate camera with Cu $K_{\alpha 1}$ ($\lambda = 1.540598$ Å) radiation. Further experimental details are explained in the subsequent sections.

The reflections in each diffractogram were indexed manually against results calculated from single crystal X-ray diffraction experiments. The lattice parameters were determined by a least squares fit of the diffraction intensities using the program *Rietica*.[2]

2.2.2 Single Crystal X-ray Diffraction. Additional structural information was obtained through single crystal X-ray diffraction. Potential single crystals were selected from the bulk samples using an optical microscope and affixed to a silica fiber with epoxy. Two single crystal X-ray diffractometers were used for data collection, a *Bruker SMART APEX CCD* and a *STOE-IPDS II*. The single crystal diffractometers both used Mo K_α (λ = 0.71073 Å) radiation. Once the data were collected, structure refinements were carried using the *SHELXTL* program.[3]

The *Bruker SMART APEX CCD* collected the full hemisphere of reciprocal space in 0.3° increments with an exposure time of 10-20 seconds per frame. The data were then analyzed using the *SAINT* and *SADABS* suite of programs.[4] Absorption was accounted for in a semi-empirical fashion according to the linear extrapolation of the atomic absorption coefficients. Although data collection using the *CCD* was relatively fast, often in less than 10 hours, the crystal quality must be very high for the instrument software to determine the orientation matrix.

The amount of data collected on the *STOE-IPDS II* can vary greatly depending on the crystal system analyzed with the details explained in the subsequent chapters. All data were processed using the *X-shape* and *X-red* programs with a numerical absorption correction based on an optimized crystal shape.[5,6] Although the software packages allowed easy identification of the orientation matrix, each frame must be exposed for 5-7 minutes often requiring more than 20 hours to complete full data collection. As a result, the *STOE* was useful to identify the crystal system and lattice parameters of poor quality crystal as long as the experiment is not time sensitive.

2.2.3 Chemical Analysis. A scanning electron microscope equipped with an energy dispersive X-ray spectrophotometer (EDX) was used for chemical analysis. In general, the data were collected on either a single crystal sample or the surface of a bulk sample that has been polished with a 1-μm diamond slurry. Phase identification was completed

using the backscattered electron (BSE) signal with a 20 kV acceleration voltage and a 30 mA beam current. From these results, the atomic distribution, i.e., homogeneity, and semi-quantitative compositions were determined.

2.2.4 Magnetic Measurements. Magnetic measurements were collected using a *Quantum Design MPMS SQUID* magnetometer. The specific experimental conditions are described in the following sections. The Curie temperatures were approximated by the intersection of a linear fit about the maximum *dM/dT* of the magnetization versus temperature plot (*M* vs. *T*). The collected data is plotted according to a linearization of the Curie-Weiss law as χ^{-1} versus T plot. By fitting the paramagnetic, i.e. linear, region of this plot using Equation 2.1, the effective magnetic moments (μ_{eff}) and the Weiss temperature (Θ) were determined.

$$\chi^{-1} = \frac{T - \Theta}{\left(\frac{N\mu_{eff}^2}{3k_B} \right)} \tag{2.1}$$

2.3 Electronic Structure Calculations

2.3.1 Extended Hückel Theory (EHT). EHT is a semiempirical method involving the construction of a (one-electron) Hamiltonian matrix that solves for the eigenfunctions in a non self-consistent manner.[7-10] As a result, this method is extremely fast. The basis set for EHT calculations utilizes Slater-type orbitals with a double zeta basis set for the *d*-elements and a single zeta basis set for the *s* and *p* elements. Traditionally, the orbital energies used in these calculations were determined from an analysis of the experimental ionization energies from the atomic spectra; however, recent methods fit the energy of the atomic orbitals to a self-consistent DFT band structure calculation.[11] Although DFT considers a two-electron term whereas EHT does not, the later approach still provides good agreement between the accurate DFT and the efficient EHT calculations.

The primary application of EHT in this research was to determine the Mulliken populations at each atomic site. The Mulliken population is the sum of the atomic-orbital population and one-half of the overlap population.[8,12] Since EHT does not require a

cutoff radii, i.e., Wigner-Seitz radii, as an input parameter, it can be useful to calculate relative atomic-orbital populations for structures with many independent coordination environments. EHT, however, has a few major drawbacks. First, dividing the overlap population equally between two atomic sites is a rudimentary approximation. Other methods, such as Bader's analysis, which defines the site population as the lowest density between two atoms, can also be used. However, this method has drawbacks (discussed in Chapter 4) for application to the research presented here. Second, spin-polarization is not considered in these calculations. Fortunately, the relative Mulliken populations in these systems do not tend to change based on spin and thus the approximation holds.

2.3.2 Plane-wave Methods. Plane-waves are a set of orthonormal-normalized wavefunctions that can be written using Bloch's theorem as a product of a wave-like part and periodic part, Equation 2.2.

$$\varphi_{i\mathbf{k}} = \exp(i\mathbf{kr})u_i(\mathbf{r}) \tag{2.2}$$

Due to the periodicity of extended solids, $u_i(\boldsymbol{r})$ can be expanded as a set of plane-waves, Equation 2.3, where **B** is the reciprocal lattice vector.

$$u_i(\mathbf{r}) = \sum_{\mathbf{B}}{}' C_{i\mathbf{B}} \exp(i\mathbf{Br}) \tag{2.3}$$

Finally, the plane-waves can be written as a linear combination of plane-waves following Equation 2.4.

$$\varphi_{i\mathbf{k}}(\mathbf{r}) = \sum_{\mathbf{B}} C_{i\mathbf{B}} \exp(i(\mathbf{k}+\mathbf{B})\mathbf{r}) \tag{2.4}$$

In extended solids, these functions contain two domains, one that is highly oscillating, near the atomic core, and a smooth exponential decay. This dual characteristic is one of the main limitations of a plane-wave basis set. To correctly describe the fluctuating wavefunction near the core requires an exceedingly large number of plane-waves, i.e., a *very* high cutoff energy.[13] Although systems with light elements and high symmetry can employ the necessary cutoff energies, the computational costs become too much when considering transition metals or complex materials. To overcome this limitation two method are used. The first employs pseudopotentials (VASP) and the second uses an empirical tight-binding approach (TB-LMTO).

2.3.3 Pseudopotentials and the Vienna *ab initio* simulation package (VASP). One of the ways to handle the core wavefunctions is to simply replace them with a strong ion-electron potential through a pseudopotential.[12] The exponential decay of the potential is then modeled through the pseudopotential. Although pseudopotentials are not as straightforward as the atomic orbital basis set, Blöchl's description of projector-augmented wave (PAW) pseudopotentials provides a means of retaining information about the correct nodal behavior of the valence electron wavefunctions.[14] This allows pseudopotentials to be analyzed based on orbital descriptions, similar to the LCAO method that is familiar to chemists.

The Vienna *ab initio* simulation package (VASP) is based on density functional theory utilizing a plane-wave basis code and employs pseudopotentials to handle core electrons.[15-18] A few of the key uses for VASP in this research are: (i) total (electronic) energy calculations, (ii) structural optimizations, calculated the relative total energy of different magnetic models, (iv) determining electron localization through charge-density plots, and (v) performing a Bader's volume/charge analysis.

One of the main advantages of VASP is that by employing pseudopotentials with the plane-wave basis set, the electron densities are independent of the atomic positions. As a result, structural optimizations and the total energy calculations on many hypothetical structures converge with relative ease. The main drawback is the requirement to input size cutoffs, like a Wigner-Seitz radii, to calculate integrated values such as the partial DOS, magnetic moment, or charge density. These values are often rather arbitrary and require a keen chemical sense to substantiate their sizes.

2.3.2 Tight-Binding, Linear Muffin-Tin Orbital-Atomic Sphere Approximation (TB-LMTO-ASA). Another DFT method used to circumvent the oscillations in the wavefunctions is the linearized, tight-binding (TB) method. In this case, the core and valence electrons are treated by independent functions rather than a pseudopotential. The valence electrons are treated as a plane-wave (Eq. 2.4) while the core electrons are treated as an atom-like function, Equation 2.5, described by a linear combination of radial functions $R_{k,l}(r)$ and their spherical harmonics $Y_l^m(\vartheta,\varphi)$.

$$\Psi_k = \sum_{lm} c_{lm,k} R_{k,l}(r) Y_l^m(\vartheta, \varphi) \qquad (2.5)$$

The radial functions are expanded as a Taylor series, which is generally truncated after the second term.[12]

The tight-binding, linear muffin-tin orbital (TB-LMTO) method extended with the Atomic Spheres Approximation (ASA)[19,20] uses the linearized TB method, however, it is transformed into a highly localized basis set. This provides an opportunity to interpret the numerical results based on chemical reasoning. TB-LMTO was used in the research primarily to: (i) analyze the band structure diagrams, (ii) investigate the DOS and the partial DOS, (iii) perform a COHP analysis, and (iv) calculate the relative total energies of magnetic models.

TB-LMTO is an extremely efficient method for band structure calculations utilizing large numbers of k-points. Furthermore, TB-LMTO contains the scheme to calculate energy-weighted orbital overlaps, i.e., COHP curves. The biggest disadvantage is the requirement of Wigner-Seitz radii to build the atomic spheres. In simple systems, such as binary systems, it is possible to optimize these parameters. For systems that are more complex the number of variables is far too great. Furthermore, when comparing hypothetical structures, it can be difficult to maintain constant radii, which is a requirement for many of the arguments considered in this work.

2.4 References

(1) Guinier, A. *Théorie et Technique de la Radiocristallographie*; Dunod: Paris, 1956.
(2) Hunter, B. A.; 1.71 ed.; International Union of Crystallography, Commission of Powder Diffraction: 1997.
(3) Sheldrick, G. M.; University of Göttingen: Göttingen, Germany, 1997.
(4) Sheldrick, G. M.; University of Göttingen: Göttingen, Germany, 2001.
(5) STOE; 2.03 ed. Darmstadt, Germany, 2003.
(6) STOE Darmstadt, Germany, 2003.
(7) Ammeter, J. H.; Buergi, H. B.; Thibeault, J. C.; Hoffmann, R. *J. Am. Chem. Soc.* **1978**, *100*, 3686.
(8) Burdett, J. *Chemical Bonding in Solids*; Oxford University Press: New York, 1995.
(9) Hoffmann, R. *J. Chem. Phys.* **1963**, *39*, 1397.

(10) Hoffmann, R. *Solids and Surfaces: A Chemist's View of Bonding in Extended Structures*; VCH: New York, 1988.
(11) Schmidt, J. T.; Lee, S.; Fredrickson, D. C.; Conrad, M.; Sun, J.; Harbrecht, B. *Chem. Eur. J.* **2007**, *13*, 1394.
(12) Dronskowski, R.; Hoffmann, R. *Computational Chemistry of Solid State Materials: A Guide for Materials Scientists, Chemists, Physicists and Others*; John Wiley & Sons, 2008.
(13) Evarestov, R. A. *Quantum Chemistry of Solids: The LCAO First Principles Treatment of Crystals*; Springer: New York, 2007.
(14) Blöchl, P. E. *Phys. Rev. B* **1994**, *50*, 17953.
(15) Kresse, G.; Furthmüller, J. *Comput. Mater. Sci.* **1996**, *6*, 15.
(16) Kresse, G.; Furthmüller, J. *Phys. Rev. B* **1996**, *54*, 11169.
(17) Kresse, G.; Furthmüller, J. *Phys. Rev. B* **1996**, *54*, 11169.
(18) Kresse, G.; Hafner, J. *Phys. Rev. B* **1993**, *47*, 558.
(19) Andersen, O. K. *Phys. Rev. B* **1975**, *12*, 3060.
(20) Andersen, O. K.; Jepsen, O. *Phys. Rev. Lett.* **1984**, *53*, 2571.

CHAPTER 3

Structure, Bonding, and Magnetic Response in Two Complex Borides: $Zr_2Fe_{1-\delta}Ru_{5+\delta}B_2$ and $Zr_2Fe_{1-\delta}(Ru_{1-x}Rh_x)_{5+\delta}B_2$

Modified from a publication in the *Journal of Solid State Chemistry*
(*J. Solid State Chem.* **2010**, *183*, 2917)

Jakoah Brgoch,[1] Steven Yeninas,[2] Ruslan Prozorov,[2] Gordon J. Miller[1]

[1]Department of Chemistry, Iowa State University, Ames, Iowa, 50011, USA
[2]Ames Laboratory and Department of Physics and Astronomy, Iowa State University, Ames, Iowa, 50011, USA

3.1 Abstract

Polycrystalline samples of two complex intermetallic borides, $Zr_2Fe_{1-\delta}Ru_{5+\delta}B_2$ and $Zr_2Fe_{1-\delta}(Ru_{1-x}Rh_x)_{5+\delta}B_2$ (δ = ca. 0.10; x = 0.20), were synthesized by high-temperature methods and characterized by single-crystal X-ray diffraction, energy dispersive spectroscopy, and magnetization measurements. Both structures are variants of $Sc_2Fe(Ru_{1-x}Rh_x)_5B_2$ and crystallize in the space group *P*4/*mbm* (no. 127) with the $Ti_3Co_5B_2$-type structure. These structures contain single-atom, Fe-rich Fe/Ru or Fe/Ru/Rh chains along the *c*-axis with an interatomic metal-metal distance of 3.078(1) Å, a feature which makes them viable for possible low-dimensional temperature-dependent magnetic behavior. Magnetization measurements indicated weak ferrimagnetic ordering with ordering temperatures ca. 230 K for both specimens. Tight-binding electronic structure calculations on a model "$Zr_2FeRu_5B_2$" using LDA yielded a narrow peak at the Fermi level assigned to Fe-Fe antibonding interactions along the *c*-axis, a result that indicates an electronic instability toward ferromagnetic coupling along these chains. Spin-polarized calculations of various magnetic models were examined to identify possible magnetic ordering within, and between, the single-atom, Fe-rich chains.

3.2 Introduction

Many structural variants of the tetragonal $Ti_3Co_5B_2$ structure type[1] have recently been discovered.[2-4] The original structure type consists of stacked cobalt nets that form trigonal, tetragonal, and pentagonal prisms in which boron atoms occupy the trigonal prisms and titanium atoms occupy the tetragonal and pentagonal prisms. One variant, $Sc_2FeRu_5B_2$,[3-5] contains ruthenium nets with boron, again, in the trigonal prisms, scandium in the pentagonal prisms, and iron replacing titanium in the square prisms. The resulting crystal structure creates chains of iron atoms with interatomic distances of approximately 3.0 Å, and provides an opportunity to study possible low-dimensional itinerant magnetism. In fact, other structures of this type exhibit a wide range of magnetic ordering including ferromagnetism, ferrimagnetism, and antiferromagnetism, depending on the valence electron count. For instance, substituting rhodium for ruthenium has successfully yielded the isostructural series $Sc_2Fe(Ru_{1-x}Rh_x)_5B_2$ (x = 0-1) with the compounds with low Rh content (x = 0-0.4) exhibiting antiferromagnetism, while those with higher Rh content (x = 0.6-1) are ferromagnetic.[4,5]

Samolyuk *et. al*. theoretically investigated the change in magnetic order as a function of valence electron count for this pseudo-quaternary system, $Sc_2Fe(Ru_{1-x}Rh_x)_5B_2$ (x = 0-1), by calculating effective exchange parameters based on the linear-response method in the long wavelength approximation.[6] The exchange parameters between Fe atoms and the surrounding Ru/Rh mixed sites indicated strong coupling (J_{Fe-Rh} = 3.77 meV) for the fully substituted Rh case (x = 1), and very weak coupling (J_{Fe-Ru} = 0.07 meV) for the Ru case (x = 0). Therefore, the magnetic ordering of the system is significantly influenced by the valence electron count, which affects features of certain nearest neighbor orbital interactions near the corresponding Fermi levels. Other strategies to probe the magnetic ordering as a function of valence electron count in these complex phases includes replacing Sc with Group 4 metals and Fe atoms with surrounding 3*d* metals.

Herein, we report on two new compounds adopting the tetragonal $Ti_3Co_5B_2$-type with compositions $Zr_2Fe_{1-\delta}Ru_{5+\delta}B_2$ and $Zr_2Fe_{1-\delta}(Ru_{1-x}Rh_x)_{5+\delta}B_2$, in which Sc was replaced with Zr in $Sc_2Fe(Ru_{1-x}Rh_x)_5B_2$. The quaternary phase was originally observed as the major product in an attempt to replace Ti with Zr in $Ti_9Fe_2Ru_{18}B_8$, i.e., "$Zr_9Fe_2Ru_{18}B_8$".

The electronic structures, including a chemical bonding analysis obtained by Crystal Orbital Hamiltonian Population (COHP) curves are presented to interpret structural features and their magnetic behavior.

3.3 Experimental Section

3.3.1 Synthesis. Polycrystalline samples loaded as "$Zr_2FeRu_5B_2$" and "$Zr_2FeRu_4RhB_2$" were synthesized by arc-melting stoichiometric mixtures of the elements in a water-cooled copper crucible under a purified argon atmosphere using thoriated tungsten as a second electrode. The starting materials (Zr: pieces, 99.99%, Material Preparation Center, Ames National Lab; Fe: chips, 99.98%, Sigma Aldrich; Ru: pieces, 99.99%, Material Preparation Center, Ames National Lab; Rh: pieces, 99.95%, Material Preparation Center, Ames National Lab; B: crystalline pieces, 99.999%, Alfa Aesar) were weighed in the corresponding stoichiometric ratios with a total mass of approximately 0.6g and arc-melted a minimum of six times with turning to ensure homogeneity. The argon was purified over titanium sponge at 800 ^{o}C.

The as-cast products were gray in appearance, and single crystals could be selected from the arc-melted samples. Annealing was completed in sealed tantalum tubes within silica jackets under reduced pressure (ca. 50×10^{-6} torr). Samples were heated from room temperature to 1000 ^{o}C at 25 ^{o}C/hr and held for approximately 14 days before quenching to ambient temperature. Samples were then analyzed by powder X-ray diffraction, energy dispersive spectroscopy, and single crystal X-ray diffraction. The purity of the samples was checked by powder X-ray diffraction on a Huber 670 Guinier (image-plate) camera with Cu $K\alpha_1$ radiation (λ= 1.540598 Å). All products were visually stable to decomposition in air at room temperature over several months. Lattice parameters were refined from the powder diffraction pattern using the program *Rietica*.[7]

Rhodium substitution was attempted for the entire range (x = 0-1) in "$Zr_2Fe_1(Ru_{1-x}Rh_x)_5B_2$", but the desired phase is present as the major phase only for $x \leq$ 0.2. Loaded samples richer in Rh, x = 0.4-1, yielded $Zr(Ru/Rh)_3$ as the primary phase determined by EDX and powder X-ray diffraction. Moreover, as discussed below, repeated synthesis of loaded "$Zr_2FeRu_5B_2$" always resulted in Fe deficiency, ranging

from δ = 0.13(8) to 0.37(5) in $Zr_2Fe_{1-\delta}Ru_{5+\delta}B_2$. Through a combination of synthetic variation and X-ray powder diffraction, the maximum Fe deficiency is ca. δ = 0.50.[8] After various annealing strategies, however, the highest quality products characterized were those richest in Fe content. Therefore, we restricted our efforts to optimize yields of the Fe-richest samples, $Zr_2Fe_{1-\delta}Ru_{5+\delta}B_2$ and $Zr_2Fe_{1-\delta}(Ru_{1-x}Rh_x)_{5+\delta}B_2$, for further experimental and theoretical studies.

3.3.2 Structure Determination. Single crystals were selected from the annealed samples and fixed on a glass capillary. Data were collected using a STOE IPDS-II diffractometer with graphite monochromated Mo Kα (λ = 0.71073 Å) radiation. Reflections were collected in two sets of frames: the first with $\phi = 78^o$ and ω ranging from 11^o to 160^o with 1^o increments (149 frames), the second with $\phi = 258^o$ and ω ranging from 0^o to 62^o with 1^o increments (62 frames), for 211 total frames with an exposure time of 5 minutes per frame. Intensities were corrected by numerical absorption correction using *X-RED* and the crystal shape optimized with the aid of *X-SHAPE* software.[9,10] The structures were refined by full matrix least-squares refinement based of F^2 with the *SHELXTL* package,[11] using anisotropic displacement for all metal atom sites and isotropic displacement for the boron site. All crystal structure drawings were produced using the program *Diamond*.[12]

3.3.3 Chemical Analysis. Characterization was accomplished using a variable pressure scanning electron microscope (Hitachi S-2460N) and Energy-Dispersive X-ray Spectroscopy (EDS) (Oxford Instruments Isis X-ray analyzer). Samples were first polished with a 1-micron diamond slurry and then coated with approximately 20 nm of carbon. The samples were examined at 20 kV and a beam current ca. 0.5 nA that produced 3000 cps with 30% deadtime. Spectra were collected for 80 seconds. An Oxford Instruments *Tetra* backscattered electron (BSE) detector was used to image the samples using the BSE signal. Multiple points were examined in each phase within multiple grains of a specimen. Compositional estimates were calculated using Oxford's *SEMQuant* software to correct intensities for matrix effects. Pure element standards were used as intensity references for Ru, Rh, Fe, and Zr; B was not quantitatively analyzed.

Atomic size, absorption, and fluorescence were corrected using a standard ZAF matrix correction and used to convert intensity ratios to compositions.

3.3.4 Electronic Structure Calculations. Calculations of the electronic and possible magnetic structures were performed using the tight-binding, linear muffin-tin orbital method with the atomic spheres approximation (TB-LMTO-ASA)[13,14] using the Stuttgart code.[15] Exchange and correlation were treated by the local density approximation (LDA) and the local spin density approximation (LSDA).[16] In the ASA method, space is filled with overlapping Wigner-Seitz (WS) spheres. The symmetry of the potential is considered spherical inside each WS sphere and a combined correction is used to take into account the overlapping part. The WS radii are: 1.50-1.55 Å (Ru), 1.70 Å (Zr), 1.58 Å (Fe), and 0.98 Å (B). No empty spheres were necessary in these models, and the WS sphere overlaps were limited to no larger than 16%. The basis set for the calculations included Ru (5*s*, 5*p*, 4*d*, 4*f* downfolded), Zr (5*s*, 5*p*, 4*d*, 4*f* downfolded), Fe (4*s*, 4*p*, 3*d*), B (2*s*, 2*p*, 3*d* downfolded) wavefunctions. The convergence criteria was set to 1×10^{-4} eV. A mesh of 54 **k**-points in the irreducible wedge of the first Brillouin zone was used to obtain all integrated values, including the density of states (DOS) and crystal orbital Hamilton population (COHP) curves.[17]

3.3.5 Magnetization Measurements. The magnetization measurements were collected on the two samples using a *Quantum Design* MPMS SQUID magnetometer over the temperature range 5-300 K with applied fields of up to 5 T. The samples were placed in gel capsules for measurement. The three largest polycrystalline pieces of sample I were manually selected and secured using *Apiezon* N grease. Sample II was a fine powder, which was securely compacted using Kimwipes®. The diamagnetic core contributions to the magnetization are ca. -1.62×10^{-4} emu/mol for both samples.

3.4 Results and Discussion

All high-temperature synthetic attempts to prepare $Zr_2Fe_{1-\delta}Ru_{5+\delta}B_2$ and $Zr_2Fe_{1-\delta}(Ru_{1-x}Rh_x)_{5+\delta}B_2$ yielded some Fe deficiency, i.e., $\delta > 0$, and a maximum Rh content of $x = 0.2$. The highest quality products, as determined by a combination of EDS and powder and single crystal X-ray diffraction, were those samples richest in Fe. Thus,

in the following discussion, "sample I" refers to the quaternary phase characterized as $Zr_2Fe_{0.87(8)}Ru_{5.13}B_2$, and "sample II" labels the quintinary phase, $Zr_2Fe_{0.82}(Ru_{0.8}Rh_{0.2})_{5.18}B_2$.

3.4.1 Chemical Analysis. EDS was employed to qualitatively determine the composition and elemental distribution of the prepared samples, as well as to compare with subsequent refinements from single crystal X-ray diffraction. An X-ray map (see supporting information) was employed to identify the distribution of the phases in relation to each other, with compositional information collected for each phase. Two phases were identified present in bulk pieces of sample I: the major phase showed an average molar ratio of metals to be 2.2(1) Zr : 0.7(1) Fe : 5.11(2) Ru, which is close to the loaded metals composition of 2 Zr : 1 Fe : 5 Ru. The minor phase was determined to have an average stoichiometric composition of 1.1(1) Fe : 2.00(7) Ru. This phase was not observed in powder X-ray diffraction patterns (see Supporting Information for X-ray powder diffraction patterns of both samples), and, as a result, is less than ca. 5 % of the total crystalline component in the sample. EDS on sample II was also collected and showed the presence of multiple phases. The major phase yielded an average molar ratio of metals to be 2.3(1) Zr : 0.7(1) Fe : 3.99(8) Ru : 0.99(9) Rh, which is very close to the loaded metals composition. This sample, however, also contains inclusions of elemental Zr, 0.51(3) Fe : 0.49(3) Ru ("RuFe"), 1.0(3) Zr : 0.50(4) Ru : 2.33(9) Rh, and 2.6(3) Zr : 1.0(2) Fe : 2.5(5) Ru : 5.8(1) Rh. Boron was not quantitatively analyzed for any of the samples.

Refinements of site occupancies based on single crystal X-ray diffraction data, discussed in more detail in the next section, always led to mixing of Fe and either Ru or a Ru/Rh mixture on a single crystallographic site (Wyckoff 2*a* site) to eliminate non-positive definite displacement parameters at this position. The Rh and Ru contents were fixed according to the loading composition. Refined compositions averaged over three single crystal measurements for each sample were $Zr_2Fe_{0.87(8)}Ru_{5.13}B_2$ for sample I and $Zr_2Fe_{0.82(3)}(Ru/Rh)_{5.18}B_2$ for sample II. These refined compositions agree with the EDS analysis of the majoring components in each sample.

3.4.2 Structure Determination. The observed powder X-ray diffraction patterns of samples I and sample II yielded, respectively, refined lattice parameters of a = 9.3361(1); c = 3.0700(1) and a = 9.3489(1); c = 3.0663(1) . The volume increases by less than 1% with the substitution of Rh for Ru. A volume increase of a similar magnitude is also observed in the substitutional variants of the scandium analogues.[5] The results of single crystal diffraction on specimens extracted from annealed samples I and II are listed in Tables 1 and 2. These (pseudo)-quaternary derivative of the tetragonal $Ti_3Co_5B_2$-type structure is shown in Figure 1 as a projection along the [001] direction. Its structure contains distorted pentagonal, square, and trigonal prisms formed by Ru/Rh atoms. Zr atoms occupy the 4*g* sites within each pentagonal prism, while B atoms occupy the 4*g* sites in every trigonal prism. The magnetically active element, Fe, is located within the 2*a* distorted square prisms and forms chains along the [001] direction, as in the $Sc_2Fe(Ru_{1-x}Rh_x)_5B_2$ series. Here, however, single crystal data always indicate a mixture of Fe and Ru or Ru/Rh atoms at the 2*a* sites in both samples.

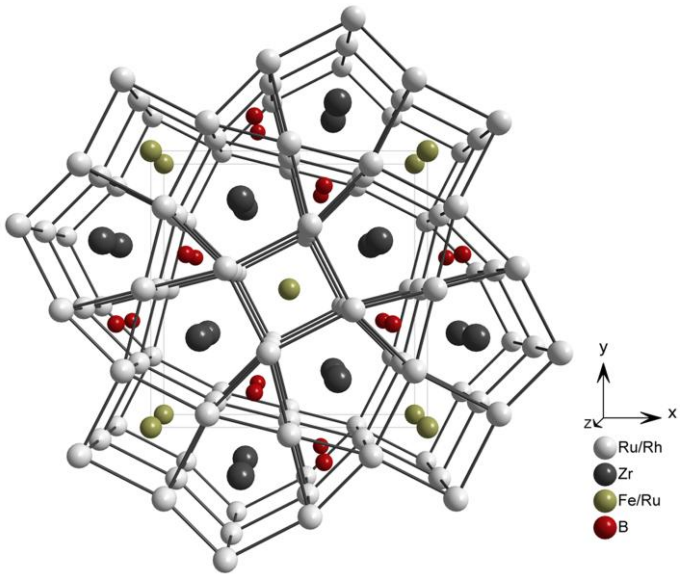

Figure 1. Perspective view of the crystal structure of $Zr_2Fe_{0.87}Ru_{5.13}B_2$ (sample I) along the [001] direction. $Zr_2Fe_{0.82}(Ru/Rh)_{5.18}B_2$ (sample II) is isostructural with possible random distribution of Ru and Rh atoms.

Table 1. Crystallographic data for samples I and II at 293(2) K.

Specimen	Sample I	Sample II
Refined Formula	$Zr_2Fe_{0.91(3)}Ru_{5.09}B_2$	$Zr_2Fe_{0.84(4)}(Ru/Rh)_{5.16}B_2$
F.W. (g/mol); *F*(000)	769.48; 675	774.51; 680
Space group; *Z*	*P*4/*mbm* (No. 127); 2	*P*4/*mbm* (No. 127); 2
Lattice Parameters (Å)	*a* = 9.3361(1) *c* = 3.0700(1)	*a* = 9.3489(1) *c* = 3.0663(1)
Volume (Å^3)	267.60(1)	268.00(1)
d_{calc} (Mg/m^3)	9.434	9.449
Absorption Correction	Numerical	Numerical
μ (mm^{-1})	19.781	20.023
θ range (deg)	3.08 < θ < 33.29	3.08 < θ < 33.29
hkl ranges	−14< *h* < 14, −14 < *k* < 12, −4 < *l* < 4	−14< *h* < 14, −14 < *k* < 12, −4 < *l* < 4
No. reflections; R_{int}	3776; 0.0427	4187; 0.0399
No. independent reflections	318	327
No. parameters	19	21
R_1; wR_2 (all *I*)	0.0436; 0.0761	0.0397; 0.1036
Goodness of fit	1.447	1.072
Diffraction peak and hole (e$^-$/Å^3)	2.227 and −3.692	1.660 and −3.298

Table 2. Atomic coordinates and equivalent isotropic displacement parameters of (a) sample I and (b) sample II. U_{eq} is defined as one-third of the trace of the orthogonalized U^{ij} tensor (Å^2 ×10^2).
(a)

Atom	Wyckoff Position	Occ.	*x*	*y*	*z*	U_{eq}
Ru1	8*j*	1	0.2158(1)	0.0706(1)	½	6(1)
Ru2	2*c*	1	½	0	½	5(1)
Zr	4*g*	1	0.3244(1)	0.8244(1)	0	6 (1)
Fe/Ru	2*a*	0.91(3)/0.09	0	0	0	4(1)
B	4*g*	1	0.3741(2)	0.1259(2)	0	13(3)

Table 2 Continued

(b)

Atom	Wyckoff Position	Occ.	*x*	*y*	*z*	U_{eq}
Ru/Rh1	8*j*	1	0.2167(1)	0.07059(8)	½	7(1)
Ru/Rh2	2*c*	1	½	0	½	6(1)
Zr	4*g*	1	0.3243 (1)	0.8243(1)	0	7(1)
Fe/(Ru/Rh)	2*a*	0.84(4)/0.16	0	0	0	6(1)
B	4*g*	1	0.377(1)	0.127(1)	0	10(2)

The smaller size and valence electron count of Ru make it the likely candidate over Zr to co-occupy the centers of square prisms (2*a* sites) with the Fe atoms. An alternative refinement strategy in which Zr and Fe were mixed at the 2*a* sites did not achieve the statistical agreement that the refinements in Tables 1 and 2 yielded. Furthermore, ZrRu adopts the CsCl-type structure with Zr-Ru nearest neighbor distances of 2.817 Å[18] while the distorted cubic prisms in these complex borides have much shorter distances of 2.623 Å and 2.630 Å, respectively, for $Zr_2Fe_{0.87(8)}Ru_{5.13}B_2$ and $Zr_2Fe_{0.82(3)}(Ru/Rh)_{5.18}B_2$.

The magnetically active Fe atoms are separated by at least 3.1 Å along the [001] direction and 6.7 Å along the {110} directions in sample I, whereas $Sc_2FeRu_{5-x}Rh_xB_2$ shows distances of at least 3.01 Å along the [001] direction and 6.6 Å along the {110} directions, dependent on the Rh concentration. The Ru-Ru distances are nearly identical in both the Zr and Sc phases with distances between 2.74-3.00 Å. Zr-Ru contacts have an average length of 2.89 Å compared to the Sc-Ru average length of 2.84 Å. Such similar distances among the majority components may result in comparable behavior of the magnetically active atoms; however, the metal atom mixing at the 2*a* sites may also dramatically alter the long-range magnetic order.

3.4.3 Electronic Structure and Chemical Bonding. The electronic structure of the hypothetical structure "$Zr_2FeRu_5B_2$", with a valence electron (VE) count of 62 electrons, was investigated computationally to interpret the electronic structure. This model was selected after first examining the effect of Fe/Ru mixing at the 2*a* site on the theoretical electronic structure. The total DOS curves of three models, "$Zr_2FeRu_5B_2$",

"$Zr_2Fe_{0.5}Ru_{5.5}B_2$", and "$Zr_2Ru_6B_2$" were compared to determine the effect any atomic mixing on the electronic structure. The resulting curves, illustrated in the supporting information, show very slight differences. As a result, "$Zr_2FeRu_5B_2$", with the 2*a* site fully occupied by Fe atoms, was utilized to investigate the electronic structures and bonding in $Zr_2Fe_{1-\delta}(Ru_{1-x}Rh_x)_{5+\delta}B_2$.

Analysis of both the non-spin polarized (LDA) and spin polarized (LSDA) total DOS curves shows nonzero values at the Fermi level (E_F), suggesting metallic behavior. Moreover, the E_F falls on a local maximum of the DOS curve from the LDA calculation, a result that is indicative of a possible electronic instability. When spin polarization is taken into account, a narrow pseudogap develops from 60 to 63 VEs (−0.25 eV to 0.25 eV). The LSDA DOS curves are shown in Figure 2 with E_F (62 VE) set as the energy reference. The DOS curves show contributions from the valence orbitals of all elements throughout the entire energy range, but with some indications of the relative electronegativities of these elements.

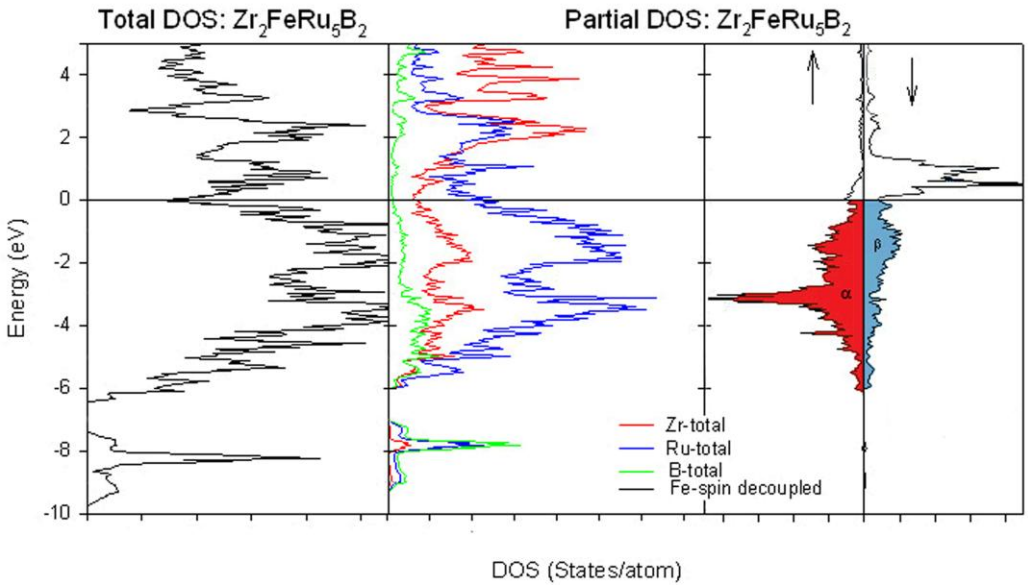

Figure 2. Partial DOS curves of "$Zr_2FeRu_5B_2$" obtained from spin-polarized (LSDA) calculation plotted as the sum of "spin 1" and "spin 2" for the Zr, Ru, B. The individual spins for the magnetic Fe are also plotted with the ICOHP values shade with the α (red) = 5.4 electrons and β (blue) = 2.6 electrons (The E_F is set to zero)

The bands 7.5 to 10 eV below the Fermi level are mostly B 2*s*-orbitals with some mixing of Ru and Zr 5*s*-orbitals as well. Between −6 eV and E_F, the states are largely Ru 4*d*-orbitals with some Ru 5*s*-orbitals present between −6 and −4 eV. In the same region, there are significant contributions from B 2*p*-orbitals. Zr valence orbitals constitute ca. 25% of the total DOS between −6 eV and E_F and increase to ca. 50% of the total DOS above the pseudogap. The spin polarized partial DOS of Fe atom orbitals falls between −5 and +3 eV, with the majority spin states having 68% of the occupied states and the minority spin states having 32%. In addition, the minority bands are compressed into a 2 eV window above E_F. As a result, the mostly filled Ru orbitals below the Fermi level and the virtual Zr orbitals above E_F, combined with the strong spin-polarization of Fe, cause the deep pseudogap at the Fermi level between 60-63 VE and allow for stabilization of the structure.

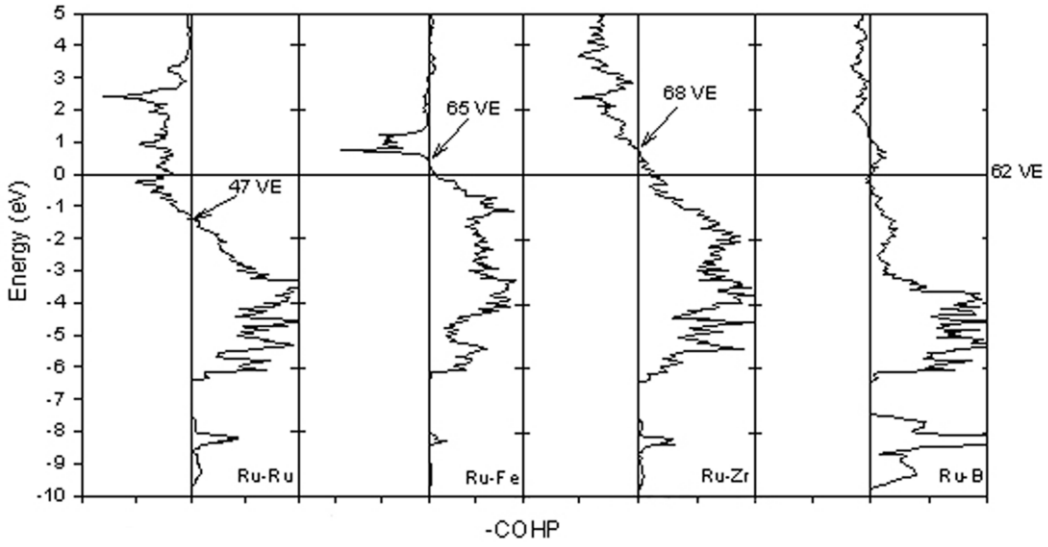

Figure 3. Spin-polarized (LSDA) COHP curves for nearest neighbor contacts in "$Zr_2FeRu_5B_2$". (+ is bonding/ − is antibonding, E_F et to zero)

The crystal orbital Hamilton population (−COHP) curves were also analyzed from these electronic structure calculations and the resulting curves are illustrated as the averaged spin-polarized interactions in Figure 3 with the integrated values listed in Table 3. In addition, the Integrated COHP (−ICOHP) values for various interatomic contacts in this complex structure are compared with –ICOHP values evaluated for binary or

elements species containing similar metal atom ratios and coordination environments. "$Zr_2FeRu_5B_2$" shows nonbonding Ru-B interactions at E_F and an averaged −ICOHP value of 2.93 eV/bond. The Ru-Zr interactions show bonding at E_F with the optimized interaction occurring at 67 VE (+0.9 eV). The Ru-Fe interaction shows nearly optimal bonding (–ICOHP = 1.28eV/bond) with the crossover at 65 VE. Ru-Ru interactions fall in an antibonding region, with the crossover well below E_F at 47 VE (−1.5 eV); however, the net interaction remains bonding. These results indicate a mostly filled Ru 4*d* band, which is seen in the partial DOS curve (Figure 2).

Table 3. Homoatomic and heteroatomic bonding for $Zr_2FeRu_5B_2$, associated –ICOHP values and literature structures with calculated –ICOHP values.

Bond	Distances (Å)	−ICOHP (eV/bond)	Bond	Distances (Å)	−ICOHP (eV/bond)
Ru-Ru	2.6-3.0	0.851-1.09	Ru-Ru (hcp)	2.67	1.69
				2.75	1.45
Ru-Zr	2.851	2.02	Ru-Zr ($ZrRu_2$)[19]	3.01-3.05	1.16-1.22
	2.947	1.58			
Ru-Fe	2.621	1.28			
Ru-B	2.225	2.93	Ru-B (Ru_8B_{11})[20]	2.165	2.78
Fe-Fe [001]	3.067	0.44	Fe-Fe ($RbFeS_2$)[21]	2.702	0.58

The Fe-Fe orbital interactions were investigated along the [001] direction for the non-spin polarized case, illustrated in Figure 4a, as well as for the decoupled majority and minority spins in Figure 4b. The non-spin polarized Fe-Fe interaction is optimized at 60 VE (−0.32 eV) with E_F falling in a region of strongly antibonding states. Spin polarization optimizes the Fe-Fe interaction of the majority spin wavefunctions and shifts the crossover of the minority spin states to 63 VE (+0.20 eV).

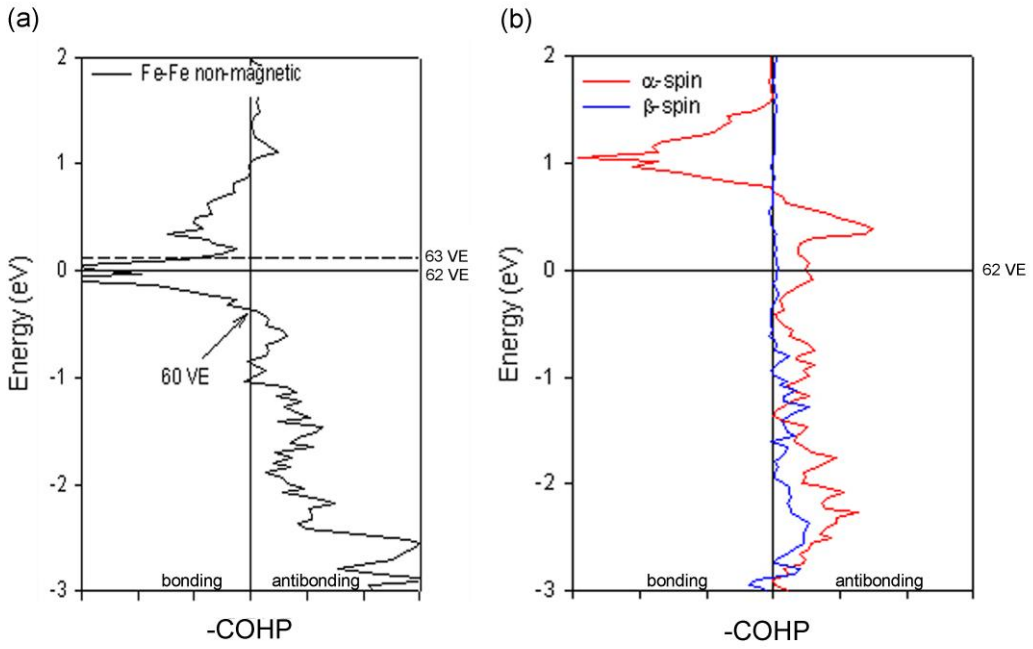

Figure 4. (a) Nonmagnetic (LDA) COHP curves for the Fe-Fe contacts in the [001]. (b) Decoupled α (red) and β (black) spins. 62 VE: $Zr_2FeRu_5B_2$, 63 VE: $Zr_2FeRu_4RhB_2$. (E_F is set to zero)

The occupation of relatively narrow states at the Fermi level in a non-spin polarized calculations, states which are antibonding between magnetically active metal atoms, has previously been described to indicate ferromagnetic ordering.[22-24] Upon spin polarization, the energies of the majority spin states drop due to reduced screening, and the orbital overlaps decrease as the wavefunctions become less diffuse, so that both bonding and antibonding orbital interactions are reduced. On the other hand, the energies of the minority spin states increase and exhibit greater dispersion. The resulting Fermi level frequently sits at the crossover between bonding and antibonding states in the minority spin DOS.[22-24] Following this premise, the Fe-Fe interactions are predicted to be ferromagnetic. The increase in valence electron count by substituting Rh for Ru (from 62 to 63 VE) ("$Zr_2Fe(Ru/Rh)_5B_2$") is plotted as the dashed line in Figure 4 using the rigid band approximation. The resulting Fermi level remains among antibonding states; so ferromagnetic behavior should remain. Magnetic coupling through bonds cannot be studied by the COHP analysis, so we did not evaluate these curves for distances between adjacent [001] chains.

Since the COHP curves can only be used to suggest magnetic ordering for near neighbor contacts and not through-bond couplings, various magnetically ordered models of "$Zr_2FeRu_5B_2$" were constructed to explore inter-chain magnetic orderings as well as alternative intra-chain antiferromagnetic (AFM) couplings. Four different models were constructed in the space group *P*4/*m* and required a unit cell doubled along the *c*-axis. The symmetry reduction from *P*4/*mbm* to *P*4/*m* splits the crystallographically equivalent 2*a* sites into two individual sites: 1*a* (0 0 0) and 1*b* (½ ½ 0), which is necessary for the magnetic models. See supporting information for illustrations of the four starting magnetic orderings. Local moments were placed exclusively on the Fe atoms as starting points for invoking spin polarization. All calculations were allowed to converge according to the same criteria, while the preferred model was selected by a comparison of the total energies per formula unit. These results are summarized in Table 4.

Table 4. Magnetic models to predict preferred magnetic ordering and local magnetic moments for a hypothetical composition, "$Zr_2FeRu_5B_2$".

Magnetic Model		AFM1	AFM2	AFM3	FM
Total Energy (meV/unit cell)		----	+63.1	+71.9	+120
Total Moment (μ_B)		0	0	0	11.566
Local Magnetic Moment (μ_B/atom)	Fe1 (1*a*)	2.981	±2.888	±2.931	2.931
	Fe2 (1*b*)	−2.981	±2.888	±2.931	2.931
	Ru1	0.068	0.000	0.000	0.022
	Ru2	−0.068	0.000	0.000	0.022
	Zr	0.000	−0.005	0.001	−0.037

The most energetically favorable model (AFM1) contains ferromagnetic (FM) ordering along each Fe atom chain, and AFM ordering between these chains along {110} directions. The local magnetic moments at the Fe atoms in these chains are close to 3 unpaired electrons per Fe atom (2.981 μ_B). Nearest neighbor Zr atoms hold no magnetic moment, while the Ru atoms also contain small moments ordered ferromagnetically with respect to the closest Fe atom chain. The next most energetically favorable model (AFM2) contains AFM ordering within each chain, i.e., along [001], as well as between

the chains along the {110} directions. The magnitudes of the local moments on the Fe atoms are slightly smaller than the AFM1 case; however, the nearest neighbor Ru atoms now develop zero magnetic moment. Changing the inter-chain ordering of these AFM chains to FM along the {110} directions, which is modeled in AFM3, further increases the total energy. The 8.8 meV/unit cell increase from AFM2 to AFM3 signifies the weak exchange coupling between the magnetic chains. The least energetically favorable model, FM, which involves FM coupling within and between chains, creates local moments of 0.022 μ_B/atom at the Ru atoms and small moments (0.037 μ_B/atom) also building up on the Zr (the moments at Zr counter the overall moments of the Fe and Ru sites). The magnitudes of the local moments on the Fe atoms are calculated to be similar for each magnetic model.

The results of analysis of the Fe-Fe intra-chain COHP curves as well as evaluation of total energies for different magnetic models complement each other. Both results agree that intra-chain Fe-Fe exchange coupling is preferentially FM for "$Zr_2FeRu_5B_2$" (62 VE). Total energies revealed that AFM coupling between near neighbor chains along the {110} directions is favorable over FM coupling, a result which could lead to an overall low net magnetization of these samples. A rigid band model was applied to predict the effect of Rh substitution on the total energies of each model: these energies of the different magnetic structures order identically to "$ZrFeRu_5B_2$." The local magnetic moments at the Fe sites are not affected by the Rh substitution, maintaining moments that are ca. ±2.9 μ_B/atom. The long range magnetic ordering for the isostructural and isoelectronic $Sc_2FeRu_3Rh_2B_2$ and $Sc_2FeRu_2Rh_3B_2$ both show ferromagnetism by experiment and theory.[5,6] The origin for these differences in magnetic order with composition and valence electron count for this entire class of magnetically responsive borides is currently under study.

3.4.4 Magnetization Measurements. The Curie temperatures (T_C), Weiss temperatures (θ), and μ_a values are listed in Table 5 for samples I and II. Both samples appear to be ferrimagnetic showing a hysteresis curve with small magnetic moments developing per Fe atom. However, neither specimen reaches saturation at 5 K and 5 T. Analysis of these magnetization results yield effective moments of 0.235(4) μ_B/Fe and 0.373(4)

μ_B/Fe, respectively, for samples I and II at 5 K and B_0 = 5 T. Both loops show hysteresis with very small remanence and coercivity, features that are indicative of soft ferrimagnets.

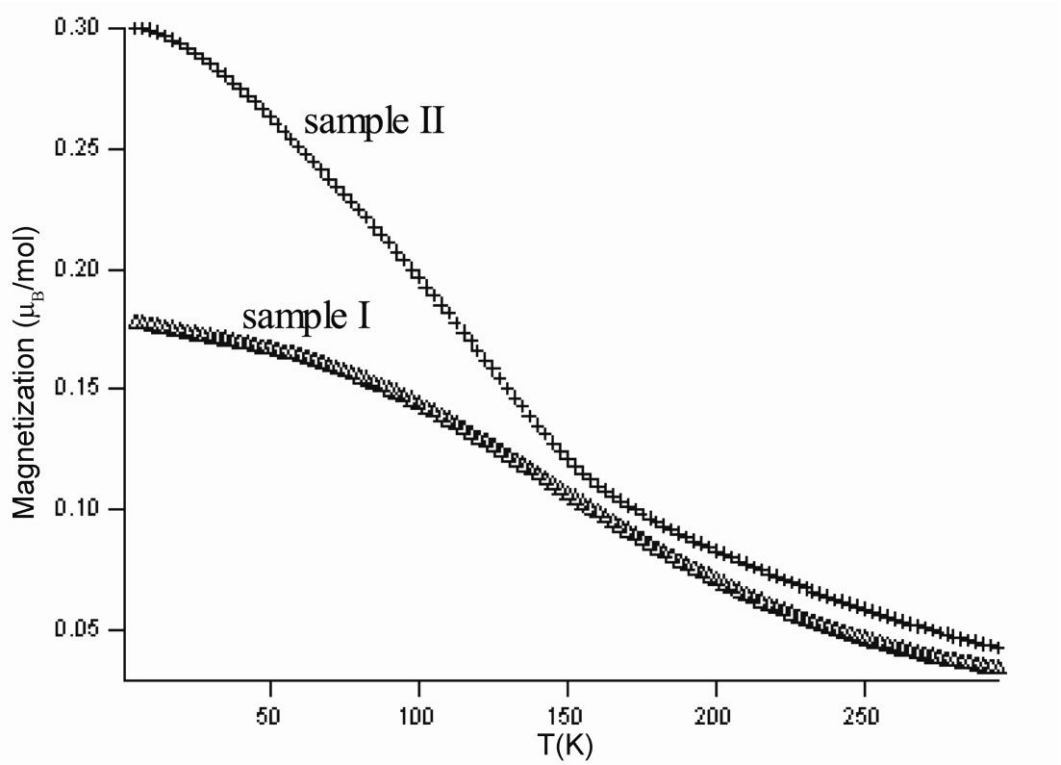

Figure 5. Shown here are M(T) curves at fields of 2.5 T. Both structures suggest ferrimagnetic ordering at ca. 230 K with a higher order transitions occurring in the Rh substituted sample ca. 150 K.

Table 5. SQUID magnetic measurements of the bulk sample I and sample II

	Sample I	Sample II
T_c (K)	239(2)	233(6)
θ (K)	129.0(9)	138(2)
μ_a (μ_B/Fe)	0.235(4)	0.373(4)
Coercivity (Oe)	1087(67)	323(122)
Remanence (μ_B/mol)	0.0250(3)	0.0710(6)

* μ_a at 5 K and 5 T

The Curie Temperatures were approximated by the intersection of a linear fit about the maximum *d*M/*d*T of the magnetization vs. temperature (M vs. T), see Figure 5.[25] A plot of χ^{-1} vs. T for sample I in Figure 6a follows Curie-Weiss behavior at temperatures

exceeding ca. 220 K. Although the SQUID measurements were collected on the bulk multiphase sample, the data collected for sample I should originate solely from the desired phase. The secondary phase in sample I, $FeRu_2$, has been shown in previous work on hexagonal close packed Fe-Ru alloys to be a Pauli-paramagnet. In fact, with greater substitution of Ru, the magnetic moments drop dramatically above ca. 5 at %.[26] Furthermore, a theoretical investigation on the substitution of iron with a 4*d* metal also shows a dramatic decrease in the magnetic moment with greater substitution of 4*d* metal.[27] As a result of these factors, the magnetic moments in sample I most likely arise from the desired phase rather than any impurity phases.

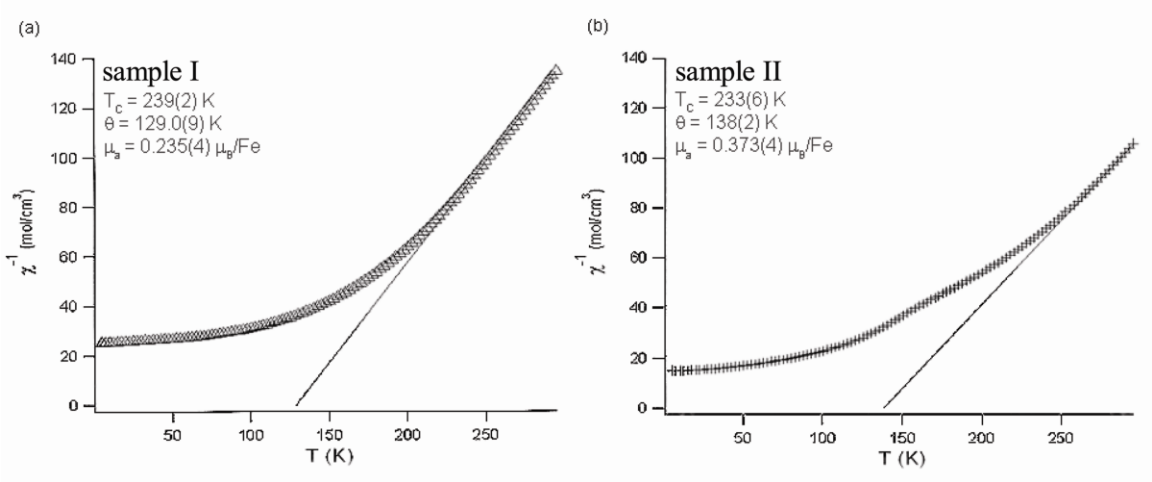

Figure 6. (a) χ^{-1} versus T for sample I shows onset of Curie-Weiss behavior above 200 K. (b) χ^{-1} versus T for sample II with a fit of the paramagnetic region at the onset of Curie-Weiss behavior just under 300 K.

A Curie-Weiss fit was performed for sample II in Figure 6b, although the linear regime of the paramagnetic curve is near the upper limit of the temperatures probed. Due to the multiple phases present in sample II, interpretation of the data is much more complex. However, the Curie temperature and the Weiss temperature are close to sample I. Therefore, we believe the primary magnetic transition at ca. 230 K is a result of our desired phase and not the impurities. However, sample II shows a second magnetic transition present at 150 K, a transition that could be a result of an impurity, and is currently under investigation.

The magnetic moment per atom in sample I has a value that is approximately 10% of the theoretically predicted value (2.878 μ_B/Fe) and the electronically similar scandium analogue, $Sc_2FeRu_3Rh_2B_2$ (63 VE), which has a reported moment of 3 μ_B/Fe.[5] However, in both of these cases, the 2*a* site is fully occupied by Fe atoms. Previous theoretical work determined that Ru has a very small pairwise exchange, J_{Fe-Ru} = 0.07 meV, and thus limits magnetic coupling.[6] As a result, mixing of Ru and Fe at the 2*a* site, as seen in sample I, will likely disrupt any long range magnetic ordering. Additionally, Rh was shown to have a larger exchange (J_{Fe-Rh} = 3.77 meV) and, thus, enhance both magnetic exchange and the total magnetic moment of the system.[5] This is seen experimentally in the series $Sc_2Fe(Ru_{5-x}Ru_x)B_2$ (x = 3, 4, 5) with the magnetic moments increasing from 3 μ_B/Fe to 3.1 μ_B/Fe to 3.3 μ_B/Fe depending on the level of Rh substitution. A similar result is found here with an increase in the magnetic moment by ca. 40 % with Rh substitution. A further study on the effects of magnetic ordering with respect to atomic mixing at the 2*a* site is currently underway.

3.5. Conclusions

The isotypic structures, $Zr_2Fe_{0.87(8)}Ru_{5.13}B_2$ and $Zr_2Fe_{0.82(3)}(Ru/Rh)_{5.18}B_2$, have been prepared by high-temperature methods and structurally characterized to show partial mixing of Fe and Ru/Rh atoms independent of the total valence electron count. TB-LMTO electronic structure calculations of the nearest stoichiometric model, "$Zr_2FeRu_5B_2$", show strong polarization of the Fe atoms (2.98 μ_B/Fe) and weak polarization of the surrounding net of 4*d* metals Ru net (−0.04-0.002 μ_B/Fe), while the electronic structure of "$Zr_2FeRu_4RhB_2$" has been suggested by a rigid band approximation to the electronic structure of "$Zr_2FeRu_5B_2$". Ferromagnetic ordering was predicted via through a COHP analysis of the DOS, while mixed magnetic ordering is predicted from the total energies of the model systems. Finally, SQUID magnetic measurements show soft ferrimagnetism for both structures with smaller total moments than predicted theoretically. Neutron scattering, with an emphasis on magnetic scattering results, coupled with further theoretical studies of Fe-deficient models $Zr_2Fe_{1-\delta}(Ru_{1-x}Rh_x)_{5+\delta}B_2$ are warranted to substantiate these conclusions.

3.6 Acknowledgements

J.R.B. would like to thank Dr. Boniface Fokwa, Christian Goerens, Dr. Shalabh Gupta for many helpful discussions and Debanjan K. Ghosh for experimental assistance. EDS was collected with the assistance of the Materials Analysis and Research Lab (MARL) at Iowa State University. The authors acknowledge the generous financial support provided by the U.S. National Science Foundation (NSF DMR 08-06507).

3.7 References.

(1) Kuz'ma, Y. B.; Yarmolyuk, Y. P. *Zhurnal Strukturnoi Khimii* **1971**, *12*, 458.
(2) Jung, W.; Schiffer, J. *Z. Anorg. Allg. Chem* **1990**, *581*, 135.
(3) Nagelschmitz, E. A.; Jung, W. *Chem. Mater.* **1998**, *10*, 3189.
(4) Nagelschmitz, E. A.; Jung, W.; Feiten, R.; Müller, P.; Lueken, H. *Z. Anorg. Allg. Chem* **2001**, *627*, 523.
(5) Fokwa, B. P. T.; Lueken, H.; Dronskowski, R. *Chem. Eur. J.* **2007**, *13*, 6040.
(6) Samolyuk, G. D.; Fokwa, B. P. T.; Dronskowski, R.; Miller, G. J. *Phys. Rev. B* **2007**, *76*, 094404.
(7) *Rietica: A Visual Rietveld Program*, 1.71 ed., Hunter, B. A., 1997.
(8) Brgoch, J.; Miller, G. J., Unpublished Results.
(9) *X-SHAPE; crystal optimization for numerical absorption correction*, 2.03 ed., STOE, Darmstadt, Germany, 2003.
(10) *X-RED; data reduction program*, STOE, Darmstadt, Germany, 2003.
(11) *SHELXL-97, A Program for the Refinement of Crystal Structures*, Sheldrick, G. M., Göttingen, Germany, 1997.
(12) *DIAMOND: Visual Crystal Information System*, Brandenburg, K., Bonn, Germany, 1999.
(13) Andersen, O. K. *Phys. Rev. B* **1975**, *12*, 3060.
(14) Andersen, O. K.; Jepsen, O. *Phys. Rev. Lett.* **1984**, *53*, 2571.
(15) *TB-LMTO-ASA Program*, 4.7 ed., Krier, G.; Jepsen, O.; Burkhardt, A.; Andersen, O. K., Stuttgart, Germany, 1995.
(16) von Barth, U.; Hedin, L. *J. Phys. C: Solid State Phys.* **1972**, *5*, 1629.
(17) Dronskowski, R.; Blöchl, P. E. *J. Phys. Chem.* **1993**, *97*, 8617.
(18) Dwight, A. H. *Transactions of the Metallurgical Society of Aime* **1959**, *215*, 283.
(19) Wallbaum, H. J. *Naturwissenschaften* **1942**, *30*, 149.
(20) Aselius, J. *Acta Chemica Scandinavica* **1960**, *14*.
(21) Bronger, W.; Kyas, A.; Muller, P. *J. Solid State Chem.* **1987**, *70*, 262.
(22) Dronskowski, R.; Korczak, K.; Lueken, H.; Walter, J. *Angew. Chem. Int. Ed.* **2002**, *41*, 2528.
(23) Landrum, G. A.; Dronskowski, R. *Angew. Chem. Int. Ed.* **1999**, *38*, 1389.
(24) Landrum, G. A.; Dronskowski, R. *Angew. Chem. Int. Ed.* **2000**, *39*, 1560.
(25) Fokwa, B. P. T.; Samolyuk, G. D.; Miller, G. J.; Dronskowski, R. *Inorg. Chem.* **2008**, *47*, 2113.

(26) Fujimori, H.; Saito, H. *J. Phys. Soc. Jpn.* **1969**, *26*, 1115.
(27) Drittler, B.; Stefanou, N.; Blügel, S.; Zeller, R.; Dederichs, P. H. *Phys. Rev. B* **1989**, *40*, 8203.

3.8 Supporting Information

Table S1. Anisotropic displacements parameters ($Å^2 x\ 10^3$) for $Zr_2Fe_{0.82}Ru_{5.18}B_2$ at 293(2) K. The anisotropic displacement factor exponent takes the form: $-2\pi^2[\ h^2\ a^{*2}U^{11} + ...\ + 2\ h\ k\ a^*\ b^*\ U^{12}\ ]$

	U^{11}	U^{22}	U^{33}	U^{23}	U^{13}	U^{12}
Ru(1)	10(1)	10(1)	13(1)	0	0	0(1)
Ru(2)	9(1)	9(1)	11(1)	0	0	1(1)
Zr(3)	11(1)	11(1)	11(1)	0	0	-2(1)
Fe(4)	9(1)	9(1)	12(1)	0	0	0
Ru(4)	9(1)	9(1)	12(1)	0	0	0
B(5)	13(3)	13(3)	13(6)	0	0	8(4)

Figure S1. Total density of states for the ideal composition ($Zr_2FeRu_5B_2$), close to the crystallographic composition ($Zr_2Fe_{0.5}Ru_{5.5}B_2$) and a hypothetical composition ($Zr_2Ru_6B_2$) the difference curve between the two compositions. The presence of a pseudogap is not dependent on the total Fe content.

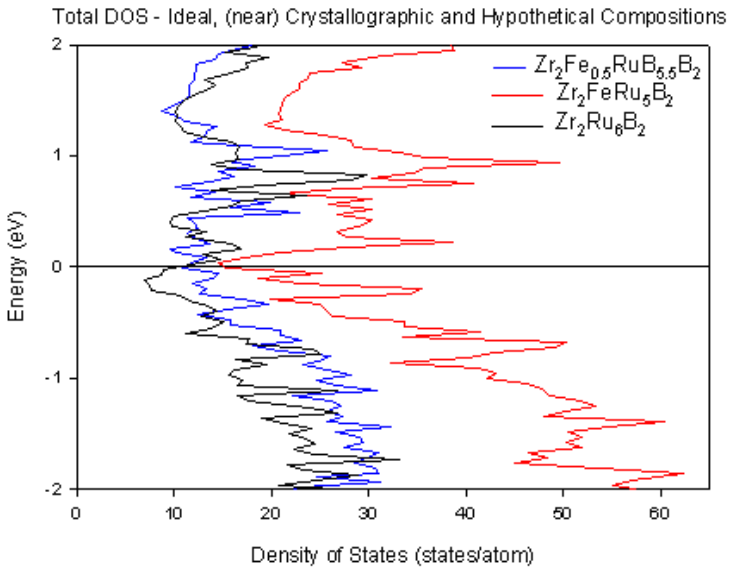

Figure S2. (a) SEM-BSE micrograph with EDS X-ray map of $Zr_2FeRu_5B_2$ (b) Spots (yellow cross hairs) where the individual compositions were collected, the light phase is the desired phase $Zr_2FeRu_5B_2$ and the matrix. The darker phase is the minor phase, Fe_6Ru_{10}

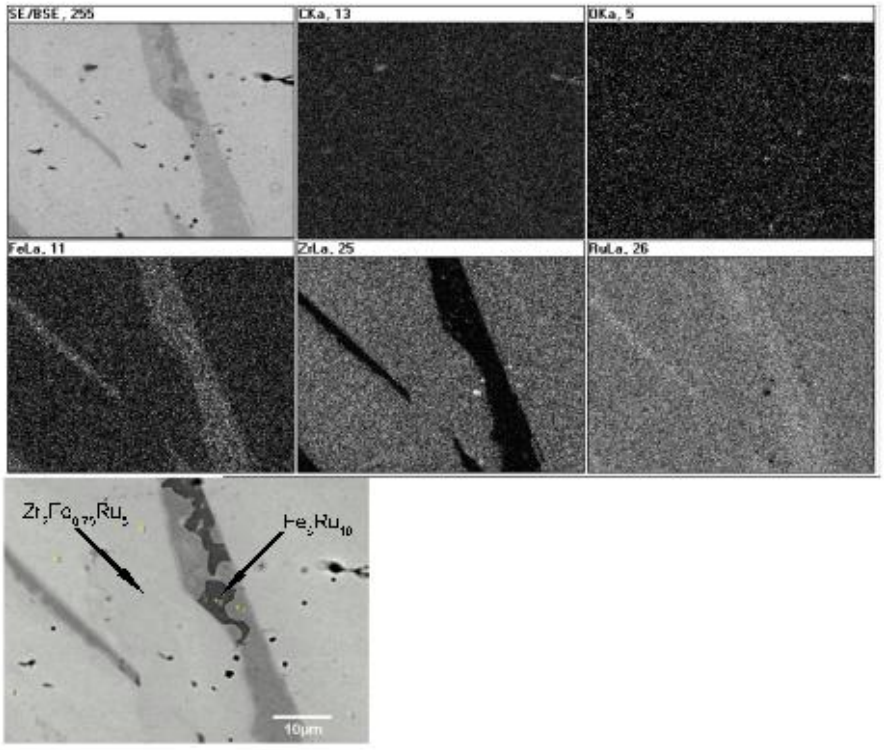

Figure S3. Spin Polarized Ru-Fe COHP interaction

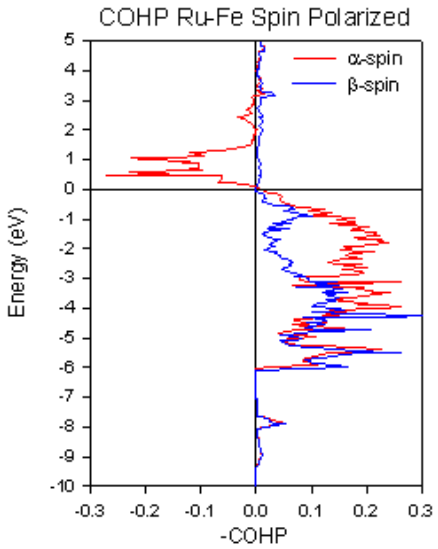

Figure S4. Starting magnetic models

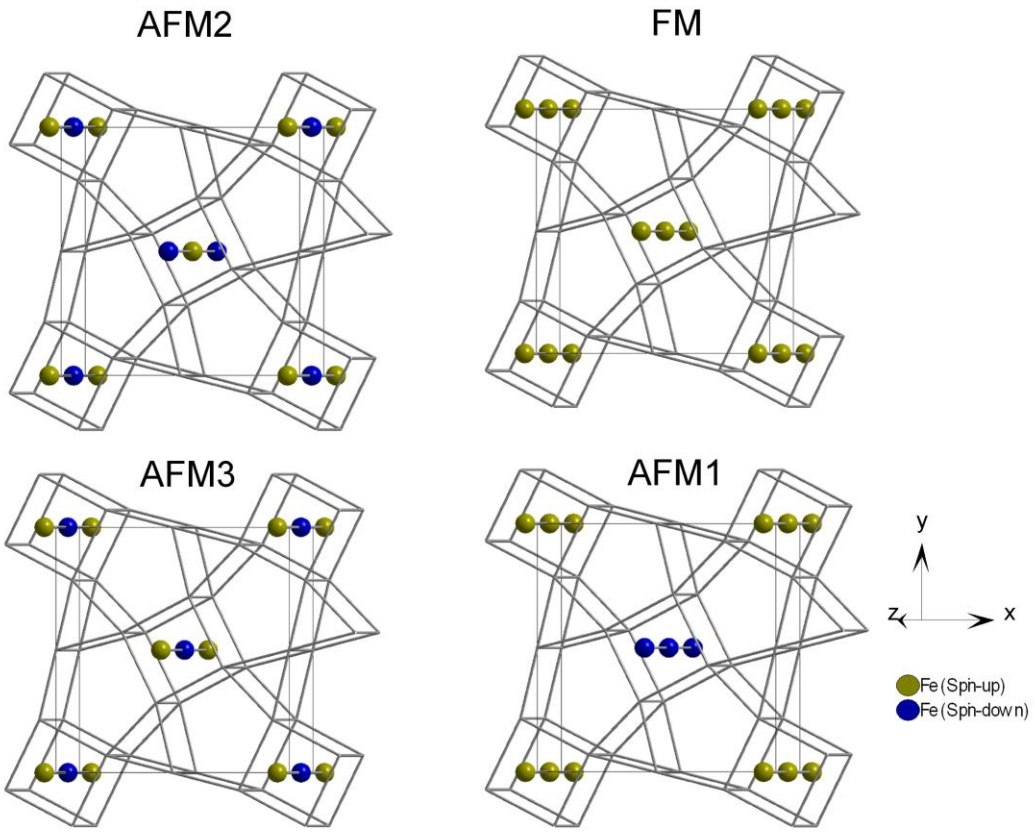

CHAPTER 4

Determining Atomic Site Preference and its Effect on Magnetic Structure in a Class of Intermetallic Borides

*Jakoah Brgoch, Yassir A. Mahmoud, Gordon J. Miller**

Department of Chemistry, Iowa State University, Ames, Iowa, 50011, USA

*Corresponding Author: gmiller@iastate.edu (G.J. Miller)

4.1 Abstract

The site preference for a class of intermetallic borides following the general formula, $M_2Fe(Ru_{0.8}T_{0.2})_5B_2$ (M = Sc, Ti, Zr; T = Ru, Rh, Ir), has been explored using *ab initio* and semi-empirical electronic structure calculations. This intermetallic boride series contains two potential sites, the Wyckoff 2*c* and 8*j* sites, for Rh or Ir to replace Ru atoms. Since the 8*j* site is a nearest neighbor to the magnetically active Fe atom, whereas the 2*c* site is a next nearest neighbor, the substitution pattern should play an important role in the magnetic structure of these compounds. The substitution preference is calculated based on the site energy and bond energy terms, which are known to dictate the locations of atoms in extended solids. From these calculations, we can conclude the valence electron-rich Rh and Ir atoms will prefer to occupy the 8*j* site, a result also corroborated by experimental evidence. Additionally, substitution of Rh or Ir at the 8*j* site, as predicted, results in a larger Fe-Fe magnetic exchange, as well as an increased local magnetic moment on the Fe atoms.

4.2 Introduction

Recent research has shown intermetallic borides can provide a platform to investigate changes in magnetic properties as a function of valence electron (VE) count.[1-5] One specific class of borides has been identified for a wide range of compositions following the general formula $M_2Fe_{1-\delta}(T_{1-x}T'_x)_{5+\delta}B_2$ (M = Sc, Ti, Zr; T/T′ = Ru, Rh, Ir; x = 0-1; δ = 0-0.2), all of which crystallize in space group *P*4/*mbm* (no. 127, $Ti_3Co_5B_2$-type structure[6]). This structure contains pseudo-cubic prisms of T/T′ atoms that can be occupied by magnetically active elements, such as Fe atoms, which, in turn, form magnetic chains along the [001] direction with interatomic distances of ca. 3.0 Å. These chains show long range magnetic ordering that varies as a function of the VE count. Additionally, two magnetic chains are present in each unit cell separated by ca. 6.5 Å. Although this distance is too long for through-space magnetic interactions, the chains are connected via ⋯Fe-M-Fe⋯ and ⋯Fe-T-T-Fe⋯ units with only the latter mediating inter-chain magnetic exchange.

One example of affecting long range magnetic ordering by changing the VE count occurs in the system $Sc_2Fe(Ru_{1-x}Rh_x)_5B_2$ (60-65 VEs),[3] which can be synthesized across the entire range, $0 \leq x \leq 1$. Using SQUID magnetometry, antiferromagnetic ordering was identified at high Ru content, while ferromagnetism was found at high Rh content, with the transition occurring between 62 VE and 63 VE. The exact mechanism behind this change has yet to be fully identified, however, it is postulated to stem from the occupation of Fe-Fe and Fe-Ru/Rh antibonding orbitals at the Fermi level for higher VE counts ($x > 0.3$), and nonbonding orbitals in the Ru-rich cases ($x < 0.3$).[7] Furthermore, differences in Fe-Ru and Fe-Rh magnetic exchange coupling were identified and likely play a role in the long range ordering. Calculations of the exchange parameters, J_{ij}, yielded a larger parameter for Fe-Rh contacts ($J_{Fe\text{-}Rh}$ = 3.77 meV) in $Sc_2FeRh_5B_2$, than for Fe-Ru contacts ($J_{Fe\text{-}Ru}$ = 0.07 meV) in $Sc_2FeRu_5B_2$.[8] This difference not only enhances the local magnetic moment at Fe atom in $Sc_2FeRh_5B_2$ as compared to $Sc_2FeRu_5B_2$, but it could also assist in the observed changes in long range ordering.

In the $Ti_3Co_5B_2$-type structure of $M_2Fe(T_{1-x}T'_x)_5B_2$, illustrated in Figure 1, the T/T′ atoms have two potential occupation sites, Wyckoff 2*c* and Wyckoff 8*j*. Since

different J_{ij} values exist between the Ru/Rh atoms, predicting the magnetic structure accurately requires correct modeling of the site substitution. For instance, if the substitution occurs at the 8*j* site, a Fe atom chain is a nearest neighbor and should have a large effect on the magnetic response relative to occupation of the 2*c* site, a next nearest neighbor. Although conventional X-ray diffraction cannot unequivocally distinguish Ru and Rh given their similar scattering power, it can differentiate Ru and Ir. Therefore, this substitution can experimentally indicate the site preference. In fact, a preference for the electron-rich atoms to occupy the 8*j* site has been confirmed using single crystal X-ray diffraction for the Ir substitution.[9] However, it remains an assumption that Rh and Ir will have the same site preference. To refine Ru and Rh independently, neutron diffraction would be necessary and synthesizing the large quantities of crystalline sample necessary has proven difficult.

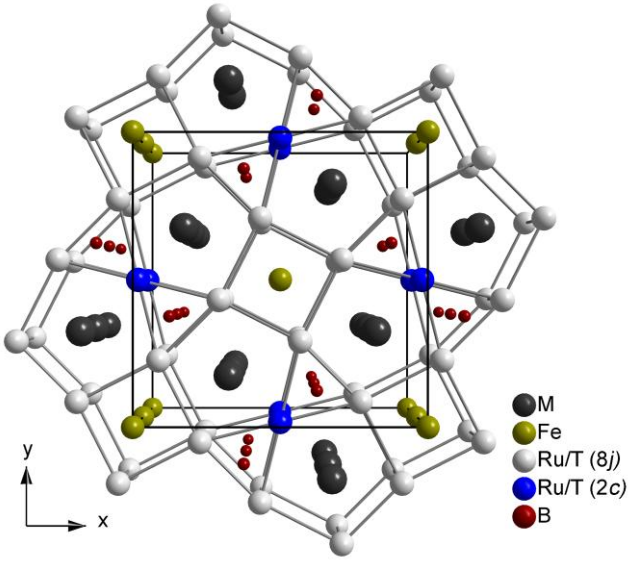

Figure 1. A perspective view along the [001] direction of $M_2Fe(Ru_{0.8}T_{0.2})_5B_2$ (M = Sc, Ti, Zr; T = Ru, Rh, Ir).

Herein, we perform electronic structure calculations on the specific series $M_2Fe(Ru_{0.8}T_{0.2})_5B_2$ (M = Sc, Ti, Zr; T = Ru, Rh, Ir) to determine the total energy, which will indicate the most electronically favorable substitution model. The relative site energy and bond energy terms from a tight-binding evaluation of the band energy are then utilized to identify a site preference in the structure.[10] These results are compared

against experimental Ir substitution patterns to establish rules for 4*d*/5*d* site substitution in these compounds.[9] Additionally, because the magnetic structures of these compounds can be controlled as a function of composition and potentially atomic location, magnetic models are employed to determine any changes in itinerant magnetism that may result from the location of the substituted 4*d*/5*d* atoms.

4.3 Theory

Total energy calculations were completed with the Vienna *ab initio* simulation package (VASP, version 4.6).[11-13] The symmetry was reduced to space group *P*1 to avoid any energetic differences due to lost band degeneracies that may occur upon changing symmetry for different substitution patterns. The calculations were performed using the projector augmented-wave (PAW) method of Blöchl[14] and adapted in VASP by Kresse and Joubert.[15] Exchange and correlation were treated based on the local density functional of Ceperley and Alder,[16] parameterized by Perdew and Zunger[17] with the gradient corrections following Perdew and Wang.[18] Spin polarization was taken into account according to Von Barth and Hedin's[19] local spin density theory, using the spin interpolation proposed by Vosko.[20] A 4 × 4 × 8 Monkhorst-Pack ***k***-points grid[21] was used to sample the first Brillouin zone for reciprocal space integrations. The energy cut-off of the plane wave basis was 400 eV. With these settings, the total energies converged to less than 1 meV per formula unit (f.u.). Additionally, the converged VASP calculations were used to determine the volume surrounding each atomic site. By using a grid-based analysis, i.e., Bader's analysis,[22-24] the volume of the calculated surface indicates how much space the 8*j* and 2*c* sites have for atoms to occupy.

The site energies were calculated using the Mulliken populations from the semi-empirical Extended Hückel Theory (EHT).[25-28] In EHT, the atomic orbitals are expressed as Slater-type orbitals with double-ζ functions for transition metals and a single-ζ function for the B atoms. Diagonal Hamiltonian matrix elements are given by valence state orbital energies derived by calibrating to a DFT calculated band structure;[29] while off-diagonal Hamiltonian matrix elements are approximated by the weighted Wolfsberg-

Helmholz approximation.[25] The atomic orbital parameters are provided in Table S1 of Supporting Information.

The bond energy term is related to the energy-weighted total overlap population. These values can be estimated by integrating the crystal orbital Hamilton population (COHP)[30] curves to the Fermi level giving ICOHP values for each pairwise interaction. The –COHP curves were calculated with the tight-binding, linear muffin-tin orbital method under the atomic-sphere approximation (TB-LMTO-ASA)[31,32] using the Stuttgart code.[33] For the LMTO calculations, exchange and correlation were treated by the local density approximation (LDA), which was parameterized according to von Barth and Hedin.[19] Although these structures show magnetic order, we have found the bond energy term is not sensitive to spin-polarization, thus, LDA is sufficient. For comparison, the spin-polarized (LSDA) bond energies are presented in Table S2 of Supporting Information. The corresponding Wigner-Seitz (WS) radii for the LMTO calculations are presented in Supporting Information. Space-filling, empty spheres were not necessary in these models. The basis set for each calculation includes: B (2*s*, 2*p*), Fe (4*s*, 4*p*, 3*d*), Sc (4*s*, 4*p*, 3*d*), Ti (4*s*, 4*p*, 3*d*), Zr (5*s*, 5*p*, 4*d*), Ru (5*s*, 5*p*, 4*d*), Rh (5*s*, 5*p*, 4*d*), and Ir (6*s*, 6*p*, 5*d*) wavefunctions. A mesh of 63 ***k*** points in the irreducible wedge of the first Brillouin zone was used to obtain all integrated values, e.g., –COHP and the density of states (DOS) curves.

4.4 Results and Discussion

4.4.1 Total Energy Calculations. Initially, VASP was utilized to calculate the relative total energies of three models used to simulate atomic site preferences. The three structural models have the total composition $M_2Fe(Ru_{0.8}T_{0.2})_5B_2$ (M = Sc, Ti, Zr; T = Rh, Ir), illustrated in Figure 2, and used the atomic positions and lattice parameters determined experimentally,[1,3,5] regardless of the local composition. The first model (Model 1) contains Rh or Ir at the Wyckoff 2*c* site and Ru at all 8*j* sites. Model 2 replaces ¼ (25%) of the Ru atoms at the 8*j* site with Rh/Ir and contains Ru at the 2*c* site. This resulted in two ⋯Rh-Rh⋯ (or ⋯Ir-Ir⋯) chains along the [001] direction in each unit cell. Model 3 follows the same atomic substitution in the *ab* plane as Model 2, but

the stacking along the [001] direction forms four alternating ⋯Ru-Rh⋯ (or ⋯Ru-Ir⋯) chains per unit cell. To accommodate the 25% substitution in the 8*j* site, the symmetry of Models 2 and 3 were reduced from *P*4/*mbm* to *P*1. Calculations varying locations of the Rh/Ir atoms in the 8*j* site in Models 2 and 3 showed negligible (<25 meV) differences. As a result, substitution at any of the 8*j* sites was valid to describe the structural models. We must note the symmetry of Model 1 was also reduced to space group *P*1, even though the symmetry of space group *P*4/*mbm* is retained, to eliminate any energetic differences that may arise from loss of any band degeneracies, allowing a direct comparison between all three models.

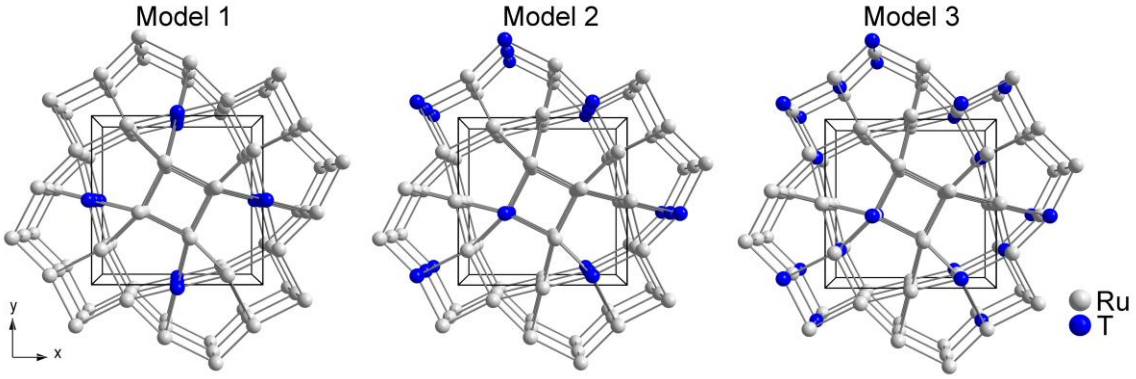

Figure 2. (a) Model 1, substituting Rh/Ir for Ru atom in the 2*c* Wyckoff position. (b) Model 2, substituting ¼ of the Ru atoms for Rh/Ir in the 8*j* Wyckoff position. (c) Model 3, substituting ¼ of the Ru atoms for Rh/Ir in the 8*j* Wyckoff position varying the position along the [001] direction. All structures have total compositions of $M_2Fe(Ru_{0.8}T'_{0.2})_5B_2$ (M = Sc, Ti, Zr; T′ = Rh, Ir). The DOS curves of these models are presented in Supporting Information.

Table 1. VASP total energies, relative to the lowest energy model. Ferromagnetic ordering was used to determine the total energy of the spin polarized models. Antiferromagnetic models resulted in the same preference, and thus, is provided in Supporting Information

	Model 1 (meV/cell)	Model 2 (meV/cell)	Model 3 (meV/cell)
$Sc_2Fe(Ru_{0.8}Rh_{0.2})_5B_2$	+233.9	0	+18.5
$Ti_2Fe(Ru_{0.8}Rh_{0.2})_5B_2$	+320.2	0	+2.0
$Zr_2Fe(Ru_{0.8}Rh_{0.2})_5B_2$	+255.4	0	+6.9
$Sc_2Fe(Ru_{0.8}Ir_{0.2})_5B_2$	+350.7	+34.5	0
$Ti_2Fe(Ru_{0.8}Ir_{0.2})_5B_2$	+461.4	+105.9	0
$Zr_2Fe(Ru_{0.8}Ir_{0.2})_5B_2$	+360.4	+96.6	0

The total energies of Models 1, 2, and 3 are presented in Table 1 relative to the lowest energy model. In all cases, Model 1 was significantly higher in energy ranging from +234 to +320 meV/cell for Rh substitution and +351 to +461 meV/cell for Ir. When Ir was placed in the structure, the total energy was over 120 meV/cell higher relative to when Rh was placed in the same positions. This difference could be related to the volume of the 8*j* and the 2*c* sites in these intermetallics. Using structural models of $M_2FeRu_5B_2$ (M = Sc, Ti, Zr), a Bader's analysis[22] indicated the volume of the 2*c* and 8*j* sites, presented in Table 2. In all cases, regardless of the M atoms, the 8*j* site had a larger Bader volume as a result of their respective coordination environments and, thus, more space to accommodate atoms.

Table 2. Bader volumes for $M_2FeRu_5B_2$ (M = Sc, Ti, Zr) calculated using VASP.

	Bader Surface Volume (Å^3)		
	$Sc_2FeRu_5B_2$ (60 VE)	$Ti_2FeRu_5B_2$ (62 VE)	$Zr_2FeRu_5B_2$ (62 VE)
2*c*	15.25	14.82	14.85
8*j*	17.01	15.88	16.50

These size differences result in the calculated preference for the electron rich atoms (Rh or Ir) to occupy the 8*j* site as they attempt to distance themselves from the surrounding atoms. Additionally, Ir is slightly larger (1.355 Å) relative to Rh (1.342 Å) so it should have an ever greater energetic preference to occupy the 8*j* site, as observed from the total energy calculations.[34]

The relative total energies of Models 2 and 3 are nearly equivalent. In $M_2Fe(Ru_{0.8}Rh_{0.2})_5B_2$ (M = Sc, Ti, Zr) the difference between these two is less than 20 meV/f.u., signifying they are likely identical under ambient conditions. These energies are inline with the calculations that varied the location of the Rh atoms in the 8*j* site. In both cases the total energy indicates a statistical distribution is present across all of the 8*j* sites and that no superstructures, or long-range ordering, should be expected. In $M_2Fe(Ru_{0.8}Rh_{0.2})_5B_2$ (M = Sc, Ti, Zr), the difference between Models 2 and 3 is slightly greater, with Model 2 ranging between +35 to +100 meV/f.u. larger than Model 3. Again, the larger size of Ir will result in additional stress when surrounded by other large Ir atoms. By ordering the Ir atoms in a manner similar to Model 3, the larger Ir atoms are separated forming only heteroatomic contacts, relieving the local size constraints.

The similar total energies of Models 2 and 3 illustrate the presence of statistical disorder at the 8*j* site, which is manifested by atomic mixing between Ru/Rh and Ru/Ir. Furthermore, Model 1 has the highest relative energy of all structural models revealing the site preference for Rh or Ir to occupy the 8*j* site over the 2*c* site. These total energy calculations not only confirm the site preference observed experimentally for Ir substitution[9] but they also confirm that Rh should substitute follow a similar substitution pattern to Ir.

4.4.2 Site Preference. Although Rh or Ir prefer to occupy by the 8*j* site based on the total energy calculations, identifying the forces that govern this substitution pattern will allow the creation of general "substitution rules" that can be employed for future directed synthesis.

The electronic band energy can be broken down as a sum of two terms[10], shown in Equation 1.

$$E = \sum_i q_i \alpha_i + \sum_i \sum_{j \neq i} p_{ij} (\beta_{ij} - S_{ij} \alpha_i) \quad (1)$$

The first term is called the 'site energy' and is the sum of the product of the atomic orbital (AO) populations (q_i) and the valence AO energies (α_i) for every atomic site, *i*, in the models. Comparing the site energy for each model indicates whether an accumulation of electrons (q_i) is present at any one site. The build-up of negative charge at a given site can be viewed in two ways. The simplest interpretation is that for a site to satisfy the additional charge requirement, a more electron-rich atom is preferred to occupy that position. A second explanation is that to maintain constant energy, when q_i increases α_i must decrease (assuming bonding does not change). The lower the AO energies the more electronegative an atom tends to be. Since electronegativity tends to increase from left to right across the periodic table, by decreasing the AO energy electrons are inherently added to the system. In either case, the build-up of negative charge indicates the potential substitution of a more electron-rich, or electronegative atom.[35] The second term is the 'bond energy' and contains the overlap population (p_{ij}), the resonance integral (β_{ij}), and the overlap integral (S_{ij}). This term is minimized by filling bonding orbitals and keeping antibonding orbitals empty. Comparing the bond energy term and site energy term of various structural models can establish which term regulates site occupation. One drawback to this method is that the term $S_{ij}\alpha_i$ in Equation 1 is not necessarily constant because the average electrostatic potential is not defined in DFT based methods. Calculations often set the potential to zero to counteract this issue; however, the relative position of "zero" can vary from system to system. Without a true energy "zero" across all systems, it is inappropriate to strictly compare the bond energy terms of the different models. However, by maintaining a constant volume and total composition of the structural models, these effects will be mitigated.[10]

To calculate the relative site energy terms, the same atomic potential must be placed in the sites of interest to allow a direct comparison of the final Mulliken populations. Three compositions were investigated with Ru occupying both the 2*c* and 8*j* sites with total compositions of: $Sc_2FeRu_5B_2$, $Ti_2FeRu_5B_2$, and $Zr_2FeRu_5B_2$. These compositions were selected since the lattice parameters and atomic positions were

determined experimentally, whereas other compositions, e.g., $Zr_2FeRh_5B_2$, have yet to be synthesized.[1,3,5]

Table 3. Mulliken populations of $M_2FeRu_5B_2$ (M = Sc, Ti, Zr) for the Wyckoff 2*c* and 8*j* sites calculated using EHT. The positive difference between Wyckoff sites (Δ8*j*–2*c*) indicates a preference for the 8*j* site to contain Rh/Ir.

	$Sc_2FeRu_5B_2$	$Ti_2FeRu_5B_2$	$Zr_2FeRu_5B_2$
8*j*	8.240	7.471	7.906
2*c*	7.741	7.047	7.391
Δ8*j*–2*c*	0.499	0.424	0.515

The site energies, listed in Table 3, were calculated through an analysis of site (Mulliken) populations from EHT. In all three cases, the 8*j* site clearly develops a larger population compared to the 2*c* site. This trend holds true regardless of the M atom, although the difference between the two sites (Δ8*j*–2*c*) does show slight variations with M.

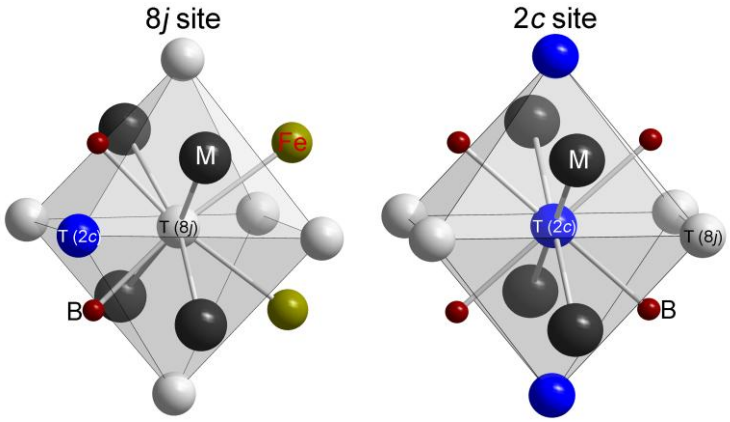

Figure 3. The coordination spheres for the 8*j* site (left) and the 2*c* site (right). Two coordination spheres are shown, (i) the distorted octahedral coordination of the 4*d*/5*d* atoms and (ii) the atoms that cap the faces of the octahedrons.

An atom-centered description, Figure 3, shows the coordination for the 2*c* and 8*j* sites, surrounding which ultimately cause charge to build-up at the 8*j* site. Both of these sites are coordinated by a distorted octahedron of 4*d* or 5*d* atoms, with the 8*j* site more distorted than the 2*c* site. The local symmetry of the 2*c* site is D_{2h} while the symmetry of

the 8*j* site is C_s. The equatorial atoms around the 2*c* site are equivalent (the 8*j* site), and equidistant with bond lengths of ca. 2.7 Å. The equatorial atoms around the 8*j* site include two additional 8*j* atoms and two 2*c* atoms with bond distances ranging between 2.7 Å to just over 3.0 Å in the case of $Zr_2FeRu_5B_2$. The axial atoms complete the octahedra and have the same bond distance for both Wyckoff sites, dictated by the *c*-lattice parameter. Considering the differences in bond lengths, the 8*j* site should contain larger Mulliken populations due to the decreased orbital overlap. Additionally, the faces of the octahedra are capped by M atoms, Fe atoms, and boron. It is clear from Figure 2 that four M atoms and two boron atoms cap six of the eight octahedral faces at both sites. Two additional boron atoms coordinate the 2c site while two Fe atoms coordinate faces at the 8*j* site. Comparing the absolute electronegativities of these different coordination environments should provide insight into the population differences. In fact, boron is slightly more electronegative, 4.29 eV, compared to Fe, 4.06 eV.[36] Thus, the coordination of boron atoms should result in a more electron withdrawing environment relative to Fe coordination. Although the bond distances and angles vary depending on the M atom, the trends are the same for all of these structures. Consequently, if site preference were based solely on site energy, the electron rich Rh/Ir atoms would occupy the 8*j* site as occurs experimentally.

The bond energy term is calculated using the structural models described above. These terms are derived from a summation of all individual –ICOHP values for Models 1 and 2. By comparing the energies of these three models, the most favorable bonding network can be determined. As shown in Table 4, when Rh is substituted in the structure, the atom will prefer to occupy the 8*j* sites, as in Model 2. The bonding network is the weakest (smallest –ICOHP value) for Model 1, placing Rh in the 2*c* site. These results are parallel with the total energy calculations, which predict substitution to occur at the 8*j* site.

Table 4. The total –ICOHP values for Models 1, 2 and 3 calculated by summing the –ICOHP values of each coordination sphere in the structures using TB-LMTO. The **bold** models are the most favorable structural model.

	Total –ICOHP (eV/unit cell)		
	Model 1	Model 2	Model 3
$Sc_2Fe(Ru_{0.8}Rh_{0.2})_5B_2$	155.4	**161.0**	158.2
$Ti_2Fe(Ru_{0.8}Rh_{0.2})_5B_2$	195.6	**199.3**	195.9
$Zr_2Fe(Ru_{0.8}Rh_{0.2})_5B_2$	181.5	184.2	**187.5**
$Sc_2Fe(Ru_{0.8}Ir_{0.2})_5B_2$	**178.2**	176.2	173.6
$Ti_2Fe(Ru_{0.8}Ir_{0.2})_5B_2$	**164.9**	163.3	161.7
$Zr_2Fe(Ru_{0.8}Ir_{0.2})_5B_2$	**171.9**	170.2	171.3

The substitution of Ir shows the opposite trend in bond energy terms, preferring to occupy the 2*c* site, Model 1. Although there is a striking difference between the site preferred by Rh and Ir from on the bond energy term, the site selection can be justified based on the respective coordination spheres. Table 4 provides a comparison of the local –ICOHP values and the number of contacts in the coordination sphere around the five Wyckoff positions.

Table 5. The –ICOHP values for the local coordination environments surrounding each Wyckoff position. The values include the nearest neighbor and the next nearest neighbor (distances ≤ ca. 3.5 Å). $Sc_2Fe(Ru_{0.8}T_{0.2})_5B_2$ (T = Rh, Ir) is presented here, M = Ti, Zr is presented in Table S4 of Supporting Information.

Atom Center	Total # of Contacts	Local –ICOHP (eV/coordination sphere)		
		$Sc_2Fe(Ru_{0.8}Rh_{0.2})_5B_2$		
		Model 1	Model 2	Model 3
T (8*j*)	9	18.7	17.8	18.0
T (2*c*)	9	18.5	21.5	21.0
Sc (4*g*)	10	9.7	9.1	9.6
Fe (2*a*)	9	12.7	12.6	12.2
B (4*g*)	6	18.2	19.5	18.2

Table 5 Continued

		$Sc_2Fe(Ru_{0.8}Ir_{0.2})_5B_2$		
		Model 1	Model 2	Model 3
T (8*j*)	9	18.3	17.9	18.2
T (2*c*)	9	22.6	21.0	20.9
Sc (4*g*)	10	12.3	12.3	12.0
Fe (2*a*)	9	16.1	16.1	16.3
B (4*g*)	6	19.7	20.6	19.2

In the compounds containing Rh, the bonds formed between the 2*c* site and the surrounding atoms appear to dictate the structural preference. For instance, when Ru is placed in the 2*c* site (Model 2), the bond energy of the local coordination sphere is 14% larger relative to when Rh occupies the same site. This increased bond energy is influenced by Ru-M and Ru-Ru (along the [001] direction) interactions, which are 17% and 30% larger, respectively, compared to the analogous Rh contacts. Additionally, the bond energy is 5% larger when Ru is placed in the 8*j* site (Model 1). From a bond energy perspective, this is indicative of Rh substitution into this structure being potentially arduous.

Substituting Ir shows a different trend, preferring to occupy the 2*c* site, in stark contrast to the Rh substitution. The bonding spheres in this case are more comparable with Models 1 and 2, differing by only 7% at the 2*c* and 8*j* sites. The difference in bond energy comes from the Rh-B and Ir-B bonds. An analysis of the partial DOS, illustrated in Figure 4, of the 2*c* site shows Rh and Ir both contain states between −10 and −7.5 eV that are, respectively, from the 4*d* and 5*d* orbitals. By integrating the DOS (IDOS), a larger number of states are present for the Ir relative to the Rh atoms. Considering the B partial DOS contains nearly an identical number of 2*p* orbitals in the same energy window as these 4*d*/5*d* orbitals, the bonding should be affected solely by the location of the *d*-states. Since there are more orbitals in the same energy window for the Ir atom, they form a relatively stronger Ir-B bond, i.e., larger –ICOHP values, relative to the Rh-B interactions. With two B atoms surrounding the 2*c* site, the effects at the 2*c* site should

be amplified. As a result, according to the bond energy term Ir will prefer to occupy the 2*c*, the opposite of experimental observations, while Rh will prefer to occupy the 8*j* site.

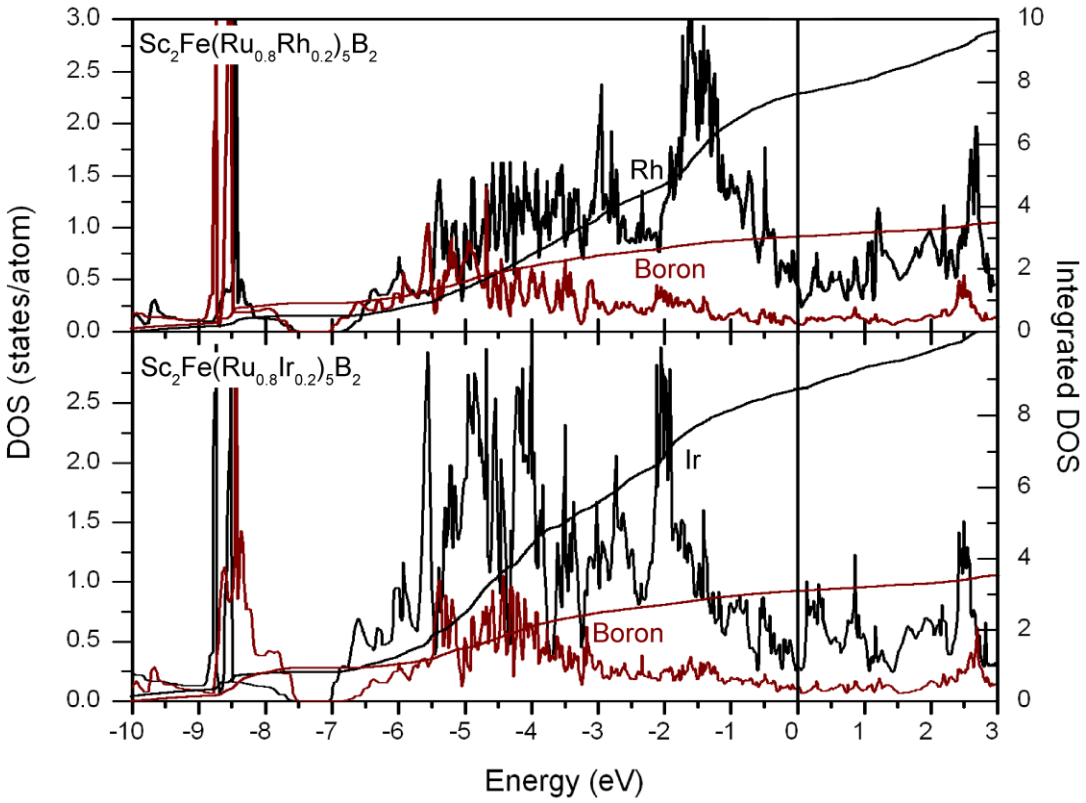

Figure 4. The partial DOS of Rh, Ir, and boron from $Sc_2Fe(Ru_{0.8}T_{0.2})_5B_2$ (T = Rh/Ir) and their respective integrated DOS.

Comparing the site energy and bond energy terms to the experimental results and total energy calculations, a site preference can be identified. The substitution of Rh is dictated by both the site and bond energy terms, whereas Ir shows opposing site energy and bond energy terms. In structures where these two terms agree atomic sites will tend to have contain a stronger site preference relative to when the two terms are opposite. Experimentally, this will be manifested in the compounds as a larger difference in the occupation of 8*j* site relative to the 2*c* site in the Rh series and a smaller difference in the Ir series.

By combining the results of the site energy and bond energy calculations, with the substitution pattern determined experimentally, a set of "substitution rules" can be

assigned for these structures to predict future experimental results. (i) First, since the site energy regulates the site preference, determining the most electron withdrawing environments will indicate where valence electron rich atoms will likely substitute. (ii) Using a Bader's analysis in the intermetallic compounds is a useful way of quantifying the site volume to determine the site volume to predict where larger, and more electron rich atoms will occupy; (iii) due to the interactions of the B 3 *p*-orbitals with the 4*d*/5*d* transition metal, the bond energy term, i.e., –ICOHP values, must be analyzed carefully for each system.

4.3.3 Effects of Substitution on Magnetism. According to the previously reported exchange parameters,[8] the presence of Rh should increase the magnitude of $J_{Fe\text{-}Fe}$ in the chain resulting in a modified magnetic structure. Since the Fe atoms in all three models described above contain different Rh/Ir coordination environments, they are ideal systems to investigate magnetism as a function of surroundings. For instance, Model 1 contains zero Rh/Ir atoms as Fe nearest neighbors (0 Rh/Ir:1 Fe) while both of the Fe chains in Model 2 contain two Rh/Ir atoms as nearest neighbors (2 Rh/Ir:1 Fe). Model 3 has two independent coordination environments of the Fe chains, with one Fe chain having two Rh/Ir nearest neighbors (2 Rh/Ir:1 Fe) and the other having only one nearest neighbor Rh/Ir (1 Rh/Ir: 1 Fe). Thus, it can be predicted that based on the differing exchange energies a greater number of Rh/Ir atoms as nearest neighbors so increase the magnetic exchange. Therefore, Model 2 should have the largest magnetic exchange while Model 1 should have the smallest.

If the exchange parameter is in fact modified as a function of the Rh/Ir position, the relative energies of the models that include magnetic ordering will be strong indicators. Therefore, Models 1, 2, and 3 were expanded to include two types of magnetic ordering. One is ferromagnetic (FM), in which all of the Fe spins are parallel. (These models are denoted as FM-1, FM-2, and FM-3). The second type incorporates antiferromagnetic (AFM) ordering, containing alternating spins along the [001] direction and parallel spins in the *ab*-plane. (These are designated as AFM-1, AFM-2, and AFM-3). These six magnetic models are also illustrated in Supporting Information. Although

FM and AFM ordering is by no means an exhaustive analysis of all possible magnetic structures, they provide grounds for a direct comparison of the total energy as a function of atom location.

The relative energies of each magnetic model (E_{AFM} and E_{FM}) are presented in Table 6. A larger energy difference ($E_{AFM} - E_{FM}$) exists between the two models for nearly all compositions when Rh or Ir are nearest neighbors to Fe atoms, i.e., FM-2 − AFM-2, validating the previously reported exchange values. The magnetic ordering always has the smallest energy difference when Rh/Ir is located in the 2*c* (AFM-1 − FM-1), which is expected since the coordination sphere of the Fe chains (0 Rh/Ir:1 Fe) does not contain any Rh/Ir atoms. Although Models 2 and 3 are much closer in energy with each other, the two distinctive coordination environments in Model 3 result in an average exchange value that falls between Models 1 and 2.

Table 6. The relative total energies (in meV/f.u.) of FM and AFM magnetic ordering for structural ($E_{AFM} - E_{FM}$)

	Model 1 (AFM-1 − FM-1)	Model 2 (AFM-2 − FM-2)	Model 3 (AFM-3 − FM-3)
$Sc_2Fe(Ru_{0.8}Rh_{0.2})_5B_2$	12.03	20.06	17.16
$Ti_2Fe(Ru_{0.8}Rh_{0.2})_5B_2$	29.44	33.87	33.62
$Zr_2Fe(Ru_{0.8}Rh_{0.2})_5B_2$	4.89	18.49	10.36
$Sc_2Fe(Ru_{0.8}Ir_{0.2})_5B_2$	11.22	22.12	12.59
$Ti_2Fe(Ru_{0.8}Ir_{0.2})_5B_2$	29.97	36.77	32.42
$Zr_2Fe(Ru_{0.8}Ir_{0.2})_5B_2$	2.37	10.03	11.80

Substituting Rh or Ir at the 8*j* site also increases the magnetic moments on the Fe atoms presumably stemming from larger J_{ij} values. In all cases, the local magnetic moments in Model 1 are the smallest while Model 2 has the largest, confirming the respective weakest and strongest relative exchange parameters. In Model 3, the two coordination environments result in different magnetic moments at each Fe atom. For instance, Fe atoms surrounded by 2 Rh/Ir atoms has a magnetic moment that is nearly the same as those calculated in Model 2, whereas Fe atoms with only 1 Rh/Ir nearest

neighbor has a local magnetic moment closer to Model 1. The increase in magnetic moments for the larger number of coordinated Rh/Ir atoms further corroborates the change in exchange constants as a function of coordination environment.

Table 7. Magnetic moment (in μ_B/Fe) calculated from VASP for the compositions $M_2Fe(Ru_{0.8}T_{0.2})_5B_2$ (M = Sc, Ti, Zr; T= Rh, Ir)

	Model 1 (0 Rh/Ir:1 Fe)		Model 2 (2 Rh/Ir:1 Fe)		Model 3 (2 Rh/Ir:1 Fe)		Model 3 (1 Rh/Ir:1 Fe)	
	FM-1	AFM-1	FM-2	AFM-2	FM-3	AFM-3	FM-3	AFM-3
$Sc_2Fe(Ru_{0.8}Rh_{0.2})_5B_2$	2.44	2.29	2.47	2.35	2.46	2.36	2.40	2.28
$Ti_2Fe(Ru_{0.8}Rh_{0.2})_5B_2$	2.51	2.38	2.58	2.49	2.60	2.51	2.56	2.51
$Zr_2Fe(Ru_{0.8}Rh_{0.2})_5B_2$	2.71	2.64	2.77	2.74	2.83	2.72	2.79	2.73
$Sc_2Fe(Ru_{0.8}Ir_{0.2})_5B_2$	2.40	2.24	2.45	2.24	2.41	2.28	2.34	2.22
$Ti_2Fe(Ru_{0.8}Ir_{0.2})_5B_2$	2.53	2.41	2.53	2.45	2.54	2.45	2.53	2.45
$Zr_2Fe(Ru_{0.8}Ir_{0.2})_5B_2$	2.67	2.60	2.73	2.63	2.68	2.63	2.67	2.60

The differing exchange energies appear to vary with the dispersion of the 4*d*/5*d* bands. To investigate this proposition, a set of hypothetical magnetic models with the general formula "$Sc_2Fe(Ru_{0.8}T''_{0.2})_5B_2$" (T″ = Ru-Ag; Re-Au) were created. The models that contained the 4*d* atoms, Ru-Ag, used $Sc_2Fe(Ru_{0.8}Rh_{0.2})_5B_2$ as the initial structural parameters, while the models with a 5*d* atom, Re-Au, used the $Sc_2Fe(Ru_{0.8}Ir_{0.2})_5B_2$ structure.

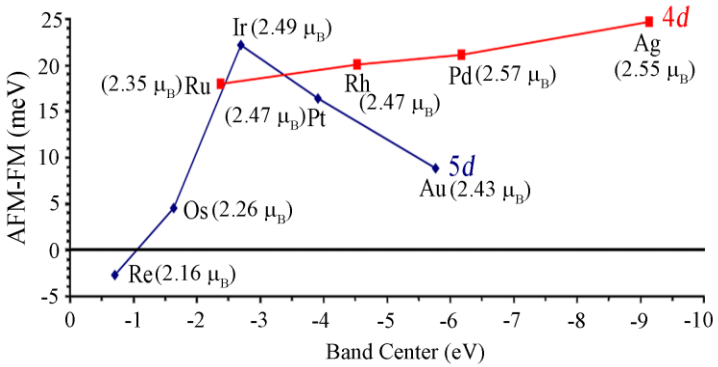

Figure 5. The energy difference ($E_{AFM-2}-E_{FM-2}$) for compounds with a general composition $Sc_2Fe(Ru_{0.8}T''_{0.2})_5B_2$" (T″ = Ru-Ag; Re-Au) as a function of *d*-band center. The average magnetic moments from each FM-2 model are presented in parenthesis. The band centers were calculated using TB-LMTO.

From Figure 5, it is clear going from Ru through Ag, the relative energy difference increase nearly linearly. This trend is correlated to the dispersion of the *d*-bands for the T″ atom, which decrease in energy from ca. −2 eV to −9 eV. This indicates that substituting a 4*d* atom that is even more electron rich than Rh should further enhance the magnetic interactions in the Fe-chains. Replacing the T″ atom with a 5*d* metal causes an even sharper increase in the magnetic interactions in the going from Re to Ir, however, a maximum is reached at Ir with the energy difference then decreasing going to Pt and Au. Additionally, the average local magnetic moments follow the same trend as the energy difference between the two magnetic models. The 4*d* substitution results in an increasing magnetic moment as the VE count is increased. Going from Re to Ir the magnetic moment increases and then decreases going to Au. Even though the 4*d* and 5*d* magnetic models do not appear to follow the same trend, it is necessary to remember the *d*-bands of the heavier 5*d* elements will experience relativistic effects that perturb the position of the *d*-orbitals. As a result, substituting an electron-rich atom should enhance the magnetic structure, while placing Pt or Au in the 8*j* site would likely have an opposite effect on the magnetic structure.

Nevertheless, based on these magnetic model calculations, it is clear the magnetic response in this class of intermetallic borides is influenced by the location of the electron rich Rh/Ir atoms. Since there is a site preference for these Rh/Ir atoms to occupy the 8*j* site, we can expect a stronger magnetic response along the Fe chains including increased local magnetic moments on the Fe atoms.

4.5 Conclusions

The class of intermetallic borides following the general formula, $M_2Fe(T_{1-x}T'_x)_5B_2$ (M = Sc, Ti, Zr; T/T′ = Ru, Rh, Ir; x = 0-1) demonstrates magnetic response as a function of valence electron count.[1,3,5] However, the presence of two potential substitution sites in the structure makes it challenging to predict the effects on

the magnetic chains. From the calculations presented here, the preference for electron-rich atoms to substitute at the nearest neighbor site (8*j* site) is established by the site energy and the bond energy term in a tight-binding calculation of the band energy. Of these two terms, it appears the site energy term is the dominating factor in the site preference. The results are substantiated by single crystal X-ray diffraction for the compounds $M_2Fe(Ru_{1-x}Ir_x)_5B_2$ (M = Ti, Zr; x = 0-1), which clearly show a site preference for Ir to occupy the Wyckoff 8*j* site.[9] Magnetic models were explored to determine the effect of substitution on the magnetic chains. In all cases, placing the Rh/Ir atoms in the nearest neighbor site increases the energy difference between the FM and AFM model by 2-36 meV/f.u. The resulting magnetic moments on the Fe atoms respond by developing the larger magnetic moments in the systems with the largest exchange parameters. Therefore, substitution of the electron rich atoms at the 8*j* site will occur and greatly influence the magnetic structure of these compounds. Replacing the atom at the 8*j* site with a 4*d* atom that is even more electron rich than Rh will likely increase magnetic exchange while 5*d* atom substitution has some limitations. In the future, the identification of rules used for atomic will allow directed synthesis to not only target desired compounds but also help to tailor desired magnetic properties.

4.6 Acknowledgments

J.B. would like to thank Professor Danny Fredrickson at the University of Wisconsin-Madison for assistance in determining the Extended Hückel parameters as well as *Piv.-Doz.* Dr. Boniface Fokwa and Martin Hermus for providing crystallographic information. The authors acknowledge the generous financial support provided by the U.S. National Science Foundation (NSF DMR 08-06507).

4.7 References

(1) Brgoch, J.; Yeninas, S.; Prozorov, R.; Miller, G. J. *J. Solid State Chem.* **2010**, *183*, 2917.
(2) Dronskowski, R.; Korczak, K.; Lueken, H.; Walter, J. *Angew. Chem. Int. Ed.* **2002**, *41*, 2528.
(3) Fokwa, B. P. T.; Lueken, H.; Dronskowski, R. *Chem. Eur. J.* **2007**, *13*, 6040.
(4) Fokwa, B. P. T. *Eur. J. Inorg. Chem.* **2010**, 3075.

(5) Fokwa, B. P. T.; Lueken, H.; Dronskowski, R. *Eur. J. Inorg. Chem.* **2011**, doi: 10.1002/ejic.20110031.
(6) Kuz'ma, Y. B.; Yarmolyuk, Y. P. *Zhurnal Strukturnoi Khimii* **1971**, *12*, 458.
(7) Samolyuk, G. D.; Miller, G. J. *J. Comp. Chem.* **2008**, *29*, 2177.
(8) Samolyuk, G. D.; Fokwa, B. P. T.; Dronskowski, R.; Miller, G. J. *Phys. Rev. B* **2007**, *76*, 094404.
(9) Hermus, M.; Fokwa, B. P. T. *Z. Anorg. Allg. Chem* **2011**, *637*, 947.
(10) Miller, G. J. *Eur. J. Inorg. Chem.* **1998**, 523.
(11) Kresse, G.; Furthmüller, J. *J. Comput. Mat. Sci.* **1996**, *6*, 15.
(12) Kresse, G.; Furthmüller, J. *Phys. Rev. B* **1996**, *54*, 11169.
(13) Kresse, G.; Hafner, J. *Phys. Rev. B* **1993**, *47*, 558.
(14) Blöchl, P. E. *Phys. Rev. B* **1994**, *50*, 17953.
(15) Kresse, G.; Joubert, D. *Phys. Rev. B* **1999**, *59*, 1758.
(16) Ceperley, D. M.; Alder, B. J. *Phys. Rev. Lett* **1980**, *45*, 566.
(17) Perdew, J. P.; Zunger, A. *Phys. Rev. B* **1981**, *23*, 5048.
(18) Perdew, J. P.; Wang, Y. *Phys. Rev. B* **1992**, *45*, 13244.
(19) von Barth, U.; Hedin, L. *J. Phys. C: Solid State Phys.* **1972**, *5*, 1629.
(20) Vosko, S. H.; Wilk, K.; Nusair, M. *Can. J. Phys.* **1980**, *58*, 1200.
(21) Monkhorst, H. J.; Pack, J. D. *Phys. Rev. B* **1976**, *13*, 5188.
(22) Henkelman, G.; Arnaldsson, A.; Jónsson, H. *Comput. Mater. Sci.* **2006**, *36*, 254.
(23) Sanville, E.; Kenny, S. D.; Smith, R.; Henkelman, G. *J. Comp. Chem.* **2007**, *28*, 899.
(24) Tang, W.; Sanville, E.; Henkelman, G. *J. Phys.: Condens. Matter* **2009**, *21*, 084204.
(25) Ammeter, J. H.; Buergi, H. B.; Thibeault, J. C.; Hoffmann, R. *J. Am. Chem. Soc.* **1978**, *100*, 3686.
(26) Hoffmann, R. *J. Chem. Phys.* **1963**, *39*, 1397.
(27) Burdette, J. *Chemical Bonding in Solids*; Oxford University Press: New York, 1995.
(28) Hoffmann, R. *Solids and Surfaces: A Chemist's View of Bonding in Extended Structures*; VCH: New York, 1988.
(29) Schmidt, J. T.; Lee, S.; Fredrickson, D. C.; Conrad, M.; Sun, J.; Harbrecht, B. *Chem. Eur. J.* **2007**, *13*, 1394.
(30) Dronskowski, R.; Blöchl, P. E. *J. Phys. Chem.* **1993**, *97*, 8617.
(31) Andersen, O. K. *Phys. Rev. B* **1975**, *12*, 3060.
(32) Andersen, O. K.; Jepsen, O. *Phys. Rev. Lett.* **1984**, *53*, 2571.
(33) *TB-LMTO-ASA Program*, 4.7 ed., Krier, G.; Jepsen, O.; Burkhardt, A.; Andersen, O. K., Stuttgart, Germany, 1995.
(34) Pauling, L. *J. Am. Chem. Soc.* **1947**, *69*, 542.
(35) Brgoch, J.; Goerens, C.; Fokwa, B. P. T.; Miller, G. J. *J. Am. Chem. Soc.* **2011**, *133*, 6832.
(36) Pearson, R. G. *Inorg. Chem.* **1988**, *27*, 734.

4.8 Supporting Information

Table S1. Extended Huckel Theory valence state orbital energies for Sc, Ti, Zr, Fe, Ru, B. The energies are derived by calibrating to a DFT calculated band structure.

Atom	H_{ii} (*s*)(eV)	ζ (*s*)	H_{ii} (*p*)(eV)	ζ (*p*)	H_{ii} (*d*)(eV)	ζ1 (*d*)	c1	ζ2 (*d*)	c2
Sc	−7.81	1.52	−2.26	1.52	−6.96	4.35	0.4155	1.84	0.7450
Ti	−8.97	1.50	−5.44	1.50	−10.81	4.55	0.4391	1.60	0.7397
Zr	−10.79	2.08	−5.74	2.04	−14.62	5.38	0.5573	2.30	0.6642
Fe	−9.22	1.90	−5.37	1.90	−12.28	5.55	0.5366	1.80	0.6678
Ru	−10.79	2.08	−5.74	2.04	−14.62	5.38	0.5573	2.30	0.6642
B	−15.20	1.30	−8.50	1.30	---	---	---	---	---

Table S2. Pairwise interactions and corresponding (LSDA) –ICOHP values of structural Models 1, 2 and 3 for (a) $Sc_2Fe(Ru_{0.8}Rh_{0.2})_5B_2$ (b) $Sc_2Fe(Ru_{0.8}Ir_{0.2})_5B_2$. The table is organized by coordination sphere of nearest neighbor and next nearest neighbor around each Wyckoff site.

(a)

$Sc_2Fe(Ru_{0.8}Rh_{0.2})_5B_2$														
Model 1					Model 2					Model 3				
Contact		#	Dist	ICOHP	Contact	#	Dist	ICOHP	Contact	Contact	#	Dist	ICOHP	Contact
Ru14					**Rh14**					**Rh39**				
(8j)	Ru7	1x	2.821	1.136	**(8j)**	Ru7	1x	2.821	0.989	**(8j)**	Ru27	1x	2.821	1.011
	Ru11	1x	2.983	1.112		Ru11	1x	2.983	1.006		Ru28	1x	2.983	1.129
	Ru12	1x	2.983	1.112		Ru12	1x	2.983	1.016		Ru24	1x	2.983	0.962
	Rh15	1x	2.742	1.129		Rh15	1x	2.742	1.117		Ru21	1x	2.742	0.953
	Ru14	2x	3.012	1.917		Ru14	2x	3.012	1.531		Ru20	2x	3.012	1.734
	Sc1	2x	2.931	1.526		Sc1	2x	2.931	1.531		Sc4	2x	2.931	1.298
	Sc3	2x	2.832	1.787		Sc3	2x	2.832	1.281		Sc2	2x	2.832	1.494
	Fe6	2x	2.591	2.745		Fe6	2x	2.591	2.532		Fe10	2x	2.591	2.528
	B20	2x	2.184	6.089		B20	2x	2.184	5.396		B29	2x	2.184	5.438
			Total	**18.554**				**Total**	**16.400**				**Total**	**16.547**
Ru14										**Rh25**				
(8j)	Ru7	1x	2.821	1.136	**Ru (8j)**	Ru7	1x	2.821	1.992	**(8j)**	Ru23	1x	2.821	1.153
	Ru11	1x	2.983	1.112		Ru11	1x	2.983	1.022		Ru28	1x	2.983	1.100
	Ru12	1x	2.983	1.112		Ru12	1x	2.983	1.022		Ru24	1x	2.983	1.100
	Rh15	1x	2.742	1.129		Rh15	1x	2.742	1.356		Ru21	1x	2.742	1.311
	Ru14	2x	3.012	1.917		Ru14	2x	3.012	1.783		Ru15	2x	3.012	2.074
	Sc1	2x	2.931	1.526		Sc1	2x	2.931	1.712		Sc3	2x	2.931	1.515
	Sc3	2x	2.832	1.787		Sc3	2x	2.832	2.006		Sc1	2x	2.832	1.757
	Fe6	2x	2.591	2.745		Fe6	2x	2.591	3.259		Fe10	2x	2.591	2.800
	B20	2x	2.184	6.089		B20	2x	2.184	6.190		B31	2x	2.184	6.005
			Total	**18.554**				**Total**	**20.341**				**Total**	**18.814**

Table S2 Continued

Rh14					**Ru15**					**Ru13**				
(8j)	Ru7	1x	2.821	0.989	**(2c)**	Ru7	1x	2.742	1.287	**(2c)**	Ru15	1x	2.742	1.321
	Ru11	1x	2.983	1.006		Ru8	1x	2.742	1.274		Ru20	1x	2.742	1.326
	Ru12	1x	2.983	1.016		Ru13	1x	2.742	1.276		Rh38	1x	2.742	1.147
	Rh15	1x	2.742	1.117		Ru14	1x	2.742	1.117		Rh37	1x	2.742	1.146
	Ru14	2x	3.012	1.531		Ru15	2x	3.012	1.594		Ru28	2x	3.012	1.597
	Sc1	2x	2.931	1.531		Sc1	2x	2.751	1.877		Sc5	2x	2.751	1.850
	Sc3	2x	2.832	1.281		Sc2	2x	2.751	1.882		Sc6	2x	2.751	1.850
	Fe6	2x	2.591	2.532		B19	2x	2.223	5.309		B34	2x	2.223	5.373
	B20	2x	2.184	5.396		B20	2x	2.223	5.309		B36	2x	2.223	5.373
			Total	**16.400**				**Total**	**20.925**				**Total**	**20.983**
Sc4					**Sc4**					**Sc4**				
(4g)	Ru8	2x	2.832	1.789	**(4g)**	Ru8	2x	2.832	1.779	**(4g)**	Ru17	2x	2.832	1.778
	Ru9	2x	2.931	1.528		Rh9	2x	2.931	1.284		Rh38	2x	2.931	1.283
	Ru11	2x	2.931	1.528		Ru11	2x	2.931	1.493		Ru13	2x	2.931	1.850
	Ru13	2x	2.832	1.787		Ru13	2x	2.832	1.765		Ru20	2x	2.832	1.514
	Rh16	2x	2.751	1.566		Ru16	2x	2.751	1.877		Ru18	2x	2.751	1.746
	Fe5	1x	3.443	0.138		Fe5	1x	3.443	0.139		Fe9	1x	3.443	0.149
	Fe6	1x	3.443	0.138		Fe6	1x	3.443	0.139		Fe10	1x	3.443	0.145
	B17	1x	2.824	0.344		B17	1x	2.824	0.343		B29	1x	2.824	0.336
	B18	1x	2.655	0.527		B18	1x	2.655	0.524		B30	1x	2.655	0.528
	B19	1x	2.824	0.344		B19	1x	2.824	0.344		B31	1x	2.824	0.336
			Total	**9.688**				**Total**	**9.686**				**Total**	**9.665**
Fe6					**Fe6**					**Fe10**				
(2a)	Ru11	2x	2.591	2.745	**(2a)**	Ru11	2x	2.591	2.796	**(2a)**	Ru15	3x	2.591	4.240
	Ru12	2x	2.591	2.745		Ru12	2x	2.591	2.818		Ru16	2x	2.591	2.786
	Ru13	2x	2.591	2.745		Ru13	2x	2.591	2.821		Ru20	2x	2.591	2.822
	Ru14	2x	2.591	2.745		Rh14	2x	2.591	2.532		Rh39	1x	2.591	1.264

Table S2 Continued

	Sc1	1x	3.443	0.138		Sc1	1x	3.443	0.139		Sc1	1x	3.443	0.145
	Sc2	1x	3.443	0.138		Sc2	1x	3.443	0.139		Sc2	1x	3.443	0.146
	Sc3	1x	3.443	0.138		Sc3	1x	3.443	0.139		Sc4	1x	3.443	0.145
	Sc4	1x	3.443	0.138		Sc4	1x	3.443	0.139		Sc3	1x	3.443	0.144
	Fe6	2x	3.012	0.828		Fe6	2x	3.012	0.431		Fe12	2x	3.012	0.493
			Total	**12.359**				**Total**	**11.953**				**Total**	**12.185**
B18					**B18**					**B29**				
(4g)	Ru10	2x	2.184	6.089	**(4g)**	Ru10	2x	2.184	5.862	**(4g)**	Ru13	2x	2.184	5.423
	Ru11	2x	2.184	6.089		Ru11	2x	2.184	5.862		Ru20	2x	2.184	6.174
	Rh16	2x	2.223	4.851		Rh16	2x	2.223	5.309		Rh37	2x	2.223	5.428
	Sc1	1x	2.824	0.344		Sc1	1x	2.824	0.344		Sc2	1x	2.824	0.530
	Sc3	1x	2.655	0.527		Sc3	1x	2.655	0.524		Sc3	1x	2.655	0.336
	Sc4	1x	2.824	0.344		Sc4	1x	2.824	0.344		Sc4	1x	2.824	0.336
			Total	**18.244**				**Total**	**18.244**				**Total**	**18.226**

(b)

$Sc_2Fe(Ru_{0.8}Ir_{0.2})_5B_2$

Model 1					Model 2					Model 3				
Contact		#	Dist.	ICOHP	Contact		#	Dist.	ICOHP	Contact		#	Dist.	ICOHP
Ru8					**Ir8**									
(8j)	Ru1	1x	2.863	0.836	**(8j)**	Ru1	1x	2.863	0.875	**Ir39 (8j)**	Ru27	1x	2.863	0.867
	Ru5	1x	2.955	0.783		Ru5	1x	2.955	0.839		Ru28	1x	2.955	0.757
	Ru6	1x	2.955	0.783		Ru6	1x	2.955	0.904		Ru24	1x	2.955	0.764
	Ir10	1x	2,748	1.225		Ru10	1x	2,748	1.192		Ru21	1x	2,748	1.086
	Ru8	2x	3.012	1.330		Ir8	2x	3.012	1.588		Ru20	2x	3.012	1.491
	Sc13	2x	2.81	2.116		Sc13	2x	2.81	2.175		Sc4	2x	2.81	1.513
	Sc12	2x	2.935	1.748		Sc12	2x	2.935	1.778		Sc2	2x	2.935	1.720
	Fe16	2x	2.576	3.537		Fe16	2x	2.576	3.734		Fe10	2x	2.576	2.902
	B20	2x	2.188	5.998		B20	2x	2.188	6.667		B29	2x	2.188	5.393
			Total	**18.356**				**Total**	**19.753**				**Total**	**16.493**

Table S2 Continued

Ir10					**Ru10**					**Ru13**				
(2c)	Ru1	1x	2.748	1.225	**(2c)**	Ru1	1x	2.748	1.154	**(2c)**	Ru15	1x	2.742	1.428
	Ru2	1x	2.748	1.225		Ru2	1x	2.748	1.167		Ru20	1x	2.742	1.386
	Ru7	1x	2.748	1.225		Ru7	1x	2.748	1.165		Rh38	1x	2.742	1.106
	Ru8	1x	2.748	1.225		Ir8	1x	2.748	1.192		Rh37	1x	2.742	1.279
	Ir10	2x	3.012	1.405		Ru10	2x	3.012	1.258		Ru28	2x	3.012	1.327
	Sc11	2x	2.791	2.221		Sc11	2x	2.791	2.189		Sc5	2x	2.751	2.101
	Sc12	2x	2.791	2.221		Sc12	2x	2.791	2.154		Sc6	2x	2.751	2.101
	B19	2x	2.24	5.950		B19	2x	2.24	5.421		B34	2x	2.223	4.888
	B20	2x	2.24	5.950		B20	2x	2.24	5.332		B36	2x	2.223	4.905
			Total	**22.647**				**Total**	**21.032**				**Total**	**20.520**
Sc12					**Sc12**					**Sc4**				
(4g)	Ru2	2x	2.935	1.748	**(4g)**	Ru2	2x	2.935	1.800	**(4g)**	Ru17	2x	2.832	2.109
	Ru3	2x	2.81	2.116		Ru3	2x	2.81	2.082		Rh38	2x	2.931	1.741
	Ru6	2x	2.81	2.117		Ru6	2x	2.81	2.121		Ru13	2x	2.931	1.741
	Ru8	2x	2.935	1.748		Ru10	2x	2.791	2.154		Ru20	2x	2.832	2.086
	Ir10	2x	2.791	2.221		Ir8	2x	2.935	1.778		Ru18	2x	2.751	0.979
	Fe15	1x	3.426	0.289		Fe15	1x	3.426	0.292		Fe9	1x	3.443	0.261
	Fe16	1x	3.426	0.289		Fe16	1x	3.426	0.292		Fe10	1x	3.443	0.261
	B17	1x	2.578	0.897		B17	1x	2.578	0.834		B29	1x	2.824	0.523
	B19	1x	2.877	0.440		B19	1x	2.877	0.487		B30	1x	2.655	0.788
	B20	1x	2.877	0.440		B20	1x	2.877	0.487		B31	1x	2.824	0.516
			Total	**12.303**				**Total**	**12.327**				**Total**	**11.005**
Fe16					**Fe6**					**Fe6**				
(2a)	Ru5	2x	2.576	3.537	**(2a)**	Ru5	2x	2.591	3.402	**(2a)**	Ru11	2x	2.591	3.077
	Ru6	2x	2.576	3.537		Ru6	2x	2.591	3.726		Ru12	2x	2.591	3.087
	Ru7	2x	2.576	3.537		Ru7	2x	2.591	3.402		Ru13	2x	2.591	2.992
	Ru8	2x	2.576	3.537		Ir8	2x	2.591	3.734		Ir14	2x	2.591	2.897

Table S2 Continued

	Sc11	1x	3.426	0.289		Sc11	1x	3.443	0.288		Sc1	1x	3.443	0.273
	Sc12	1x	3.426	0.289		Sc12	1x	3.443	0.288		Sc2	1x	3.443	0.264
	Sc13	1x	3.426	0.289		Sc13	1x	3.443	0.288		Sc3	1x	3.443	0.272
	Sc14	1x	3.426	0.289		Sc14	1x	3.443	0.288		Sc4	1x	3.443	0.262
	Fe16	2x	3.012	0.769		Fe16	2x	3.012	0.698		Fe6	2x	3.012	1.042
			Total	**16.071**				**Total**	**16.111**				**Total**	**14.166**
B18					**B18**					**B18**				
(4g)	Ru4	2x	2.188	5.998	**(4g)**	Ru4	2x	2.188	6.067	**(4g)**	Ru10	2x	2.184	5.901
	Ru5	2x	2.188	5.998		Ru5	2x	2.188	6.067		Ru11	2x	2.184	5.850
	Ir9	2x	2.24	5.950		Ru9	2x	2.24	5.421		Ir16	2x	2.223	5.416
	Sc11	1x	2.578	0.897		Sc11	1x	2.578	0.834		Sc1	1x	2.824	0.511
	Sc13	1x	2.877	0.440		Sc13	1x	2.877	0.487		Sc3	1x	2.655	0.737
	Sc14	1x	2.877	0.440		Sc14	1x	2.877	0.487		Sc4	1x	2.824	0.509
			Total	**19.722**				**Total**	**19.363**				**Total**	**18.924**

Table S3. Wigner-Seitz (WS) Radii used in LMTO-ASA calculations. Ranges are shown for elements used in multiple compositions.

Atom	WS (Å)
Sc	1.58
Ti	1.70
Zr	1.71
Fe	1.44-1.55
Ru	1.51-1.60
Rh	1.51-1.57
Ir	1.57-1.67
B	1.12-1.14

Table S4. –ICOHP values for the local coordination environments surrounding each Wyckoff position for (a) $Ti_2Fe(Ru_{0.8}T_{0.2})_5B_2$ and (b) $Zr_2Fe(Ru_{0.8}T_{0.2})_5B_2$ (T = Rh, Ir)

(a)

Atom Center	Total # of Contacts	Local –ICOHP (eV/coordination sphere)		
		$Ti_2Fe(Ru_{0.8}Rh_{0.2})_5B_2$		
		Model 1	Model 2	Model 3
T (8*j*)	9	20.00	19.64	19.74
T (2*c*)	9	20.75	22.58	22.46
Sc (4*g*)	10	18.59	18.76	18.75
Fe (2*a*)	9	18.24	17.94	17.85
B (4*g*)	6	20.19	20.68	19.09
		$Ti_2Fe(Ru_{0.8}Ir_{0.2})_5B_2$		
		Model 1	Model 2	Model 3
T (8*j*)	9	14.28	14.42	13.84
T (2*c*)	9	19.40	1837	18.35
Sc (4*g*)	10	11.25	11.20	11.19
Fe (2*a*)	9	3.87	3.97	3.82
B (4*g*)	6	18.63	18.68	18.64

(b)

Atom Center	Total # of Contacts	Local –ICOHP (eV/coordination sphere)		
		$Zr_2Fe(Ru_{0.8}Rh_{0.2})_5B_2$		
		Model 1	Model 2	Model 3
T (8*j*)	9	20.34	18.58	20.23
T (2*c*)	9	19.67	22.75	22.63
Sc (4*g*)	10	15.65	15.75	16.31
Fe (2*a*)	9	15.65	15.30	15.80
B (4*g*)	6	19.45	18.71	18.77
		$Zr_2Fe(Ru_{0.8}Ir_{0.2})_5B_2$		
		Model 1	Model 2	Model 3
T (8*j*)	9	17.85	18.05	18.46
T (2*c*)	9	22.49	20.04	20.80

Sc (4*g*)	10	14.59	14.46	17.74
Fe (2*a*)	9	11.31	12.54	12.33
B (4*g*)	6	19.71	20.02	19.34

Table S5. The relative total energies calculated using antiferromagnetic ordering.

	Model 1 (meV/cell)	Model 2 (meV/cell)	Model 3 (meV/cell)
$Sc_2Fe(Ru_{0.8}Rh_{0.2})_5B_2$	+461	0	+48
$Ti_2Fe(Ru_{0.8}Rh_{0.2})_5B_2$	+566	0	+31
$Zr_2Fe(Ru_{0.8}Rh_{0.2})_5B_2$	+489	0	+46
$Sc_2Fe(Ru_{0.8}Ir_{0.2})_5B_2$	+983	+82	0
$Ti_2Fe(Ru_{0.8}Ir_{0.2})_5B_2$	+1015	+65	0
$Zr_2Fe(Ru_{0.8}Ir_{0.2})_5B_2$	+820	+18	0

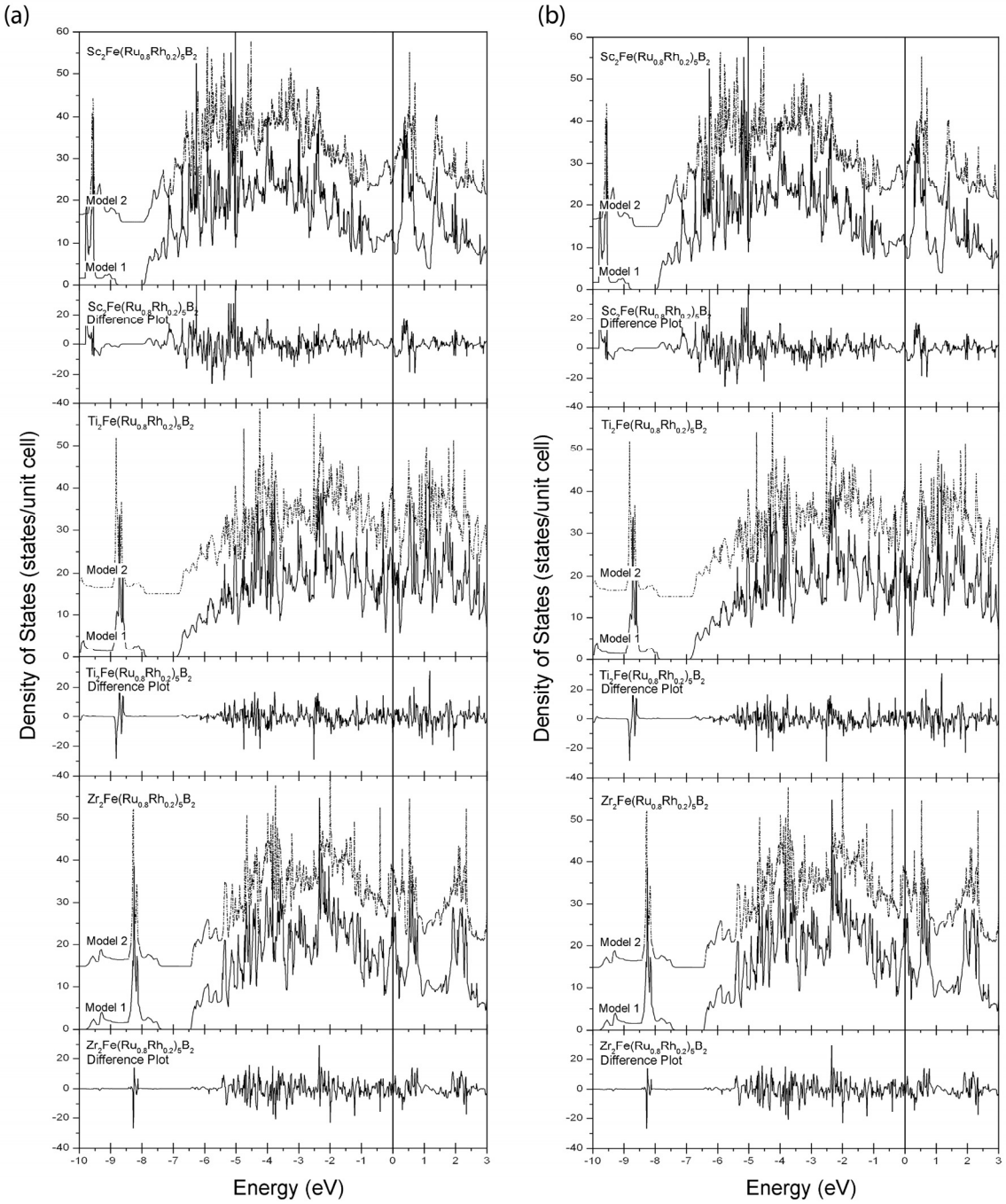

Figure S1. (a) Total DOS of Model 1 (solid line) and Model 2 (dashed line) for $M_2Fe(Ru_{0.8}Ir_{0.2})_5B_2$ (M = Sc, Ti, Zr). (b) **.** Total DOS of Model 1 (solid line) and Model 2 (dashed line) for $M_2Fe(Ru_{0.8}Rh_{0.2})_5B_2$ (M = Sc, Ti, Zr). The difference (Model 1−Model 2) is also plotted for each composition. Fermi level is set to zero.

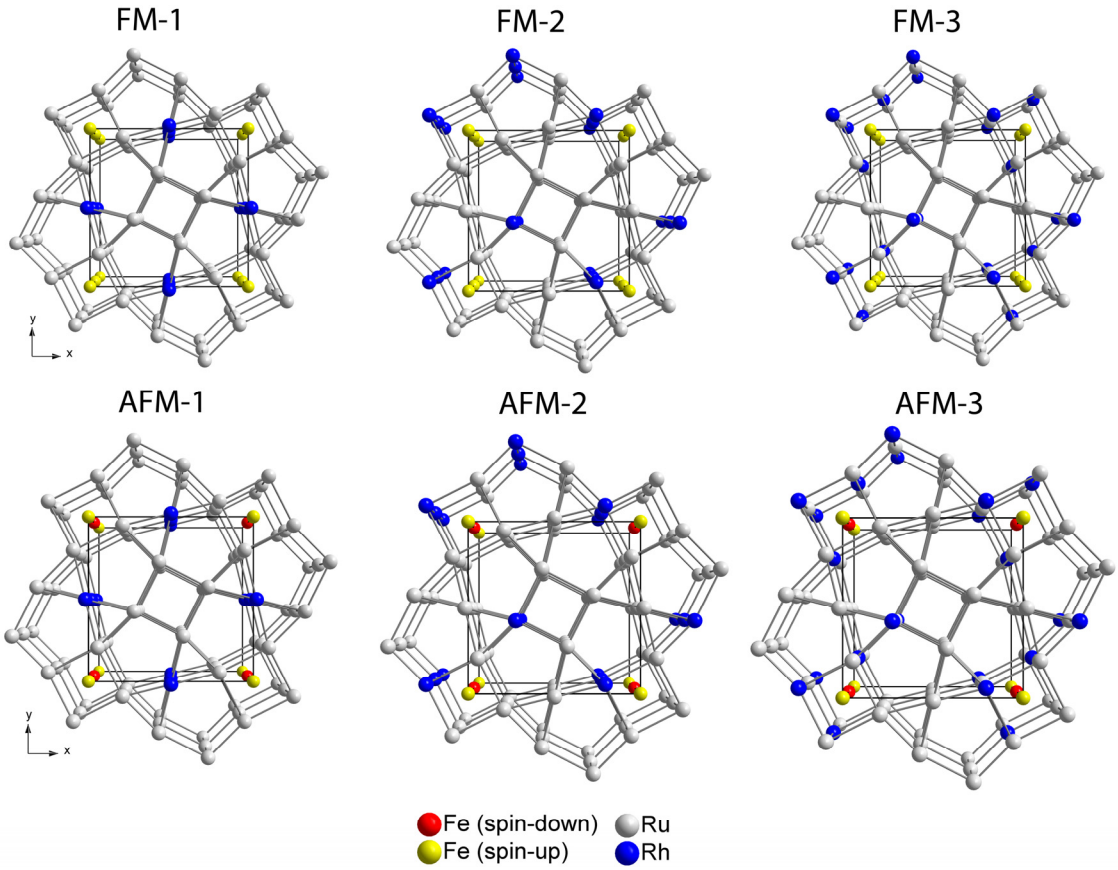

Figure S2. Magnetic models used to determine the effect of atomic position on relative total energies.

CHAPTER 5

Scaffolding, Ladders, Chains, and Rare Ferrimagnetism in Intermetallic Borides: Synthesis, Crystal Chemistry, and Magnetism

Modified from a publication in *Inorganic Chemistry*
(*Inorg. Chem.* **2011**, *50*, 6289.)

*Christian Goerens[1], Jakoah Brgoch[2], Gordon J. Miller[2], Boniface P.T. Fokwa[*1]*

[1]Institute of Inorganic Chemistry, RWTH Aachen University, Landoltweg 1, D-52064 Aachen, Germany
[2]Department of Chemistry, Iowa State University, Ames, Iowa 50011, USA

5.1 Abstract

Single phase polycrystalline samples and single crystals of the complex boride phases $Ti_8Fe_3Ru_{18}B_8$ and $Ti_7Fe_4Ru_{18}B_8$ have been synthesized by arc-melting the elements. The phases were characterized by powder and single-crystal X-ray diffraction as well as energy-dispersive X-ray analysis. They are new substitutional variants of the $Zn_{11}Rh_{18}B_8$ structure type, space group *P*4/*mbm* (No. 127). The particularity of their crystal structure lies in the simultaneous presence of dumbbells which form ladders of magnetically active iron atoms along the [001] direction and two additional mixed iron/titanium chains occupying Wyckoff sites 4*h* and 2*b*. The ladder substructure is ca. 3.0 Å from the two chains at the 4*h*, which create the sequence chain-ladder-chain, establishing a new structural and magnetic motif, the scaffold. The other chain (at 2*b*) is separated by at least 6.5 Å from this scaffold. According to magnetization measurements, $Ti_8Fe_3Ru_{18}B_8$ and $Ti_7Fe_4Ru_{18}B_8$ order ferrimagnetically below 210 K and 220 K respectively, with the latter having much higher magnetic moments than the former. However, the magnetic moment observed for $Ti_8Fe_3Ru_{18}B_8$ is unexpectedly smaller than the recently reported $Ti_9Fe_2Ru_{18}B_8$ ferromagnet. The variation of the magnetic moments observed in these new phases can be adequately understood by assuming a ferrimagnetic ordering involving the three different iron sites. Furthermore, the recorded hysteresis loops indicates a semi-hard magnetic behavior for the two phases. The highest H_c value (28.6 kA/m), measured for $Ti_7Fe_4Ru_{18}B_8$, lies just at the border of those of hard magnetic materials.

5.2 Introduction

Cooperative magnetic phenomena such as ferromagnetism, ferrimagnetism, and antiferromagnetism remain in the focus of condensed matter scientists for both experimentalists and theorists.[1-4] The ability to understand and predict the aforementioned magnetic properties is the goal of our research efforts. Intermetallic compounds and especially intermetallic borides are an ideal playground to reach this goal because the stoichiometry is so flexible that, for example, the valence electron count can be tuned by elemental substitution in a given structure type. We have performed several investigations on intermetallic magnets, where the relationship between electronic and structural factors was studied systematically. For instance, the itinerant magnets of the $Ti_3Co_5B_2$ structure type,[5] containing magnetically active elements in well-separated chains, turned out to be an excellent playground to tune the magnetic properties by adjusting the valence electron count (VEC). These new compounds exhibited a wide range of magnetic behavior ranging from Pauli-paramagnetism, antiferromagnetism, to metamagnetism and ferromagnetism.[6-11] Other transition-metal borides, adopting the $Zn_{11}Rh_{18}B_8$ structure type which is related to the $Ti_3Co_5B_2$ structure type, also contain similar chains composed of a magnetically active element. One example is the compound series $Zn_{10}MRh_{18}B_8$ (M = Mn, Fe, Co, Ni)[12], although the magnetic properties of these compounds have not been published. Recently we reported on a new ferromagnet adopting the $Zn_{11}Rh_{18}B_8$ structure type, namely $Ti_9Fe_2Ru_{18}B_8$ which contains a remarkable substructure regarding the iron atoms,[2] i.e. well-separated chains of iron dumbbells. Such a ladder substructure has not been previously reported for a magnetically active 3d metal (Cr, Mn, Fe, Co, Ni) in intermetallic phases, but does occur in AFe_2S_3 (A = K, Rb, Cs) compounds.[13] This ladder was found to be responsible for the ferromagnetic ordering of the $Ti_9Fe_2Ru_{18}B_8$ phase below ca. 200 K.

The desire to establish two different low-dimensional subunits in the same structure built up by a magnetically active element is the main idea behind this work: One-dimensional chains (as in the $Ti_3Co_5B_2$ structure type) and ladders (as in $Ti_9Fe_2Ru_{18}B_8$), interacting magnetically with each other.

The $Ti_9Fe_2Ru_{18}B_8$ structure also has a set of four different chains of titanium atoms, from which two (at Wyckoff sites 2*b* and 4*h*) are potential candidates for being substituted (partially or totally) by chains of magnetically active elements. These titanium atoms are found in a tetragonal prismatic environment of a 4d transition metal (ruthenium in this case), a coordination environment which was also found to accommodate iron in many phases of the $Ti_3Co_5B_2$ structure type, for example in the $Sc_2FeRu_{5-n}Rh_nB_2$ series.[10] Substitution at these sites will result in new substructures (chains) which may then give rise to several possibilities for the magnetic ordering, depending on their interaction with the iron ladder. The distances separating the ladders and the chains are such that magnetic interactions between these substructures are expected, with a strong potential to enhance the ferromagnetic ordering observed in $Ti_9Fe_2Ru_{18}B_8$ and to even achieve the rare ferrimagnetic ordering. In fact, two chains (at 4*h*) build together with the ladder substructure the sequence chain-ladder-chain, thus enabling a new structural motif ("scaffold") for a magnetic element.

Here we report on the designed synthesis, the structural characterization, and the magnetic properties of the new complex intermetallic borides $Ti_8Fe_3Ru_{18}B_8$ and $Ti_7Fe_4Ru_{18}B_8$. A companion publication[14] focuses on the results of electronic structure calculations and magnetic ordering in these phases.

5.3 Experimental Section

5.3.1 Synthesis. Single phase polycrystalline samples of $Ti_8Fe_3Ru_{18}B_8$ and $Ti_7Fe_4Ru_{18}B_8$ as well as single crystals of $Ti_8Fe_3Ru_{18}B_8$ were successfully synthesized by arc-melting the elements in a water-cooled copper crucible under an argon atmosphere using a tungsten tip as a second electrode. The synthesis of "$Ti_6Fe_5Ru_{18}B_8$" was also attempted but the desired phase was not achieved. The starting materials, titanium (chunks, 99.9%, Degussa), iron (powder, 99.9%, ABCR), ruthenium (powder, 99.9%), and boron (crystalline pieces, 99.999%, Alfa Aesar) were weighed in the corresponding stoichiometric ratio (total mass 0.3 g), pressed into pellets, and arc-melted under argon until homogeneous melting occurred. The argon was purified over silica gel, molecular sieves, and a titanium sponge (950 K). The products were turned and melted several

times to ensure good homogeneity of the samples. Weight losses during the melting process were less than 1 %. A product with metallic luster containing several needle-shaped crystals suitable for X-ray structure analysis was obtained. The product was stable in air both as a compact bulk and as a finely ground powder. The purity of each sample was checked by X-ray powder diffraction with the Guinier technique using Cu $K\alpha_1$ radiation (λ = 1.54059 Å). The presence of the metals and their ratios were characterized by energy-dispersive X-ray analysis (EDX) on a high-resolution, low-energy LEO 1530 SEM (Zeiss, Oberkochen, Germany) equipped with an INCA EDX system (Oxford Instruments). Averages of EDX measurements on several selected crystals agreed well with the ratios calculated from the metallic elements in the phases, although a small but noticeable deviation of the Ti:Fe ratio was observed: The obtained average Ti:Fe:Ru metal ratios were 1:0.36(3):2.23(1) and 1:0.53(3):2.55(1) for $Ti_8Fe_3Ru_{18}B_8$ and $Ti_7Fe_4Ru_{18}B_8$, respectively.

5.3.2 Structure Determination. Rietveld refinements were carried out not only for the two new phases but also for the already reported $Ti_9Fe_2Ru_{18}B_8$, using the *FULLPROF*[15] software. The results are reported in Table 1. The model used for the refinement of $Ti_7Fe_4Ru_{18}B_8$ was based on the single crystal data of the $Ti_8Fe_3Ru_{18}B_8$ phase, but modifying the composition accordingly. An example of the Rietveld plot for the $Ti_7Fe_4Ru_{18}B_8$ sample is shown in Figure 1.

Table 1. Rietveld Refinement results for the Quaternary Borides $Ti_9Fe_2Ru_{18}B_8$, $Ti_8Fe_3Ru_{18}B_8$ and $Ti_7Fe_4Ru_{18}B_8$.

	$Ti_9Fe_2Ru_{18}B_8$	**$Ti_8Fe_3Ru_{18}B_8$**	**$Ti_7Fe_4Ru_{18}B_8$**
space group; *Z*		*P4/mbm* (N°. 127); 2	
lattice parameters (Å)	*a* = 17.525(3); *c* = 2.9678(5)	*a* = 17.519(2); *c* = 2.9670(4)	*a* = 17.487(2); *c* = 2.9621(3)
unit-cell volume(Å^3)	911.4(3)	910.6(2)	905.9(2)
θ range (deg)		10.00° < θ < 90.00°	
refinement method		RIETVELD, least squares method	
profile function		Pseudo-Voigt	

Table 1 Continued

structural model	$Ti_9Fe_2Ru_{18}B_8$ single crystal data [1]	$Ti_8Fe_3Ru_{18}B_8$ single crystal data with Ti/Fe: 2/1 at 4*h* and 2*b*	$Ti_8Fe_3Ru_{18}B_8$ single crystal data with Ti/Fe: 1/2 at 4*h* and 2*b*
no. of refined parameters	52	52	52
R_{Bragg}	6.52	5.48	4.43
R_F	4.34	3.62	3.27

The suitable single crystals found for the $Ti_8Fe_3Ru_{18}B_8$ composition were fixed on glass capillaries and the data were collected using a CCD single-crystal diffractometer (BRUKER SMART APEX) with graphite monochromatised Mo Kα radiation (λ = 0.71073 Å). Absorption correction was done using a semi empirical procedure.[16] The crystal structure was solved by direct methods and refined by full-matrix least squares refinement[17] based on F^2, using anisotropic displacement parameters for all of the metals (Ti, Fe, Ru) and isotropic parameters for boron. All relevant crystallographic data and experimental details concerning the data collection are listed in Table 2. Table 3 contains the atomic coordinates and displacement parameters, while Table 4 summarizes selected interatomic distances.

Table 2. Crystallographic and Structure-Refinement Data for $Ti_{8.1(1)}Fe_{2.9}Ru_{18}B_8$.

Formula	$Ti_{8.1(1)}Fe_{2.9}Ru_{18}B_8$
formula weight (g/mol); F(000)	2455.58; 2171
space group; *Z*	*P4/mbm* (N°. 127); 2
lattice parameters (Å)	*a* = 17.519(2); *c* = 2.9670(4)
unit-cell volume ($Å^3$)	910.6(2)
calculated density (g/cm^3)	8.97
absorption correction	Semi-empirical
absorption coefficient (mm^{-1})	19.98

Table 2 Continued

Diffractometer	Bruker APEX CCD, Mo Kα, graphite monochromator
Θ range (deg)	$4.80° < \theta < 35.83°$
hkl ranges	$-28 \leq h \leq 26$
	$-28 \leq k \leq 26$
	$-4 \leq l \leq 4$
no. of reflections; R_{int}	9564; 0.051
no. of indipendent reflections	1241
no. of parameters	57
refinement method	*SHELXL-97*, full matrix against F^2
R_1; wR_2 (all *I*)	0.0396; 0.0556
goodness of fit	1.074
diffraction peak and hole (e/Å^3)	1.988 / -2.017

Table 3. Atomic Coordinates and Displacement Parameters (Å^2) for $Ti_{8.1(1)}Fe_{2.9}Ru_{18}B_8$. U_{eq} is defined as one-third of the trace of the orthogonalized U_{ij} tensor. For boron, U_{eq} is the isotropic thermal parameter (U_{iso}).

Atom	Wyckoff Site	*x*	*y*	*z*	*Occupancy*	U_{eq}
Ru1	8*i*	0.91920(2)	0.25288(2)	½	1	0.0042(1)
Ru2	4*g*	0.91545(2)	0.41545(2)	½	1	0.0042(1)
Ru3	8*i*	0.93039(2)	0.09699(2)	½	1	0.0044(1)
Ru4	8*i*	0.05297(2)	0.32561(2)	½	1	0.0052(1)
Ru5	8*i*	0.78786(2)	0.16823(2)	½	1	0.0050(1)
Ti1	4*h*	0.80345(6)	0.30345(6)	0	1	0.0065(2)
Ti2	8*j*	0.03505(6)	0.18682(6)	0	1	0.0062(2)
Ti3/ Fe3	4*h*	0.17181(5)	0.32819(5)	0	0.74(3)/ 0.26	0.0062(3)
Ti4/ Fe4	2*b*	0	0	0	0.63(4)/ 0.37	0.0048(4)
Fe1	4*h*	0.05079(5)	0.44921(5)	0	1	0.0062(2)

Table 3 Continued

B1	8*j*	0.8778(3)	0.1691(3)	0	1	0.006(1)
B2	8*j*	0.9625(3)	0.3342(3)	0	1	0.005(1)

Table 4: Selected Interatomic Distances in $Ti_{8.1(1)}Fe_{2.9}Ru_{18}B_8$.

		d_{min} (Å)	d_{max} (Å)
Ru	B	2.153(4)	2.213(4)
	Ti	2.662(1)	2.863(2)
	Ti/Fe	2.515(2)	2.562(1)
	Fe	2.623(1)	2.856(1)
	Ru	2.666(1)	2.965(1)
Fe	Fe	2.514(2)	2.965(1)
Ti/Fe	Ti/Fe	-	2.965(1)
	Fe	-	2.996(2)
	Ti	3.259(2)	3.443(2)

5.3.3 Magnetization Measurements. Magnetization measurements were performed on polycrystalline samples using a SQUID magnetometer (MPMS-5S, Quantum Design, San Diego, CA) in the temperature range 4–300 K with applied fields up to 5 T. The data were corrected for the sample holder (Teflon® tubes). Corrections for diamagnetic and conduction electron contributions were not applied.

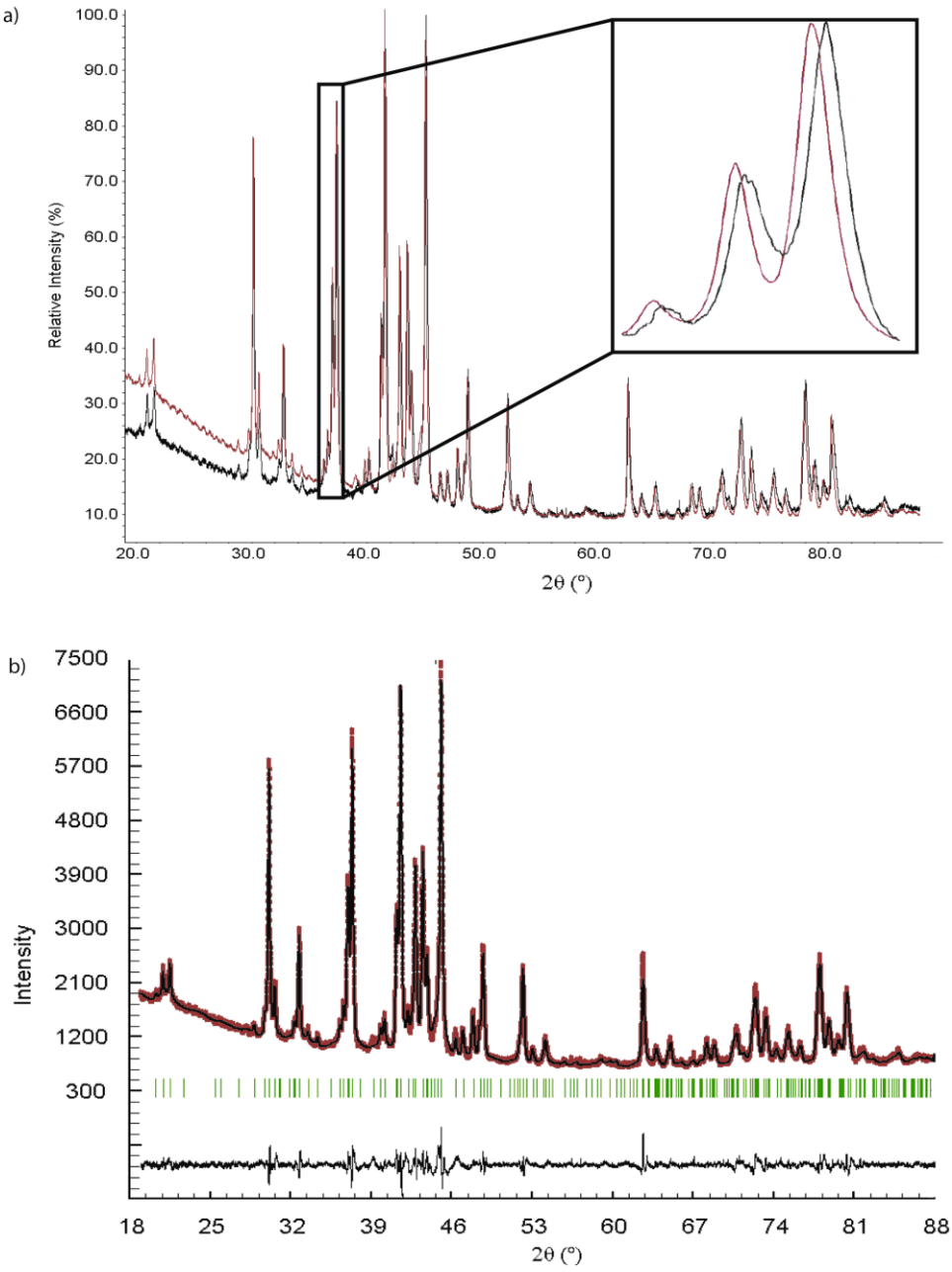

Figure 1. a) Powder patterns of $Ti_8Fe_3Ru_{18}B_8$ (red curve) and $Ti_7Fe_4Ru_{18}B_8$ (black curve). The highlighted area is magnified in the upper right corner. b) Rietveld refinement of the X-ray powder pattern of $Ti_7Fe_4Ru_{18}B_8$ showing measured and fitted intensities (top), the position of the Bragg peaks (middle), and the difference intensity curve (bottom).

5.4 Results and Discussion

5.4.1 Phase Analysis and Structure Refinement. As in the synthesis of $Ti_9Fe_2Ru_{18}B_8$,[2] the two new $Ti_8Fe_3Ru_{18}B_8$ and $Ti_7Fe_4Ru_{18}B_8$ phases could be obtained as single phase. The structural model of the phase $Ti_9Fe_2Ru_{18}B_8$ was first used for the Rietveld refinements of the iron-rich phases; however, the intensities were not correctly matched. Also, the resulting lattice parameters were not only significantly smaller than those of the parent phase, but they also decrease with increasing iron amount (see Table 1), as expected when the larger titanium is substituted by the smaller iron [r_a(Ti) = 1.38 Å, half the bonding distance in the titanium metal, and r_a(Fe) = 1.25 Å].[18] There are four titanium sites in the $Ti_9Fe_2Ru_{18}B_8$ structure, which can be occupied by Fe. Of these four sites, two sit in pentagonal prisms and the other two in tetragonal prisms. Therefore, the probability of a size-dependent substitution is very high. Two models were developed to match the total amount of iron in the two phases: A statistical model, where all titanium sites were filled with both titanium and iron and a size-dependent model, where only the tetragonal prisms were filled with both elements. Although the occupancies of the two elements could not be unequivocally refined from these powder data, the results for both compounds clearly favor the size-dependent model. Single crystal refinement was then necessary for the validation of this model and for the determination of the titanium and iron occupancies on the mixed sites.

Fortunately, some single crystals were obtained from both samples, but only one originating from the iron poorer composition was good enough for single-crystal refinements. The standardized $Ti_9Fe_2Ru_{18}B_8$ structure[2] was used as a starting model for the single-crystal structure refinements. After a few refinement cycles, the structure type was confirmed. However, a careful inspection of the displacement parameters of all atoms revealed that those of two of the four available titanium positions were unusually small suggesting more electron density on these two sites. Because EDX analysis and powder X-ray diffraction (single-phase products and smaller lattice parameters) suggested, that the amount of iron should be higher than in $Ti_9Fe_2Ru_{18}B_8$, a titanium/iron mix-occupancy refinement was applied on all titanium sites. However, iron could be found together with titanium only on the above mentioned two (2*b* and 4*h*) Wyckoff sites

after convergence of the refinement (see Table 3), thereby confirming the size-dependent model. The refined composition was richer in iron than in the $Ti_9Fe_2Ru_{18}B_8$ case and leads to the final composition $Ti_{8.1(1)}Fe_{2.9}Ru_{18}B_8$. A site preference between the Ti/Fe mixing also was investigated. Although 10(4)% more iron is located at 2*b* than at 4*h*, due to the large standard deviations no significant site preference can be determined between the sites. However, as observed in $Ti_9Fe_2Ru_{18}B_8$ electronic reasons may be decisive. A similar result is also obtained from electronic structure calculations. Although the electron counts of the two sites are very similar, there is a slight site preference for a more electron rich atom to occupy the 2*b*-chain site (see the companion publication[14] for details).

A Rietveld refinement based on the single crystal data of $Ti_{8.1(1)}Fe_{2.9}Ru_{18}B_8$ was applied for the $Ti_7Fe_4Ru_{18}B_8$ phase because no suitable single crystal could be obtained as mentioned above. Given the negligible site preference in the two mixed sites in $Ti_{8.1(1)}Fe_{2.9}Ru_{18}B_8$, a statistical Ti/Fe occupation of these sites (33/67% for each) was successfully used in this refinement (see Table 1 and Figure 1). In some areas peak profile-fitting is insufficient in this complex powder pattern. In fact, the peaks are slightly broadened; this is probably due to a small phase width, which can be expected because of the competition in site occupations observed between the two Ti/Fe sites (described above). In this iron richest phase, iron is the main component in both mixed chains and, thus, affects the magnetic properties of $Ti_9Fe_2Ru_{18}B_8$ to a greater extent than in the previous case ($Ti_8Fe_3Ru_{18}B_8$), where titanium prevails in the mixed sites (see the magnetism section).

To conclude this section, the single phase nature of the powder samples, the significantly smaller lattice parameters, the semi-quantitative EDX analyses and the single-crystal refinement results indeed confirm the successful synthesis of the two $Ti_8Fe_3Ru_{18}B_8$ and $Ti_7Fe_4Ru_{18}B_8$ phases. Because the two phases have the same structure model compared to $Ti_9Fe_2Ru_{18}B_8$ phase, they may be generalized by the formula $Ti_{9-n}Fe_{2+n}Ru_{18}B_8$ (n = 1, 2).

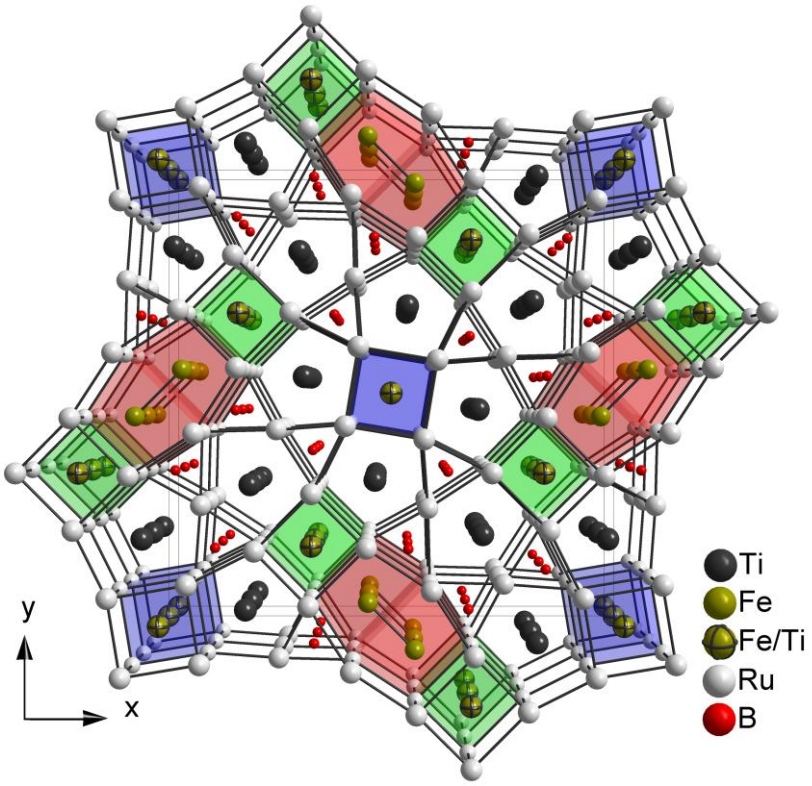

Figure 2. Projection of the crystal structure of $Ti_8Fe_3Ru_{18}B_8$ and $Ti_7Fe_4Ru_{18}B_8$ phases along the [001] direction. Polyhedra around the iron-containing sites are highlighted: Ti/Fe on 2*b* site (blue); Ti/Fe on 4*h* site (green); Fe on another 4*h* site (red).

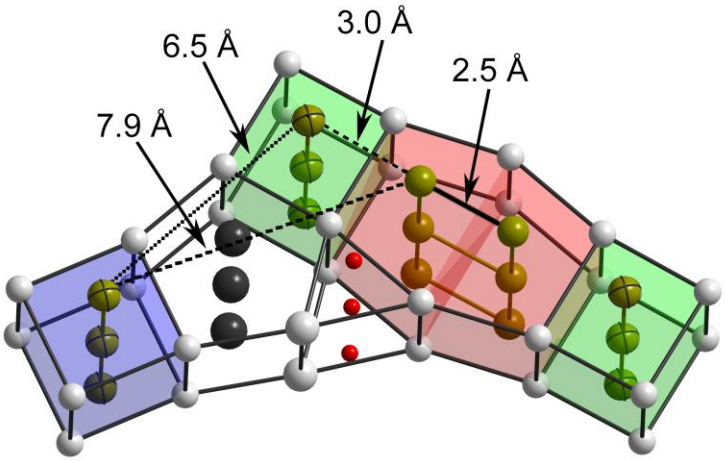

Figure 3. Iron ladder (in the red channel), Ti/Fe mixed chains (in the green & blue channels) and distances between the three iron-containing substructures in the $Ti_8Fe_3Ru_{18}B_8$ compound.

5.4.2 Crystal Chemistry. Figure 2 shows a perspective view of the crystal structure of $Ti_{9-n}Fe_{2+n}Ru_{18}B_8$ (n = 1, 2) phases, which belongs to the $Zn_{11}Rh_{18}B_8$-type, space group $P4/mbm$ (No. 127). This structure is built up by trigonal, tetragonal, pentagonal and elongated hexagonal prisms of Ru atoms stacked on top of each other, thus building channels along the [001] direction. Here boron atoms center the trigonal prisms, the pentagonal prisms accommodate the titanium atoms, and the elongated hexagonal prisms contain the Fe_2-dumbbells which build a ladder substructure along the [001] direction. The centers of the tetragonal prisms at Wyckoff sites 2*b* and 4*h*, however, are filled by two different mixtures of titanium and iron atoms, resulting in two chains of Ti/Fe atoms along [001]. Compared with the structure of the isotypic $Ti_9Fe_2Ru_{18}B_8$, iron is found together with titanium at only two of the four titanium chains generating two Ti/Fe-chains. The distances from the two mixed chains (at 2*b* and 4*h*) to the iron ladder are 7.9 Å and 3.0 Å, respectively. Therefore, based on these distances a direct magnetic interaction is only expected between the iron ladder and the mixed chain at the 4*h* sites. In fact, two mixed chains at 4*h* sandwich the iron ladder to build a "scaffold" which is a new structural unit for a magnetically active element (red and blue units of Figure 2). As a result, the magnetic properties found in $Ti_9Fe_2Ru_{18}B_8$ likely will be strongly perturbed, depending on the interactions of these mixed Ti/Fe-chains with the iron ladder. However, the two Ti/Fe mixed chains (blue & green chains in Figures 2 and 3) are separated by 6.5 Å and consequently no significant direct or through-space interactions are expected.

All of the bond distances in $Ti_8Fe_3Ru_{18}B_8$ are not only in the same range as those observed in the isotypic $Ti_9Fe_2Ru_{18}B_8$,[2] $Ti_{10}Ru_{19}B_8$,[19] and $Ti_9M_2Ru_{18}B_8$ (M = Cr, Mn, Co - Zn) phases[20], but they are also comparable to those found in other borides containing at least three of the elements used: $Ti_{1.6}Os_{1.4}RuB_2$,[21] and $Fe_xRu_{7-x}B_3$ ($0 < x \leq 1.5$).[22] In the isotypic $Ti_9M_2Ru_{18}B_8$ (M = Cr - Zn) phases, the heteroatomic Ru–B and Ru–Ti interactions were found to be mainly responsible for their structural stability. In the new phases, these heteroatomic interactions are also the main structural stabilizing factors, as found by COHP bonding analysis of the hypothetical "$Ti_{8.5}Fe_{2.5}Ru_{18}B_8$" phase which also belongs to the $Ti_{9-n}Fe_{2+n}Ru_{18}B_8$ series. A detailed chemical bonding analysis is given in

a companion publication (theoretical section).[14] The bond distances in $Ti_7Fe_4Ru_{18}B_8$, obtained from the Rietveld analysis follows the trend imposed by the lattice parameters and are thus shorter than in the two iron poorer phases. Earlier investigations on the $Ti_9Fe_2Ru_{18}B_8$ compound made clear, that in terms of volume, one-half of the elongated hexagonal prism (i.e. the volume accommodating only one atom of the dumbbell) is smaller than a single pentagonal prism but larger than a tetragonal prism. The fact that the iron atoms occupy the hexagonal prism in the $Ti_9Fe_2Ru_{18}B_8$ compound cannot be explained by size factors, and electronic reasons are playing a key role. As for the new compounds discussed here, size factors seem to play an important role regarding the additional iron atoms incorporated into the $Ti_9Fe_2Ru_{18}B_8$ structure. The additional iron atoms (mixed with titanium atoms on their sites) are found exclusively at the centers of the smaller tetragonal prisms of ruthenium atoms, while the larger pentagonal prisms are filled by the larger titanium atoms.

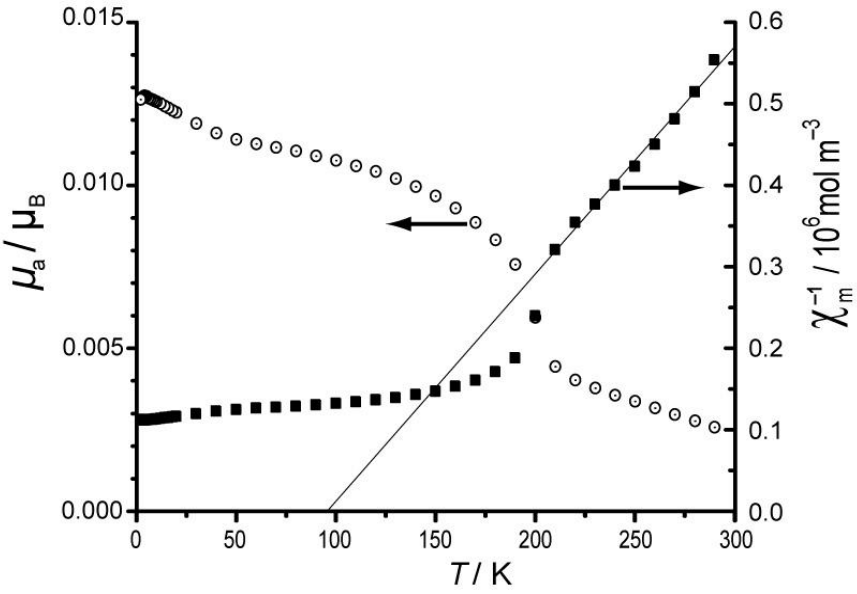

Figure 4. Atomic magnetic dipole moment (white circles) and reciprocal susceptibility (black squares) as functions of temperature at an applied field of 0.01 T for $Ti_8Fe_3Ru_{18}B_8$.

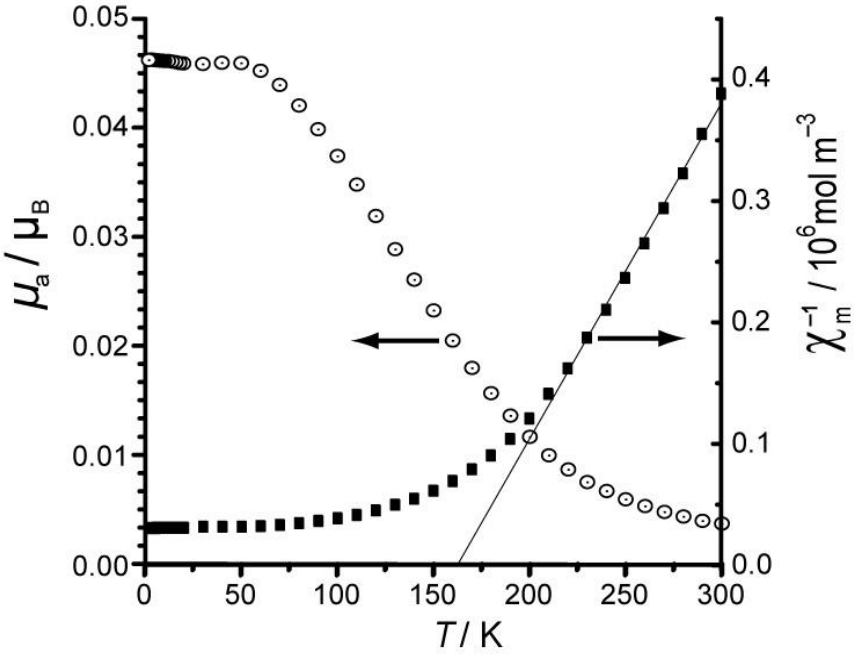

Figure 5. Atomic magnetic dipole moment (white circles) and reciprocal susceptibility (black squares) as functions of temperature at an applied field of 0.01 T for $Ti_7Fe_4Ru_{18}B_8$.

5.4.3 Magnetism. Magnetization measurements on the $Ti_9Fe_2Ru_{18}B_8$ compound revealed a ferromagnetic ordering between 10 and 200 K. The model for ferromagnetism in this ladder-based structure was identified to be a ferromagnetic coupling among neighboring spin-triplet Fe_2 dimers along the *c* axis. Table 5 summarizes the key magnetic quantities for the new $Ti_8Fe_3Ru_{18}B_8$ and $Ti_7Fe_4Ru_{18}B_8$ phases. Figures 4 and 5 show both the magnetic dipole moment vs. temperature (μ_a–*T*) and the reciprocal molar susceptibility vs. temperature (χ_m^{-1} – T) curves at 0.01 T for the $Ti_8Fe_3Ru_{18}B_8$ and $Ti_7Fe_4Ru_{18}B_8$ phases, respectively. The presentation of the magnetic data follows the recommendation of Hatscher et al. (SI units).[23]

Table 5. Magnetic Quantities for $Ti_8Fe_3Ru_{18}B_8$ and $Ti_7Fe_4Ru_{18}B_8$

	$Ti_8Fe_3Ru_{18}B_8$	$Ti_7Fe_4Ru_{18}B_8$
T_C (K)	210	220
μ_a (μ_B), at 5 T and 5 K	0.868	1.814
H_C (kAm^{-1})	10.3	28.6
Curie-Weiss Range (K)	210-300	220-300
θ (K)	95	169
C ($m^3 \cdot K \cdot mol^{-1}$)	$3.59 \cdot 10^{-4}$	$3.35 \cdot 10^{-4}$

The χ_m^{-1} – T curves for the $Ti_8Fe_3Ru_{18}B_8$ (Figure 4) and $Ti_7Fe_4Ru_{18}B_8$ (Figure 5) phases show Curie-Weiss behaviors for the temperature ranges 210-300 K and 220-300 K, respectively. Weiss constants were found to be θ = +94 K and θ = +169 K for both structures as well, indicating that ferromagnetic interactions dominate in the two phases. From the μ_a–T curves, magnetic ordering temperatures of 210 K and 220 K are derived, which are only slightly larger than the 200 K found for the ferromagnetic $Ti_9Fe_2Ru_{18}B_8$ phase. The value of T_C was deduced from the intersection of a linear fit to the steepest part of the magnetization curve with the temperature axis at low applied fields ($\leq$ 0.1 T). The observed Curie temperatures and the positive Weiss constants clearly exclude antiferromagnetic or metamagnetic orderings for the two new phases. The magnetic ordering in these phases may, therefore, be either ferro- or ferrimagnetic, because in addition to the iron ladder (present in $Ti_9Fe_2Ru_{18}B_8$) two other sites containing iron (Ti/Fe sites) are found in the crystal structures of the iron richer phases. In the case of ferromagnetic ordering the total magnetic moment must increase relative to $Ti_9Fe_2Ru_{18}B_8$, whereas a ferrimagnetic ordering may either increase or decrease the moment. Therefore, from these magnetic measurements, a ferrimagnetic ordering will only be safely proven if the total magnetic moment of the phase is lower than that of $Ti_9Fe_2Ru_{18}B_8$.

For $Ti_9Fe_2Ru_{18}B_8$, measurements of the atomic magnetic dipole moment (μ_a) versus applied field (at 5 K), showed that a small field (0.05 T) was needed to obtain a μ_a-

value of 0.300 μ_B. At a high field (5 T), saturation was still not achieved and a μ_a-value of 0.885 μ_B was measured. For $Ti_8Fe_3Ru_{18}B_8$ a μ_a = 0.868 μ_B at 5 T and 5 K can be determined, which is 0.017 μ_B smaller than in $Ti_9Fe_2Ru_{18}B_8$. Upon further iron substitution, en route to $Ti_7Fe_4Ru_{18}B_8$, μ_a dramatically increases to 1.814 μ_B. Can we understand these two different behaviors?

As stated above, a decrease of the magnetic moment in $Ti_8Fe_3Ru_{18}B_8$ is well explained by assuming ferrimagnetic ordering between the three different iron containing sites, i.e., assuming that both ferromagnetic and antiferromagnetic interactions are present. One way to achieve ferrimagnetic ordering with a smaller total magnetic moment than that of $Ti_9Fe_2Ru_{18}B_8$ phase (Figure 6a) is to assume: a) ferromagnetic interactions in the iron ladder b) ferromagnetic interactions in the mixed chain (at 4*h*) interacting antiferromagnetically with the iron ladder and c) antiferromagnetic interactions in the other mixed Ti/Fe chain (at 2*b*). This means that the total magnetic moment of the phase will come from the scaffold unit (chain-ladder-chain) because the mixed chain at 2b is isolated and should produce a zero moment (antiferromagnetic interactions in the chain, see Figure 6c for a sketch of the proposed model). Furthermore, the fact that titanium prevails in the two Ti/Fe mixed chains in the $Ti_8Fe_3Ru_{18}B_8$ structure indicates that these sites will carry much smaller magnetic moments than the iron ladder, and thus the total magnetic moment of the phase will be closer to that of $Ti_9Fe_2Ru_{18}B_8$, as mentioned above. In fact, the ferrimagnetic ordering and the decrease of the magnetic moment in the phase are also supported by density functional theory (DFT) calculations on different magnetic models using the Simpson´s integration method (see DFT calculations published in *JACS*).[14]

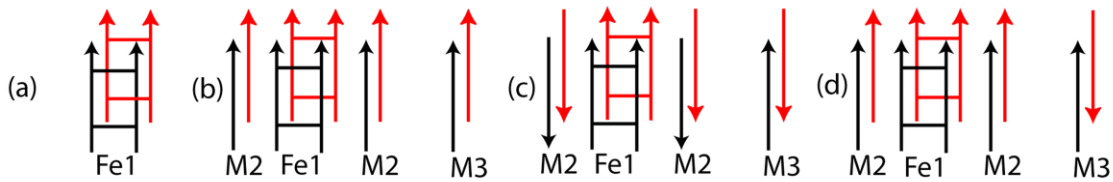

Figure 6. Some magnetically ordered models for $Ti_{9-n}Fe_{2+n}Ru_{18}B_8$ series (a) The ferromagnetic model for n = 0; (b) the least probable ferromagnetic model for n = 1, 2; (c) the proposed ferrimagnetic model for n = 1 and (d) the proposed ferrimagnetic model for n = 2. The arrows indicate the orientations of the magnetic moments for the Fe1

(ladder), M2 (Ti3/Fe3, 4*h*-chain), and M3 (Ti4/Fe4, 2*b*-chain) sites. The two different colors signify two different unit cells along the [001] direction. The sizes of all arrows are arbitrary.

In the $Ti_7Fe_4Ru_{18}B_8$ phase, the total magnetic moment is more than double the magnetic moment of $Ti_9Fe_2Ru_{18}B_8$. Again, either ferro- or ferrimagnetic ordering can be assumed. However, ferromagnetic ordering is unlikely in this phase, particularly because until now all ruthenium-rich phases containing "isolated" chains of iron atoms were found to be dominated by antiferromagnetic exchange interactions in the chains, for example Fe–Fe antiferromagnetic interactions in the $Sc_2FeRu_{5-n}Rh_nB_2$ (n = 0, 1, 2) phases and in $Zr_2Fe_{5-\delta}(Ru_{1-x}Rh_x)_{5+\delta}B_2$ (x = 0.2 ca. δ = 0.1)[24]. Because iron is the main component in the mixed Ti/Fe chains of this phase a similar behavior is expected for the "isolated" chain (2*b* site). Assuming an antiferromagnetic ordering of this isolated chain, an increase of the total magnetic moment can only be explained by a ferromagnetic interaction between the remaining two interacting units (the Ti/Fe chain at 4*h* and the Fe ladder, see Figure 6d for a sketch of the proposed model), thereby leading to a strong ferrimagnet. Also here the DFT calculations have predicted ferrimagnetic ordering to be more energetically favorable than the ferromagnetic case.[14] However the trend in total magnetic moment differ from the experimental findings, but this is likely due to changes which stem from differences in mixed Ti/Fe occupancies at the two Ti/Fe sites, as stated above. The effect of atomic mixing on long range magnetic ordering is currently under investigation.

The low temperature behavior of the phase $Ti_9Fe_2Ru_{18}B_8$ indicated a possible second magnetic ordering near 4 K due to the presence of a broad maximum in the μ_a–T curve. This broad maximum is also observed at nearly the same temperature in the $Ti_8Fe_3Ru_{18}B_8$ phase. In the iron richest $Ti_7Fe_4Ru_{18}B_8$ phase, however, a broad maximum is also observed but at around 70 K, possibly also a second magnetic ordering. The present data do not allow a safe explanation of the low temperature behavior. Therefore ferrimagnetic ordering exists in $Ti_8Fe_3Ru_{18}B_8$ phase over the temperature range 10 K to 210 K, and over the temperature range 75 K to 220 K in $Ti_7Fe_4Ru_{18}B_8$ phase. Mößbauer

and neutron diffraction experiments (at temperatures below 75 K) are planned to investigate the low temperature behavior in all three phases.

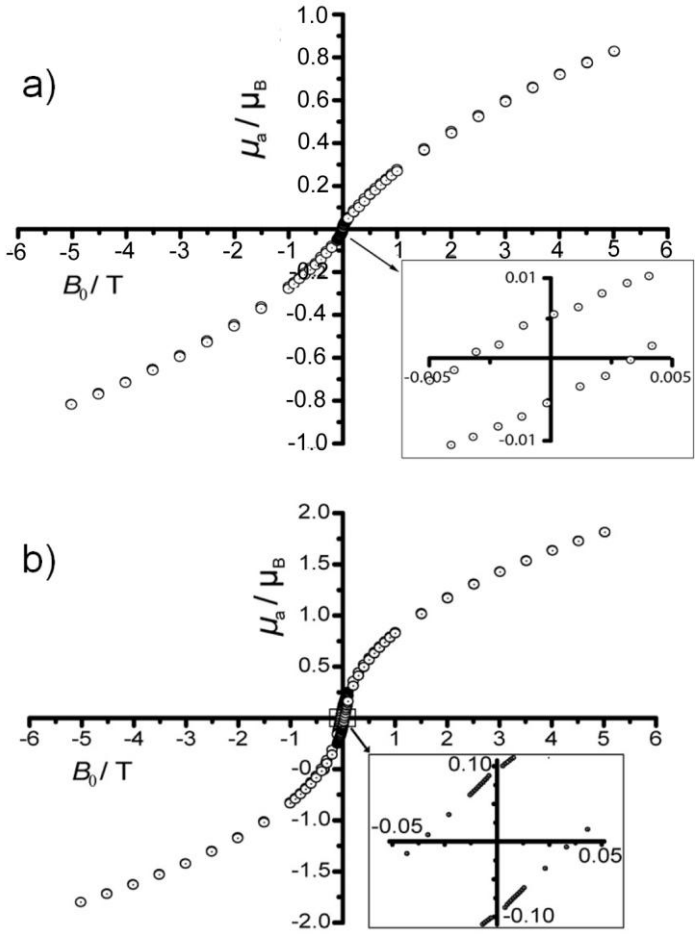

Figure 7. Hysteresis loops for (a) $Ti_8Fe_3Ru_{18}B_8$ and (b) $Ti_7Fe_4Ru_{18}B_8$ at 10 K Inset: Enlarged part of the hysteresis showing the coercive field and the remanence.

Special attention was finally devoted to the hysteresis measurements performed at 10 K and applied fields $-5\ \mathrm{T} \le B_0 \le +5\ \mathrm{T}$. The measured hysteresis loops (μ_a vs. B_0) for both phases do not saturate up to the highest measured field of 5 T (see Figure 7). From these hysteresis loops the coercivities, H_c, have been calculated in order to classify the magnetic hardness of these materials ($H_c < 1\ \mathrm{kAm^{-1}}$ stands for 'soft' and $H_c > 30\ \mathrm{kAm^{-1}}$ for 'hard').[3,4] The calculated coercivities of both phases lie between 1 and 30 $\mathrm{kAm^{-1}}$

(Table 5) and are therefore in the range of semi-hard magnetic materials, with the iron richest phase being even closer to a hard ferrimagnet. It was recently found that the presence of titanium in a Ru-rich boride phase may be the driving force to a hysteresis enlargement in the family of transition metal-rich borides.[25] This effect was observed when studying the magnetic properties of the $Ti_2FeRu_{5-n}Rh_nB_2$ (n = 1 – 5, VEC = 63 - 67) series[21] as a function of the valence electron count (VEC). In fact, an evolution from soft to semi-hard ferromagnetic materials was obtained when decreasing VEC from 67 to 63, that is, by increasing the ruthenium content. This behavior was not observed in the homologous $Sc_2FeRu_{5-n}Rh_nB_2$ (n = 0 – 5, VEC = 60 - 65),[10,11] where only soft magnetic materials were reported at the same VECs (63 , 64 and 65) as in the Ti-based series. Thus, both titanium and ruthenium are indeed playing a crucial role in this hysteresis enlargement process.

5.5 Conclusions

We have successfully synthesized the new phases $Ti_8Fe_3Ru_{18}B_8$ and $Ti_7Fe_4Ru_{18}B_8$, which are new substitutional variants of the $Zn_{11}Rh_{18}B_8$ structure type. They were characterized using powder and single-crystal X-ray analysis as well as EDX measurements. Both phases contain besides a ladder substructure built up by the magnetically active iron atoms, two additional one-dimensional chains composed of titanium and iron atoms, with only one of the chains directly interacting with the iron ladder thereby building a scaffold unit (chain-ladder-chain). Magnetization measurements suggest ferrimagnetic ordering for the two phases below 210 K and 220 K respectively. According to their coercive fields, the new phases show semi-hard magnetic behavior. Theoretical models based on the hypothetical "$Ti_6Fe_5Ru_{18}B_8$" with iron fully occupying the two one-dimensional chain sites in combination with a rigid-band approach correctly predict the preferred magnetic structure for all of the structures discussed here. In fact, at low iron content, i.e. $Ti_9Fe_2Ru_{18}B_8$, ferromagnetic ordering is predicted, whereas ferrimagnetic ordering is predicted for the iron richer substitution, i.e. $Ti_8Fe_3Ru_{18}B_8$ and $Ti_7Fe_4Ru_{18}B_8$. In all three cases the theoretical calculations help to confirm the results found experimentally.

5.6 Acknowledgments

The authors wish to acknowledge the generous financial support through a joint grant provided by the Deutsche Forschungsgemeinschaft (Germany) and the National Science Foundation (USA; NSF DMR 05-02671 and 08-06507) through the Materials World Network program. We also thank Ms. Resi Zaunbrecher (IPC, RWTH-Aachen) for the EDX analyses, Mr. Klaus Kruse and Dr. Paul Müller for various X-ray data collections. C.G. thanks the National Research Fund, Luxembourg, for awarding him a PhD fellowship.

5.7 References.

(1) Fokwa, B. P. T. *Eur. J. Inorg. Chem.* **2010**, 3075.
(2) Fokwa, B. P. T.; Samolyuk, G. D.; Miller, G. J.; Dronskowski, R. *Inorg. Chem.* **2008**, *47*, 2113.
(3) Chikazumi, S. *Physics of Ferromagnetism*; Clarendon Press: Oxford, 1997.
(4) Lueken, H. *Magnetochemie*; Teubner: Stuttgart, 1999.
(5) Kuz'ma, Y. B.; Yarmolyuk, Y. P. *Zhurnal Strukturnoi Khimii* **1971**, *12*, 458.
(6) Nagelschmitz, E. A.; Jung, W. *Chem. Mater.* **1998**, *10*, 3189.
(7) Nagelschmitz, E. A.; Jung, W.; Feiten, R.; Müller, P.; Lueken, H. *Z. Anorg. Allg. Chem* **2001**, *627*, 523.
(8) Nagelschmitz, E. A. Ph.D. Thesis, University of Cologne, 1995.
(9) Dronskowski, R.; Korczak, K.; Lueken, H.; Walter, J. *Angew. Chem. Int. Ed.* **2002**, *41*, 2528.
(10) Fokwa, B. P. T.; Lueken, H.; Dronskowski, R. *Chem. Eur. J.* **2007**, *13*, 6040.
(11) Samolyuk, G. D.; Fokwa, B. P. T.; Dronskowski, R.; Miller, G. J. *Phys. Rev. B* **2007**, *76*, 094404.
(12) Eibenstein, U.; Jung, W. *Z. Anorg. Allg. Chem* **1998**, *624*, 802.
(13) Mitchell, R. H.; Ross, K. C.; Potter, E. G. *J. Solid State Chem.* **2004**, *177*, 1867.
(14) Brgoch, J.; Goerens, C.; Fokwa, B. P. T.; Miller, G. J. *J. Am. Chem. Soc.* **2011**, *133*, 6832.
(15) Rodriguez-Caravajal, J. Fullprof Version 3.2, Laboratoire Léon Brillouin, 1997.
(16) Sheldrick, G. M. SADABS, Göttingen, Germany, 2001.
(17) Sheldrick, G. M. SHELXL-97, A Program for the Refinement of Crystal Structures, Göttingen, Germany, 1997.
(18) Pauling, L.; Kamb, B. *Proc. Natl. Acad. Sci. USA* **1986**, *83*, 3569.
(19) Fokwa, B. P. T. *Z. Anorg. Allg. Chem* **2009**, *635*, 2258.
(20) Fokwa, B. P. T.; Goerens, C.; Gilleßen, M. *Z. Kristallogr.* **2010**, *225*, 180.
(21) Fokwa, B. P. T.; von Appen, J.; Dronskowski, R. *Chem. Comm.* **2006**, 4419.
(22) Fokwa, B. P. T.; Dronskowski, R. *J. Alloys Compd.* **2007**, *428*, 84.

(23) Hatscher, S. T.; Schilder, H.; Lueken, H.; Urland, W. *Pure Appl. Chem.* **2005**, *77*, 497.
(24) Brgoch, J.; Yeninas, S.; Prozorov, R.; Miller, G. J. *J. Solid State Chem.* **2010**, *183*, 2917.
(25) Fokwa, B. P. T.; Lueken, H.; Dronskowski, R. *Eur. J. Inorg. Chem.* **2011**, *2011*, 3926.

CHAPTER 6

Scaffolding, Ladders, Chains, and Rare Ferrimagnetism in Intermetallic Borides: Electronic Structure Calculations and Magnetic Ordering

Modified from a publication in the *Journal of the American Chemical Society* (*J. Am. Chem. Soc.* **2011**, *133*, 6832)

Jakoah Brgoch[1], *Christian Goerens*[2], *Boniface P. T. Fokwa*[2], *Gordon J. Miller*[1]

[1]Department of Chemistry, Iowa State University, Ames, Iowa, 50010, USA
[2]Institute of Inorganic Chemistry, RWTH-Aachen University, Landoltweg 1, D-52056 Aachen, Germany

6.1 Abstract

The electronic structures of "$Ti_{9-n}Fe_{2+n}Ru_{18}B_8$" ($n$ = 0, 0.5, 1, 2, 3), in connection to the recently synthesized $Ti_{9-n}Fe_{2+n}Ru_{18}B_8$ (n = 1, 2), have been investigated and analyzed using LSDA tight-binding calculations to elucidate the distribution of Fe and Ti, to determine the maximum Fe content, and to explore possible magnetic structures to interpret experimental magnetization results. Through a combination of calculations on specific models and using the rigid band approximation, which is validated by the DOS curves for "$Ti_{9-n}Fe_{2+n}Ru_{18}B_8$" ($n$ = 0, 0.5, 1, 2, 3), mixing of Fe and Ti is anticipated at both the 2*b*- and 4*h*-chain sites. The model "$Ti_{8.5}Fe_{2.5}Ru_{18}B_8$" ($n$ = 0.5) revealed that both Brewer-type Ti-Ru interactions as well as ligand field splitting of the Fe 3*d* orbitals regulated the observed valence electron counts between 220 and 228 electrons/formula unit. Finally, models of magnetic structures were created using "$Ti_6Fe_5Ru_{18}B_8$" (n = 3). A rigid band analysis of the LSDA DOS curves concluded preferred ferromagnetic ordering at low Fe content ($n \leq 0.75$) and ferrimagnetic ordering at higher Fe content ($n >$ 0.75). Ferrimagnetism arises from antiferromagnetic exchange coupling in the scaffold of Fe1-ladder and 4*h*-chain sites.

6.2 Introduction

In the past two decades, a class of complex intermetallic borides has been synthesized containing magnetically active 3*d* atoms in close proximity to each other, allowing for studies of magnetic exchange as a function of valence electron count.[1-4] Some of these compounds are variants of the $Zn_{11}Rh_{18}B_8$-type structure, which crystallizes in the *P*4*/mbm* (no. 127) space group. Substitution of zinc by both titanium and iron, along with replacing rhodium with ruthenium, leads to the previously reported compound $Ti_9Fe_2Ru_{18}B_8$.[5] This structure contains 'ladders' of iron atoms where the 'rungs' are formed by Fe-dimers with an interatomic distance of ca. 2.5 Å and separated by ca. 3.0 Å along the [001] direction. The distances are short enough for through-space magnetic exchange to occur; as a result, the magnetic properties of this compound were investigated both experimentally and theoretically.[5]

$Ti_9Fe_2Ru_{18}B_8$ was determined to order ferromagnetically with a magnetic moment of 1.2 μ_B at 7 T and a Curie temperature (T_C) of 200 K. The Weiss constant (θ) is approximately +290 K, further indicating a strong (Fe–Fe) ferromagnetic exchange interaction.[5] The magnetic ordering was also predicted to be ferromagnetic by theory. An analysis of the Crystal Orbital Hamilton Populations (COHP) and the density of states (DOS) curves showed the occupation of Fe-Fe antibonding states and a local maximum in the nonmagnetic DOS at the Fermi level, both of which point towards electronic instability in the system.[6,7] Allowing the structure to relax through spin polarization resulted in the removal of both the Fe-Fe antibonding states and the peak in the DOS and effects ferromagnetic ordering along the rungs of the 'ladders.' A comparison of total energies among various magnetically ordered models confirmed ferromagnetic ordering to be preferred; e.g., the model with antiferromagnetic ordering along the [001] direction is 45.4 meV/formula unit above the ferromagnetic model. In these models, the 'rungs' of the ladder were treated as ferromagnetic stemming from a triplet spin state of neutral iron dimers in a D_{2h} crystal field.

Further addition of iron to this species, by replacing Ti according to $Ti_{9-n}Fe_{2+n}Ru_{18}B_8$ (n = 1, 2), has been synthesized and shows Fe-based 'ladders' as well as additional 'chains,' about which the reader is referred to reference [8].[8] These 'chains'

are similar to those present in the isostructural $Zn_{10}FeRh_{18}B_8$ and the analogous $Sc_2Fe(Ru_{5-x}Rh_x)B_2$ (x = 0-5) and $Zr_2Fe_{1-\delta}(Ru_{1-x}Rh_x)_{5+\delta}B_2$ (δ = ca. 0.2, x = 0, 1).[1,3,4,9] The Fe atoms in the title structure partially substitute for Ti in the pseudo-cubic prisms at Wyckoff sites 2*b* and 4*h*. The 2*b* sites form chains along the [001] direction, well separated from the other sites occupied by 3*d* metals, whereas the 4*h* sites are ca. 3.0 Å from the Fe 'ladders'. The proximity of the 4*h* chains to the ladders can also be described as a tetramer of atoms that, when considered along the [001] direction, forms a 'scaffold' structure. Thus, direct (through-space) magnetic exchange interactions between the 4*h*-chain and the 'ladder' can also be expected. Fe atoms occupying the 2*b*-chains are located ca. 6.5 Å from the 4*h*-chain and 7.9 Å from the 'ladder,' a feature that could result in indirect (through-bond) exchange interactions, but weaker through-space interactions. Therefore, the $Ti_{9-n}Fe_{2+n}Ru_{18}B_8$ (n = 1, 2) system provides an interesting platform for investigating various long-range magnetic ordering in intermetallic borides.

Here, we present a theoretical analysis of the electronic structures of "$Ti_{9-n}Fe_{2+n}Ru_{18}B_8$" ($n$ = 0, 0.5, 1, 2, 3), which represent the experimentally determined compounds $Ti_{9-n}Fe_{2+n}Ru_{18}B_8$ (n = 1, 2).[8] These analyses elucidate factors influencing the extent of Fe content as well as the ordering of 3*d* metals Ti and Fe among various crystallographic sites. Additionally, an investigation of magnetic structures stemming from preliminary experimental data for $Ti_{9-n}Fe_{2+n}Ru_{18}B_8$ (n = 1, 2) is undertaken through the development of a hypothetical "$Ti_6Fe_5Ru_{18}B_8$", i.e., n = 3 in $Ti_{9-n}Fe_{2+n}Ru_{18}B_8$, illustrated in Figure 1b, in which those sites occupied by Ti and Fe, i.e., the 2*b* and 4*h* positions, are fully occupied by Fe atoms. This hypothetical structure is electron rich as compared to all experimentally observed cases, so its density of states is integrated to the experimental valence electron (VE) range, 220-228 VE, via a rigid-band model in order to determine the preferred magnetic model.

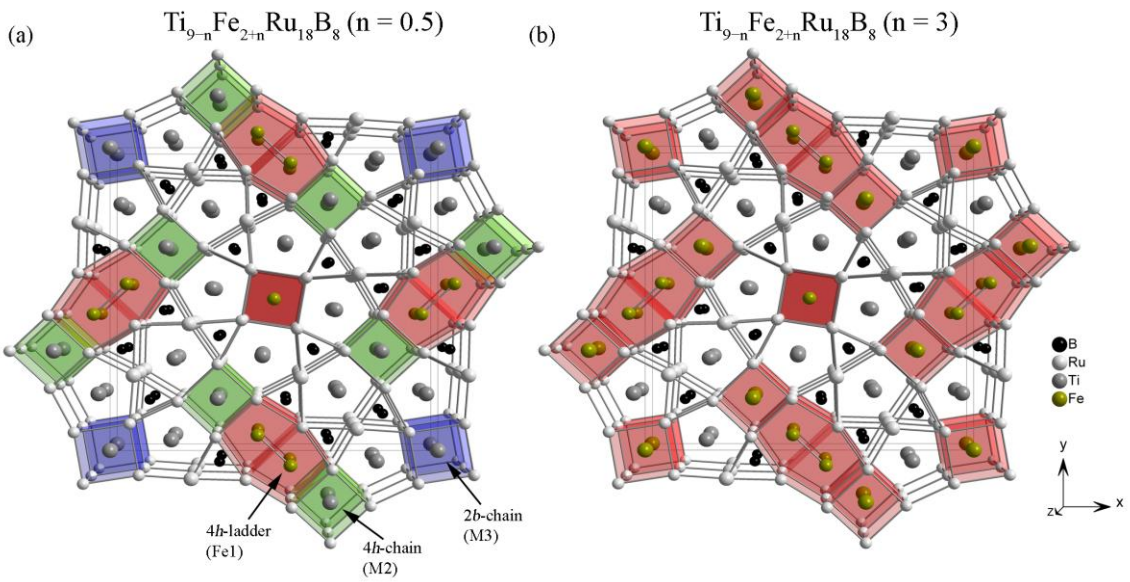

Figure 1. (a) "$Ti_{9-n}Fe_{2+n}Ru_{18}B_8$" ($n$ = 0.5) and (b) the fully occupied "$Ti_{9-n}Fe_{2+n}Ru_{18}B_8$" ($n$ = 3) shown as a perspective view along the [001] direction. The red polyhedra are occupied by Fe, the blue polyhedra are occupied by Ti in the 2*b*-chains, and the green polyhedra are occupied by Ti in the 4*h*-chains.

6.3 Electronic Structure Calculations

The calculations of the electronic and magnetic structures were performed using the tight-binding, linear muffin-tin orbital method with the atomic-spheres approximation (*TB-LMTO-ASA*)[10,11] using the Stuttgart code.[12] Exchange and correlation were treated by the local density approximation (LDA) and the local spin density approximation (LSDA), which was parameterized according to von Barth and Hedin.[13] In the ASA method, space is filled with overlapping Wigner-Seitz (WS) spheres. The symmetry of the potential is considered to be spherical inside each WS sphere and a combined correction is used to take into account the overlapping part. The corresponding WS radii are: 1.53-1.58 Å (Ru), 1.67-1.72 Å (Ti), 1.43-1.44 Å (Fe), and 1.12 Å (B). Space-filling, empty spheres were necessary in all models, with five spheres present in the single crystallographic unit cell and ten spheres present in the doubled unit cell. All of the empty spheres have WS radii between 0.53 and 0.84 Å and are clustered within the elongated hexagonal prism around the iron 'ladders'. Their locations are presented in Supporting Information.

The electronic structures of "$Ti_{9-n}Fe_{2+n}Ru_{18}B_8$" ($n$ = 0, 0.5, 1, 2, 3) were calculated using the tetragonal space groups $P4/mbm$ (no. 127), $P4/m$ (no. 83), and $P4$ (no. 75) as needed. The basis set of each calculation includes: B (2*s*, 2*p*), Ru (5*s*, 5*p*, 4*d*), Ti (4*s*, 4*p*, 3*d*), and Fe (4*s*, 4*p*, 3*d*) wavefunctions. A mesh of 143 ***k*** points in the irreducible wedge of the first Brillouin zone was used to obtain all integrated values, including the density of states (DOS), integrated DOS (IDOS) values, which are valence electron counts, and crystal orbital Hamilton population (COHP)[14] curves. To model antiferromagnetic ordering, a unit cell doubled along the [001] direction was created using space group $P4$ (no. 75). The magnetic ordering models were calculated using 54 **k** points.

6.4 Results and Discussion

Several structural models were constructed to investigate theoretically the site preferences for Fe atoms, the maximum Fe content, the electronic structures, and possible magnetic ordering patterns in $Ti_{9-n}Fe_{2+n}Ru_{18}B_8$. These models of $Ti_{9-n}Fe_{2+n}Ru_{18}B_8$ include n = 0, 0.5, 1, 2, 3; their VE counts, space groups, and distributions of the 3*d* metal atoms (Fe and Ti) are listed in Table 1.

Table 1. Substitution patterns, valence electron (VE) counts, and space groups constructed for the calculation of $Ti_{9-n}Fe_{2+n}Ru_{18}B_8$ (n = 0, 0.5, 1, 2, 3).

			$Ti_{9-n}Fe_{2+n}Ru_{18}B_8$: Substitution Pattern		
Atom	VE Count	Space Group	2*b*-chain (M3)	4*h*-chain (M2)	4*h*-ladder (Fe1)
n = 0	220	$P4/mbm$	Ti	Ti	Fe
n = 0.5	222	$P4/m$	Ti/Fe	Ti	Fe
n = 1	224	$P4/mbm$	Fe	Ti	Fe
n = 2	228	$P4/mbm$	Ti	Fe	Fe
n = 3	232	$P4/mbm$	Fe	Fe	Fe

"$Ti_{9-n}Fe_{2+n}Ru_{18}B_8$" ($n$ = 0, 1, 2, 3) were all calculated using the space group, $P4/mbm$, placing the Fe atoms at the 2*b*- or 4*h*-chains to achieve the desired stoichiometry. "$Ti_{8.5}Fe_{2.5}Ru_{18}B_8$" ($n$ = 0.5 case) was calculated in the subgroup $P4/m$ to

allow the additional Fe atoms to replace Ti atoms in one-half of the 2*b*-chain sites of the parent $Ti_9Fe_2Ru_{18}B_8$. Lowering the symmetry from *P*4/*mbm* to *P*4/*m* splits numerous Wyckoff positions in the original crystal structure: (1) the 8*i* positions of the Ru net are reduced to two sets of 4*j* positions; (2) the 8*j* positions of Ti are split into two 4*k* positions; (3) the 8*j* positions of B are reduced to two 4*k* positions; and (4) the 2*b* sites are lowered to a 1*b* and a 1*d* site. Among these, only the 2*b* sites exhibited mixed occupancy by Ti and Fe in the experimental $Ti_{9-n}Fe_{2+n}Ru_{18}B_8$ (n = 1, 2).[9] This splitting of the 2*b* site creates alternating ···Fe–Ti··· chains along the [001] direction and allows theoretical assessment of the atomic mixing at this chain site (see Figure 1a). "$Ti_{8.5}Fe_{2.5}Ru_{18}B_8$" ($n$ = 0.5), therefore, was constructed in this manner for three reasons: (1) to allow tetragonal symmetry to be maintained; (2) to place the additional Fe atoms in crystallographic sites satisfying the experimentally determined site preference; and (3) to retain mixing of the 3*d* metal atoms for the 2*b*-chains.

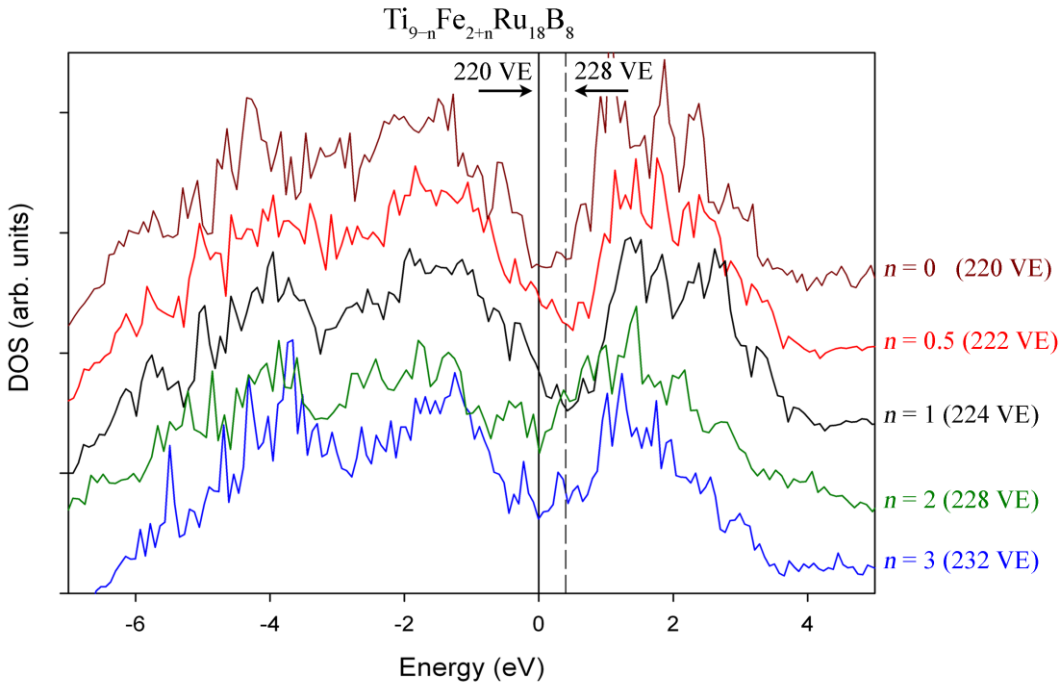

Figure 2. Total DOS curves for the $Ti_{9-n}Fe_{2+n}Ru_{18}B_8$ (n = 0, 0.5, 1, 2, 3) using LSDA. The reference energy (0 eV) is set to 220 VE; the dashed line is set to 228 VE. The DOS curves are offset for clarity.

The total DOS curves based on LSDA for the five cases "$Ti_{9-n}Fe_{2+n}Ru_{18}B_8$" ($n$ = 0, 0.5, 1, 2, 3), illustrated in Figure 2, show extensive similarities, which ratify using the rigid-band approximation for an interpretation of many experimental details (The DOS curves based on LDA are available in Supporting Information). The most notable features for each DOS curve include a pseudogap and VE counts that place the Fermi levels within this region of the DOS. Observed $Ti_{9-n}Fe_{2+n}Ru_{18}B_8$ phases exhibit VE counts between 220 and ca. 228 electrons, i.e., n = 0 and n = 2. The deepest pseudogaps occur for the n = 0, 0.5, and 1 models; they become shallow for n = 2, and then more distinguishable for the n = 3 case. As we will explain further in an examination of the model "$Ti_{8.5}Fe_{2.5}Ru_{18}B_8$" ($n$ = 0.5), the major peak below each pseudogap arises primarily from Ru 4*d* states, the major peak above each pseudogap originates from Ti 3*d* states, and Fe 3*d* states fall largely within each pseudogap. Thus, as the Fe content rises, and, thus, the Ti content drops, the pseudogaps become less distinct as Fe content, i.e., n, increases in the DOS curves of "$Ti_{9-n}Fe_{2+n}Ru_{18}B_8$." Spin polarization of the Fe 3*d* orbitals enhances the pseudogap in the DOS curve of "$Ti_6Fe_5Ru_{18}B_8$" (n = 3).

6.4.1 The Coloring of Ti and Fe Atoms at the 2*b*- and 4*h*-Chains. An important factor influencing the distribution of similar atomic species in a structure is minimizing both the site energies and bond energies for the atoms under consideration.[15] Computationally, one can also evaluate total electronic energies for various structural models for a fixed chemical composition. However, in *TB-LMTO-ASA*, these total energies are significantly dependent on the various Wigner-Seitz radii used for the different atoms and a less reliable method of interpretation. Therefore, to investigate factors affecting the distribution of Ti and Fe atoms at the 2*b* and 4*h*-chain sites of "$Ti_{9-n}Fe_{2+n}Ru_{18}B_8$," for which a rigid-band approximation is reasonable for $n \leq 3$. An analysis of the partial IDOS values (using LSDA) of these sites over the range of experimental VE counts[9] using "$Ti_9Fe_2Ru_{18}B_8$" as a model, with Ti atoms fully occupying the 2*b* and 4*h*-chain sites, was carried out and summarized in Table 2.

Table 2. Partial IDOS values for the 2*b*-chain ("Ti"), 4*h*-chain ("Ti"), and 4*h*-ladder ("Fe") between 220 and 228 VE counts obtained from the DOS of "$Ti_9Fe_2Ru_{18}B_8$." The WS radii, respectively, for Ti and Fe atoms are 1.62 Å and 1.45 Å.

VE Count	2*b*-chain (M3)	4*h*-chain (M2)	4*h*-ladder (Fe1)
220	4.39	4.31	8.28
222	4.42	4.33	8.58
224	4.44	4.35	8.84
228	4.46	4.39	9.53

Although the IDOS values listed in Table 2 are also dependent on the WS radii, various radii values were examined, and those that produced the lowest total electronic energy of "$Ti_9Fe_2Ru_{18}B_8$" were analyzed. We carried out a similar analysis using "$Ti_6Fe_5Ru_{18}B_8$," with Fe atoms fully occupying the 2*b*- and 4*h*-chain sites. These results are qualitatively identical; the numerical results may be obtained in Supporting Information. The VE counts of these two chain sites, based on IDOS values, are similar in magnitude through the entire electron count range, with a slight preference for a more electron-rich element (Fe) to occupy the 2*b*-chain site over the entire range. However, the small differences in IDOS values (ca. 0.1 electron) for the 2*b* and 4*h*-chain sites suggest that it will be difficult to differentiate fully the Ti/Fe site preferences experimentally.

An analysis of the results in Table 2 emphasize the site energy term in the total valence electron energy.[15] A comparison of the two local environments reveals differences in the second nearest neighbor shell of atoms. The 3*d* metal in both the 2*b*- and 4*h*-chains are surrounded by 8 Ru nearest neighbors in a distorted cube and then by 6 Ti/Fe atoms in the second shell. This second shell of atoms surrounding each 2*b* site includes four Ti atoms in the equatorial *ab*-plane and then other 2*b*-site atoms along the *c*-direction. For the 4*h* sites, the equatorial *ab*-plane has three Ti and one Fe second nearest neighbor (see Figure 1a). Thus, based on site energies, the 2*b*-chain prefers a higher Fe content than the 4*h*-chain because the 2*b* site is surrounded by more electropositive metals. But, these neighboring sites also engage in orbital interactions, which contribute to the bond energy term that can also influence atomic distributions.

Table 3 summarizes an analysis of integrated –COHP (–ICOHP) values for nearest and next nearest neighbor contacts at the 2*b*-chain (M3) and 4*h*-chain (M2) when they are occupied by either Fe or Ti for "$Ti_{9-n}Fe_{2+n}Ru_{18}B_8$". The total –ICOHP value for each atom(site) entry summed over all neighboring interactions is also given. In both sites, this sum is greater for Ti than for Fe, but the difference of these values is greater at the 2*b*-chain (M3) site than at the 4*h*-chain (M2) site. This result suggests that, due to bond energies, there is a greater energetic preference for Ti atoms to occupy the 2*b*-chain site than Fe.

Table 3. –ICOHP values for nearest and next nearest neighbor contacts at the 2*b*-chain (M3) and 4*h*-chain (M2) sites in "$Ti_{9-n}Fe_{2+n}Ru_{18}B_8$" ($n$ = 1, 2).

Atom(Site)	Contact	Distance (Å)	#	–ICOHP (eV/bond)	Total –ICOHP (eV)
Fe(2*b*)–	Ru	2.575	8×	1.917	15.336
	Ti	3.338	4×	0.519	2.076
	Fe[001]	2.968	2×	0.792	1.584
				Summed –ICOHP =	18.996
Ti(2*b*)–	Ru	2.575	8×	2.094	16.752
	Ti	3.338	4×	0.626	2.504
	Ti[001]	2.968	2×	0.907	1.814
				Summed –ICOHP =	21.070
Fe(4*h*)–	Ru	2.575	4×	1.905	7.620
	Ru	2.576	4×	2.021	8.084
	Ti	3.259	1×	0.598	0.598
	Ti	3.435	2×	0.512	1.024
	Fe	3.033	1×	0.775	0.775
	Fe[001]	2.968	2×	0.756	1.512
				Summed –ICOHP =	19.613
Ti(4*h*)–	Ru	2.575	4×	2.072	8.288
	Ru	2.576	4×	2.223	8.892
	Ti	3.259	1×	0.704	0.704
	Ti	3.435	2×	0.388	0.776
	Fe	3.033	1×	0.658	0.658
	Ti[001]	2.968	2×	0.894	1.788
				Summed –ICOHP =	21.106

Thus, an analysis of the coloring of Ti and Fe atoms at the crystallographically distinct chains, 2*b* (M3) and 4*h* (M2) sites, reveals competing and opposing tendencies for the atomic distribution. The experimentally assessed site preference[9] concluded a statistical distribution, which would be in line with the competition between the resulting competition between site energy and bond energy influences. On the other hand, within two standard deviations, one might conclude a slight preference for Fe to occupy the 2*b*-chains over the 4*h*-chains,[8] for which the site energy, which is dictated by the potential set up by the structural environment, exerts a slightly greater effect than the just the neighboring orbital interactions.

6.4.2 "$Ti_{8.5}Fe_{2.5}Ru_{18}B_8$" Electronic Structure. In summary, both site energy and bond energy terms affect the distribution of Fe and Ti atoms on the 3*d* metal sites, i.e., 2*b*-chains and 4*h*-chains. Although the refined composition from single crystal analysis for one Fe-rich specimen is $Ti_{8.1(1)}Fe_{2.9}Ru_{18}B_8$ (223.6 VE), mixed Ti/Fe occupancies are refined at both the 2*b* and 4*h* sites.[8] Given the slight preference for Fe atoms in the 2*b* site, the hypothetical "$Ti_{8.5}Fe_{2.5}Ru_{18}B_8$" ($n$ = 0.5; 222 VE) was constructed to examine its electronic structure and gain insights about the maximum Fe content. The total DOS and the atomic partial DOS curves using LDA, presented as DOS/atom, are shown for "$Ti_{8.5}Fe_{2.5}Ru_{18}B_8$" in Figure 3, with the Fermi levels associated with the range of VE counts, i.e. 220-228 VE, noted. The reference energy of these curves is the Fermi level for 222 VE. A broad "pseudogap," which spans states integrating between 195 VE (−0.9 eV) and 235 VE (0.73 eV), is disrupted by a peak that represents a significant mixture of Fe and Ru states. The nonzero DOS values at all Fermi levels suggest metallic character for the $Ti_{9-n}Fe_{2+n}Ru_{18}B_8$ compounds. Furthermore, a local maximum present near these Fermi levels, and arising largely from the Fe 3*d* orbitals, indicates a possible electronic instability in this system.

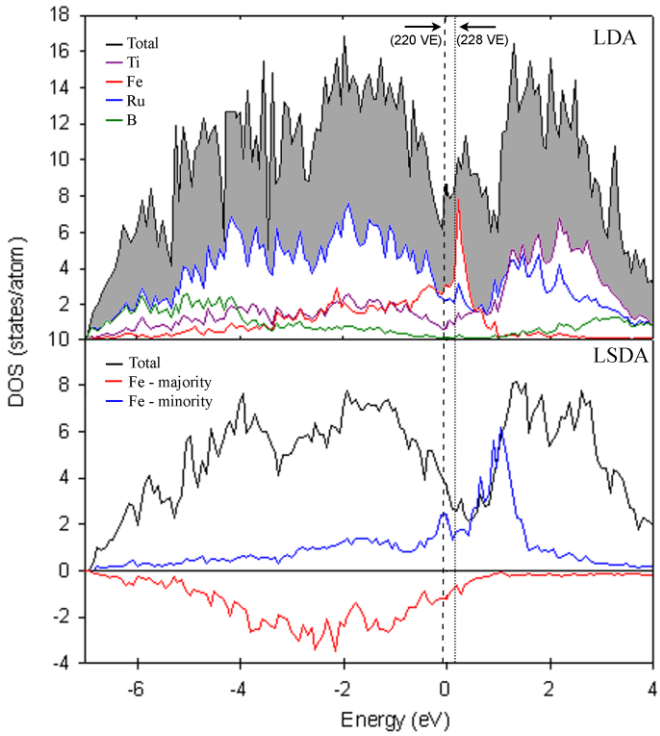

Figure 3. (Top) Total and partial DOS curves using LDA for "$Ti_{8.5}Fe_{2.5}Ru_{18}B_8$" ($n$ = 0.5; 222 VE). The total DOS is scaled by a factor of four for clarity. (Bottom) Total DOS curves using LSDA (black) is overlaid with two partial Fe DOS curves, majority spin (red) and minority down (blue). The reference energy, 0 eV, is set for 222 VE.

The partial DOS curves reveal that states −10 to −7 eV are primarily from boron, viz., 55% of the total states, which then tail off nearly 0% at 0 eV. Ru states are 40% of the total states over the same energy range and increase to 65% of the total states from −5 to −3 eV. The Ru band contribution decreases significantly between −3 eV and 0 eV, becoming a secondary component for states near 0 eV. Of the remaining states 3-5 eV below the VE count range shown, 20% are Ti states and 10% arise from the Fe atoms. The Fe orbitals increase to a sharp maximum at 230 VE (+0.5 eV), and then decrease rapidly to nearly zero. These states originate primarily from the Fe 'ladders', while states from the Fe 1*d* sites (original 2*b*-chains) show a very narrow peak just above 0 eV, close to 228 VE, which corresponds to "$Ti_7Fe_4Ru_{18}B_8$". Above +1.5 eV, Ti and Ru valence *d*-orbitals dominate the DOS curve with the Ru states tailing off at even higher energy. Consequently, the broad pseudogap-like feature in the total DOS curve stems from an increase of the partially filled Ti bands above the observed VE counts and a decrease of

the Ru bands over this same energy range. The peak between 220 and 228 VE arises significantly from Fe-based orbitals.

The spin-polarized total DOS curve, using LSDA, is also shown in Figure 3. Gross features of the spin-polarized (LSDA) and non-spin-polarized (LDA) DOS curves are quite similar except for states near 0 eV. This similarity arises from the preponderance of Ru, B, and Ti orbitals composing the electronic structure. The difference between the two DOS curves is the absence of the Fe-based peak and expression of a deep pseudogap near 0 eV in the spin-polarized curve. This pseudogap appears because the Fe spin orbitals split into a majority spin band, which moves below 0 eV, and a minority spin band, which is largely pushed above 0 eV (see also Figure 3). The observed VE counts for $Ti_{9-n}Fe_{2+n}Ru_{18}B_8$, i.e., 220-228 VE, correspond to Fermi levels are within the pseudogap once spin-polarization is activated. Furthermore, the Stoner model[16,17] for itinerant magnetism is satisfied in "$Ti_{8.5}Fe_{2.5}Ru_{18}B_8$". In this case, the large Fe-based partial DOS at the Fermi level combined with the exchange-correlation integral determined by Janak[18] for BCC Fe does, in fact, exceed unity. Therefore, the formation of spontaneous magnetic moments at the Fe sites is likely.

Chemical bonding features of $Ti_{9-n}Fe_{2+n}Ru_{18}B_8$ based on "$Ti_{8.5}Fe_{2.5}Ru_{18}B_8$" can be analyzed on the basis of COHP[14] curves, shown in Figure 4, and their integrated areas, i.e. –ICOHP values. Interatomic distances and –ICOHP values for nearest neighbor contacts in "$Ti_{8.5}Fe_{2.5}Ru_{18}B_8$" are compared to chemical systems having similar environments and distances to elemental metals and listed in Table 4.

Table 4. Various interatomic distances and associated –ICOHP values in "$Ti_{8.5}Fe_{2.5}Ru_{18}B_8$" and related binary compounds and elemental metals.

Bond	Distances (Å)	−ICOHP (eV/bond)
Ru-Ru	2.670-2.852	0.58-1.19
Ru-Ru (hcp)	2.651-2.708	1.45-1.69
Ru-Ti (pentag. prism)	2.807	1.48
Ru-Ti (cubic prism)	2.578	2.22
Ru-Ti (CsCl-type)[19]	2.656	1.97

Table 4 Continued

Ru-Fe	2.520-2.858	0.52-1.65
Ru-B	2.151-2.204	2.70-2.72
Ru-B ($Ru_{11}B_8$)[20]	2.057-2.245	2.78
Fe1-Fe1	2.497	1.04
Fe1-M2	3.010	0.66
Fe-Fe (BCC)	2.483	1.53

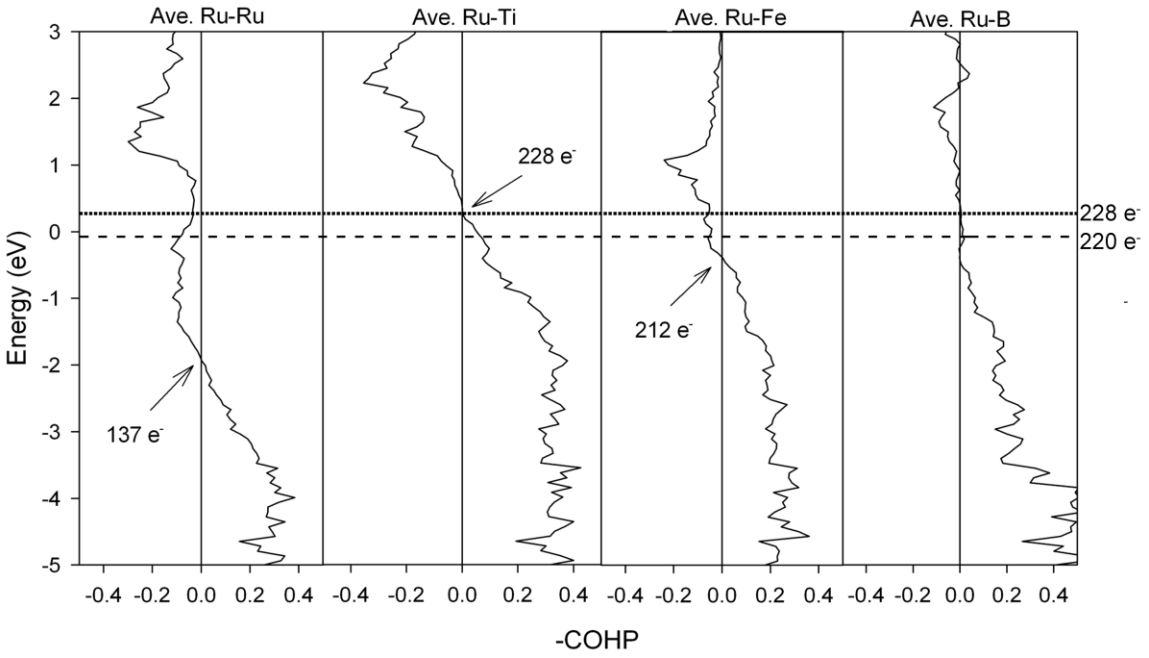

Figure 4. Averaged spin polarized –COHP curves for the nearest neighbor heteroatomic and homoatomic contacts in "$Ti_{8.5}Fe_{2.5}Ru_{18}B_8$" ($n$ = 0.5). The reference energy (0 eV0 is set to 222 VE. The dashed and solid lines, respectively, correspond to 220 VE and 228 VE, which are the lower and upper bounds of observed VE counts in $Ti_{9-n}Fe_{2+n}Ru_{18}B_8$.

The bonding network has been described previously in the analogous $Ti_9Fe_2Ru_{18}B_8$ and $Ti_9M_2Ru_{18}B_8$ (M = Cr, Mn, Co, Ni, Cu, Zn) to contain an extensive Ru-B interaction.[5,21] The structure also shows a substantial metallic bonding network consisting of Ru-Ru, Ti-Ru, and Ru-Fe interactions. The most substantial contributors are the early transition metal (Ti)-late transition metal (Ru) orbital interactions, which

have been described by Brewer.[22] Ti atoms in the cubic prisms (2*b*- and 4*h*- chains) have a strong interaction with the surrounding Ru atoms with an –ICOHP value of 2.22 eV/bond, which is similar to the value calculated for CsCl-type TiRu, which also shows similar interatomic Ti-Ru distances. Ti-Ru interactions for Ti atoms sitting in the pentagonal prisms (4*h* and 8*j* sites) have longer lengths and correspondingly smaller –ICOHP values.

The –COHP curves for averaged Ru-Ru, Ti-Ru, Ru-Fe, and Ru-B interactions reveal that the upper bound of VE counts for $Ti_{9-n}Fe_{2+n}Ru_{18}B_8$ is largely controlled by Ti-Ru and, to lesser extents, by Ru-Fe and Ru-B orbital interactions. Averaged Ti-Ru interactions are optimized almost precisely at 228 VE, a valence electron count appropriate for "$Ti_7Fe_4Ru_{18}B_8$." Since the averaged Ru-Ru and Ru-Fe interactions are noticeably antibonding at this VE count, and Ru-B interactions are nonbonding, the maximum Fe content, which will lead to the highest VE count in $Ti_{9-n}Fe_{2+n}Ru_{18}B_8$ is ca. n = 2, which is in good agreement with experiment.[8]

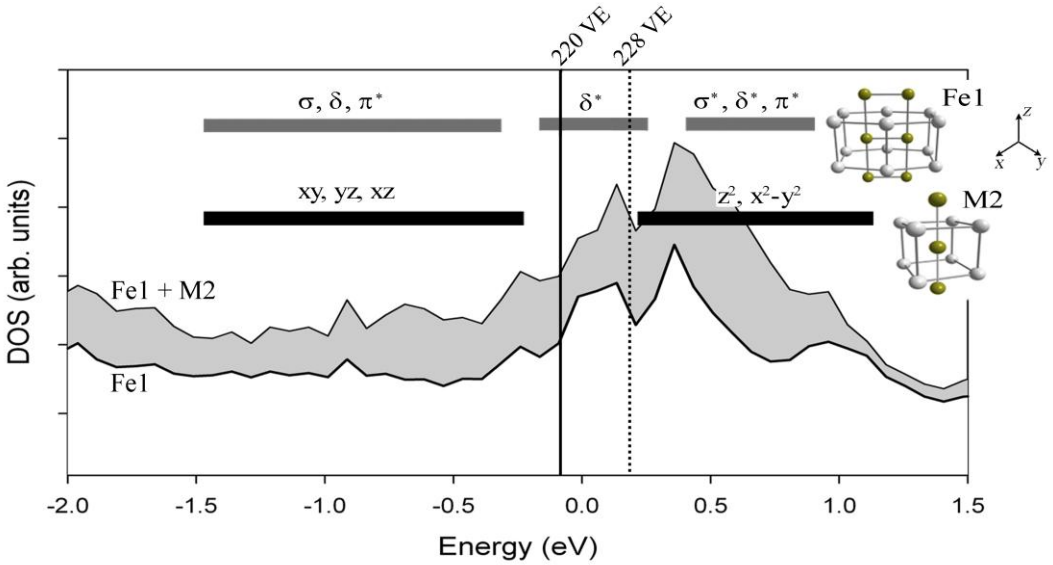

Figure 5. Partial DOS (LDA) of Fe1-ladder and Fe2 (2*b*-chain) of "$Ti_{8.5}Fe_{2.5}Ru_{18}B_8$" ($n$ = 0.5) with the corresponding ligand field splitting of the separate coordination environments superimposed as lines indicating band widths. The splitting pattern was determined using a 'fatband' analysis of the electronic band structure.

Another factor influencing the observed range of VE counts in $Ti_{9-n}Fe_{2+n}Ru_{18}B_8$ includes states associated with the Fe1-ladders and the 3*d* metal 2*b*-chains. The ligand

field splitting of these Fe atomic orbitals was determined through a 'fatband' analysis of the bands between −1.5 eV and 1.5 eV; the results of which are illustrated in Figure 5. The 3*d* orbitals of each Fe atom at the 1*d* sites (original 2*b*-chains), which are located within square prisms of Ru atoms, are split into the nearly triply degenerate *xy*, *yz*, and *xz* atomic orbitals (b_2 + e wavefunctions in C_{4v} site symmetry) lower in energy than the nearly doubly degenerate z^2 and x^2-y^2 atomic orbitals (a_1 + b_1 wavefunctions). The nearly degenerate energetic disposition of these orbitals reflects the nearly cubic field of the 8 nearest neighbor Ru atoms surrounding each 1*d* Fe atom site. Furthermore, the experimental VE counts fall exactly in the gap of these ligand field split 3*d* orbitals. The 3*d* orbitals forming the Fe1-ladder have net Fe-Fe bonding interactions in the dimer with the σ, δ and π* dimer orbitals lowest in energy, followed by the δ* orbital, and then π*, δ*, and σ* orbitals highest in energy. The symmetrically equivalent near neighbor Fe1-Fe1 (dimer) interaction results in a band dispersion over a wide energy range spreading the π* interaction across the energy window shown. Whereas, the π bonding interactions of the dimer are found primarily below the energy window examined, perturbed by the surrounding Ru orbitals, which lie in an orientation that make them likely to interact these orbitals of the Fe1-ladder. Interestingly, the observed VE counts fall almost exclusively within the band of δ^* interactions of the Fe1-Fe1 dimer. Thus, the range of observed $Ti_{9-n}Fe_{2+n}Ru_{18}B_8$ phases are influenced by both the robust Ti-Ru and Ru-B interactions as well as the ligand field splitting of the 3*d* orbitals at the magnetically active Fe atoms.

The Fe atoms and their orbital interactions also influence the magnetic behavior of the $Ti_{9-n}Fe_{2+n}Ru_{18}B_8$ system. Resolving the total DOS from these Fe orbitals into majority and minority spin bands shows substantial spin-polarization (see Figure 3) and large local magnetic moments at each Fe site. The ground state magnetic ordering of "$Ti_{8.5}Fe_{2.5}Ru_{18}B_8$" was determined to be ferrimagnetic, i.e., an antiferromagnetic interaction between the Fe1-ladder site and the 1*d* site is 2 meV/ formula unit lower in energy than a ferromagnetic interaction after convergence. The magnetic moment on the Fe1-ladder site is 2.23 μ_B/Fe while the moment at the 1*d* site is antiparallel to the Fe1-ladder with a magnitude 2.23 μ_B/Fe. These magnetic moments at Fe atoms also induce

moments on the surrounding Ru atoms, ranging from −0.02 to 0.13 μ_B/Ru (the sign of the moment is given with respect to that of the Fe1-ladder). The moments of the Ru atoms nearest to the Fe atoms order parallel to Fe, while all other Ru atom moments order antiparallel. The Ti and B atoms hold very small local moments, ranging from −0.01-−0.06 μ_B/Ti atom and −0.01-0 μ_B/B atom.

6.4.3 Magnetic Ordering in $Ti_{9-n}Fe_{2+n}Ru_{18}B_8$. As mentioned above, the magnetization of $Ti_{9-n}Fe_{2+n}Ru_{18}B_8$ samples arises primarily from the Fe sites with some polarization of nearest neighbor Ru sites. A summary of the local Fe magnetic moments calculated for "$Ti_{9-n}Fe_{2+n}Ru_{18}B_8$" ($n$ = 0, 0.5, 1, 2, 3) is presented in Table 5.

Table 5. The calculated total magnetic moments and local magnetic moments (given as μ_B/atom) at the 3*d* metal sites containing Fe atoms for models of "$Ti_{9-n}Fe_{2+n}Ru_{18}B_8$" ($n$ = 0, 0.5, 1, 2, 3) according to Table 1. For these calculations, the WS radii, respectively, of Ti and Fe are 1.62 Å and 1.45 Å.

n	VE Count	Magnetic Moment (μ_B)						
		Total	2*b*-chain (M3)		4*h*-chain (M2)		4*h*-ladder (Fe1)	
n = 0	220	8.90	Ti	0.00	Ti	0.00	Fe	2.24
n = 0.5	222	13.5	Ti Fe	0.00 2.23	Ti	0.00	Fe	2.23
n = 1	224	14.1	Fe	2.24	Ti	0.00	Fe	2.26
n = 2	228	21.1	Ti	0.00	Fe	2.34	Fe	2.53
n = 3	232	26.8	Fe	2.24	Fe	2.37	Fe	2.60

The calculated local magnetic moment for the isolated Fe1-ladder in $Ti_9Fe_2Ru_{18}B_8$ is 4.48 μ_B/Fe_2-dimer, with the Ti atoms in the two 'chain' sites carrying negligible moments. Substituting Fe atoms for Ti atoms in the "isolated" 2*b*-chain (M3) sites (see Figure 1) does not affect the theoretical moment at the 'ladder' site, while the additional Fe atoms exhibit a local moment of 2.23 μ_B/Fe. However, the incorporation of Fe atoms at the 4*h*-chain (M2) sites, which forms the 'scaffold' structure with the 'ladder,' creates a calculated magnetic moment that is 0.1 μ_B/Fe larger than in the 2*b*-chains. Interestingly, the 'ladder' portion of the 'scaffold' has a significantly larger magnetic moment of 5.06 μ_B/Fe_2. In fact, the substitution of Fe atoms at sites with near neighbor

Fe atoms tends to result in larger magnetic moments than when the Fe atoms occupy isolated sites. As a result, with small incorporations of Fe atoms, e.g., as in "$Ti_{8.5}Fe_{2.5}Ru_{18}B_8$", one may expect a minimal change in the measured magnetic moment based on the site preference for the 2*b*-chain site. With greater Fe content, e.g., as in "$Ti_7Fe_4Ru_{18}B_8$", the measured magnetic moment should increase because substitution at the 4*h*-chain site will lead to a considerable increase in Fe content, an enhanced local moment from substitution at the 4*h*-chain, as well as the amplified magnetic moment in the 'ladder'. In fact, preliminary experimental data show the measured magnetic moment in $Ti_8Fe_3Ru_{18}B_8$ is smaller than $Ti_9Fe_2Ru_{18}B_8$, whereas the initial data show the measured moment in $Ti_7Fe_4Ru_{18}B_8$ is much larger.[8] Although these models explain the increase in moment for $Ti_7Fe_4Ru_{18}B_8$, it does not explain the decrease in moment for $Ti_8Fe_3Ru_{18}B_8$. Therefore, a more complete analysis of magnetically ordered models in $Ti_{9-n}Fe_{2+n}Ru_{18}B_8$ must be established.

First, we will investigate possible magnetic structures through an analysis of the magnetic and nonmagnetic –COHP curves using the "$Ti_6Fe_5Ru_{18}B_8$" (n = 3) model in which the 2*b*- and 4*h*-chain sites contain Fe atoms. In this instance, we invoke the rigid-band approximation from the Fe-rich side, an approximation that is reasonably validated by the DOS curves shown in Figure 2. The substitution at the 4*h*-chain site results in the formation of a tetramer of Fe atoms along the directions, and that in the [001] direction forms an extended 'scaffold' structure (see Figure 1b). The central two atoms of the 'scaffold', which formerly made up the 'rungs' of the Fe ladders (Fe1-Fe1), have nearly identical –COHP curves to the previously reported $Ti_9Fe_2Ru_{18}B_8$ along both the {100} and [001] directions,[5] which are shown in Figures 6a and 6b. The –COHP curves for the Fe1-M2 interactions, making up the outside of the 'scaffold', as well as the M2-M2 interactions along the [001] direction, are all illustrated in Figure 6c. In the non-spin polarized case, Fe1-M2 interactions are nearly optimized, while the M2-M2 interactions along [001] show an occupation of antibonding states between 220 and 228 VE. M3-M3 interactions along the [001] direction, however, have bonding states occupied for the same (observed) VE counts.

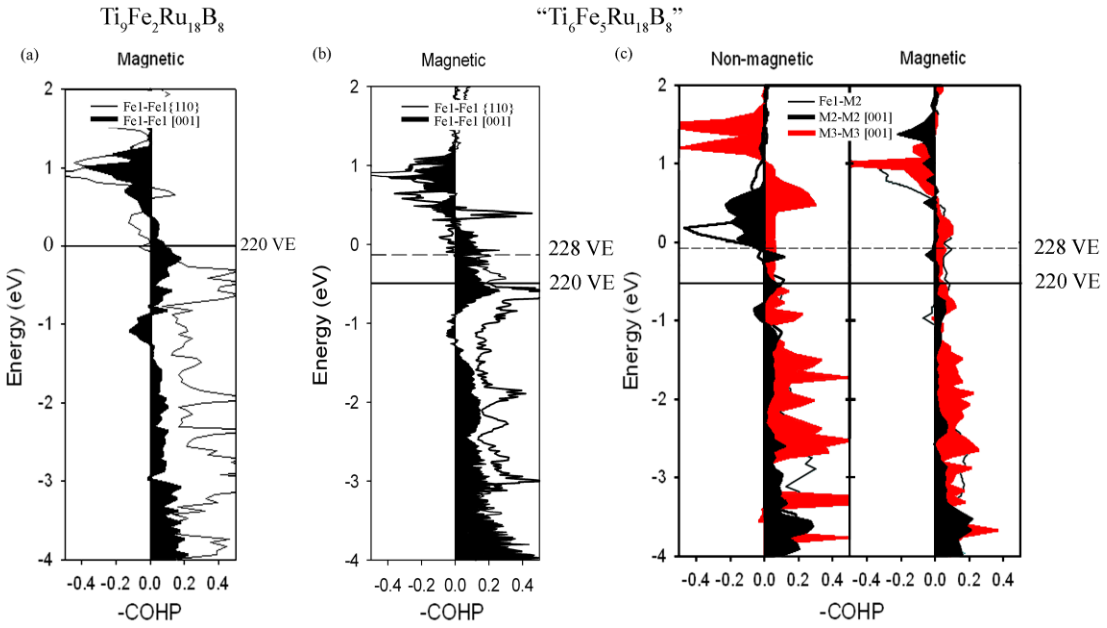

Figure 6. (a) The −COHP (LSDA) curves of the Fe1-Fe1 (ladder) interactions in $Ti_9Fe_2Ru_{18}B_8$. (b) The −COHP (LSDA) curves of the Fe1-Fe1 (ladder) interactions in "$Ti_6Fe_5Ru_{18}B_8$" (n = 3). (c) The −COHP (LDA, left, and LSDA, right) curves of the Fe1 (ladder)-M2 (4*h*-chain), M2-M2, and M3-M3 interactions. The second two contacts are along the [001] direction. The solid line identifies the Fermi level for 220 VE; the dashed line for 228 VE.

Spin polarization affects these orbital interactions, moving the optimized interactions for Fe1-M2 and M3-M3 contacts well above 228 VE and creating M2-M2 nonbonding states occupied over the range 220-228 VE. At a given VE count, the occupation of antibonding states between magnetically active atoms has been previously described to indicate ferromagnetic ordering, whereas when nonbonding or bonding states between magnetic atoms are occupied, antiferromagnetic coupling is preferred.[6,7,23] Therefore, from the –COHP curves presented in Figure 6c, along the [001] direction the magnetic moments at the M2 and M3 sites should order, respectively, ferromagnetically and antiferromagnetically. Furthermore, the Fe1-M2 interaction along {110} should be ferromagnetic.

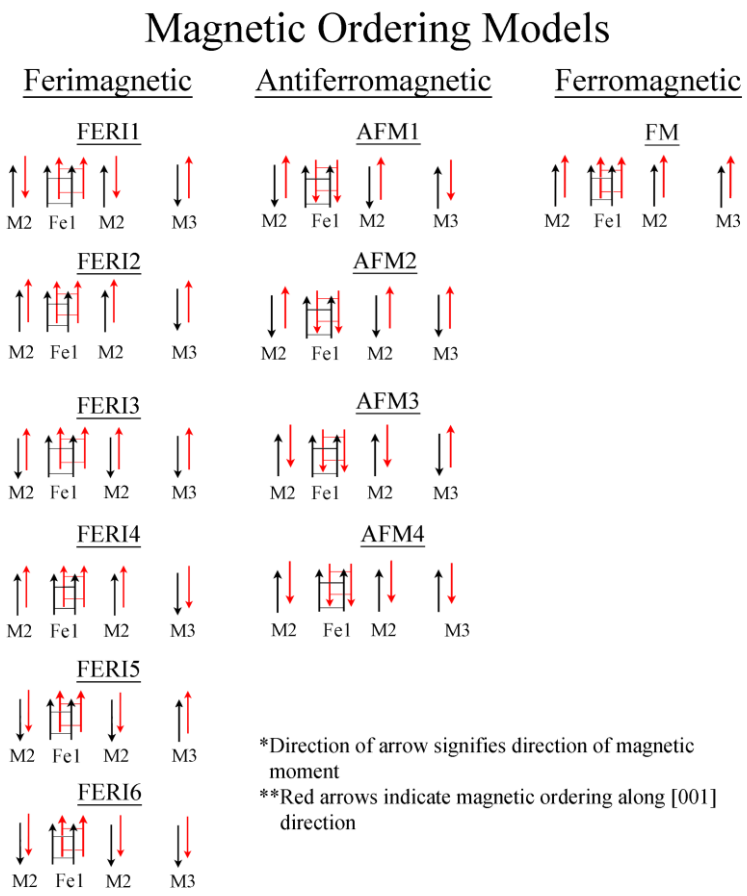

Figure 7. Magnetically ordered models of "$Ti_6Fe_5Ru_{18}B_8$" (n = 3) with arrows indicating the orientations of the magnetic moments for the Fe1 (ladder), M2 (4*h*-chain), and M3 (2*b*-chain) sites. The two different colors signify two different unit cells along the [001] direction. The sizes of all arrows are arbitrary.

Clearly, there are numerous magnetic exchange paths in $Ti_{9-n}Fe_{2+n}Ru_{18}B_8$ for n > 0. Using –COHP curves to predict magnetic exchange will only be useful for through-space interatomic interactions, as in Fe1-M2, M2-M2, and M3-M3 contacts. Long-range, through-bond interactions cannot be assessed by this technique. As we mentioned earlier, the Ru atoms that are nearest neighbors with the magnetically active Fe atoms will be polarized. Therefore, long-range Fe1-M3 and M2-M3 magnetic coupling can exist in $Ti_{9-n}Fe_{2+n}Ru_{18}B_8$. To determine such long-range magnetic ordering, one ferromagnetic (FM), six ferrimagnetic (FERI), and four antiferromagnetic (AFM) models of "$Ti_6Fe_5Ru_{18}B_8$" (n = 3) were constructed by varying the initial local moments on the three inequivalent Fe sites, i.e., Fe1, M2, and M3, and allowing the calculations to converge

self-consistently. These models are depicted schematically in Figure 7. Then, using a rigid band approximation, the total energies were calculated for the range of VE counts, i.e., 220-230 VE, by integrating the total DOS for each magnetic model to the desired electron count with Simpsons' integration method.[24] The magnetic moments of the most magnetically active elements, i.e., all Fe atoms and their nearest neighbor Ru atoms, were calculated using the differences between the IDOS values of the majority and minority spin bands at the desired valence electron counts.

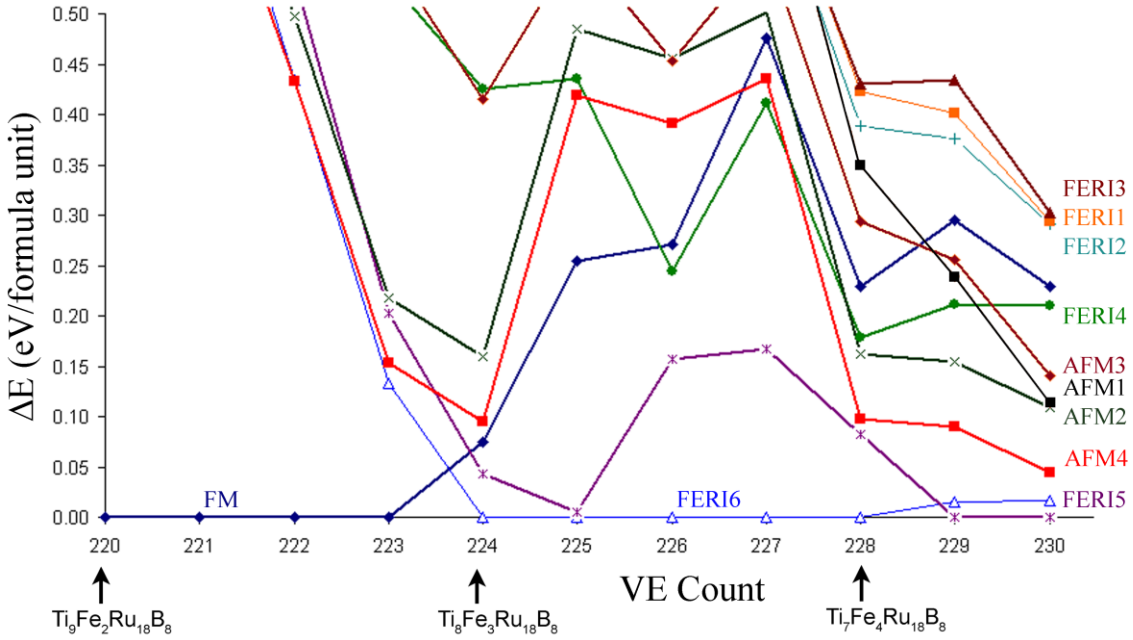

Figure 8. Relative total energies vs. VE count for the various magnetically ordered models of "$Ti_{9-n}Fe_{2+n}Ru_{18}B_8$". The lowest energy model is given as 0.00 eV; VE counts range from 220 VE ($Ti_9Fe_2Ru_{18}B_8$) to 230 VE ("$Ti_{6.5}Fe_{4.5}Ru_{18}B_8$").

A graph of the valence electron count versus the total energy, relative to the lowest energy model at each VE count, is plotted in Figure 8 with the full energy range provided in Supporting Information. The resulting magnetic moments for each lowest energy case are listed in Table 6.

Table 6. Favored magnetically ordered models as a function of VE count for $Ti_{9-n}Fe_{2+n}Ru_{18}B_8$ based on a rigid band approximation of the DOS of "$Ti_6Fe_5Ru_{18}B_8$" (n = 3). When two models are listed, their energy difference is less than 50 meV/formula unit. The local magnetic moments (in μ_B/atom) are derived using the corresponding IDOS values of the spin-polarized calculations. The signs of the magnetic moments represent parallel (+) or antiparallel (–) to the moments at the M3 sites. The Ru atoms are labeled by the nearest magnetic atom.

VE count	Favored model	Magnetic Moment (μ_B/atom)						
		Total Moment (μ_B/f.u.)	4*h*-ladder (Fe1)	4*h*-chain (M2)	2*b*-chain (M3)	Ru (Fe1)	Ru (M2)	Ru (M3)
220	FM	12.75	2.28	2.20	2.23	0.18	0.14	0.09
221	FM	12.78	2.27	2.19	2.22	0.19	0.15	0.09
222	FM	12.82	2.28	2.19	2.21	0.20	0.15	0.09
223	FM	12.92	2.28	2.17	2.19	0.21	0.16	0.09
224	FERI6	1.61	–2.16	2.12	2.14	0.43	0.02	–0.06
225	FERI6	1.45	–2.17	2.09	2.14	0.51	–0.01	–0.06
225	FERI5	3.08	2.21	–2.06	2.19	–0.08	0.09	0.01
226	FERI6	1.50	–2.16	2.07	2.13	0.51	–0.01	–0.06
227	FERI6	1.52	–2.15	2.04	2.13	0.51	–0.00	–0.06
228	FERI6	1.51	–2.13	2.02	2.12	0.51	–0.00	–0.07
229	FERI5	3.64	2.20	–1.98	2.19	–0.12	0.11	0.01
229	FERI6	1.47	–2.12	2.00	2.11	0.52	–0.00	–0.07
230	FERI5	3.54	2.20	–1.98	2.19	–0.12	0.10	0.01
230	FERI6	1.48	–2.11	2.03	2.09	0.52	–0.00	–0.07

At low VE counts and, therefore, low Fe content (220-222 VE), the most favorable model is FM by at least 400 meV/formula unit. Although this prediction of magnetic order arises from a rigid band approximation applied to "$Ti_6Fe_5Ru_{18}B_8$", it does follow the experimental findings of ferromagnetic ordering in $Ti_9Fe_2Ru_{18}B_8$.[5] The total calculated magnetic moment at 220 VE, however, is much larger than the calculated

using $Ti_9Fe_2Ru_{18}B_8$, i.e., 12.75 μ_B for "$Ti_6Fe_5Ru_{18}B_8$" (n = 3) versus 5.1 μ_B[5] for $Ti_9Fe_2Ru_{18}B_8$. The larger estimated total moment arises from the elevated concentration of Fe site potentials in "$Ti_6Fe_5Ru_{18}B_8$" (n = 3) and the lower spin polarization associated with Ti valence states. However, the local magnetic moments on the individual Fe atoms are slightly smaller than in the parent structure.[5]

A magnetic ordering transition occurs from FM to FERI6 at 224 VE, flipping the moments of the chain site atoms (M2 and M3) from parallel to anti-parallel with respect to the Fe1 'ladder'. The most favorable model between 224 and 228 VE is FERI6, with ferromagnetic ordering within the Fe1 'ladder' but antiferromagnetic ordering between the Fe1 'ladder' and the 4*h*-chain (M2) sites, making a ferrimagnetic 'scaffold'. Over this range of VE counts, the total moment is low and nearly constant, within 0.1 μ_B because the magnetic moments of both the M2 and M3 sites are antiparallel to the Fe1 'ladders'. Moreover, there is a substantial polarization of the Ru sites closest to the Fe1 'ladders,' a polarization which is antiparallel to the ladder site moments and further lowers the total calculated moment. Experimentally, an initial analysis of the experimental magnetic data for $Ti_8Fe_3Ru_{18}B_8$ (224 VE) has a measured magnetic moment that is smaller than $Ti_9Fe_2Ru_{18}B_8$,[5] which likely stems from ferrimagnetic ordering. The theoretical prediction of the FERI6 model for this electron count fits the data well. In this case the opposing spins of the M2 and M3 sites with respect to the ladder site would result in an overall lower magnetic moment, which is in excellent agreement with the preliminary experimental data.

Further addition of valence electrons to 229 and 230 VE shows two probable magnetic models, FERI6 and FERI5, which both containing a ferrimagnetic 'scaffold' and are separated by ca. 15 meV/formula unit. The difference between these two models is the magnetic ordering of the 2*b*-chain (M3) with respect to the 4*h*-chain (M2), which is, respectively, parallel and antiparallel to each other in FERI6 and FERI5. The distance between the 2*b*-chain (M3) and the 4*h*-chain (M2) sites is ca. 6.5 Å, which is sufficiently long that through-space exchange is small, but that through-bond using bridging Ru sites is necessary. In FERI5, there is greater polarization of Ru sites closest to M2 than to M3, which affects these relative energies. Finally, the total magnetic moment of the FERI5

models is larger than the FERI6 models because of preferred parallel magnetic ordering of the M3 moments with respect to the moments at the Fe1 'ladder'.

For the range of compounds in $Ti_{9-n}Fe_{2+n}Ru_{18}B_8$ that have been obtained synthetically, i.e., n = 0, 1, and 2, the predictions of magnetic structures and trends in total magnetic moments, presented in Table 6 and Figure 8, coincide well with experimental observations. The models with the higher electron counts; e.g. $Ti_7Fe_4Ru_{18}B_8$ (228 VE), do begin to differ from the experimental findings, but this is likely due to changes which stem from differences in mixed Ti/Fe occupancies at the M2 and M3 sites. The effect of atomic mixing on long range magnetic ordering is currently under investigation.

6.5 Conclusions

We have presented the theoretical electronic structures of "$Ti_{9-n}Fe_{2+n}Ru_{18}B_8$" ($n$ = 0, 0.5, 1, 2, 3), which pertaining to the substituted intermetallic borides, $Ti_{9-n}Fe_{2+n}Ru_{18}B_8$ (n = 1, 2).[8] The total DOS curves reveal a pseudogap at the corresponding Fermi levels, while invoking spin polarization results in the formation of large, localized magnetic moments at the Fe atoms and some polarization induced at the neighboring Ru atoms. An analysis of –COHP curves shows a bonding network similar to those described in $Ti_9Fe_2Ru_{18}B_8$ and $Ti_9M_2Ru_{18}B_8$ (M = Cr, Mn, Co, Ni, Cu, Zn).[5,21] Through an analysis of site energies and bond energies, Ti/Fe mixing may occur at both the 2*b*- and 4*h*-chain sites in $Ti_{9-n}Fe_{2+n}Ru_{18}B_8$. Moreover, Fe substitution at the 4*h*-chain (M2) sites, which creates magnetic scaffolds, increases the local moments at the Fe1-'ladder' sites. The electronic structure of the model "$Ti_{8.5}Fe_{2.5}Ru_{18}B_8$" ($n$ = 0.5) provided a detailed description of the chemical bonding features in the $Ti_{9-n}Fe_{2+n}Ru_{18}B_8$ series and identified two important factors regulating the observed VE counts to lie between 220 and 228: (i) optimized Ti-Ru orbital interactions; and (ii) ligand field splitting of Fe 3*d* orbitals in the Fe1-'ladders' and 2*b*-chain (M3) sites. A rigid band approximation, which is reasonably valid over the observed range of VE counts, predicted ferromagnetic behavior at low Fe content, i.e., $n \leq 0.75$ in $Ti_{9-n}Fe_{2+n}Ru_{18}B_8$, but complex ferrimagnetic behavior at higher Fe content, i.e., $n > 0.75$, in agreement with experiment.

6.6 Acknowledgments

The authors wish to acknowledge the generous financial support through a joint grant provided by the National Science Foundation (USA; NSF DMR 05-02671) and the Deutsche Forschungsgemeinschaft (Germany) through the Materials World Network program.

6.7 References

(1) Eibenstein, U.; Jung, W. *Z. Anorg. Allg. Chem* **1998**, *624*, 802.
(2) Nagelschmitz, E. A.; Jung, W. *Chemistry of Materials* **1998**, *10*, 3189.
(3) Nagelschmitz, E. A.; Jung, W.; Feiten, R.; Müller, P.; Lueken, H. *Z. Anorg. Allg. Chem* **2001**, *627*, 523.
(4) Fokwa, B. P. T.; Lueken, H.; Dronskowski, R. *Chemistry - A European Journal* **2007**, *13*, 6040.
(5) Fokwa, B. P. T.; Samolyuk, G. D.; Miller, G. J.; Dronskowski, R. *Inorg. Chem.* **2008**, *47*, 2113.
(6) Landrum, G. A.; Dronskowski, R. *Angew. Chem. Int. Ed.* **1999**, *38*, 1389.
(7) Landrum, G. A.; Dronskowski, R. *Angew. Chem. Int. Ed.* **2000**, *39*, 1560.
(8) Goerens, C.; Brgoch, J.; Miller, G. J.; Fokwa, B. P. T. *Inorg. Chem.* **Submitted**.
(9) Brgoch, J.; Yeninas, S.; Prozorov, R.; Miller, G. J. *J. Solid State Chem.* **2010**, *183*, 2917.
(10) Andersen, O. K. *Phys. Rev. B* **1975**, *12*, 3060.
(11) Andersen, O. K.; Jepsen, O. *Phys. Rev. Lett.* **1984**, *53*, 2571.
(12) *TB-LMTO-ASA Program*, 4.7 ed., Krier, G.; Jepsen, O.; Burkhardt, A.; Andersen, O. K., Stuttgart, Germany, 1995.
(13) von Barth, U.; Hedin, L. *J. Phys. C* **1972**, *5*, 1629.
(14) Dronskowski, R.; Blöchl, P. E. *J. Phys. Chem.* **1993**, *97*, 8617.
(15) Miller, G. J. *Eur. J. Inorg. Chem.* **1998**, 523.
(16) Stoner, E. C. *Proc. Roy. Soc. London A* **1936**, *154*, 656.
(17) Stoner, E. C. *Proc. Roy. Soc. London A* **1938**, *165*, 372.
(18) Janak, J. F. *Phys. Rev. B* **1977**, *16*, 255.
(19) Raub, E.; Roeschel, E. *Zeitschrift fuer Metallkunde* **1963**, *54*, 455.
(20) Aselius, J. *Acta Chemica Scandinavica* **1960**, *14*.
(21) Fokwa, B. P. T.; Goerens, C.; Gilleßen, M. *Z. Kristallogr.* **2010**, *225*, 180.
(22) Brewer, L. *Science* **1968**, *161*, 115.
(23) Dronskowski, R.; Korczak, K.; Lueken, H.; Walter, J. *Angew. Chem. Int. Ed.* **2002**, *41*, 2528.
(24) Atkinson, K. *An Introduction to Numerical Analysis*; 2nd. ed.; John Wiley & Sons, 1989.

6.8 Supporting Information

Table S1. Location and size of empty spheres for a doubled unit cell in *TB-LMTO-ASA* calculations.

Sphere	Fractional Coordinates			WS Radii (Bohr)
	x	*y*	*z*	
E	½	0	−0.0846	1.619
E1	½	0	0.0846	1.619
E2	0.4496	−0.0503	0.1691	1.153
E3	0.4496	−0.0503	0	1.153
E4	0.3891	−0.1268	0.1691	1.052
E5	0.3891	−0.1268	0	1.052
E6	0.4894	0.0870	−0.0846	1.117
E7	0.4142	0.0124	−0.0846	1.064
E8	0.4142	0.0124	0.0846	1.064
E9	0.0489	0.0869	0.0842	1.117

Table S2. (a) IDOS values for different compositions of $Ti_{9-n}Fe_{2+n}Ru_{18}B_8$ while maintaining a constant WS radii. (b) IDOS values and elements for the magnetic atom sites in each model. (c) IDOS values for "$Ti_6Fe_5Ru_{18}B_8$" VE count range 220-228 using a rigid band approximation.

(a)	IDOS Values (valence electrons)								
Atom	Ru1	Ru2	Ru3	Ru4	Ru5	Ti1	Ti3	B1	B2
WS Radius (Å)	1.41	1.43	1.39	1.36	1.37	1.69	1.72	1.12	1.14
$Ti_9Fe_2Ru_{18}B_8$	7.69	7.84	7.34	7.42	7.36	4.79	4.98	3.05	3.01
$Ti_8Fe_3Ru_{18}B_8$	7.69	7.83	7.46	7.31	7.41	4.81	5.01	3.05	3.02
$Ti_7Fe_4Ru_{18}B_8$	7.67	7.86	7.52	7.36	7.32	4.80	4.99	3.05	3.01
$Ti_6Fe_5Ru_{18}B_8$	7.68	7.83	7.82	7.37	7.39	4.81	5.00	3.05	3.01

(b)	IDOS Values (valence electrons)					
Atom	2*b*-chain		4*h*-chain		4*h*-ladder	
$Ti_9Fe_2Ru_{18}B_8$	Ti	4.87	Ti	4.8	Fe	8.35
$Ti_8Fe_3Ru_{18}B_8$	Fe	8.62	Ti	4.89	Fe	8.38
$Ti_7Fe_4Ru_{18}B_8$	Ti	4.55	Fe	8.56	Fe	8.26
$Ti_6Fe_5Ru_{18}B_8$	Fe	8.51	Fe	8.55	Fe	8.27
WS Radii (Å)	Ti:	1.62	Fe:	1.45		

(c)	Integrated DOS of $Ti_6Fe_5Ru_{18}B_8$		
VE Count	2*b*-chain (M3)	4*h*-chain (M2)	4*h*-ladder (Fe1)

220		8.24	8.19	8.32
222		8.32	8.26	8.46
224		8.38	8.32	8.80
228		8.51	8.48	9.21
	W.S. (Å) Fe:	1.45		

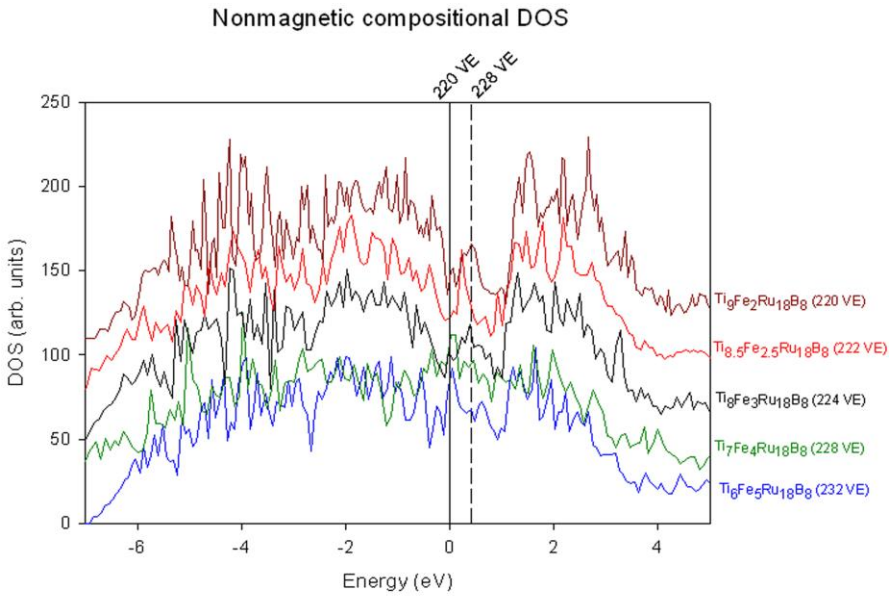

Figure S1. Compositional dependent (LDA) density of states. The lines shown correspond to electron counts for $Ti_9Fe_2Ru_{18}B_8$ (220 VE) and $Ti_7Fe_4Ru_{18}B_8$ (228 VE)

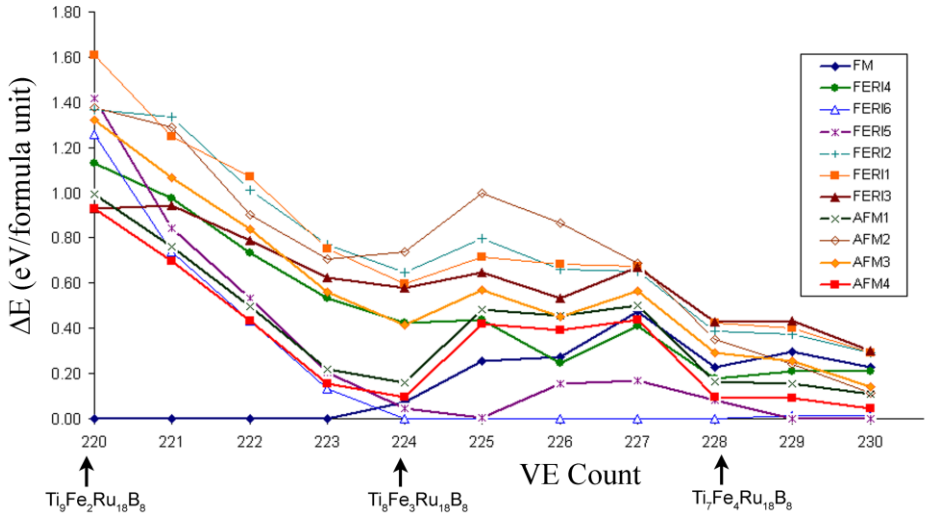

Figure S2. The entire energy range for the relative total energy vs. valence electron count between the 220 VE and 230 VE with the most favorable model for each electron count set to zero.

CHAPTER 7

$Ti_{9-x}M_{2+x}Ru_{18}B_8$ (M = Cr – Ni; x = 0 – 1): A Valence Electron Sensitive Boride Series

Christian Goerens, Jakoah Brgoch, Gordon J. Miller, Boniface P.T. Fokwa

[1]Institute of Inorganic Chemistry, RWTH Aachen University, Landoltweg 1, D-52064
[2]Aachen, Germany, and Department of Chemistry, Iowa State University, Ames, Iowa 50011

7.1 Abstract

Polycrystalline samples of the compound series $Ti_{9-x}M_{2+x}Ru_{18}B_8$ (M = Cr, Mn, Co, Ni: x = 1) have been synthesized by arc-melting the elements. The phases were characterized by powder X-ray diffraction (Rietveld refinement) as well as energy-dispersive X-ray analysis. They are substitutional variants of the $Zn_{11}Rh_{18}B_8$ structure type, space group *P*4/*mbm* (No. 127). According to DFT calculations the Ru-X (X = B, Ti, Ti/M) bonding interactions are nearly constant throughout the series and responsible for the structural stability of these phases, whereas the M-M and Ru-M interactions vary significantly with varying valence electron count. Furthermore density of states (DOS) analyses predict the phases with M = Mn and Ni to develop a total magnetic moment but not the M = Co phase. Susceptibility measurements confirm the Co phase to be paramagnetic, as predicted. Non-vanishing DOS at the Fermi level indicates metallic character for all phases.

7.2 Introduction

The discovery of $Ti_9Fe_2Ru_{18}B_8$,[1] yielding the first ruthenium-rich ferromagnetic transition metal boride, has resulted in the exploration of an entire family of compounds which are attractive both experimentally and theoretically for their interesting magnetic properties. These phases crystallize in the $Zn_{11}Rh_{18}B_8$-type structure (space group *P*4/*mbm*, No. 127), and contain ladders of iron atoms, which are mainly responsible for the ordering below 200K. Furthermore, theoretical investigations on $Ti_9Fe_2Ru_{18}B_8$ revealed that phases containing more valence electrons (VE) (with up to 13 VE more than 220 VE for $Ti_9Fe_2Ru_{18}B_8$) should be even more favorable. Consequently, the isostructural VE-rich phases, $Ti_9M_2Ru_{18}B_8$ (M = Co, Ni, Cu and Zn), with electron counts up to 228 VE, have been successfully synthesized and characterized.[2] Although phases were not predicted to be formed with fewer than 220 VE, the members with M = Cr (216 VE) and Mn (218 VE) were also successfully synthesized. However, an attempt to further remove electrons from the system by substituting M = Ti (212 VE) was unsuccessful. In this case titanium, which should fully occupy the M-site was found to mix statistically with ruthenium. Therefore, it was determined that titanium has too few valence electrons and must mix with the more electron rich ruthenium to satisfy the site requirements. Consequently, the structure has a total composition of $Ti_{10}Ru_{19}B_8 \equiv Ti_9(TiRu)Ru_{18}B_8$ (with 216 VE), where a Ti/Ru mixture builds the ladder substructure.[3] From these experiments, a VE-range for the compounds in the $Ti_9M_2Ru_{18}B_8$ series of phases lies between 216 and 228 VE.

Another way to increase the VE count in these types of phases is to substitute titanium atoms in $Ti_9M_2Ru_{18}B_8$ for more electron rich elements. The first examples of such phases are $Ti_8Fe_3Ru_{18}B_8$ (224 VE) and $Ti_7Fe_4Ru_{18}B_8$ (228 VE) were successfully synthesized recently.[4] These phases contain a new structural unit, the "magnetic scaffold," which contains the magnetically active element and is mainly responsible for the observed itinerant ferrimagnetism below 210 K and 220 K, respectively. These compounds were also investigated theoretically based on the hypothetical structural models of"$Ti_{8.5}Fe_{2.5}Ru_{18}B_8$"(222 VE).[5] The electronic structure calculations revealed that both Ti-Ru interactions, as well as ligand field splitting of the Fe 3*d* orbitals, regulated

the observed VE counts between 220 and 228 electrons/formula unit, further proof of the strong VE-dependency in these phases. Furthermore, magnetic models using a hypothetical "$Ti_6Fe_5Ru_{18}B_8$" (232 VE) phase and a rigid band analysis of the LSDA DOS curves concluded preferred ferromagnetic ordering at low Fe content ($x \leq 0.75$) and ferrimagnetic ordering at higher Fe content ($x > 0.75$) in the $Ti_{9-x}Fe_{2+x}Ru_{18}B_8$ series.

Based on this knowledge, we applied synthetic and computational means to search for other VE-rich phases structurally related to $Ti_8Fe_3Ru_{18}B_8$ (224 VE) and $Ti_7Fe_4Ru_{18}B_8$ (228 VE) and having the general formula $Ti_{9-x}M_{2+x}Ru_{18}B_8$ (M = Cr – Ni).

7.3 Experimental Section

7.3.1 Synthesis and Characterization. The synthesis of each sample following $Ti_8M_3Ru_{18}B_8$ (M = Cr, Mn, Co, Ni) was carried out by arc-melting the elements in a water-cooled copper crucible under an argon atmosphere using a tungsten tip as a second electrode. The starting materials, titanium (chunks, 99.9%, Degussa), chromium (powder, 99.9%, ABCR), manganese (powder, 99.9%, ABCR), cobalt (powder, 99.9%, ABCR), nickel (powder, 99.9%, ABCR) ruthenium (powder, 99.9%), and boron (powder, 97%, ABCR, or crystalline pieces, 99.999%, Alfa Aesar) were weighed in the corresponding stoichiometric ratios (total mass 0.3 g), pressed into pellets, and arc-melted under argon until homogeneous melting occurred. The argon was purified over silica gel, molecular sieves, and a titanium sponge (950 K). The products were melted several times to ensure homogeneity of the samples. Weight losses during the melting process were less than 1 %. A product with metallic luster was obtained in each case. These products were stable in air both as a compact bulk and as a finely ground powder. The purity of each sample was checked by X-ray powder diffraction with the Guinier technique using Cu $K\alpha_1$ radiation (λ = 1.54059 Å) and silicon as an internal standard. The presence of the metals and their ratios were characterized by energy-dispersive X-ray analysis (EDX) on a high-resolution, low-energy LEO 1530 SEM (Zeiss, Oberkochen, Germany) equipped with an INCA EDX system (Oxford Instruments).

7.3.2 Crystal Structure Refinement. Rietveld refinements were carried out for the four new $Ti_8M_3Ru_{18}B_8$ (M = Cr, Mn, Co, Ni) phases, using the *FULLPROF* software.[6]

The model used for the refinements was based on the single crystal data of the $Ti_8Fe_3Ru_{18}B_8$ phase, replacing iron with the corresponding M-element.

7.3.3 Magnetization Measurements. Magnetization measurements were performed on a polycrystalline sample of the $Ti_8Co_3Ru_{18}B_8$ phase using a SQUID magnetometer (MPMS-5S, Quantum Design, San Diego, CA) in the temperature range 4–300 K at an applied field of 0.01 T. The data were corrected for the sample holder (Teflon® tubes). Corrections for diamagnetic and conduction electron contributions were not applied. The presentation of the magnetic data follows the recommendation of Hatscher et al. (SI units).[7]

7.3.4 Electronic Structure Calculations. All atomic positions and lattice parameters were optimized using the Vienna *ab-initio* Simulation Package (*VASP*) by following the suggested bulk relaxation process while maintaining a constant volume.[8-11] The compositions studied theoretically follow the general formula "$Ti_{8.5}M_{2.5}Ru_{18}B_8$" (M = Cr, Mn, Fe, Co, Ni). The starting point of these optimizations used the lattice parameters as determined from powder X-ray diffraction for each composition and atomic positions determined from the single crystal X-ray refinement of $Ti_8Fe_3Ru_{18}B_8$.[4] All *VASP* calculations were performed using the projector augmented-wave (PAW) method[12] and the Perdew-Burke-Ernzerhof 96 generalized gradient approximation (GGA-PBE).[13] A 3 × 3 × 9 Monkhorst-Pack ***k***-points grid[14] was used to sample the first Brillouin zone for reciprocal space integrations. The energy cut-off of the plane wave basis was 398 eV. With these settings, the total energies converged to lower than 2.5 meV/formula unit.

The optimized positions were then used for the calculations of the electronic structure using the tight-binding, linear muffin-tin orbital method with the atomic-spheres approximation (*TB-LMTO-ASA*)[15,16] using the Stuttgart code.[17] Exchange and correlation were treated by the local density approximation (LDA) and local spin density approximation (LSDA), which was parameterized according to von Barth and Hedin.[18] In the ASA method, space is filled with overlapping Wigner-Seitz (WS) spheres. The symmetry of the potential is considered spherical inside each WS sphere and a combined correction is used to take into account the overlapping part. The corresponding WS radii are: Ru, 1.38-1.47 Å; Ti, 1.62-1.73 Å; B, 1.12 Å; Cr, 1.33-1.52 Å; Mn, 1.34-1.54 Å; Fe,

1.38-1.57 Å; Co, 1.38-1.58 Å; Ni, 1.43-1.57 Å. Space-filling empty spheres were not required in these models.

Electronic structures were calculated using space group *P*4/*m* (no. 83), a subgroup of the crystallographic group *P*4/*mbm*. Lowering the crystallographic symmetry, specifically at the 2*b* site, allows total compositions ($Ti_{8.5}M_{2.5}Ru_{18}B_8$) closer to those observed experimentally ($Ti_8M_3Ru_{18}B_8$) atomic mixing to be probed. The basis sets of these calculations include: B (2*s*, 2*p*), Ru (5*s*, 5*p*, 4*d*), Ti (4*s*, 4*p*, 3*d*), Cr (4*s*, 4*p*, 3*d*), Mn (4*s*, 4*p*, 3*d*), Fe (4*s*, 4*p*, 3*d*), Co (4*s*, 4*p*, 3*d*), and Ni (4*s*, 4*p*, 3*d*) wave functions. A mesh of 54 ***k*** points in the irreducible wedge of the first Brillouin zone was used to obtain all integrated values, including the density of states (DOS) and crystal orbital Hamilton population (–COHP) curves.

7.4 Results and Discussion

7.4.1 Crystal Chemistry. Phase analysis was applied to the powder diffraction data using the Rietveld refinement method on the products with loaded compositions of "$Ti_8M_3Ru_{18}B_8$" (M = Cr, Mn, Co, Ni). A sample of the refinement for $Ti_8Co_3Ru_{18}B_8$ is illustrated in Figure 1.

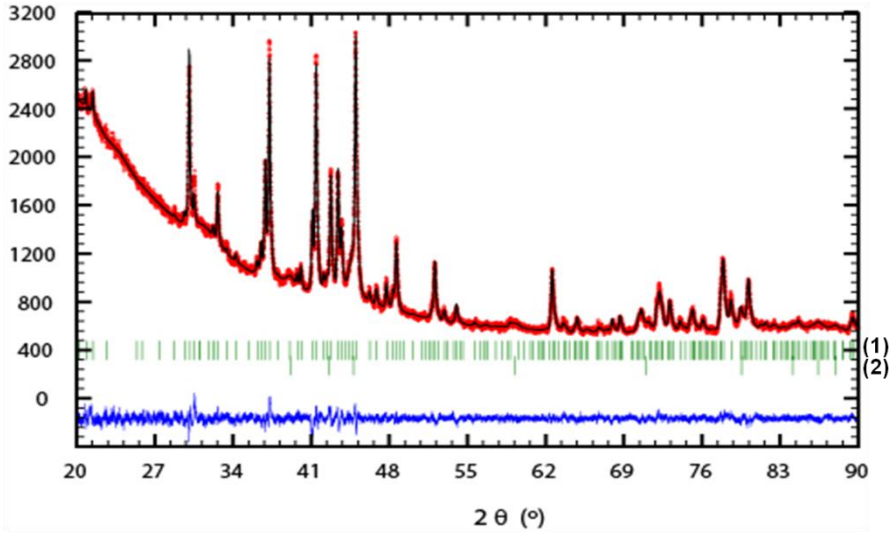

Figure 1. Rietveld refinement of the X-ray powder pattern of $Ti_8Co_3Ru_{18}B_8$ sample showing measured and fitted intensities (top), the position of the Bragg peaks (middle) for the $Ti_8Co_3Ru_{18}B_8$ phase (1) and the minor $Ru_{1-\delta}Co_\delta$ phase (2), and the difference intensity curve (bottom).

The refinements were based on the single crystal data of the previously reported $Ti_8Fe_3Ru_{18}B_8$ phase. In addition, a model that statistically mixed the M atoms in every Ti sites was also attempted; however, it yielded a poor refinement. From the starting model of $Ti_8Fe_3Ru_{18}B_8$, the correct structure type could be easily distinguished in all samples. Small amounts of one or two secondary phases, identified as the binary RuTi intermetallic phase as well as M-doped ruthenium element ($Ru_{1-\delta}M_\delta$), were found in the newly synthesized samples, see Table 1.

Table 1. Rietveld refinement results for the quaternary borides $Ti_8M_3Ru_{18}B_8$ (M = Cr, Mn, Co, Ni).

	$Ti_8Cr_3Ru_{18}B_8$	$Ti_8Mn_3Ru_{18}B_8$	$Ti_8Fe_3Ru_{18}B_8$[4]	$Ti_8Co_3Ru_{18}B_8$	$Ti_8Ni_3Ru_{18}B_8$
lattice parameters (Å)	a = 17.524(1) c = 2.9612(3)	a = 17.537(1) c = 2.9651(3)	a = 17.520(1) c = 2.9650(3)	a =17.529(3) c = 2.9641(3)	a = 17.527(2) c = 2.9645(3)
unit cell volume (Å^3)	909.3(1)	911.9(1)	910.1(1)	910.7(2)	910.7(2)
secondary phases	Cr (5%); RuTi (5%)	$Ru_{1-\delta}Mn_\delta$ (3%); RuTi (2%)		$Ru_{1-\delta}Co_\delta$ (6 %)	$Ru_{1-\delta}Ni_\delta$ (20%)
R_{Bragg}	6.75	9.04	5.24	7.02	7.56
space group; Z	*P4/mbm* (N°. 127); 2				
2θ range (°)	$10 < 2\theta < 90$				
refinement method	RIETVELD, least squares method				
profile function	pseudo-Voigt				
structural model	$Ti_8Fe_3Ru_{18}B_8$ single-crystal data with Ti/M: 2/1 at 4*h* and 2*b*[4]				

The estimated amount of the main phase was at least 90%, with the exception of the nickel phase, which was ca. 80% of the desired phase (see Table 1).

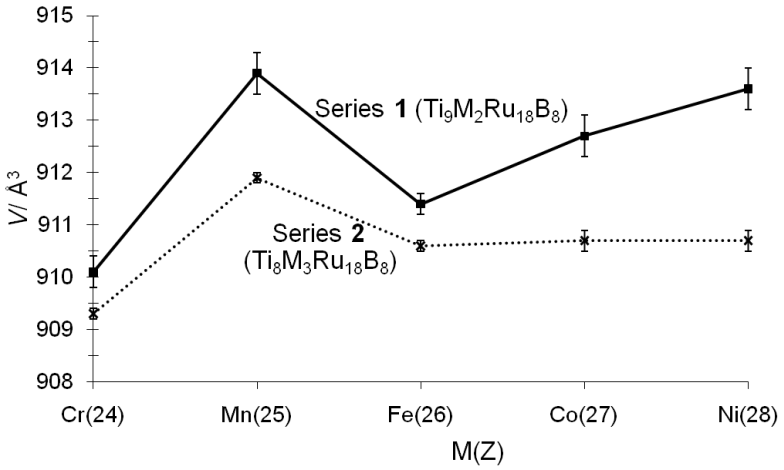

Figure 2. Refined unit cell volume versus atomic number of the M-element in series **1** ($Ti_9M_2Ru_{18}B_8$) and series **2** ($Ti_8M_3Ru_{18}B_8$).

Figure 2 shows the unit cell volume plotted as a function of M-atom for the present series (series **2**) and the already published $Ti_9M_2Ru_{18}B_8$ (M = Cr, Mn, Co, Ni) series (series **1**). As expected, series **2** shows a clear decrease in the refined unit cell volume in comparison to series **1**. This behavior stems from the influence of atomic size, because the smaller M-element substitutes for the larger titanium in $Ti_9M_2Ru_{18}B_8$[1,2] en route to $Ti_8M_3Ru_{18}B_8$ the volume decreases between the two series. Interestingly, the trends in series **1** and **2** have the same characteristic features for the first three points (M = Cr, Mn, Fe), but differ in the last two points. This may be attributed to the poor crystallinity of the samples, in particular for the M = Ni sample and its low amount. This finding is further supported by the fact that the trend of the theoretically optimized lattice parameters in series **2** is in good agreement with the experimental one, except for the M = Ni case (see Figure 4). Furthermore the unit cell volume of the compound with M = Mn is the highest in the series (see Figure 2). Size factors are mainly responsible of this behavior: In fact Mn has an atomic radius of 1.367 Å (half the Mn-Mn distance in the Element) which is considerably higher than for M= Cr, Fe, Co and Ni (1.241 – 1.253 Å). This behavior has been observed in many other boride series including the $Ti_9M_2Ru_{18}B_8$ series as can bee seen in Figure 2.

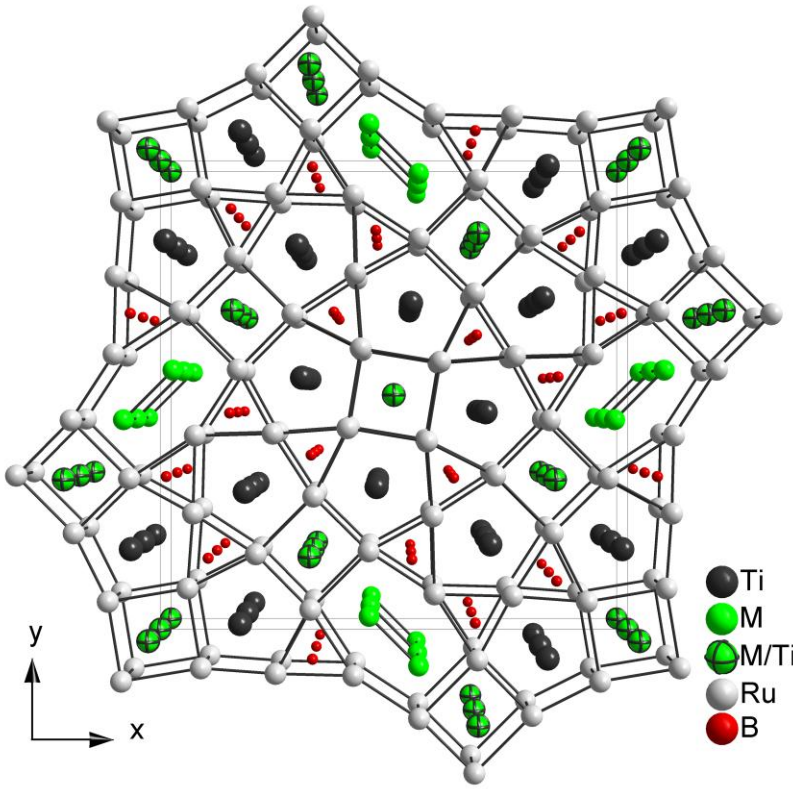

Figure 3. Perspective view of the unit cell of the $Ti_8M_3Ru_{18}B_8$ (M = Cr, Mn, Fe, Co, Ni) phases along [001].

Since suitable single crystals could not be grown for each sample in series **2**, these crystal structures were refined on the basis of their powder diffraction data by applying the Rietveld method using the single crystal data of the $Ti_8Fe_3Ru_{18}B_8$ phase as starting model, as stated above. The positions of all atoms, with the exception of boron, were successfully refined, however, all occupancies were fixed, resulting in the residual values reported in Table 1. Like the parent $Ti_8Fe_3Ru_{18}B_8$ phase, the new $Ti_8M_3Ru_{18}B_8$ phases belong to the $Zn_{11}Rh_{18}B_8$ structure type.[19] Figure 3 shows the crystal structure which is composed of nets of Ru atoms that when stacked along the [001] direction form trigonal, tetragonal, pentagonal and elongated hexagonal prisms. Boron atoms are found at the center of the trigonal prisms, the pentagonal prisms accommodate the titanium atoms, and the elongated hexagonal prisms contain the M_2-dumbbells which build a ladder substructure along the [001] direction. The centers of the tetragonal prisms at Wyckoff sites 2*b* and 4*h* are filled by two different mixtures of titanium and M-atoms, resulting in

two chains of Ti/M atoms along [001]. The combination of the elongated hexagonal prisms and the nearest neighbour tetragonal prisms (4*h*) form the "magnetic scaffold" when occupied by magnetic atoms.

It was observed in series **1**, that the structural stability of all phases in the series is dependent on the Ru-B and Ru-Ti bonds, which have nearly constant bond lengths throughout the series. However, the M-containing bonds, i.e. the M-M and Ru-M bonds, are directly affected by the change of lattice parameters. In series **2** this trend is also found, all Ru-X (X = B, Ti, Ti/M) bonds are nearly constant throughout series **2.** All M-containing bonds vary significantly. For example, the average Ru-B distance is ca. 2.19 Å while the average Ru-Ti distance (with titanium in the pentagonal Ru-prism) is ca.2.76 Å and the average Ru-Ti/M distance (with Ti/M in the tetragonal Ru-prism) is ca. 2.54 Å in each phase of the series. The average M-Ti/M distance varies from 2.94 Å (M = Mn) to 3.03 Å (M = Co), whereas the average M-Ru distance has an even greater variation from 2.69 Å (M = Co) to 2.98 Å (M = Mn), which is even topped by the average M-M distance which varies from 2.44 Å (M = Cr) to 2.69 Å (M = Mn). Overall, the longest bond lengths are observed for the M = Mn case, which is a direct consequence of having the largest unit cell volume in these phases. All of the above mentioned distances are in the same range as those found in series **1** and in other transition metal-rich boride phases containing at least three of the elements used.[20,21]

In the related zinc phases with compositions of $Zn_{10}MRh_{18}B_8$ (M = Cr, Mn, Fe, Co, Ni), substitution of Zn by the smaller M atom is only dictated by size factors, resulting in the sole substitution occurring in the 2*b* tetragonal prisms. In the case of $Ti_9M_2Ru_{18}B_8$ (series **1**) the earlier investigations made clear, that in terms of volume, one-half of the elongated hexagonal prism (i.e. the volume accommodating only one atom of the M_2-dumbbell) is smaller than a single pentagonal prism but larger than a tetragonal prism. The fact that the M-atoms occupy the hexagonal prism in the $Ti_9M_2Ru_{18}B_8$ compound series cannot be explained by size factors, and electronic reasons are playing a key role. As for the new compounds in series **2**, size factors again seem to play an important role regarding the additional M-atoms incorporated into the $Ti_9M_2Ru_{18}B_8$ structures. These additional atoms are found mixed with titanium atoms exclusively at the

centers of the smaller tetragonal prisms, while the larger pentagonal prisms are fully occupied by the larger titanium atoms, as illustrated in Figure 3. Therefore in series **2,** as in series **1**, size factors play a major role in the substitution pattern of these compounds. However, electronic factors are likely playing a crucial role as well.

7.4.2 Structural Optimizations. Structural models following "$Ti_{8.5}M_{2.5}Ru_{18}B_8$" (M = Cr-Ni) were developed to investigate the changes in bonding that occur upon substitution of the 3*d* metal. A prior description [5] of "$Ti_{8.5}Fe_{2.5}Ru_{18}B_8$" provided an initial detailed analysis of chemical bonding features in the $Ti_{9-n}Fe_{2+n}Ru_{18}B_8$ series and identified two important factors regulating the observed valence electron (VE) counts. First, early 3*d*-late 4*d*, i.e. Ti-Ru interactions, are optimized at 228 VE and, therefore, appear to limit the upper valence electron count. Second, the 3*d* orbitals associated with the Fe ladders are split by the surrounding ligand field resulting in the presence of a δ^* orbital along the {110} direction and a π^* orbital along the [001] direction at the Fermi level. Consequently, replacing iron with other 3*d* atoms provides another platform from which to investigate changes in local electronic structure as a function of valence electron count and effective nuclear charge.

The models of "$Ti_{8.5}M_{2.5}Ru_{18}B_8$" (M = Cr-Ni) were constructed following the same procedure as in "$Ti_{8.5}Fe_{2.5}Ru_{18}B_8$", using space group *P*4/*m* (no. 83) and allowing the additional M atom to replace Ti atoms in one-half of the 2*b*-chain sites, which creates two chains a Ti and Fe chain at the site. The atomic positions used for the calculations were determined from the single crystal X-ray diffraction results of $Ti_8Fe_3Ru_{18}B_8$,[4] while the lattice parameters used for each calculation were determined from the powder X-ray diffraction patterns of $Ti_8M_3Ru_{18}B_8$ (M = Cr-Ni). To ensure the structures are at an electronic ground state, the lattice parameters and atomic positions for each composition were optimized using *VASP*, as described above. The unit cell volumes were maintained, as determined from the powder X-ray diffraction patterns. As presented in Figure 4, the optimizations of the *a* parameters are underestimated, while the *c* parameters are overestimated, although the parameters differ by less than 1 % when compared to the crystallographic parameters.

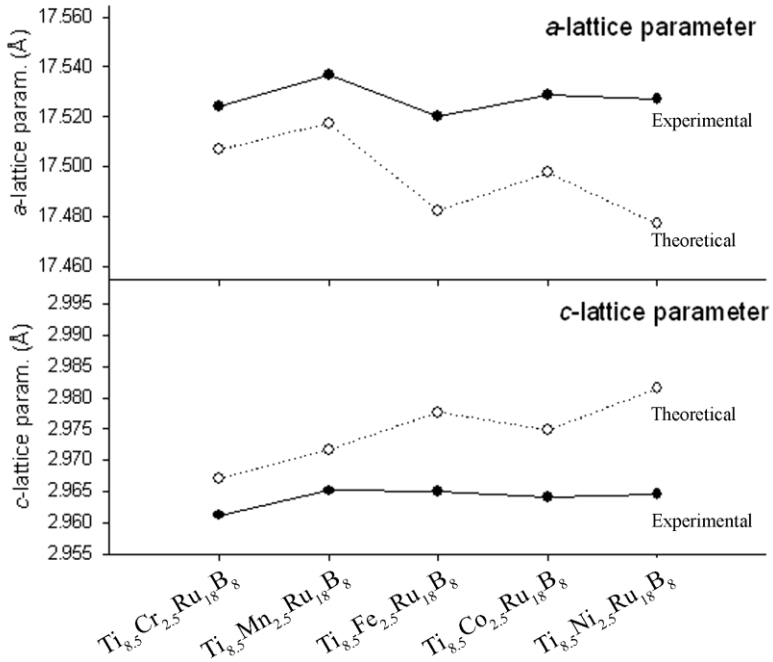

Figure 4. Optimized and experimental *a*- and *c*- lattice parameters for a theoretical composition of $Ti_{8.5}M_{2.5}Ru_{18}B_8$ (M = Cr-Ni). Experimental lattice parameters are from powder X-ray diffraction; optimized values are from *VASP* using a fixed experimental volume.

7.4.3 Chemical Bonding Analysis. Using the optimized structures of "$Ti_{8.5}M_{2.5}Ru_{18}B_8$" (M = Cr, Fe, Ni), a chemical bonding analysis was accomplished using –COHP curves, Figure 5, and their corresponding integrated –COHP (–ICOHP) values based on *TB-LMTO-ASA* calculations.

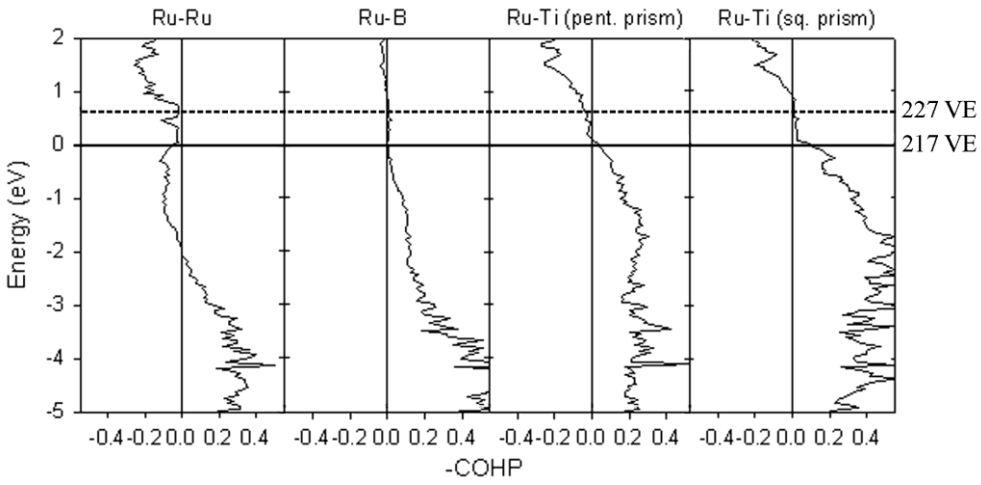

Figure 5. Nearest neighbor –COHP interactions for the nonmagnetic atoms. "$Ti_{8.5}M_{2.5}Ru_{18}B_8$." The Fermi level for 217 VE (M = Cr) is used as the energy reference for the curves shown, (specific curves for the cases M = Fe and Ni are presented in Supporting Information). The range of VE counts shown was determined using a rigid band approximation for "$Ti_{8.5}Cr_{2.5}Ru_{18}B_8$".

According to Figure 5, the interatomic orbital interactions between non-magnetically active elements, i.e. Ti, Ru, and B, are nearly all optimized at 217 VE. Increasing the VE count using a rigid band approximation to 227 VE, i.e "$Ti_{8.5}Ni_{2.5}Ru_{18}B_8$", moves the E_F of Ru-B and Ru-Ru interactions respectively into nonbonding and antibonding regions. Nonetheless, over this range of VE counts the –ICOHP values remain essentially constant (see also Supporting Information), changing by less than 3 % for these two interactions. The Ru-Ti –COHP curves, are optimized at 220 VE for the pentagonal prisms and 228 VE for the cubic prisms, with –ICOHP values decreasing by less than 2 % for each interaction as the VE count increases. However, above ca. 227 VE the occupation of antibonding orbitals dominates the Ru-Ti overlap. This is similar to the case of $Ti_{9-x}Fe_{2+x}Ru_{18}B_8$, which is limited to 228 VE from the Ru-Ti interactions. The corresponding –COHP curve for "$Ti_{8.5}Fe_{2.5}Ru_{18}B_8$" and "$Ti_{8.5}Ni_{2.5}Ru_{18}B_8$" exhibit only minor differences from those for "$Ti_{8.5}Cr_{2.5}Ru_{18}B_8$" and, so, are in Supporting Information.

Additionally, the interatomic orbital interactions involving the M-atoms show considerable changes in bonding character over the range of electron counts probed, i.e. 217 VE to 227 VE, with the rigid band approximation. For instance, the M_{Ladder}-Ru

orbital interaction, Figure 6a, is antibonding between 217-227 VE with the optimized interaction occurring well below at 181 VE.

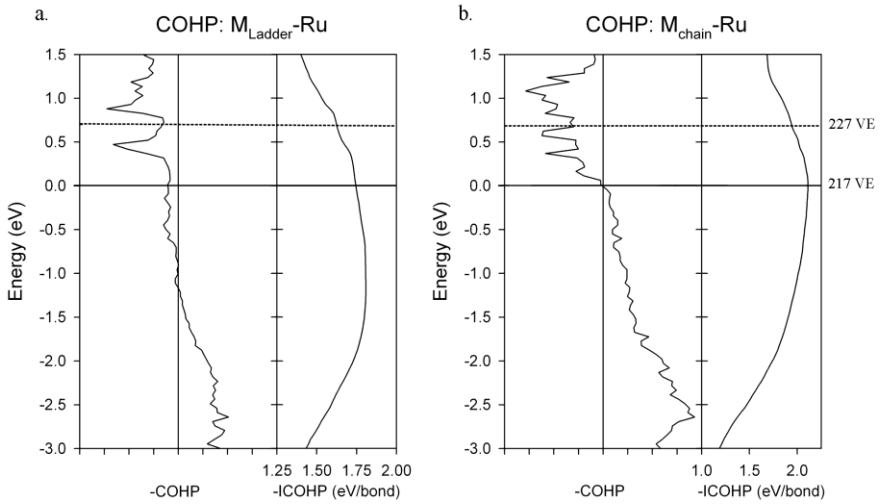

Figure 6. –COHP curves for the nearest neighbour (a) M_{Ladder}-Ru and (b) M_{chain}-Ru interactions. "$Ti_{8.5}M_{2.5}Ru_{18}B_8$" (M = Cr) (217 VE) is used as the base for the curves shown, (M = Fe and Ni are presented in the Supporting Information). The range of electron counts was determined using a rigid band approximation in "$Ti_{8.5}Cr_{2.5}Ru_{18}B_8$".

The addition of electrons to the M_{Ladder}-Ru overlap decreases the –ICOHP values from 1.74 eV/bond to 1.62 eV/bond, respectively for 217 VE to 227 VE, a change of nearly 7 %. The decrease in –ICOHP values primarily arises from the sharp peak in the –COHP curve present ca. 0.5 eV above the Fermi level. This peak was identified as a M_{Ladder}-Ru π^* orbital interaction using a "fatband" analysis. The M_{Chain}-Ru interaction, Figure 6b, exhibits a largely different –COHP curve than its ladder counterpart and is optimized at 217 VE. Adding electrons to 227 VE decreases its –ICOHP value by 10 % from 2.11 to 1.93 eV/bond.

The M-M orbital interactions occurring within the 3*d*-metal atoms along the {110} directions of the ladders were calculated using a rigid band approximation from "$Ti_{8.5}Fe_{2.5}Ru_{18}B_8$"and is illustrated in Figure 7.

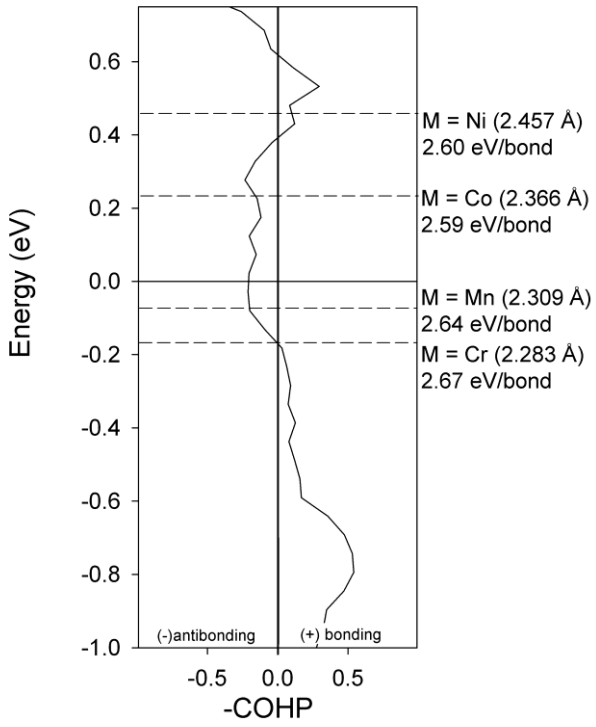

Figure 7. The M-M –COHP calculated for "$Ti_{8.5}Fe_{2.5}Ru_{18}B_8$" with the E_F set at 0 eV. The corresponding Fermi levels for "$Ti_{8.5}M_{2.5}Ru_{18}B_8$" (M = Cr, Mn, Co, Ni) were calculated using a rigid band approximation. The calculated bond distance from the *VASP* optimizations is in parenthesis. The –ICOHP for each M-M ladder is also shown.

Although single crystals suitable for X-ray diffraction were not obtained from each loaded composition, the structural optimizations can be used to estimate the atomic positions of all atoms and subsequently the bond lengths of the dimers in particular. Here, the optimized bond lengths along the {110} direction of the ladders increase with valence electron count, similar to those determined in the parent $Ti_9M_2Ru_{18}B_8$ (M = Cr-Zn).[2] The substitution from chromium to nickel decreases the –ICOHP values as calculated using the rigid band approximation. The Fermi level in "$Ti_{8.5}Cr_{2.5}Ru_{18}B_8$" (217 VE) is nearly optimized, "$Ti_{8.5}Mn_{2.5}Ru_{18}B_8$" (222 VE) is weakly antibonding, and "$Ti_{8.5}Co_{2.5}Ru_{18}B_8$" (225 VE) falls in a strongly antibonding region. In the previous report of "$Ti_{8.5}Fe_{2.5}Ru_{18}B_8$" a calculated ligand splitting diagram places a δ^* orbital near the Fermi level for the Fe-Fe overlap along the {110} direction.[5] It is likely δ^* orbitals are also present in these substituted phases, thus, occupying these orbitals will increase antibonding character and increase the bond length.

7.4.4 Density of States and Theoretical Magnetic Moments. An illustration of the total density of states (DOS) curves and M-atom partial DOS (PDOS) curves for the non-spin polarized calculations (LDA) is presented in Figure 8. In all cases, a pseudogap is present near the respective Fermi level resulting from the Ru 4*d*-states tailing off above E_F and an increase in the Ti 3*d*-states above E_F

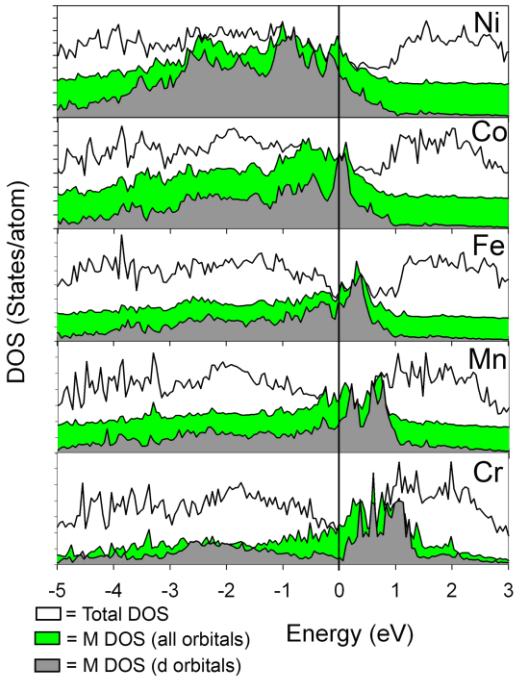

Figure 8. M atom partial DOS (gray), M atom 3*d* orbitals (dark gray) and the total DOS (white) for "$Ti_{8.5}M_{2.5}Ru_{18}B_8$" (M = Cr-Ni) with E_F set to 0 eV

The M atom PDOS curves for these structures, shown in Figure 8, illustrates the 3*d*-states of the M atoms moving lower in energy due to an increasing effective nuclear charge. Additionally, the Cr 3*d*-bands primarily exist in a narrow energy window between 0 and 1.5 eV while the substitution for later M atoms results in a more diffuse *d*-band with the Ni orbitals spread between −3 and 0.5 eV. The resulting E_F in "$Ti_{8.5}Cr_{2.5}Ru_{18}B_8$" does not lie at a local minimum in the DOS, thus, this composition is not prone to the formation of a magnetic moment. Local maxima are present (in the LDA-DOS) at E_F for "$Ti_{8.5}M_{2.5}Ru_{18}B_8$" (M = Mn, Fe, Ni), a result indicative of a possible electronic instability. Considering spin-polarization (by applying LSDA) to these

structures results in a substantial spin-polarization with a large magnetic moment developing in these three cases, as shown in Figure 9.

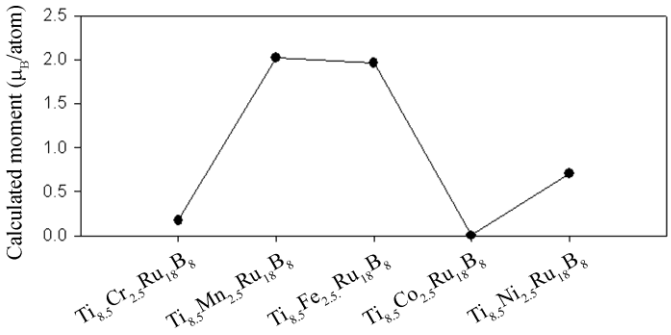

Figure 9. Calculated magnetic moment from *LMTO* for $Ti_8M_3Ru_{18}B_8$ (M = Cr-Ni).

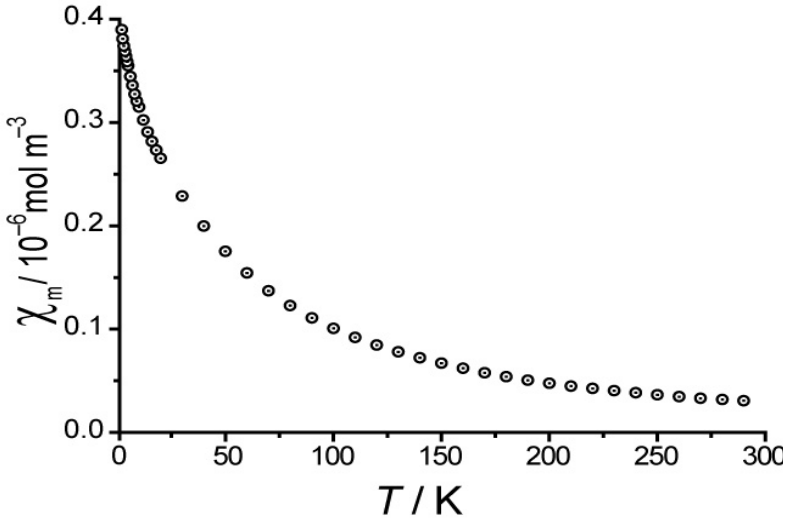

Figure 10. Molar susceptibility as a function of temperature at an applied magnetic field of 0.01 T for $Ti_8Co_3Ru_{18}B_8$.

Interestingly, the partial DOS of "$Ti_{8.5}Co_{2.5}Ru_{18}B_8$" shows a broad dispersion of Co bands across the E_F with a sharp large DOS originating from the 3*d* orbitals just above the Fermi level. Yet, spin-polarization does not result in any energetic stabilization; therefore, a theoretical magnetic moment does not develop in "$Ti_{8.5}Co_{2.5}Ru_{18}B_8$". The reason for this is not entirely clear and further investigation is warranted.

7.4.5 Magnetic Measurements. To confirm the predicted magnetic moments in these compounds, magnetization measurements on the synthesized $Ti_8Fe_3Ru_{18}B_8$[4] and $Ti_8Co_3Ru_{18}B_8$ samples were completed. $Ti_8Fe_3Ru_{18}B_8$ was previously confirmed to

develop a magnetic moment and was determined to order ferrimagnetically. The magnetization curve for $Ti_8Co_3Ru_{18}B_8$ is shown in Figure 10 and is paramagnetic with no magnetic ordering in the temperature range 4-300 K. The development of a magnetic moment in "$Ti_{8.5}M_{2.5}Ru_{18}B_8$" (M = Mn, Ni) type phases still needs to be verified experimentally.

7.5 Conclusion

The second series of transition metal-rich boride phases, $Ti_8M_3Ru_{18}B_8$ (M = Cr-Ni), containing ladders of a magnetically active element (M) have been synthesized by arc-melting of the elements. Similar to series **1** ($Ti_9M_2Ru_{18}B_8$), the crystal structure of the new phases are mainly stabilized by the heteroatomic Ru-B and Ru-Ti bonds which remain nearly constant throughout the series, whereas the M-containing bonds vary significantly with varying valence electron count. An experimental finding confirmed and even extended by COHP bonding analyses. In addition, the DOS analyses of the M-elements reveal the development of magnetic moments for the M = Mn, Fe, Ni cases but not for M = Co. Indeed, $Ti_8Co_3Ru_{18}B_8$ was found experimentally to be a paramagnet and magnetic moments were previously measured for M = Fe. The measurements for M = Mn and Ni are still pending.

7.6 Acknowledgements.

The authors wish to acknowledge the generous financial support through a joint grant provided by the National Science Foundation (USA; NSF DMR 08-06507) and the Deutsche Forschungsgemeinschaft (Germany) through the Materials World Network program. We also thank Ms. Resi Zaunbrecher (IPC, RWTH-Aachen) for the EDX analyses, Mr. Klaus Kruse and Dr. Paul Müller for various X-ray data collections. C.G. thanks the National Research Fund, Luxembourg, for awarding him a PhD fellowship.

7.7 References

(1) Fokwa, B. P. T.; Samolyuk, G. D.; Miller, G. J.; Dronskowski, R. *Inorg. Chem.* **2008**, *47*, 2113.
(2) Fokwa, B. P. T.; Goerens, C.; Gilleßen, M. *Z. Kristallogr.* **2010**, *225*, 180.
(3) Fokwa, B. P. T. *Z. Anorg. Allg. Chem* **2009**, *635*, 2258.

(4) Goerens, C.; Brgoch, J.; Miller, G. J.; Fokwa, B. P. T. *Inorg. Chem.* **2011**, *50*, 6289.
(5) Brgoch, J.; Goerens, C.; Fokwa, B. P. T.; Miller, G. J. *J. Am. Chem. Soc.* **2011**, *133*, 6832.
(6) Rodriguez-Caravajal, J. Fullprof Version 3.2, Laboratoire Léon Brillouin, 1997.
(7) Hatscher, S. T.; Schilder, H.; Lueken, H.; Urland, W. *Pure Appl. Chem.* **2005**, *77*, 497.
(8) Kresse, G.; Furthmüller, J. *Comput. Mater. Sci.* **1996**, *6*, 15.
(9) Kresse, G.; Furthmüller, J. *Phys. Rev. B* **1996**, *54*, 11169.
(10) Kresse, G.; Hafner, J. *Phys. Rev. B* **1993**, *47*, 558.
(11) Kresse, G.; Marsman, M.; Furthmuller, J. *Vienna Ab-initio Simulation Package: VASP the GUIDE*, 2010.
(12) Kresse, G.; Joubert, D. *Phys. Rev. B* **1999**, *59*, 1758.
(13) Perdew, J. P.; Burke, K.; Ernzerhof, M. *Phys. Rev. Lett.* **1996**, *77*, 3865.
(14) Monkhorst, H. J.; Pack, J. D. *Phys. Rev. B* **1976**, *13*, 5188.
(15) Andersen, O. K. *Phys. Rev. B* **1975**, *12*, 3060.
(16) Andersen, O. K.; Jepsen, O. *Phys. Rev. Lett.* **1984**, *53*, 2571.
(17) Krier, G.; Jepsen, O.; Burkhardt, A.; Andersen, O. K. TB-LMTO-ASA Program, Stuttgart, Germany, 1995.
(18) von Barth, U.; Hedin, L. *J. Phys. C: Solid State Phys.* **1972**, *5*, 1629.
(19) Eibenstein, U.; Jung, W. *Z. Anorg. Allg. Chem* **1998**, *624*, 802.
(20) Fokwa, B. P. T.; Dronskowski, R. *J. Alloys Compd.* **2007**, *428*, 84.
(21) Fokwa, B. P. T.; von Appen, J.; Dronskowski, R. *Chem. Comm.* **2006**, 4419.

7.8 Supporting Information

Table S1. The *VASP* optimized lattice parameters and volume and the crystallographic lattice parameters and volume, determined from powder X-ray diffraction.

	Crystallographic Parameters			Optimized parameters		
	a (Å)	*c* (Å)	vol. (Å^3)	*a* (Å)	*c* (Å)	vol. (Å^3)
$Ti_8Cr_3Ru_{18}B_8$	17.5240	2.9612	909.35	17.5068	2.9670	909.35
$Ti_8Mn_3Ru_{18}B_8$	17.5370	2.9651	911.90	17.5175	2.9717	911.90
$Ti_8Fe_3Ru_{18}B_8$	17.5200	2.9650	910.09	17.4824	2.9777	910.09
$Ti_8Co_3Ru_{18}B_8$	17.5290	2.9641	910.78	17.4976	2.9748	910.78
$Ti_8Ni_3Ru_{18}B_8$	17.5270	2.9645	910.69	17.4770	2.9815	910.69

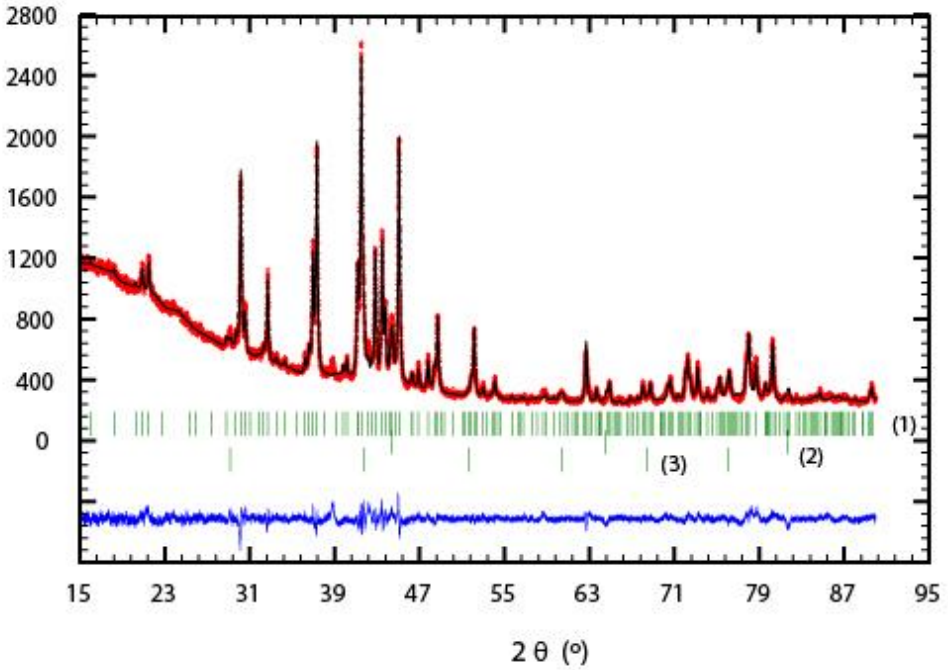

Figure S1. Rietveld refinement of the X-ray powder pattern of $Ti_8Cr_3Ru_{18}B_8$ sample showing measured and fitted intensities (top), the position of the Bragg peaks (middle) for the $Ti_8Co_3Ru_{18}B_8$ phase (1), the minor RuTi (2) and Cr phases (3), and the difference intensity curve (bottom).

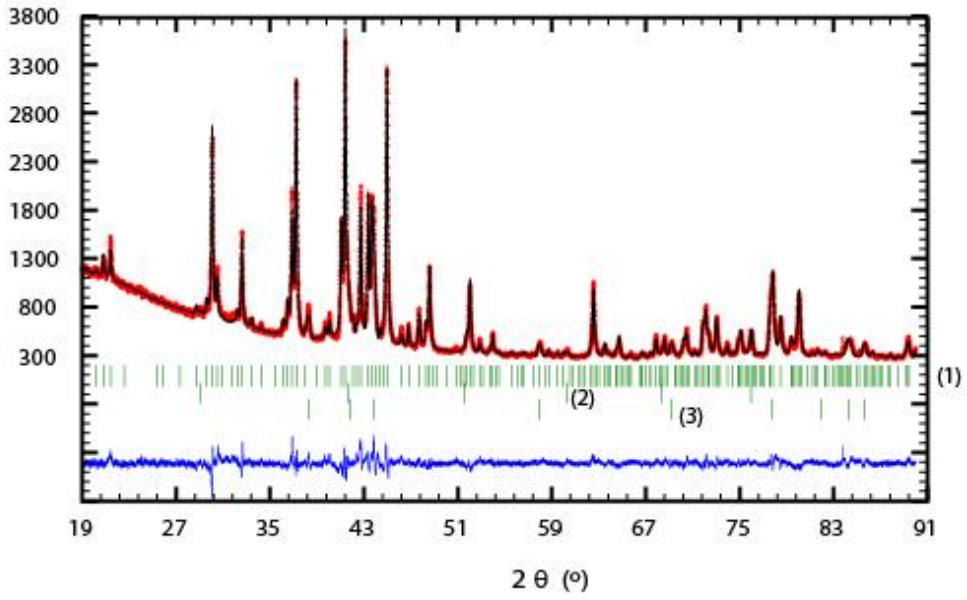

Figure S2. Rietveld refinement of the X-ray powder pattern of $Ti_8Mn_3Ru_{18}B_8$ sample showing measured and fitted intensities (top), the position of the Bragg peaks (middle) for the $Ti_8Co_3Ru_{18}B_8$ phase (1), the minor RuTi (2) and $Ru_{1-\delta}Mn_\delta$ phases (3), and the difference intensity curve (bottom).

CHAPTER 8

Validation of Interstitial Iron and Consequences of Nonstoichiometry in Mackinawite ($Fe_{1+x}S$)

Modified from a publication in the *Journal of Physical Chemistry A*
(*J. Phys. Chem. A* **2012**, *116*(*9*), 2234)

Jakoah Brgoch and Gordon J. Miller[*]

Department of Chemistry, Iowa State University, Ames, Iowa, 50011, USA

8.1 Abstract

A theoretical investigation of the relationship between chemical composition and electronic structure was performed on the non-stoichiometric iron sulfide, mackinawite ($Fe_{1+x}S$), which is isostructural and isoelectronic with the superconducting $Fe_{1+x}Se$ and $Fe_{1+x}(Te_{1-y}Se_y)$ phases. Even though $Fe_{1+x}S$ has not been measured for superconductivity, the effects of stoichiometry on transport properties and electronic structure in all of these iron-excess chalcogenide compounds has been largely overlooked. In mackinawite, the amount of Fe that has been reported ranges from a large excess, $Fe_{1.15}S$, to nearly stoichiometric, $Fe_{1.00(7)}S$. Here, we analyze, for the first time, the electronic structure of $Fe_{1+x}S$ to justify these nonstoichiometric phases. First principles electronic structure calculations using supercells of $Fe_{1+x}S$ yield a wide range of energetically favorable compositions ($0 < x < 0.30$). The incorporation of interstitial Fe atoms originates from a delicate balance between the Madelung energy and the occupation of Fe-S and Fe-Fe antibonding orbitals. A theoretical assessment of various magnetic structures for "FeS" and $Fe_{1.06}S$ indicate that striped magnetic ordering along [110] is the lowest energy structure and the interstitial Fe affects the values of moments in the square planes as a function of distance. Moreover, the formation of the magnetic moment is dependent on the unit cell volume, thus relating it to composition. Finally, changes in the composition cause a modification of the Fermi surface and ultimately the loss of a nested vector.

8.2 Introduction

With the discovery of superconductivity in the iron based compounds $Fe_{1+x}Se$ and $Fe_{1+x}(Te_{1-y}Se_y)$, research on structures with similar compositions and symmetry has expanded rapidly.[1-6] The structures in the iron chalcogenide family crystallize in the space group *P4/nmm* (no. 129) with anti-PbO-type structures and contain $[FeX_{4/4}]$ layers of edge-sharing tetrahedra (X = As, Se, or Te). These $[FeX_{4/4}]$ layers are believed to be the active conducting layer and, therefore, create a competition between superconductivity and magnetism.[1] The total composition of these structures, whether they are stoichiometric or metal-rich, has also been heavily debated.[7] McQueen *et al.* reported a superconducting phase (T_C = 8.5 K) with excess iron, $Fe_{1.01}Se$, taking special care to prevent oxide impurities in these samples. As the concentration of interstitial Fe increases to $Fe_{1.02}Se$ and $Fe_{1.03}Se$ the T_C decreases from 5 K and 0.6 K, respectively.[3] Additionally, $Fe_{1.01}Se$ undergoes a structural transition from tetragonal to orthorhombic at 90 K whereas the same transition in $Fe_{1.03}Se$ is not observed.[8] These results show the strong dependence between the properties of these materials and their composition.

The naturally occurring mineral, mackinawite, contains $[FeS_{4/4}]$ layers and is isostructural with the selenide and telluride analogues. The structure was originally reported by Berner (1962) with a composition of $Fe_{1.05}S$, determined via X-ray powder diffraction from the mineral sample.[9] Since then many groups have successfully obtained synthetic mackinawite, allowing an extensive investigation into its composition. For example, Sweeney *et al.* reported compositions ranging from $Fe_{1.09}S$ to $Fe_{1.15}S$ using a stoichiometric ratio of reactants, whereas Lennie *et al.* reported a composition of $Fe_{0.99(2)}S$ using TEM-EDAX.[10,11] Rickard *et al.* optimized the digestion chemistry to determine the structure is near $Fe_{1.00(1)}S$.[12] In addition to the total composition of mackinawite, the location of any interstitial Fe atoms, if present, is also of great interest. Although the interstitial site in $Fe_{1+x}S$ has yet to be identified, in the case of $Fe_{1+x}Te$ powder neutron diffraction showed an interstitial atom occupy the 2*c* Wyckoff site with square pyramidal coordination to the nearest tellurium atoms.[13]

Although $Fe_{1+x}S$ has never been measured for superconductivity to the best of our knowledge, the electronic structure of the tetragonal iron sulfide system may yield

insights into the superconducting properties of the chalcogenide phases. The calculated electronic structures of tetragonal and stoichiometric "FeS", "FeSe", and "FeTe" using density functional theory (DFT) with the local-density approximation (LDA) show similar band structures for "FeS" and "FeSe", but a different electronic structure in "FeTe". The two former structures contain well separated chalcogenide valence *p* and metal 3*d* states, whereas the latter shows a poorly defined pseudogap with the Te 5*p* bands moving into the same energy range as the Fe 3*d* states.[14] Fermi surfaces and phonon dispersion curves were also investigated without accounting for spin polarization. Welz and Rosenberg investigated the electronic structure of stoichiometric tetragonal "FeS" and showed the density of states (DOS) does not follow the Stoner criterion for ferromagnetism. Attempts to calculate a ferromagnetic structure resulted in a vanishing magnetic moment, a consequence of a low DOS at the Fermi level. The authors also constructed a 3*d*-orbital splitting diagram for the pseudo-T_d symmetry and is similar to the one presented here; however, no investigation into the compositional dependence was discussed.[15] Finally, a recent investigation into the electronic structure of stoichiometric "FeS" showed a calculated nonmagnetic DOS inline with those previously determined. An investigation of the preferred magnetic ordering shows magnetic striping is the most energetically favorable, identical to the FeSe and FeTe systems as well. Again, the stoichiometry of the system was not investigated.[16]

Here, we present a theoretical assessment of the energetics involved in the inclusion of interstitial iron in $Fe_{1+x}S$ ($0 \leq x \leq 1$). First principles methods are employed to examine the significance of the additional Fe atoms on the stability of the phases and changes in electronic and magnetic structures that may follow.

8.3 Electronic Structure Calculations

Two theoretical methods were utilized to investigate the electronic structure of tetragonal "FeS" and $Fe_{1+x}S$. The Vienna *ab initio* simulation package (VASP)[17-20] was used to optimize the lattice parameters and atomic coordinates of each structural model, evaluate their total energies, and determine the relative total energies of various magnetic structures. The tight-binding, linear muffin-tin orbital method with the atomic-sphere

approximation (TB-LMTO-ASA)[21,22] was employed to analyze the electronic DOS curves and perform a pairwise population (chemical bonding) analysis using crystal orbital Hamilton populations (COHP).[23] The concurrent use of these programs allows us to gain an in-depth understanding of the electronic structure, magnetic ordering, and energetics governing the inclusion of an interstitial atom in the iron-sulfide framework.

VASP calculations were carried out on models of stoichiometric tetragonal "FeS" and the following supercell structures designed to consider different amounts of interstitial Fe content: $Fe_{1.019}S$ ($Fe_{55}S_{54}$), $Fe_{1.056}S$ ($Fe_{57}S_{54}$), $Fe_{1.063}S$ ($Fe_{17}S_{16}$), $Fe_{1.125}S$ (Fe_9S_8), $Fe_{1.250}S$ (Fe_5S_4), $Fe_{1.375}S$ ($Fe_{11}S_8$), $Fe_{1.50}S$ (Fe_3S_2), $Fe_{1.75}S$ (Fe_7S_4), and Fe_2S (Fe_4S_2). These cases were chosen to determine optimal interstitial positions and concentrations, as well as to evaluate chemical bonding features and magnetic structures. Full structural optimizations, which includes lattice parameters and atomic coordinates, using VASP version 5.2, were completed in a three-step process following program protocol[24] including spin-polarization on the compositions: "FeS," $Fe_{1.125}S$ (Fe_9S_8), $Fe_{1.250}S$ (Fe_5S_4), $Fe_{1.375}S$ ($Fe_{11}S_8$), $Fe_{1.50}S$ (Fe_3S_2), $Fe_{1.75}S$ (Fe_7S_4), and Fe_2S (Fe_4S_2). Similar optimizations of $Fe_{1.019}S$ ($Fe_{55}S_{54}$), $Fe_{1.056}S$ ($Fe_{57}S_{54}$), and $Fe_{1.063}S$ ($Fe_{34}S_{32}$) were not completed due to the size of the basis set for these large supercells. Instead, these structural models were constructed using the atomic positions determined by Berner and lattice parameters extrapolated from a linear fit of the optimized lattice parameters in iron-richer $Fe_{1+x}S$ cases, i.e., for $x \leq 0.50$. Here, a monotonic decrease in lattice parameters as x increases in this range provides a linear fit, which is used to determine the extrapolated unit cell parameters. It is worth noting that unit cells without an interstitial Fe atom expanded along the *c*-axis with optimization, as we have seen in the optimization of stoichiometric "FeS". Unit cells that contain an interstitial atom are contracted, closer to the parameters reported by Berner. This effect has been averaged out across the supercells in the extrapolated models. The unit cell parameters of all supercell models are listed in Table S1 of Supporting Information.

VASP calculations were performed using the projector augmented-wave (PAW) method of Blöchl[25] and adapted in VASP by Kresse and Joubert.[26] Exchange and correlation was described by the Perdew-Burke-Ernzerhof 96 generalized gradient

approximation (GGA-PBE).[27] To invoke spin-polarization, plane-wave eigenstates were computed for the "spin-up" (α) and "spin-down" (β) channels separately. Local magnetic moments, which are defined as the difference between the number of α and β electrons, were supplied prior to the electronic structure run. These initial moments were chosen to be larger than expected after convergence, i.e. initial $\mu_{Fe} = \pm 4.0$/per atom, to avoid falling into a local (paramagnetic) minimum of the energy landscape. After self-consistency has been achieved, local magnetic moments are obtained via the difference between the α and β electrons in an atom-resolved projection of the DOS. An 11×11×8 Monkhorst-Pack ***k***-points grid[28] was used to sample the first Brillouin zone for reciprocal space integrations. The energy cut-off of the plane wave basis was 400 eV. With these settings, the total energies converged to less than 2.5 meV per formula unit. The on-site potential, GGA+U, was not considered for these calculations. Previous studies using VASP on "FeS" have shown that due to delocalization of the *d*-electrons, considering the +U correction term provides inadequate structural optimizations.[29]

Further electronic structure calculations to analyze orbital interactions in various $Fe_{1+x}S$ structural models were also completed using the tight-binding, linear muffin-tin orbital method with the atomic-sphere approximation (TB-LMTO-ASA)[21,22] using the Stuttgart code.[30] TB-LMTO allows a pairwise population analysis using crystal orbital Hamilton populations (COHP).[23] In conjunction with a rigid band approximation, we can estimate changes in chemical bonding as a function of valence electron (VE) count.

The electronic structures of selected supercells were calculated using TB-LMTO-ASA with a large number of ***k***-points to obtain the DOS and –COHP curves. Stoichiometric "FeS" was modeled using space group *P*4/*nmm* whereas $Fe_{1.50}S$ (Fe_3S_2) was calculated using $P\bar{4}m2$ (no. 115). The rest of the compositions were modeled with the space group *Pmm*2 (no. 25). Exchange and correlation in LMTO were treated by the local density (LDA) and local spin density (LSDA) approximations. The hypothetical compositions of FeS, $Fe_{1.50}S$ (Fe_3S_2), $Fe_{1.25}S$ (Fe_5S_4), $Fe_{1.125}S$ (Fe_9S_8), $Fe_{1.063}S$ ($Fe_{34}S_{32}$) and $Fe_{1.037}S$ ($Fe_{56}S_{54}$) required, respectively, 4, 2, 5, 10 and 33 empty spheres (ES) per supercell to complement the atomic spheres. The Wigner-Seitz (WS) radii were held at 1.26-1.33 Å for Fe, 1.20-1.29 Å for S, and 1.15-1.46 Å for the empty spheres (ES) to

accommodate the LMTO overlap criteria. The basis set included Fe 4*s*, 4*p*, and 3*d* orbitals, S 3*s* and 3*p* orbitals, and ES 1*s* orbitals.

Additionally, the magnetic ordering of "FeS" was examined using two magnetically ordered models: (i) a checkerboard type arrangement; and (ii) a "striping" along the [110] direction. The checkerboard was calculated using $P\bar{4}m2$, in which the two Fe atoms in the unit cell of the square net were separated into two inequivalent sites, Fe1 at (0 0 0) and Fe2 at (½ ½ 0), allowing an antiferromagnetic checkerboard. The magnetic "striping" was calculated using a doubled unit cell, space group *Pccm*, with a = 5.20 Å and c = 5.06 Å, and two inequivalent Fe sites: Fe1 at (0 0 ¼) and Fe2 at (0 ½ ¼).

8.4 Composition and Bonding in Tetragonal Iron Sulfides

To gain better understanding of computational results on models of non-stoichiometric $Fe_{1+x}S$, a thorough evaluation of the electronic DOS, chemical bonding, and magnetic ordering of stoichiometric "FeS" is warranted. Because structural characterization of these iron sulfide phases is limited[9,11] and remains controversial, as mentioned above, structural optimization using VASP was first conducted on a hypothetical, stoichiometric, tetragonal "FeS" as a benchmark for investigation of $Fe_{1+x}S$.

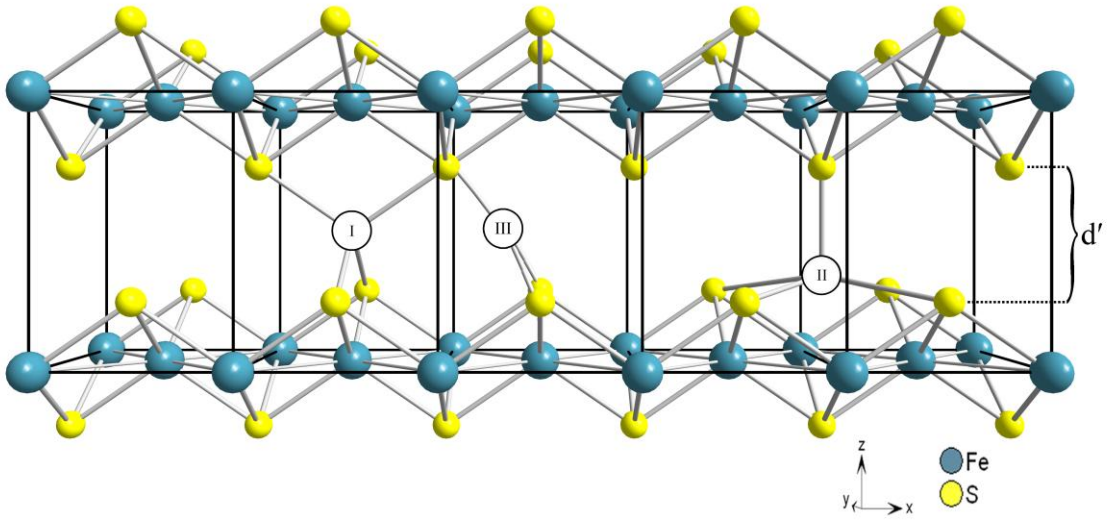

Figure 1. (010) projection of tetragonal, stoichiometric "FeS" with the distance between layers across the van der Waals gap labeled as *d′*. Three possible sites for interstitial Fe atoms are noted (see text for further discussion); the preferred site was determined to be position I.

8.4.1 Stoichiometric "FeS". The lattice parameters, a = 3.679 Å, c = 5.047 Å, and atomic positions originally reported by Berner were used as the starting point for VASP optimizations even though the original report noted the presence of excess iron.[9] The initial structure has an interlayer separation (d') of 2.523 Å while the Fe-S and Fe-Fe distances, respectively, are 2.231 Å and 2.601 Å. The interlayer S-Fe-S angles are 111.11° and 108.66°, values slightly distorted from an ideal tetrahedron. After optimization, the lattice parameters move to a = 3.580 Å, c = 5.651 Å and a unit cell volume of 72.49 Å^3, 6% larger than reported by Berner. The coordinates of sulfur shifted from (0, ½, 0.25) to (0, ½, 0.229). The distance (d') between the layers of sulfur atoms increased to 3.063 Å, while the Fe-S (2.209 Å) and Fe-Fe (2.531 Å) distances decreased. The c/a ratio during optimization increased from 1.372 to 1.578, showing a dramatic increase in the van der Waals gap when an interstitial atom is excluded explicitly. One should note that DFT-based methods can result in poor optimization of layered structures. For instance, the predicted c-lattice parameters in β-MoS_2 and $NbSe_2$ are overestimated, respectively, by ca. 20% and 10%.[31] However, implementing the DFT-D2 approach described by Grimme[32] can account for these weak dispersion forces. By applying DFT-D2 to tetragonal "FeS" a dramatic underestimation of the c-lattice parameter and a 10% decrease of the volume with respect to Berner's original report are observed. Since the dispersion terms result in an underestimation volume and excluding these terms increases the volume relative to the original report, an improved structural model was sought. Accounting for interstitial Fe by optimizing $Fe_{1.25}S$ should provide a better model for this system and were therefore calculated using DFT and DFT-D2. The average unit cell volumes are 68.83 Å^3 and 61.09 Å^3 for the respective codes. The optimized volumes of $Fe_{1.25}S$ differ by less than 0.01% using DFT and 10% using DFT-D2. Since Berner's original structure included the presence of interstitial iron, the models disregarding the dispersion correction provide better agreement with this experimental result than those including this energy term. Therefore, we employ optimized lattice parameters from DFT results for further examination of the electronic structure of "FeS" and $Fe_{1+x}S$.

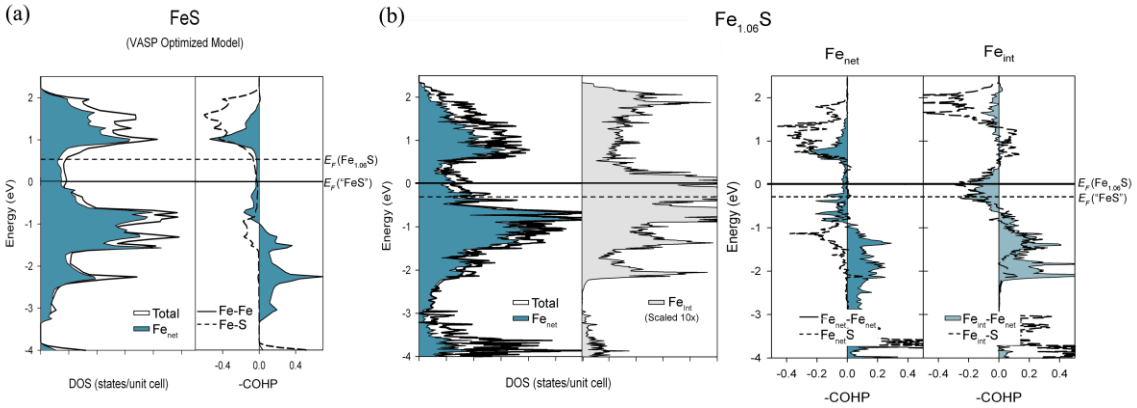

Figure 2. (a) Total spin polarized DOS, spin polarized Fe partial DOS, Fe-Fe –COHP, and Fe-S –COHP for "FeS". The solid line in the DOS is E_F for "FeS", the dashed line corresponds to a rigid band E_F for $Fe_{1.06}S$. (b), left to right, Total non-spin polarized DOS (white), Fe_{net} partial DOS (blue), Fe_{int} partial DOS, Fe_{net}-Fe_{net} –COHP, Fe_{net}-S –COHP, Fe_{net}-Fe_{int} –COHP, Fe_{int}-S -COHP. The solid line in the DOS is E_F for $Fe_{1.06}S$ and the dashed line corresponds to a rigid band E_F for "FeS"

The DOS curves for optimized tetragonal "FeS," the part of which that arises mostly from Fe 3*d* orbitals, are illustrated in Figure 2, were calculated using TB-LMTO. A deep pseudogap is present from 0.5 eV below to 1.0 eV above the Fermi level (E_F = 0 eV) for 14 valence electrons per formula unit (VE/f.u.). The DOS exhibits two distinct regions: (1) states between −6 and −4 eV, shown in Figure S1 of Supporting Information, arise primarily from the sulfur 3*p* orbitals with contributions from Fe 3*d* and 4*p* wavefunctions; and (2) states between −3 and +2 eV composed almost entirely of Fe 3*d* orbitals. This second band shows two distinct peaks, separated by the above-mentioned pseudogap, and arises from both Fe-S ligand field splitting of the Fe 3*d* orbitals as well as Fe-Fe 3*d*-3*d* orbital interactions within the square net of Fe atoms. These Fe-Fe interactions split the lower peak into a ca. 1 eV broad region that shows Fe-S antibonding character and a narrow peak that is Fe-S nonbonding, but strongly Fe-Fe bonding. The nearly 1 eV gap between regions (1) and (2) in the electronic DOS curve allows the iron atoms to be formally Fe^{2+} ($3d^6$). It is interesting to note that although the Fermi level of tetragonal "FeS" falls in a wide and deep pseudogap, leading one to believe it is structurally favorable, the ground state structure is actually hexagonal, i.e., the mineral

troilite. In hexagonal FeS, Fe atoms occupy octahedral holes within a distorted close packing of sulfide ions and shift to form triangular clusters.

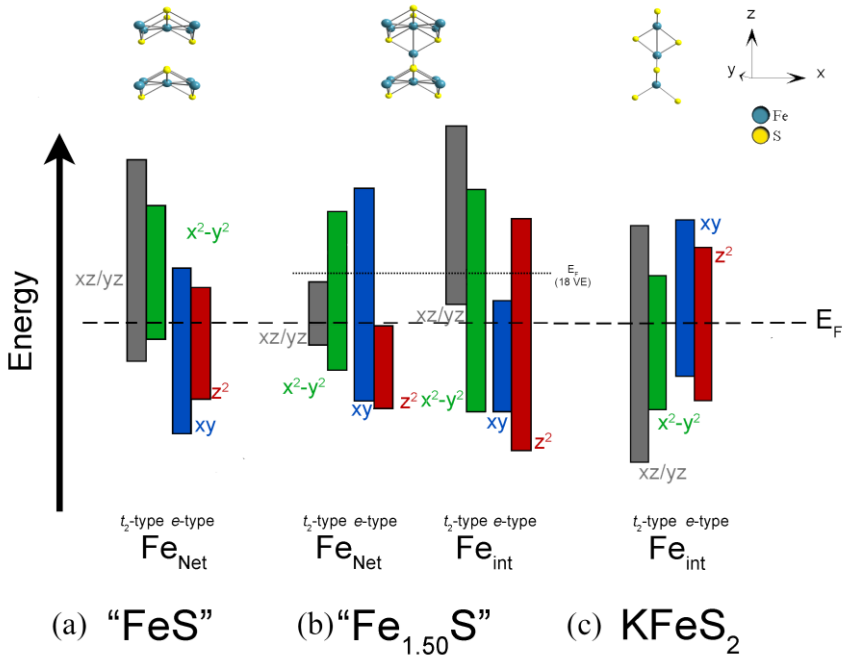

Figure 3. Bandwidth diagrams for different 3*d* orbitals at Fe atoms in "FeS" (left), $Fe_{1.50}S$ (center), and polymeric $KFeS_2$ (right).[33] All Fe atoms are nearly tetrahedrally coordinated by S atoms, so the 3*d* orbitals are separated into *e*-type and t_2-type, based on the local coordinate system. Also, although the *xz* and *yz* orbitals in $KFeS_2$ are not strictly degenerate, they are illustrated as such for clarity.

Within the tight-binding approximation, the DOS can be decomposed into local orbital contributions. Such an analysis in $Fe_{1+x}S$ is useful to determine how the Fe 3*d* orbitals and their interactions within the square nets ("Fe_{net}"), which affect their location and dispersion in the DOS curves, are affected by the addition of interstitial iron atoms ("Fe_{int}"). This decomposition of the "FeS" band structure at the Γ and M points was used to create a bandwidth diagram for each set of Fe 3*d* orbitals, using the coordinate system shown in Figure 3a. The pseudo-tetrahedral splitting of the Fe 3*d* orbitals by the sulfide ligands assigns the *e* orbitals as *xy* and z^2 and the t_2 orbitals as *xz*, *yz*, and $x^2–y^2$. Through-space Fe-Fe orbital overlaps vary from σ (*xy*) to π ($x^2–y^2$) to π/δ (*xz*, *yz*) to δ/σ (z^2). Among the *e* levels, the *xy* band is broad extending above E_F while the z^2 band is narrow, remaining just below E_F. The top of the *xy* band becomes Fe-Fe σ-antibonding and is

pushed above E_F, while σ-overlap between adjacent Fe z^2 orbitals is small, so this band remains narrow and fully occupied. On the other hand, all three t_2 orbitals show similar bandwidths but the center of the $x^2–y^2$ band lies below that of the degenerate (*xz*, *yz*) band, an effect arising from a combination of both Fe-S-Fe through-bond coupling and direct Fe-Fe through-space orbital overlap. The bottom of the exclusively π-bonding $x^2–y^2$ band drops below E_F. This suggests that the pseudogap contains the top of the *xy*-band, which is mostly σ-antibonding and the bottom of the $x^2–y^2$ band, which is mostly π-bonding. The limits of the pseudogap region are largely dictated by the top of the z^2 band at low energy and the bottom of the (*xz*, *yz*) band at high energy.

An analysis of the nearest neighbor Fe-S and Fe-Fe orbital interactions using –COHP curves, Figure 2, reinforce the description of the Fe 3*d* bands. In the pseudogap region, Fe-S and Fe-Fe –COHP curves register nearly nonbonding interactions, although both curves show some antibonding character among the occupied levels below E_F. The Fe-Fe nearest neighbor COHP curve exhibits a crossover from bonding to antibonding states at 12 VE/f.u. (ca. −0.9 eV), whereas optimized Fe-S orbital interactions occur at 10.4 VE/f.u. (ca. −1.4 eV). Fe-S bonding states end at the top of the largely sulfide 3*p* band (region 1 in the electronic DOS curve), which would correspond to 8 VE/f.u. The bottom 1.6 eV of the Fe 3*d* band (region 2) is strictly Fe-S nonbonding due in large part to symmetry restrictions of the Fe-Fe orbital interactions in this energy range. The states just below E_F are weakly Fe-S antibonding, arising from largely Fe-S π-antibonding overlap associated with the Fe-centered *e* orbitals of the tetrahedral field of the π-donor sulfide ligands. Well above E_F and just above the pseudogap in the DOS curve, these Fe-S interactions become strongly antibonding, likely corresponding to the σ-antibonding orbitals of the tetrahedral field. Regarding Fe-Fe interactions, much of the lower peaks of region 2 in the DOS show significant bonding overlap. The weakly antibonding orbitals ranging ca. 1 eV below E_F arise from a competition between σ- and δ-antibonding levels of the *e* orbitals and π-bonding levels of the t_2 orbitals. At the pseudogap, these interactions nearly cancel one another.

8.4.2 Non-stoichiometric $Fe_{1+x}S$. According to the DOS and –COHP curves of stoichiometric "FeS," the Fermi level falls in the middle of a pseudogap that is largely Fe-S and Fe-Fe nonbonding. Therefore, this structure can tolerate additional valence electrons without disrupting the two most significant orbital interactions. It is interesting that naturally occurring samples of the mineral mackinawite are known to contain small amounts of Cr, Ni, and Cu, indicative of this structure's desire to contain more than 14 valence electrons.[34]

In this case, we selected Fe as the interstitial atom based on the previous experimental reports citing Fe-rich compositions for tetragonal $Fe_{1+x}S$. This addition of interstitial Fe creates two independent types of iron: Fe occupying the square-net (Fe_{net}) and the interstitial Fe (Fe_{int}). We began our theoretical analysis of nonstoichiometric $Fe_{1+x}S$ by identifying the most energetically favorable sites for Fe_{int} atoms in tetragonal "FeS". Interstitial positions were identified based on Fe_{int}-S and Fe_{int}-Fe_{net} distances as well as with the calculation of a potential energy surface. This energy surface was constructed using Berner's lattice parameters as the starting point and dividing the (010) plane of the unit cell into a 10×10 grid. A Fe atom was placed at each grid point, and the total energy was calculated and plotted in Figure 4. Although the tetragonal symmetry of "FeS" can restrict surveying interstitial space to $¼ \le y \le ½$, placing Fe atoms in positions with a *y*-coordinate other than $y = ½$ creates Fe-S distances that are much shorter than 2.23 Å. The contour plot suggests three possible interstitial locations with (I) tetrahedral, (II) square pyramidal, and (III) trigonal planar sulfur coordination (see Figures 1 and 4). Position I sits at (½ ½ ½) in a distorted tetrahedral sulfur environment with four Fe_{int}-S distances of 2.23 Å. This location connects two adjacent square nets of Fe atoms by forming a linear Fe_{net}-Fe_{int}-Fe_{net} trimer along the *c*-direction with each Fe_{net}-Fe_{net} bridged by two S atoms. Position II is located at (0 ½ 0.343) in a square pyramidal environment with Fe_{int}-S distances 2.23-2.60 Å. The Fe_{int} atom bridges four Fe_{net} atoms within a single square-net, but does not directly connect Fe atoms in adjacent slabs. Additionally, the Fe_{int} location can be viewed as weakly coordinated by one next nearest neighbor sulfur atom to complete a pseudo-octahedral environment with a long Fe-S distance of 3.21 Å. Position III, near (⅓ ½ 0.415), is highest in energy among the three interstitial

positions with relatively short Fe_{int}-S distances of ca. 2.1 Å. Bronger *et al.*[33] reported a range of Fe-S distances in the ternary sulfides, $AFeS_2$ (A = K, Rb), to be 2.231-2.246 Å. Although the oxidation state of Fe in these compounds is 3+, they are rare examples of Fe atoms tetrahedrally coordinated by sulfide ligands. Thus, positions I and II fall near these experimentally reported bond lengths whereas position III is much shorter.

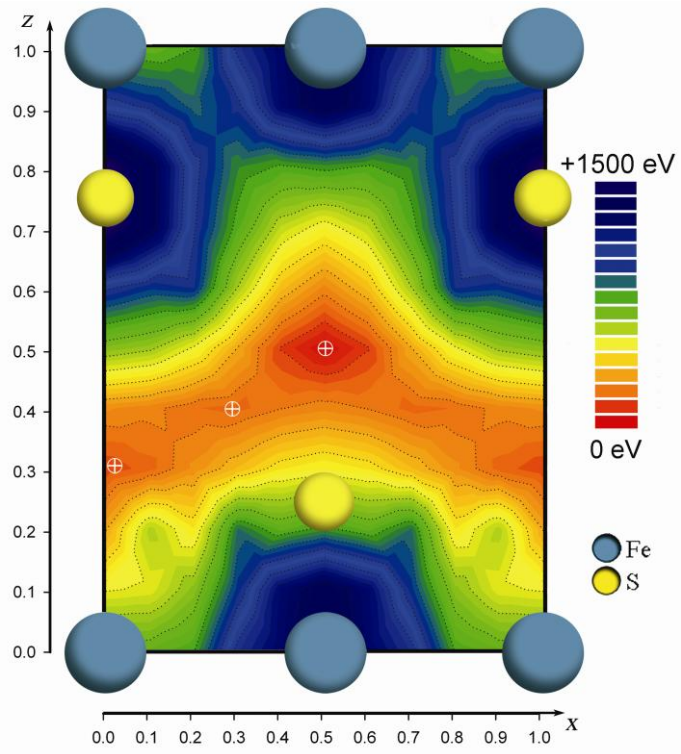

Figure 4. Contour plot of the potential energy surface for locating interstitial Fe atoms in the y = ½ plane of "FeS." Energies are given in a logarithmic scale and are presented relative to the interstitial site with lowest potential energy, site I (see also Figure 1). The three possible coordination environments are identified by a ⊕: I, tetrahedral; II, square pyramidal; and III, trigonal planar. Positions I and II are the most favorable ones.

Table 1. Optimized structural parameters for tetragonal "FeS" and the three models of $Fe_{1.50}S$, which includes an interstitial Fe atom, designated as Fe_{int}.

	Position I	Position II	Position III	No Interstitial
a (Å)	3.654	3.549	3.679	3.580
c (Å)	5.116	5.422	5.047	5.651
V (Å^3)	68.31	68.30	68.31	72.49
c/*a* ratio	1.406	1.528	1.371	1.578
(*x y z*) of Fe_{int}	(½ ½ ½)	(0 ½ 0.343)	(⅓ ½ 0.415)	----
Fe_{net}–S (Å)	2.17	2.17	2.23	2.21
Fe_{int}–S (Å)	2.29	2.32-2.59	2.09-2.11	----
Fe_{net}–Fe_{int} (Å)	2.56	2.57	2.18	----
Δ*E* (eV)	0	+1.27	+7.77	----

The three sites identified were energetically optimized to evaluate atomic positions, lattice parameters, and unit cell volumes; the resulting optimized parameters along with those for tetragonal "FeS" are presented in Table 1 and pointed out in Figure 1. When the Fe_{int} atom was located at Position III, all attempted optimization steps resulted in the interstitial relaxing to Position I. Therefore, to calculate the total energy for an interstitial Fe at Position III the lattice parameters reported by Berner were used and a static calculation was performed. In the optimization of site I and II, the presence of an interstitial Fe atom reduced the *c*-parameter and the *c*/*a* ratio compared to "FeS". The calculated trend in total energies follows the trend Position I < Position II << Position III. This is contrary to $Fe_{1.068}Te$, in which an interstitial Fe was determined to occupy the square pyramidal site (Position II) using neutron powder diffraction.[13] However, calculating the potential energy surface of iron telluride (Figure S2 in Supporting Information) in the same manner as the sulfide shows the lowest energy point occurs near Position II, in agreement with experiment. The change in site preference can be justified by the sizes of the van der Waals gaps (*d*′), a value that is 0.20 Å wider in $Fe_{1.068}Te$ than in Berner's $Fe_{1+x}S$; placing Fe atoms in interstitial Position I of FeTe would give Fe_{int}-Te and Fe_{int}-Fe_{net} bond lengths of 2.31 Å and 3.12 Å, respectively.

These values are relatively short for the Fe_{int}-Te and long for the Fe_{int}-Fe_{net} interactions. When Fe_{int} atoms are located at Position II in the telluride, these distances are 2.51-2.68 Å and 2.75 Å, both of which are in much better agreement with other experimental values of these distances.[13,35,36] Consequently, the selected location stems from the ability of the Fe_{int} atom to optimize bonding with both the chalcogenide ligands as well as near neighbor Fe atoms.

To examine the energetics of adding Fe atoms to tetragonal "FeS" the inclusion of Fe_{int} atoms in Position I was modeled for various $Fe_{1+x}S$ compositions. The energy differences were evaluated following Equation 1:

$$FeS_{(Tet)} + x\ Fe_{(BCC)} \longrightarrow Fe_{1+x}S \qquad (1)$$

$Fe_{(BCC)}$ (body-centered cubic iron) and $FeS_{(Tet)}$ (stoichiometric "FeS") were modeled using VASP optimized parameters. To consider various interstitial concentrations, supercells of $Fe_{1+x}S$ were constructed and optimized as described above.

The total energy differences following Equation 1 versus interstitial Fe mole fraction (x) are plotted in Figure 5a. The right side of Equation 1, i.e. $Fe_{1+x}S$, is energetically favored for $x < 0.30$. We can rationalize the incorporation of interstitial iron at low concentrations based on an analysis of the electrostatic interactions occurring within the van der Waals gap. These electrostatic interactions are described by the Madelung energy ($E_{Madelung}$) and are calculated using the Ewald Method with the charge at each site determined using Bader's charge analysis scheme (average charges provided in Table S3 of Supporting Information).[37-39] The addition of Fe_{int} in the van der Waals gap introduces attractive Fe_{int}-S forces that diminish the repulsive forces between adjacent sulfide layers. In fact, the $E_{Madelung}$ shows a 167 % decrease in energy, from –3.11 eV/f.u for "FeS" to –6.76 eV/f.u. for $Fe_{1.063}S$. The further addition of Fe_{int} from $Fe_{1.063}S$ to $Fe_{1.50}S$ results in only a ca. 30% decrease in $E_{Madelung}$ over this entire range. Such a large initial change in the $E_{Madelung}$ drives the incorporation of an interstitial Fe at low mole fractions and becomes less energetically favorable at higher x values.

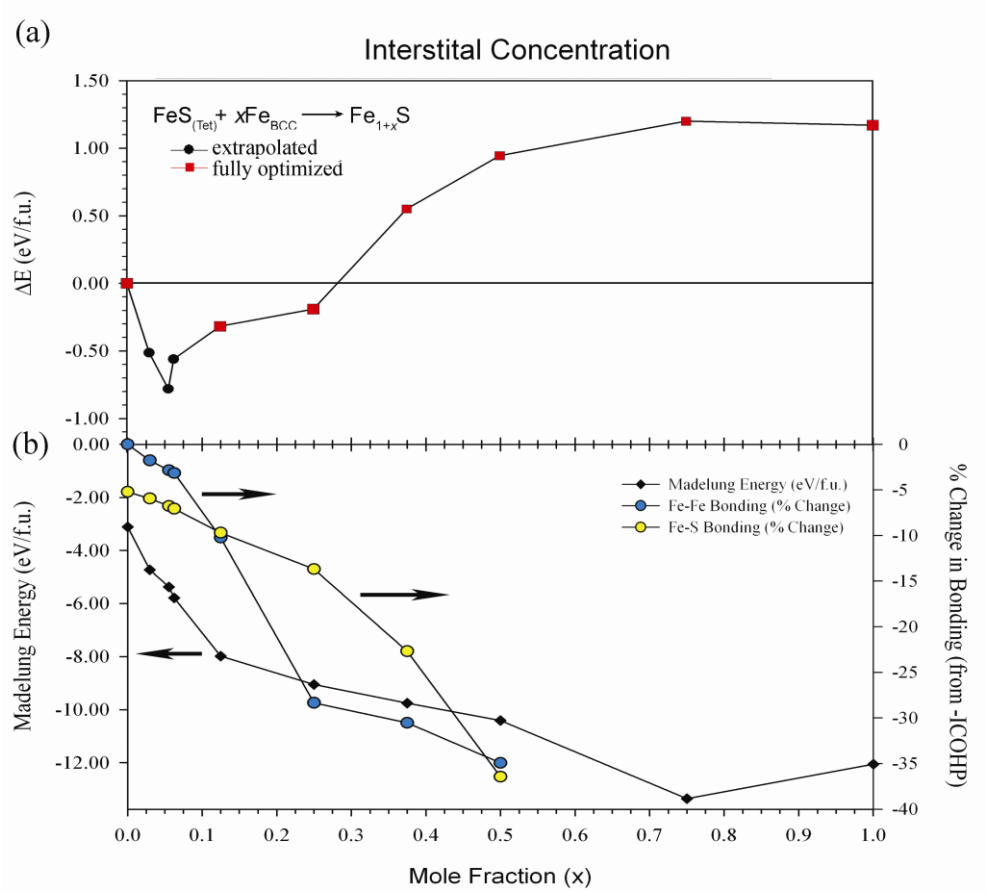

Figure 5. (a) Total energy differences between $Fe_{1+x}S$ and tetragonal "FeS" + bcc Fe vs. composition *x*. The red squares correspond to the values obtained by optimizing all structures; the black circles correspond to structures of $Fe_{1+x}S$ constructed by extrapolation of optimized structures. (b) The calculated Madelung energies (black dots), and the average percent changes in Fe_{net}-Fe_{net} (blue circles) and Fe_{net}-S (yellow circles) interactions as determined from the –ICOHP values, each as a function of interstitial Fe content (*x*).

Analysis of the $Fe_{1.06}S$ electronic structure utilized a $2a \times 2b \times 4c$ superstructure of the tetragonal FeS unit cell with two Fe atoms placed in interstitial tetrahedral holes (Position I). As mentioned above, these interstitial Fe atoms form connections along the [001] direction with the Fe_{net} atoms in two adjacent layers. Two models of $Fe_{1.06}S$ were constructed altering the arrangement of the interstitial atoms. The first contained only Fe_{net}-Fe_{int}-Fe_{net} (metal trimers) connections and the second contained Fe_{net}-Fe_{int}-Fe_{net}-Fe_{int}-Fe_{net} (metal pentamers) connections (see Figure S5 in Supporting Information). The total energies calculated by VASP shows that the model containing trimers is –92 meV

lower than the pentamers, making the trimers the most energetically favorable arrangement for the interstitial atoms. The DOS for $Fe_{1.06}S$ using the trimer model, shown in Figure 2b, contains a pseudogap at the Fermi level, similar to "FeS." The states above +0.50 eV result from both the square-net and the interstitial atoms whereas below the Fermi level (–0.25 to –1.50 eV), the states are almost exclusively from the Fe_{net} sites. Although the pseudogap remains present, upon closer examination of this energy region, there is a small peak arising from Fe_{int} orbitals at E_F. Such peaks in DOS curves are often indicative of potential electronic instabilities, which, in conjunction with an antibonding orbital at the Fermi level in the –COHP curves has been shown to result in ferromagnetic ordering.[40,41] The total spin-polarized DOS for the supercell models are provided in Figure S3 of Supporting Information.

A COHP analysis of Fe_{net}-S shows a loss of the nonbonding region present in "FeS" between –3.5 and –2.2 eV compared to "FeS." The Fe_{net}-S interaction is antibonding through the entire energy range shown. A qualitative comparison of the –COHP curves shows only minor changes from "FeS", a result that closely follows the rigid band approximation for the addition of electrons to the electronic DOS of "FeS." With the addition of a Fe_{int} atom, the Fe_{net}-Fe_{int} –COHP curve shows a sharp antibonding peak at E_F. Along with the sharp Fe_{int} peak in the DOS, a –COHP curve that is antibonding at the Fermi level is predictive of ferromagnetic ordering between the Fe_{net} and the $Fe_{int.}$[40,41]

A comparison of the partial DOS and –COHP curves from "FeS" and $Fe_{1.06}S$, Figures 2a and 2b, reveals only minor differences between these curves. In fact, comparing the DOS of the supercells (Figure S2), shows the presence of a pseudogap remains to compositions near $Fe_{1.25}S$. This fact allows the rigid band approximation in "FeS" to be applied for compositions up to ca. x = 0.25, regardless of ignoring interactions between the interstitial atom and its surroundings.

The bandwidth diagram, Figure 3b, summarizes the effects of these orbital interactions in $Fe_{1.50}S$, which effects the 3*d* blocks of the Fe_{net} and Fe_{int} atoms. Two Fermi levels are noted, a computed E_F for $Fe_{1.50}S$ (18 valence electrons per f.u.); and an E_F estimated from the rigid band approximation for $Fe_{1.06}S$ (14.5 valence electrons per

f.u.) based on results discussed in the subsequent paragraphs. According to this diagram, the tetrahedral ligand field splitting patterns of the 3*d* orbitals at both Fe_{net} and Fe_{int} are less apparent than in "FeS," an effect which is due to both through-space Fe_{net}-Fe_{int} and through-bond Fe_{net}-S-Fe_{int} interactions. For example, the *e*-type z^2 band is energetically broad due to through-space Fe_{net}-Fe_{int} σ-overlap, and the t_2-type $x^2–y^2$ band, which has through-space Fe_{net}-Fe_{int} δ-overlap, broadens due to both through-bond Fe_{net}-S-Fe_{int} coupling and symmetry-allowed mixing with *e*-type z^2 orbitals. In these two cases, the bottom of the z^2 band exhibits significant Fe_{net}-Fe_{int} σ-bonding overlap, while the bottom of the $x^2–y^2$ band loses Fe-S antibonding character. Such effects are seen in $KFeS_2$,[33,42] whose bandwidth diagram is included in Figure 3c for comparison. The outcome of this complex combination of interactions is attractive orbital interactions between the Fe_{int} atoms and the [Fe_{net}S] networks for low Fe_{int} content, which increasingly destabilizes upon increasing Fe_{int} content.

The –ICOHP values in Figure 5b for the Fe_{net}-S and Fe_{net}-Fe_{net} interactions were determined from a rigid band approximation of stoichiometric "FeS". Decreases in bonding indicate the occupation of antibonding states with increasing interstitial content in $Fe_{1+x}S$. For instance, x = 0.125, which is equivalent to adding one valence electron to "FeS", the –ICOHP value for the Fe_{net}-Fe_{net} interaction decreases by ca. 10% from its value in "FeS," whereas the Fe_{net}-S interaction decreases by 5%. Above x = 0.30, an interstitial Fe atom is no longer energetically favorable compared to "FeS" and BCC Fe, as seen in Figure 5a, due in large part to the significant loss in Fe_{net}-S and Fe_{net}-Fe_{net} bonding. The Fe_{net}-Fe_{net} and Fe_{net}-S –COHP curves for $Fe_{1.50}S$ (x = 0.50), presented in Figure S4 Supporting Information, show crossovers from (non)bonding to antibonding states fall, respectively, at ca. 14.5 and 16.5 valence electrons, which correspond to the respective compositions $Fe_{1.06}S$ and $Fe_{1.31}S$. Thus, electrostatic interactions favor the inclusion of interstitial Fe atoms while the concomitant filling of antibonding states involving the network Fe and S atoms sets an upper limit on the interstitial Fe content.

In summary, the addition of interstitial Fe atoms is a compromise between the attractive Fe_{int}-S interactions (and to a lesser extent, attractive Fe_{net}-Fe_{int} interactions), and limiting the occupation of antibonding states. The addition of Fe_{int} provides electrons to

the system that ultimately occupy Fe_{net}-Fe_{net} and Fe_{net}-S antibonding states when the Fe_{int} content becomes too large, an effect that destabilizes the overall $Fe_{1+x}S$ structure.

8.5 Magnetic Ordering

Although one can predict ferromagnetic ordering between the Fe_{int} and the Fe_{net} based on the partial DOS and the –COHP curve, as described above, this analysis cannot be used to describe long-range magnetic ordering. For this determination, multiple magnetic structural models were calculated using VASP for stoichiometric "FeS" and $Fe_{1.06}S$. One model is ferromagnetic, the second model is an antiferromagnetic, checkerboard pattern; and the third is an antiferromagnetic, striped pattern. The models are illustrated in Figure S6 of supporting information. The lowest energy model was determined from a VASP total energy calculation, while the relative total energies are reported in Table 2 with respect to the lowest energy model (striped).

Table 2. Relative total energies (in eV/f.u.) of magnetic models of $Fe_{1+x}S$ with respect to the lowest energy model. In $Fe_{1.06}S$, Checkerboard-1 has Fe_{net}-Fe_{int} antiferromagnetically coupled, whereas Checkerboard-2 has Fe_{net}-Fe_{int} ferromagnetically coupled.

	Relative total Energy (meV/f.u.)	
	"FeS"	$Fe_{1.06}S$
Striped	0	0
Checkerboard-2	+55.6	+84.9
Checkerboard-1	----	+102.3
Ferromagnetic	+176.2	+148.7

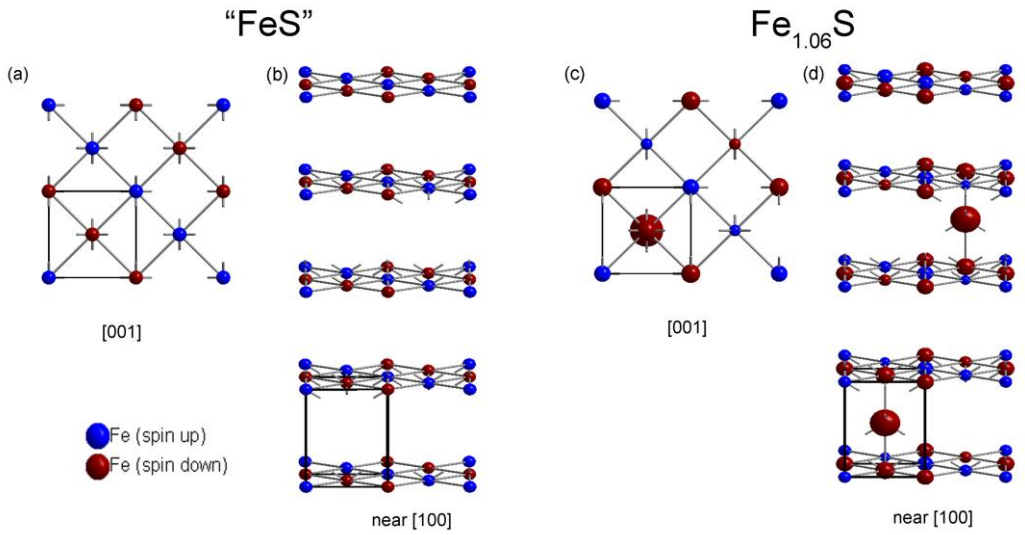

Figure 6. Preferred magnetic ordering of stoichiometric FeS and $Fe_{1.06}S$, as determined by VASP calculations. (a) and (c) illustrate [001] projections of a single plane of Fe_{net} atoms; (b) and (d) are projections nearly along the [100] direction. The sphere size is proportional to the relative magnetic moment on each atom. Sulfur atoms are omitted for clarity and a single unit cell is shown in each supercell. See Table 4 for further details concerning (c) and (d).

The most energetically favorable model for "FeS" exhibits antiferromagnetic order along the [110] direction and ferromagnetic ordering along the [001] direction, forming a "striped" magnetic pattern, shown in Figures 6a and 6b. This pattern was also previously determined theoretically to be the most energetically favorable structure for FeS using the CASTEP code,[16] and for FeSe, by implementing the WIEN2K package.[43] Experimentally, low temperature electron diffraction measurements on FeSe show changes in symmetry that result in the presence of the "striping" pattern; however, an effective magnetic moment was not determined in this case.[8]

The local moments residing on the Fe_{net} atoms in the striped "FeS" model are $\pm 1.51\ \mu_B$/Fe for Berner's structure and $\pm 1.21\ \mu_B$/Fe for the computationally optimized structure, which are smaller than those previously calculated in FeSe and FeTe. Although the values of these calculated moments may be imprecise because they are determined using LSDA, trends can still be inferred about the relative magnitudes and signs of moments on inequivalent magnetically active sites. For example, the smaller local moments in "FeS" compared to FeSe and FeTe are the result of greater Fe-Fe

through-space and Fe-S through-bond orbital overlaps within the [$FeS_{4/4}$] layers. The Fe-chalcogenide distances are shortest in "FeS" (2.23 Å), intermediate in FeSe (2.38 Å), and longest in FeTe (2.59 Å).*

The addition of interstitial Fe atoms to the $2a \times 2b \times 4c$ superstructure of "FeS," simulating the stoichiometry "$Fe_{1.06}S$", Figures 6c and 6d, maintains antiferromagnetic ordering along the [110] and ferromagnetic coupling along the [001] directions, as calculated for "FeS". For $Fe_{1.06}S$, two checkerboard patterns at the Fe_{net} sites were examined based on the coupling between the Fe_{int} site and the two neighboring Fe_{net} sites. The first checkerboard model antiferromagnetically couples the Fe_{int}-Fe_{net} interactions; and the second ferromagnetically couples the Fe_{int}-Fe_{net} interactions. Both models are higher in energy than the striped pattern (see third column of Table 2). The checkerboard-2 with a ferromagnetic interaction between Fe_{int}-Fe_{net} is lower in energy than checkerboard-1. This result is in agreement with the –COHP curve, which predicts a ferromagnetic interaction between the two atoms. The magnetic moment on the interstitial atom in $Fe_{1.06}S$ acquires the largest magnetic moment of 2.36 μ_B, similar to the FeTe system.[44] For example, the interstitial Fe sites in $Fe_{1.125}Te$ has a larger moment (2.4 μ_B/Fe) than the Fe atoms of the square net (1.6-1.8 μ_B/Fe), as calculated using VASP.[45] Neutron powder diffraction on $Fe_{1.068}Te$ confirms the magnetic moment of 2.25(8) μ_B/Fe, while revealing a double-striped magnetic ordering.[13]

* The magnetic moment calculated using TB-LMTO for the striped pattern was effectively quenched at ±0.0003 μ_B, a value in sharp contrast with the results of VASP. Moments for FeTe were calculated using VASP, so we adopt these values for comparison.

Table 3. Calculated local moments at various Fe sites in the "striped" pattern of $Fe_{1.06}S$. See also Figures 6c and 6d.

Site	Distance to Fe_{int} (Å)	Number of Neighbors	Moment (μ_B)
Fe_{int}	---	---	+2.36
$Fe_{net}(1)$	2.52	2	+1.90
$Fe_{net}(2)$	3.62	4	+1.84
$Fe_{net}(3)$	3.62	4	–1.75
$Fe_{net}(4)$	4.46	8	–1.68
$Fe_{net}(5)$	5.78	8	+1.70

The magnitudes and signs of local moments on surrounding the interstitial atom were investigated for the lowest energy magnetic structure of $Fe_{1.06}S$, and are summarized in Table 3. Our model contains five distinct Fe_{net} atoms whose magnetic moments decrease with distance from the interstitial atom. Interestingly, $Fe_{net}(3)$ atoms that are antiferromagnetically ordered to the interstitial atom exhibit a smaller magnetic moment than $Fe_{net}(2)$ atoms that are ferromagnetically coupled despite equal distances from Fe_{int}. This outcome likely stems from magnetic frustration in the model with an energetic drive to order ferromagnetically with the Fe_{int} site. The higher energy models of $Fe_{1.06}S$ listed in Table 2 show similar effects for the local moments, i.e. high values at Fe_{int} and decreasing values at Fe_{net} with distance from Fe_{int}. Again, even though the magnitudes of the calculated and experimental magnetic moments will likely differ, a large magnetic moment should certainly develop at the interstitial Fe atom, and, in turn, increase the moments on the nearest neighbor Fe atoms, i.e., Fe_{net} sites. The result is the formation of nonzero magnetization in $Fe_{1.06}S$, which would likely prevent superconductivity in $Fe_{1+x}S$. Therefore, achieving 1:1 stoichiometry in this iron sulfide phase, as well as in $Fe_{1+x}Se$ and $Fe_{1+x}(Te_{1-y}Se_y)$, appears imperative to suppress magnetic ordering and possibly achieve superconductivity.

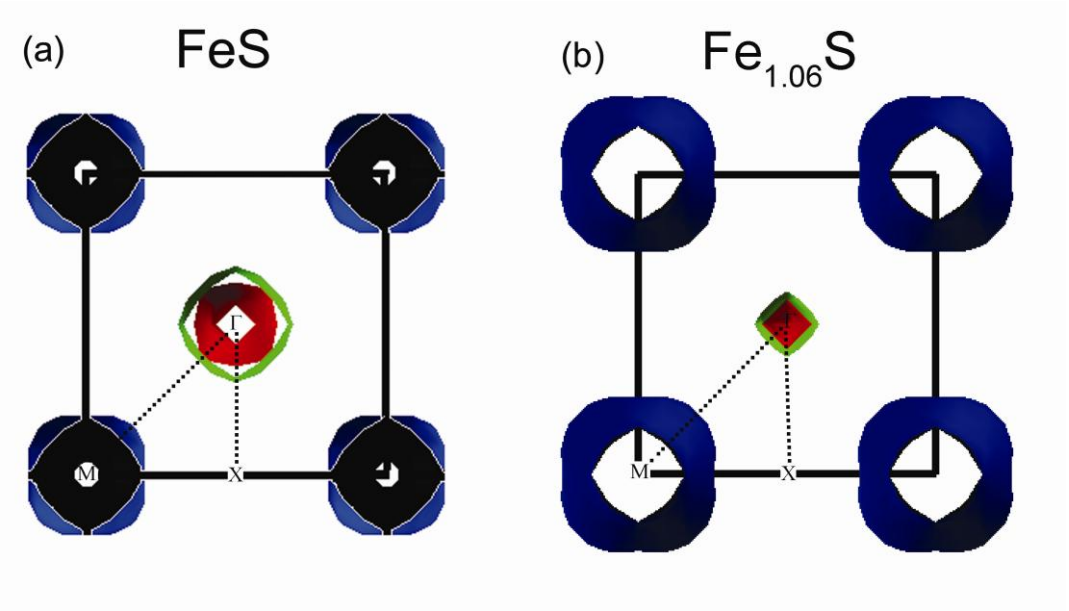

Figure 7. Fermi surface of (a) stoichiometric FeS and (b) $Fe_{1.06}S$ (from a rigid band approach) as viewed down the ***c**** axis of reciprocal space. The projection of the first Brillouin zone is emphasized with the special points labeled.

The calculated Fermi surface for "FeS," Figure 7a, shows two intersecting cylindrical electron surfaces at the zone center (Γ point) offset by two hole sections at the M points of the zone edge. The corresponding "FeS" band structure diagram is provided in Figure S7 of Supporting Information. These Fermi surfaces are very similar to those calculated for FeSe and FeTe.[15] In "FeS", a possible (π, π) nested vector connects the Γ and M points, as long as the vector magnitude is same size. Interestingly, a (π, π) nested vector is also consistent with the magnetic striping along [110] direction.[14,46] The addition of excess Fe using a rigid band approximation changes the topology of the Fermi surface, particularly at the Γ point. $Fe_{1.06}S$ shows a combination of a square topology at the zone center (Γ) and an increase in the size of the cylinder at the zone corner (M), destroying the possibility of a nested vector in $Fe_{1.06}S$. Adding just 6 atomic percent of Fe as an interstitial results in a major perturbation of the Fermi surface and destroys any mechanism for superconductivity. This proves the need for careful synthesis to prevent non-stoichiometry so that one may achieve the desired physical properties.

8.6 Conclusions

Many publications report conflicting evidence for the concentration of interstitial Fe within the tetragonal structure of $Fe_{1+x}S$.[3] The computational study using first principles methods, reported herein, explores the energetic and structural implications of placing interstitial Fe atoms in the van der Waals gap of a stoichiometric, tetragonal "FeS". The analysis shown in Figures 4 and 5 signifies that a concentration of interstitial iron ranging from ca. 0-30 atomic percent is favorable, with the preferred sites being tetrahedral voids in the van der Waals gap. This outcome for iron sulfide is different for the analogous selenide and telluride. Analysis of electronic structures indicated that the preferred compositions of interstitial Fe in $Fe_{1+x}S$ are driven by a compromise between the Madelung energy and the occupation of Fe-S and Fe-Fe antibonding states. An investigation of the magnetic ordering upon the addition of interstitial Fe atoms showed that striped magnetic ordering is maintained for $Fe_{1.06}S$. However, the interstitial Fe atoms develop large moments, which induce magnetic moments on the surrounding Fe_{net} sites, moments that decrease with distance from the interstitial atom. The consequence of the induced magnetic moments is a net magnetization (total magnetic moment) for the non-stoichiometric $Fe_{1.06}S$ phase. The addition of interstitial Fe atoms also changes the Fermi surface from that of stoichiometric "FeS", causing any nested wavevectors to be lost and suppressing superconductivity. Thus, although the electronic structure of tetragonal "FeS" does not reveal any electronic instability, this computational study indicates that careful control of reactant compositions are needed to avoid introducing non-stoichiometry. Furthermore, the presence and location of interstitial atoms, viz., Fe, in iron sulfides have profound influences on magnetic structure, which will interfere with the occurrence of superconductivity.

8.7 Acknowledgments.

J. B. would like to thank Dr. Fei Wang and Steven Yeninas for many helpful comments and suggestions. The authors acknowledge the generous financial support provided by the U.S. National Science Foundation (NSF DMR 08-06507).

8.8 References

(1) Hsu, F.-C.; Luo, J.-Y.; Yeh, K.-W.; Chen, T.-K.; Huang, T.-W.; Wu, P. M.; Lee, Y.-C.; Huang, Y.-L.; Chu, Y.-Y.; Yan, D.-C.*et al. Proc. Natl. Acad. Sci. USA* **2008**, *105*, 14262-14264.

(2) Lee, K. W.; Pardo, V.; Pickett, W. E. *Phys. Rev. B* **2008**, *78*, 1745021-1745025.

(3) McQueen, T. M.; Huang, Q.; Ksenofontov, V.; Felser, C.; Xu, Q.; Zandbergen, H.; Hor, Y. S.; Allred, J.; Williams, A. J.; Qu, D.*et al. Phys. Rev. B* **2009**, *79*, 0145221-01445227.

(4) Lumsden, M. D.; Christianson, A. D.; Goremychkin, E. A.; Nagler, S. E.; Mook, H. A.; Stone, M. B.; Abernathy, D. L.; Guidi, T.; MacDougall, G. J.; de la Cruz, C.*et al. Nat Phys* **2010**, *6*, 182-186.

(5) Wen, J.; Xu, G.; Xu, Z.; Lin, Z. W.; Li, Q.; Ratcliff, W.; Gu, G.; Tranquada, J. M. *Phys. Rev. B* **2009**, *80*, 1045061-1045064.

(6) Yeh, K.-W.; Huang, T.-W.; Huang, Y.-l.; Chen, T.-K.; Hsu, F.-C.; Wu, P. M.; Lee, Y.-C.; Chu, Y.-Y.; Chen, C.-L.; Luo, J.-Y.*et al. EPL (Europhysics Letters)* **2008**, *84*, 370021-370024.

(7) Williams, A. J.; McQueen, T. M.; Cava, R. J. *Solid State Comm.* **2009**, *149*, 1507-1509.

(8) McQueen, T. M.; Williams, A. J.; Stephens, P. W.; Tao, J.; Zhu, Y.; Ksenofontov, V.; Casper, F.; Felser, C.; Cava, R. J. *Phys. Rev. Lett.* **2009**, *103*, 0570021-0570024.

(9) Berner, R. A. *Science* **1962**, *137*, 669.

(10) Sweeney, R. E.; Kaplan, I. R. *Economic Geology* **1973**, *68*, 618-634.

(11) Lennie, A. R.; Redfern, S. A. T.; Champness, P. E.; Stoddart, C. P.; Schofield, P. F.; Vaughan, D. J. *American Mineralogist* **1997**, *82*, 302-309.

(12) Rickard, D.; Griffith, A.; Oldroyd, A.; Butler, I. B.; Lopez-Capel, E.; Manning, D. A. C.; Apperley, D. C. *Chemical Geology* **2006**, *235*, 286-298.

(13) Li, S.; de la Cruz, C.; Huang, Q.; Chen, Y.; Lynn, J. W.; Hu, J.; Huang, Y.-L.; Hsu, F.-C.; Yeh, K.-W.; Wu, M.-K.*et al. Phys. Rev. B* **2009**, *79*, 054503-054507.

(14) Subedi, A.; Zhang, L.; Singh, D. J.; Du, M. H. *Phys. Rev. B* **2008**, *78*, 1345141-1345146.

(15) Welz, D.; Rosenberg, M. *J. Phys. C: Solid State Phys.* **1987**, *20*, 3911-3924.

(16) Kwon, K. D.; Refson, K.; Bone, S.; Qiao, R.; Yang, W.-l.; Liu, Z.; Sposito, G. *Phys. Rev. B* **2011**, *83*, 0644021-0644027.

(17) Kresse, G.; Marsman, M.; Furthmuller, J. Vienna Ab-initio Simulation Package: VASP the GUIDE, 2010.

(18) Kresse, G.; Furthmüller, J. *Comput. Mater. Sci.* **1996**, *6*, 15-50.

(19) Kresse, G.; Furthmüller, J. *Phys. Rev. B* **1996**, *54*, 11169-11186.

(20) Kresse, G.; Hafner, J. *Phys. Rev. B* **1993**, *47*, 558-561.

(21) Andersen, O. K. *Phys. Rev. B* **1975**, *12*, 3060-3083.

(22) Andersen, O. K.; Jepsen, O. *Phys. Rev. Lett.* **1984**, *53*, 2571-2574.

(23) Dronskowski, R.; Blöchl, P. E. *J. Phys. Chem.* **1993**, *97*, 8617-8624.

(24) Kresse, G.; Marsman, M.; Furthmuller, J. Vienna Ab-initio Simulation Package: VASP the GUIDE, 2010.

(25) Blöchl, P. E. *Phys. Rev. B* **1994**, *50*, 17953-17979.

(26) Kresse, G.; Joubert, D. *Phys. Rev. B* **1999**, *59*, 1758-1775.
(27) Perdew, J. P.; Burke, K.; Ernzerhof, M. *Phys. Rev. Lett.* **1996**, *77*, 3865-3868.
(28) Monkhorst, H. J.; Pack, J. D. *Phys. Rev. B* **1976**, *13*, 5188-5192.
(29) Devey, A. J.; Grau-Crespo, R.; de Leeuw, N. H. *J. Phys. Chem. C* **2008**, *112*, 10960-10967.
(30) Krier, G.; Jepsen, O.; Burkhardt, A.; Andersen, O. K. TB-LMTO-ASA Program; 4.7 ed.; Max Planck Institute for Solid State Research: Stuttgart, Germany, 1995.
(31) Bučko, T.; Hafner, J.; Lebégue, S.; Ángyán, J. G. *J. Phys. Chem. A* **2010**, *114*, 11814-11824.
(32) Grimme, S. *J. Comp. Chem.* **2006**, *27*, 1787-1799.
(33) Bronger, W.; Kyas, A.; Muller, P. *J. Solid State Chem.* **1987**, *70*, 262-270.
(34) Rickard, D.; III, G. W. L. *Chem. Rev.* **2007**, *107*, 514-562.
(35) Ellner, M. *J. Less-Common Metals* **1976**, *48*, 21-52.
(36) Tengner, S. *Z. Anorg. Allg. Chem.* **1938**, *239*, 126-132.
(37) Bader, R. *Atoms in Molecules: A Quantum Theory*; Oxford University Press: New York, 1990.
(38) Ewald, P. *Ann. Phys. (Leipzig)* **1921**, *64*, 253-287.
(39) Henkelman, G.; Arnaldsson, A.; Jónsson, H. *Comput. Mater. Sci.* **2006**, *36*, 354-360.
(40) Dronskowski, R.; Korczak, K.; Lueken, H.; Walter, J. *Angew. Chem. Int. Ed.* **2002**, *41*, 2528-2532.
(41) Landrum, G. A.; Dronskowski, R. *Angew. Chem. Int. Ed.* **1999**, *38*, 1389-1393.
(42) Silvestre, J.; Hoffmann, R. *Inorg. Chem.* **1985**, *24*, 4108-4119.
(43) Li, Y.-F.; Zhu, L.-F.; Guo, S.-D.; Xu, Y.-C.; Liu, B.-G. *J. Phys.: Condens. Matter* **2009**, *21*, 1157011-1157005.
(44) Bao, W.; Qiu, Y.; Huang, Q.; Green, M. A.; Zajdel, P.; Fitzsimmons, M. R.; Zhernenkov, M.; Chang, S.; Fang, M.; Qian, B.*et al. Phys. Rev. Lett.* **2009**, *102*, 2470011-2470014.
(45) Zhang, L.; Singh, D. J.; Du, M. H. *Phys. Rev. B* **2009**, *79*, 0125061-0125064.
(46) Han, M. J.; Savrasov, S. Y. *Phys. Rev. Lett.* **2009**, *103*, 0670011-0670014.

8.9 Supporting Information

Table S1. Optimized parameters for various structural models of $Fe_{1+x}S$. In all cases, interstitial Fe atoms occupy Position I to create supercells of tetragonal "FeS." Values shown in *italics* are based on linear extrapolation of computationally optimized values at higher Fe content.

	FeS	*$Fe_{1.019}S$*	*$Fe_{1.056}S$*	*$Fe_{1.063}S$*	$Fe_{1.125}S$	$Fe_{1.25}S$	$Fe_{1.375}S$	$Fe_{1.50}S$	$Fe_{1.75}S$	Fe_2S	Berner's Report
a (Å)	3.580	*3.588*	*3.594*	*3.595*	3.609	3.627	3.620	3.654	3.644	3.542	3.679
c (Å)	5.651	*5.565*	*5.526*	*5.519*	5.427	5.232	5.073	5.116	5.144	5.453	5.047
V ($Å^3$)	72.43	*71.64*	*71.37*	*71.33*	70.69	68.83	66.49	66.46	68.31	68.41	68.31

c/a	1.578	*1.551*	*1.538*	*1.535*	1.504	1.443	1.401	1.398	1.411	1.534	1.372

Table S2: Average charge determined using Bader's analysis.

	Bader's Charge (Average)									
Position	FeS	$Fe_{1.019}S$	$Fe_{1.056}S$	$Fe_{1.063}S$	$Fe_{1.125}S$	$Fe_{1.25}S$	$Fe_{1.375}S$	$Fe_{1.50}S$	$Fe_{1.75}S$	Fe_2S
Fe_{int}	–––	+0.775	+0.718	+0.784	+0.822	+0.770	+0.779	+0.632	+0.671	+0.560
$Fe_{net}1$	–––	+0.789	+0.746	+0.769	+0.779	+0.817	+0.816	+0.776	+0.778	+0.623
$Fe_{net}2$	+0.817	+0.767	+0.779	+0.814	+0.833	+0.815	–––	+0.778	–––	–––
S1	–––	–0.942	–0.900	–1.104	–1.120	–1.137	–1.085	–1.093	–1.255	–1.220
S2	–0.817	–0.782	–0.789	–0.816	–0.840	–0.869	–––	–––	–––	–––

$Fe_{net}1$	square-net nearest to the interstitial
$Fe_{net}2$	rest of the square net
S1	sulfur nearest to the interstitial
S2	rest of the sulfur atoms

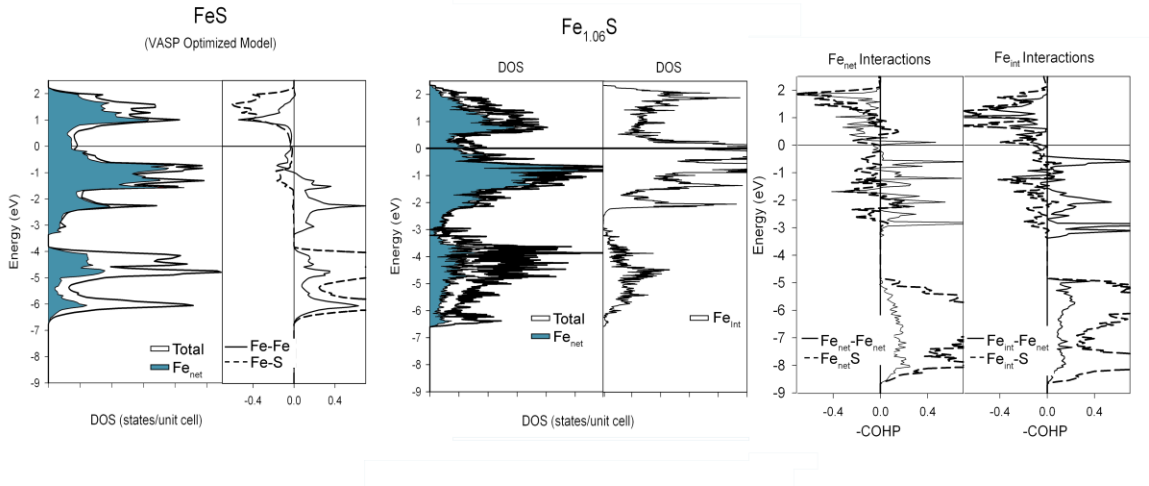

Figure S1. Electronic structure of "FeS" using *VASP* optimized parameters and $Fe_{1.06}S$.

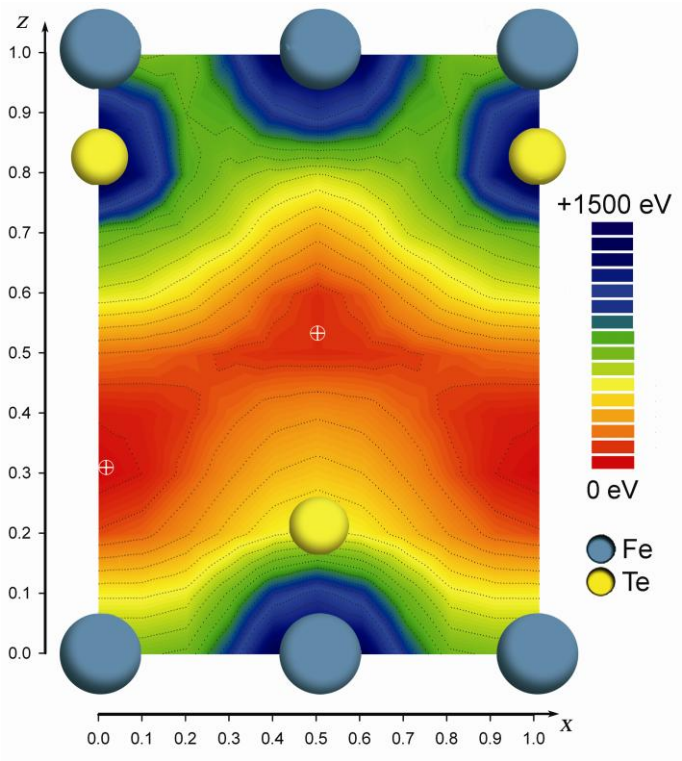

Figure S2. Contour plot of the potential energy surface for locating interstitial Fe atoms in the $y = ½$ plane of "FeTe." Energies are given in a logarithmic scale and are presented relative to the interstitial site with lowest potential energy. The lowest energy point occurs at (0 ½ 0.333), position II in Figure 4.

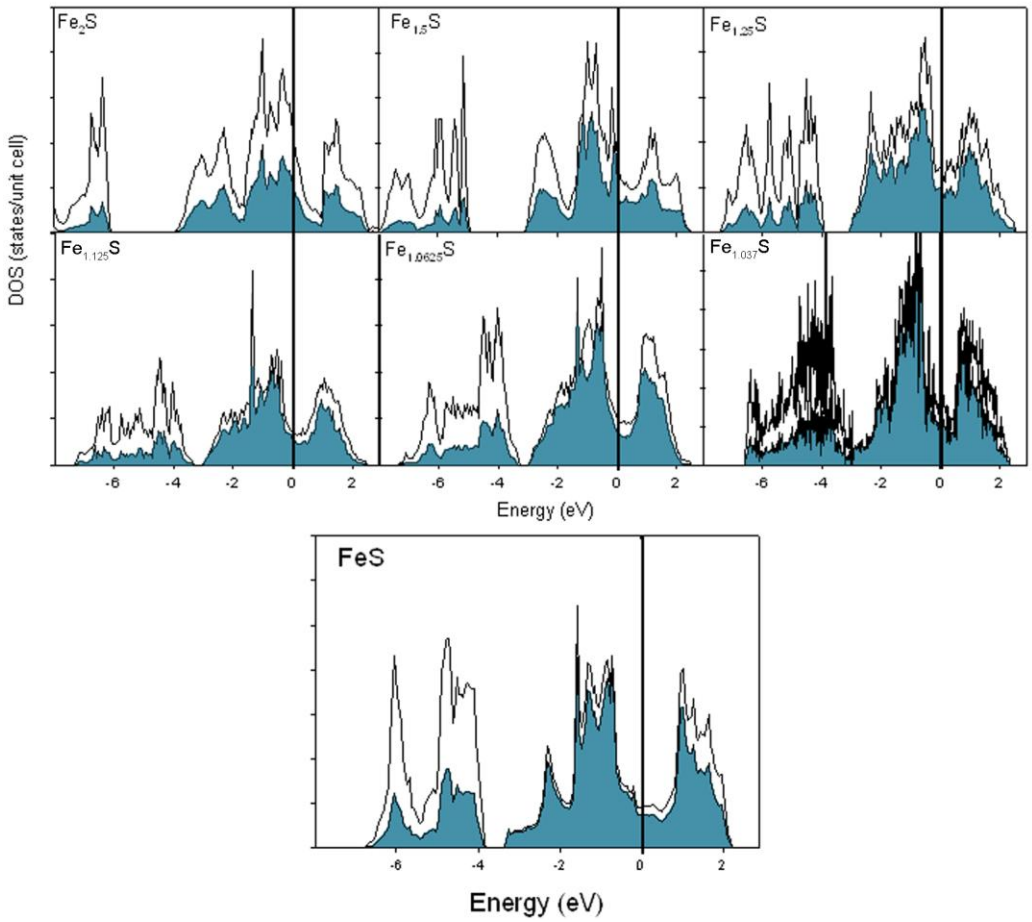

Figure S3. The spin-polarized DOS for the supercells models are listed by composition. The shaded areas are the orbital contributions from the Fe-square net only.

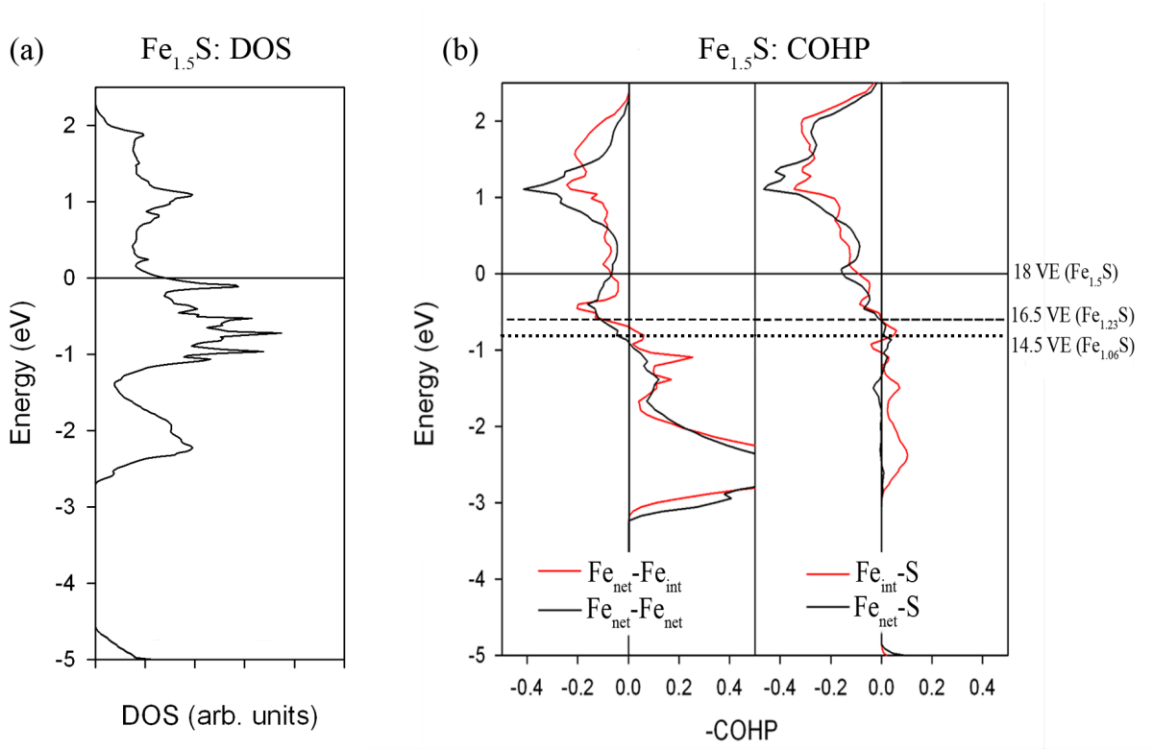

Figure S4. (a) Total DOS for $Fe_{1.5}S$ (b) The –COHP curves for $Fe_{1.5}S$. The E_F is set to 18 VE while the electron counts (and corresponding compositions) are determined using a rigid band approximation.

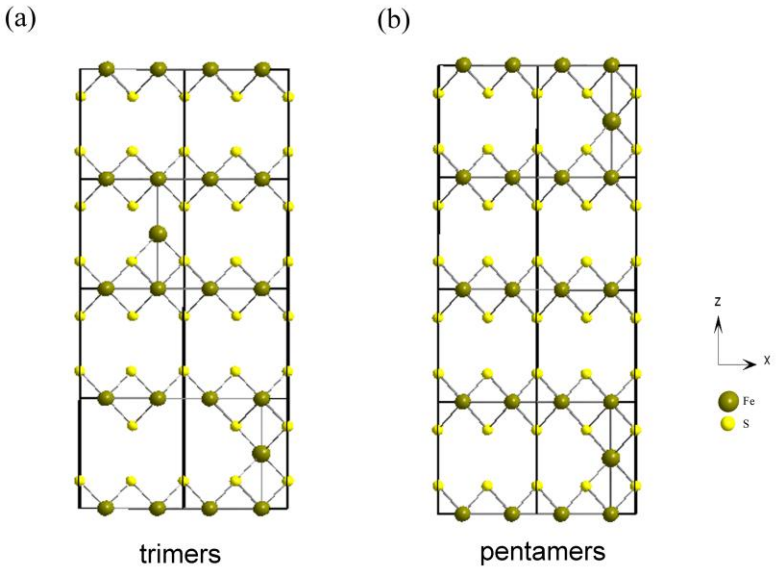

Figure S5. The supercell models used to predict the preferred interstitial atoms arrangement. (a) the isolated trimers. (b) the pentamers.

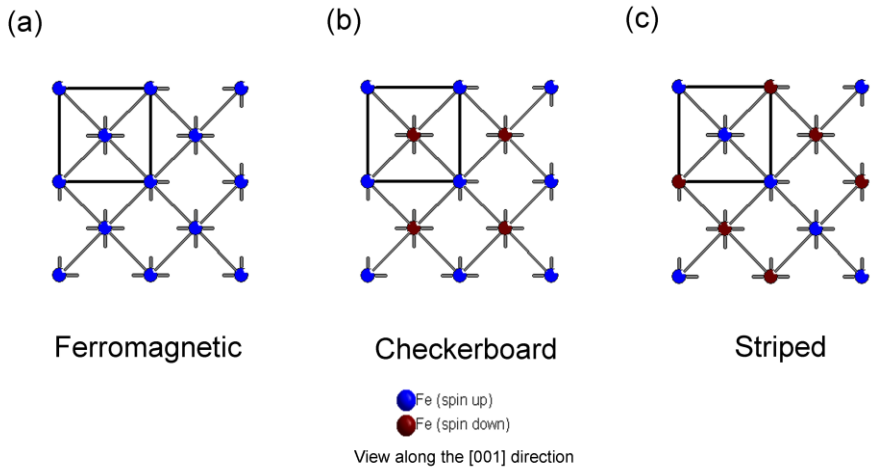

Figure S6 Magnetic models of "FeS" super cell (i) for the (a) ferromagnetic model, (b) checkerboard model, and (c)the striped magnetic model. A crystallographic unit cell is shown and the sulfur atoms are omitted for clarity. Models of "$Fe_{1.06}S$" were created by placing an interstitial atom in Position I and using these models for as the initial magnetic ordering. In this case, two checkerboard models (1) with the Fe_{int} antiferromagnetically coupled to the Fe_{net} whereas (2) places the Fe_{int} ferromagnetically to the Fe_{net}.

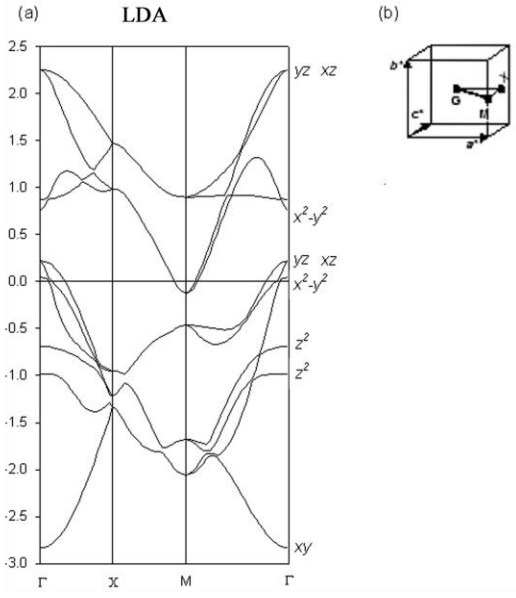

Figure S7. (a) LDA band structure of "FeS" of the Fe 3*d*-bands. The special points were chosen to show the electron hold and pocket. The bands are labeled by orbital on the right hand side. (b) the first Brillion zone for "FeS" showing the special points sampled in the band structure.

CHAPTER 9

General Conclusions and Future Work

This research primarily investigated the relationship between the composition, structure, and properties in two classes of intermetallic borides. We strived to understand how changing the composition would affect the formation of a given structure type and how the new composition would change the physical properties. By drawing conclusions from each of the chapters presented herein, we have started to establish a set of "signs" that can be used to target compositions with the desired structure type and physical properties.

Exploring the chemistry of these two phases by modifying the valence electron (VE) count, a range of electronic stability was sought. Initially, an upper-limit of the VE count for the $M_9M'_2T_{18}B_8$ structure was identified. Based on the orbital overlap population (COHP) curves, the Ru-Ti bonds are optimized at 228 VE. Beyond these electron counts, unidentified products are formed experimentally. Furthermore, an analysis of the magnetic ladder site shows the presence of antibonding orbitals above 220 VE ($Ti_9Fe_2Ru_{18}B_8$) with complete filling of these orbitals near 228 VE. Thus, the electronic stability of $M_9M'_2T_{18}B_8$ has a calculated VE limit of ca. 228 VE. The most electron-rich system synthesized, thus far, contains 230 VE ($Ti_8Ni_3Ru_{18}B_8$).

This work, however, was unable to definitively identify a lower limit for the stability of the structure. Since the ladder motif is the only subunit distinguishing the two structure types, identifying the minimum number of electrons necessary at this site will indeed help in identifying the range of electronic stability. It has been shown that the bonding interactions between the ladder, i.e., M′- M′ contacts, lie in a non-bonding region of the DOS at ca. 220 VE. Thus, reducing the VE count likely affects the electronic stability of the ladder motif negatively. Additionally, experimental results have shown that at least 4.5 VE (per M′ atom) are necessary for the formation of the ladder site. A computational investigation could help identify why a lower limit exists and how it can be modified to stabilize the structure. Ultimately, these additional signs

regarding the VE count can be added to those presented here to develop a comprehensive guide for the synthesis of these two phases.

An added development was the identification of a site preference in the $M_2M'T_5B_2$ structure. By determining where atomic substitution will occur, it was possible to predict how the magnetic structure will respond as a function of composition. For instance, with two potential substitution sites in the $M_2M'T_5B_2$ system, it was difficult to identify the effect substitution site may have on the structure. However, the new results indicated the location of the electron-rich atom in fact plays an important role in the magnetic structure. When the electron-rich atom was located as a nearest neighbor to the Fe atom, the magnetic exchange constant was larger than when it was located as the next nearest neighbor. Since the site preference was controlled primarily by the site energy term, i.e., the number of electrons at a given site, future systems can be tailored using the signs identified in Chapter 4 to direct atomic substitution. These rules can now be expanded to the more complex $M_9M'_2T_{18}B_8$ system. Rather than two independent T atom sites, this structure contains five T atom positions. With such a multitude of potential substitution patterns, this system will be ideal to determine the validity of the substitution rules posed from the simpler $M_2M'T_5B_2$ structure and confirm the effect on magnetic ordering.

Establishing the magnetic ordering in $M_9M'_2T_{18}B_8$ and $M_2M'T_5B_2$ was rather straightforward because the distance between magnetic atoms was short enough to complete a COHP analysis. The increased number of magnetic exchange pathways in the $M_{9-x}M'_{2+x}T_{18}B_8$ system results in a more complicated magnetic structure requiring an extension beyond the direct approaches (COHP) completed previously. By replacing all of the M atoms with M′ atoms, i.e., $x = 3$, magnetic models varying the initial spins were created. The DOS's of models were integrated to the desired Fermi level under the rigid band approximation using Simpson's (tetrahedron) method. In the case of $Ti_6Fe_5Ru_{18}B_8$, integrating to 220 VE predicted ferromagnetism with a transition to ferrimagnetism above 223 VE, both are in agreement with experimental observations. This approach can now be applied to additional systems that contain indirect, or through-bond, magnetic interactions to determine the preferred magnetic ordering at a given VE count. Future

work on these systems will also involve the determination of the effective exchange parameters between the magnetic atoms. These calculations will be useful to identify the communication pathways between each of the magnetic atoms.

Finally, an investigation of tetragonal iron sulfide ($Fe_{1+x}S$) deduced the changes in electronic structure as a function of interstitial Fe content (x). The additional Fe atoms are drawn into the van der Waal's layer by electrostatic forces; however, the additional electrons occupy antibonding orbitals. Hence, there is a subtle interplay between the two forces that results in a limited amount of additional Fe occupation. By adding just a few, ca. 0.5, electrons the Fermi surface does change dramatically accompanied by the formation of a spin-density wave. Since both of these factors would greatly affect the formation of a superconducting state, limiting the amount of interstitial Fe is likely key in producing a superconducting state for these systems. Future work will involve the identification of optimal interstitial concentrations in the FeSe and FeTe phases. Since these systems are known superconductors, there have been numerous publication on their electronic structure. Yet, these previous models do not account for the possibility of interstitials. Determining how electronic structure, mainly the Fermi surface, changes with excess Fe will allow future solid state chemists to adapt they synthetic approach and hopefully discover the origin of superconductivity in these phases.